



HAL
open science

Mapping Tunneling Nanotubes In Vitro & In Vivo: A Structural Approach

Diégo Cordero Cervantes

► **To cite this version:**

Diégo Cordero Cervantes. Mapping Tunneling Nanotubes In Vitro & In Vivo: A Structural Approach. Cellular Biology. Université Paris Saclay, 2019. English. NNT : 2019SACLS534 . tel-04067232

HAL Id: tel-04067232

<https://pasteur.hal.science/tel-04067232>

Submitted on 13 Apr 2023

HAL is a multi-disciplinary open access archive for the deposit and dissemination of scientific research documents, whether they are published or not. The documents may come from teaching and research institutions in France or abroad, or from public or private research centers.

L'archive ouverte pluridisciplinaire **HAL**, est destinée au dépôt et à la diffusion de documents scientifiques de niveau recherche, publiés ou non, émanant des établissements d'enseignement et de recherche français ou étrangers, des laboratoires publics ou privés.



Mapping Tunneling Nanotubes *In Vitro & In Vivo:* A Structural Approach

Thèse de doctorat de l'Université Paris-Saclay préparée à l'Institut Pasteur

École doctorale n°577:
Structure et Dynamique des Systèmes Vivants

Thèse présentée et soutenue à Paris de soutenance, le 3 décembre 2019, par

Diégo Cordero Cervantes

Composition du Jury:

Philippe Vernier , Directeur de Recherche Institut des Neurosciences Paris-Saclay	Président
Ludovic Galas , Ingénieur de Recherche INSERM à l'Université de Rouen	Rapporteur
Thierry Galli , Directeur de Recherche Institut Jacques Monod	Rapporteur
Jean Livet , Directeur de Recherche Institut de la Vision	Examineur
Xavier Nicol , Chargé de recherche Institut de la Vision	Examineur
Chiara Zurzolo , Directrice de Recherche Institut Pasteur	Directrice de thèse

Mapping Tunneling Nanotubes *In Vitro* & *In Vivo*: A Structural Approach

Keywords: Tunneling Nanotubes, Actin, Neuronal communication, Cerebellum, Connectomics

Abstract: Inter-cellular communication has long been thought to be governed by juxta-, endo-, and paracrine signaling, tight junctions, and more recently, exosomes. However, large efforts from our and other groups revealed that Tunneling Nanotubes (TNTs), actin-rich membranous protrusions that connect the cytoplasm of distant cells and allow the dynamic inter-cellular transport of biological cargo, also provide the infrastructure and machinery for effective cell-to-cell communication. Despite significant progress made to unveil TNT-mediated cell communication, the characterization of these novel organelles has been limited by unanswered questions that hail from the lack of both molecular and structural information. Exploring these gaps in the field using a series of state-of-the-art tools and novel approaches became the main focus of my dissertation. Specifically, I explored the specific role of actin-regulator complexes in the formation of TNTs connecting neuronal cells. My analyses show that molecular pathways known to be involved in the formation of other membranous protrusions behave differently in the generation of TNTs. By employing live imaging microscopy, cryo-correlative electron microscopy and tomography approaches, I also studied the nano-architecture of neuronal TNTs. My findings demonstrated that TNTs of neuronal cells are comprised of multiple individual TNTs capable of transporting vesicles and mitochondria. Owing to the difficulties of identifying TNTs *in vivo*, my work also focused on the implementation of a structural *Connectomic* approach to detect TNTs in tissue without the need for a TNT-specific marker. My findings indicate that TNT-like structures connect migratory cerebellar granule cells of neonate mice, suggesting that inter-cellular communication during migratory events in the brain could be mediated by TNT-like processes. Skeletonization of the structures identified provide my findings with geometrical information that can be compared with observations made by corroborative dye-coupling experiments. Taken together, my dissertation work sheds light on the formation and structure of neuronal TNTs *in vitro*, and novel approaches for the identification of TNTs *in vivo*.

Caractérisation des *Tunneling Nanotubes In Vitro et In Vivo*: Une approche structurale

Mots clefs: Tunneling Nanotubes, Actine, communication neuronale, cervelet, Connectomics

Resumé: On a longtemps pensé que la communication intercellulaire était essentiellement régie par les signalisations juxta-, endo- et paracrine, les *gap junctions* et, plus récemment, les *exosomes*. Cependant, les travaux de plusieurs groupes dont le nôtre ont révélé que les *Tunneling Nanotubes* (TNT), des protrusions membranaires riches en actine qui relient le cytoplasme de cellules distantes et permettent le transport intercellulaire dynamique de leur contenu biologique, fournissent également l'infrastructure et les machines pour une communication efficace entre cellules. Malgré des progrès significatifs, la caractérisation de ces nouveaux organites a été limitée par le manque d'informations moléculaires et structurelles. Comblar ces lacunes à l'aide d'une série d'outils de pointe et d'approches novatrices est devenu l'objectif principal de ma thèse. Plus précisément, j'ai exploré le rôle des complexes régulateurs de l'actine dans la formation des TNT reliant les cellules neuronales. Mes analyses montrent que les voies moléculaires connues pour être impliquées dans la formation d'autres protrusions membranaires régulent différemment la génération des TNT. En utilisant la microscopie par imagerie en direct, la microscopie électronique cryocorrélative et la tomographie, j'ai également étudié la nano-architecture des TNT neuronaux. Mes découvertes ont démontré que les TNT des cellules neuronales sont composés de plusieurs TNT individuels permettant le passage de vésicules et de mitochondries. En raison des difficultés d'identification des TNT *in vivo*, mes travaux ont également porté sur la mise en œuvre d'une approche « Connectomic » structurale pour détecter les TNT dans les tissus sans avoir besoin d'un marqueur spécifique de TNT. Mes résultats indiquent que des structures de type TNT relient les cellules granulaires cérébelleuses migratrices des souris nouveau-nées, ce qui suggère que la communication intercellulaire pendant des événements migratoires dans le cerveau pourrait être médiée par des processus mettant en jeu des TNT. La squelettisation des structures identifiées fournit des informations géométriques qui corroborent les observations faites dans des expériences de couplage de colorants. L'ensemble de mes travaux de thèse fait la lumière sur la formation et la structure des TNT neuronaux *in vitro* et sur de nouvelles approches pour l'identification des TNT *in vivo*.

Preface

The work presented in this thesis consists of an introduction (Chapter 1), two published articles (Chapter 2 and 3), and significant progress towards unpublished research (Chapter 4). The papers are listed below (*co-author) followed with a description of my contributions to each project; my contributions are also stated in the *Contributions* section of each chapter (see Table of Contents).

Chapter 2 (Article 1): Delage, E., **Cordero Cervantes, D.***, Pénard, E.*, Schmitt, C., Syan, S., Disanza, A., Scita, G., and Zurzolo, C. (2016). Differential identity of Filopodia and Tunneling Nanotubes revealed by the opposite functions of actin regulatory complexes. *Scientific Reports* 6, 39632.

In this project, in which I contributed equally as a second author when the study was well-advanced, we addressed the role of specific actin modifiers in the formation of TNTs in contrast to filopodia. I studied the role of Rac1 in the formation of neuronal TNTs by ectopic expression of the dominant negative- and constitutively active- form of the protein. Specifically, I performed the experiments, acquired the images, and manually analyzed the data collected to prepare Supplementary Figure 2. By Western Blotting, I also evaluated the expression of Eps8 in CAD and CHO cells, as well as brain (hippocampus and striatum) lysates, (see Supplementary Figure 6a). In addition, I examined the mRNA expression of Eps8 by RT-PCR in the cell lines above, (see Supplementary Figure 6b). I integrated my results and figures into the manuscript and replaced panels in Figure 1 and 5 with more representative, re-processed images. Finally, I updated several sections of the manuscript, including the Introduction, Results, Discussion, Methods, and Bibliography, and rephrased several key points throughout these sections. This work was carried out during the two-revision, peer-review process of the manuscript, which I handled all-throughout until publication of the article.

Chapter 3 (Article 2): Sartori-Rupp, A.*, **Cordero Cervantes, D.***, Pepe, A.*, Gousset, K., Delage, E., Corroyer-Dulmont, S., Schmitt, C., Krijnse-Locker, J., and Zurzolo, C. (2019). Correlative cryo-electron microscopy reveals the structure of TNTs in neuronal cells. *Nature Communications* 10, 342.

In this project, we designed and optimized a cryo-correlative electron microscopy (cryo-CLEM) approach to characterize the structure of TNTs at the nanometer resolution. I participated and contributed equally with the other two first authors in different aspects of the study. Specifically, I studied the role of Arp2/3 in the formation of neuronal TNTs by testing an Arp2/3 specific inhibitor (CK-666) in CAD cells. To this end, I performed the experiments, acquired the images, and manually analyzed the data collected to prepare Supplementary Figure 3c-3d. Setting up these experiments was fundamental for this project as CK-666 treatment of cells was used to increase the yield of TNTs on cryo-EM grids. I also labeled-, imaged-, and identified regions of interest (filopodia emanating from CAD cells) for the cryo-CLEM/cryo-electron tomography micrographs shown in Figure 5. I also obtained the cryo-TEM micrographs shown in Supplementary Figure 6, performed all the live-imaging experiments in the manuscript and implemented a plugin to analyze the speed of mitochondrial transport via TNTs (see Figure 6 and Supplementary Figure 5). I assisted with the manual analysis of cryo-ET images by computing plot profiles and fast Fourier transforms described in the manuscript and shown in Figure 4 and 5. Moreover, I contributed to the manual segmentation of TNTs in FIB-SEM volumes and re-processing electron micrographs throughout the manuscript for the preparation of figures (i.e. image stitching, alignment, enhancement, and addition of overlays and tracings). I designed and created the schematic diagrams found in Figure 1a and Figure 8. My role also included teaching one of the co-first authors (i) the protocols employed to study the effect of CK-666 in CAD cells' adherent filopodia and TNT function (see Supplementary Figure 3a-3b and 3e-3f); and (ii) the methods used to prepare samples for cryo-TEM and identification of TNTs on EM grids. Finally, I wrote the manuscript, assembled all the main and Supplementary Figures, as well as Supplementary Movies. I assembled, revised, submitted, and handled the manuscript throughout the three rounds of peer revision until publication of the article.

Acknowledgements

First, I'd like to thank Dr. Chiara Zurzolo for giving me the chance to carry out my thesis in her lab and build a project from the feet up, putting her full confidence on my practical and intellectual abilities. I trust that the lessons I learned in her lab will have a lasting impact on my future career.

I would also like to thank all the current and former members of the *Traffic & Membrane Pathogenesis Unit* for all the fun and engaging interactions we had inside and outside the laboratory over the last few years. To the members of the *Ultrastructural BioImaging Unit* and *Image Analysis hub*: thank you for all your help, it was a great pleasure working with you.

To the members of my dissertation committee: Dr. Thierry Galli, Dr. Pierre Marie Lledo, and Dr. Isabelle Cloez-Tayarani, thank you for your time, feedback, and invigorating support.

To my scientific collaborators: Dr. Jeff Lichtman (and laboratory members), thank you for welcoming me in your lab on numerous occasions and sharing your technical expertise; to Dr. Laurence Cathala and Dr. David DiGregorio, thank you for believing in my scientific quest and committing your efforts and infrastructure to my project; to William Silversmith of the Seung lab, thank you for offering your expertise and sharing your computational tools with me.

To Susanna Celli and the rest of the Pasteur-Paris University steering committee: thank you for supporting my studies and my student organization – *Graphics Visual Association (GVA)*.

To all the trainee students I had the pleasure of working with Santa Berzina, Ozlem Özen, Marie-Madeleine Trottmann, Owen Mulhern, Maximiliana Bogan, Neven Borak, Rio McLellan, Alexander Mancevski, Eric Sun, and Alex Atkin – thank you so much for your time and great work.

To my scientific and career mentor: Dr. Lida Katsimpardi, without whom I would have never made the bold 'move' to embark on a PhD in Europe, thank you for your great advice and support.

To my family – my mom, dad, and brother: *gracias por el constante apoyo a través de una formación académica exhaustiva que ha durado mas de 20 años. El empuje que me dieron en todos los aspectos me ayudó a metamorfosearme en una persona altamente calificado para enfrentar desafíos del primer mundo.*

For my family & Josephine

Contents

Title Page.....	i
Abstract(s)	ii
Preface	iii
Acknowledgements	iv
Dedication	vi
Contents.....	vii
Acronyms & Abbreviations	viii
List of Figures	xi
1 Tunneling Nanotube-mediated Cellular Connectivity & Communication	1
1.1 Introduction to Cell to Cell Communication	2
1.2 Introduction to Tunneling Nanotubes	5
1.3 Methods and Criteria used for the study of Tunneling Nanotubes	9
1.3.1 Tunneling Nanotubes: Denotation <i>In Vitro</i>	9
1.3.2 Preservation of Tunneling Nanotubes	9
1.3.3 Labeling of Tunneling Nanotubes and Actin Backbone.....	11
1.3.4 Detection by Microscopy	11
1.3.5 Quantitative Assessment	12
1.4 Tunneling Nanotubes: Biogenesis	14
1.4.1 Cell dislodgement mechanism	14
1.4.2 Actin-driven protrusion mechanism	15
1.4.2.1 Filopodia: Introduction.....	17
1.4.2.2 Filopodia: Mechanisms of Formation.....	19
1.4.2.3 Filopodia: Ultra-Structure.....	23
1.5 Tunneling Nanotubes: Molecular Formation.....	25
1.5.1 Role of Actin Cytoskeleton and Actin Protein Regulators.....	25
1.5.2 Rab Cascades.....	26
1.5.3 PI3K/AKT/mTOR Signaling Pathway.....	29
1.5.4 M-Sec/TNFAip2/B94.....	29
1.5.5 MyosinX	30
1.6 Tunneling Nanotubes: Intrinsic and Extrinsic Induction.....	32
1.6.1 Reactive Oxygen Species.....	32
1.6.2 Hypoxia	33
1.6.3 Apoptosis Signaling	33
1.6.4 Stressful Environment.....	34
1.7 Tunneling Nanotube: Ultra-Structure.....	36
1.8 Tunneling Nanotube-like structures <i>In Vivo</i>	41
1.9 Roles in Disease	46
1.9.1 Neurodegenerative Diseases	46
1.9.2 Viral Diseases	48

1.9.3	Bacterial Infection	48
1.9.4	Cancer	49
1.10	References	51
2	<i>Role of Actin Regulatory Networks in Neuronal Tunneling Nanotube Formation.....</i>	65
2.1	Results.....	66
2.1.1	Summary	66
2.1.2	Aims of the project.....	66
2.1.3	Contribution	67
2.1.4	Article 1: Differential identity of Filopodia and Tunneling Nanotubes revealed by the opposite functions of actin regulatory complexes.....	68
3	<i>Tunneling Nanotubes: Ultra-Structural Identity Missing Links.....</i>	90
3.1	Results.....	91
	Summary	91
3.1.1	Aims of the project.....	92
3.1.2	Contribution	92
3.1.3	Article 2: Correlative cryo-electron microscopy reveals the structure of TNTs in neuronal cells	94
4	<i>Mapping of Tunneling Nanotube-Like Structures In the Developing Cerebellum.....</i>	122
4.1	Introduction	123
4.1.1	Connectomics.....	123
4.1.1.1	Nano-Connectomics: Wiring Diagrams	124
4.1.2	From Connectomics to Tunneling Nanotubes: Paving the Road.....	127
4.1.2.1	Neuronal Tunneling Nanotubes	127
4.1.2.2	<i>In Vivo</i> Tunneling Nanotube-like structures	127
4.1.3	Survey of the Developing Cerebellum for Tunneling Nanotubes.....	127
4.1.3.1	Cerebellum Anatomy and Ontogenesis.....	127
4.1.3.2	External Granule Layer	128
4.2	Results.....	132
4.2.1	Datasets	132
4.2.2	GCPs form Tunneling Nanotube-like connections	134
4.2.3	3D skeletonization of meshes reveals geometrical features.	136
4.2.4	Orientation of GCP-GCP vs. dividing GCPs	138
4.2.5	Assessment of dividing GCPs in the EGL	143
4.2.6	Dye-coupling reveals GCP TNT-like structure connectivity	146
4.3	Methods.....	150
4.3.1	Connectomics.....	150
4.3.1.1	Sample preparation	150
4.3.1.2	Image Visualization	151
4.3.2	Skeletonization.....	151
4.3.3	Angle Measurements	151
4.3.4	Immunohistochemistry	154
4.3.5	Microscopy.....	154
4.3.6	Image Analysis.....	154
4.3.7	Dye Coupling	155

4.4	Discussion	156
4.5	References	161
5	<i>Dissertation Perspectives</i>	165
5.1	Conclusion and future work.....	165

Acronyms and Abbreviations

-A-

AI Artificial intelligence	12
Arp2/3 Actin-related protein 2/3.....	19

-B-

BHK-21 Baby hamster kidney 21.....	7
BMP Bone morphogenetic protein	39

-C-

CAD Cath.a-differentiated.....	6
CDC42 Cell Division Control Protein 42.....	21
cryo-ET cryo-electron tomography	23
cryo-TEM Cryo-transmission electron microscopy	23
Cx43 Connexin 43	2

-D-

DIC Differential interference contrast	12
--	----

-E-

EB Epithelial bridges	7
Eps8 Epidermal growth factor receptor kinase substrate 8.....	21
EV Extracellular vesicle	3

-F-

FACS Fluorescence Activated Cell Sorting.....	13
Fgf Fibroblast growth factor	39

-G-

GEF Guanine nucleotide Exchange Factor	26
GJ Gap Junction.....	2

-H-

HEK Human Embryonic Kidney	5
HeLa Henrietta Lacks	12
HIV-1 Immunodeficiency Virus Type 1.....	31
HSC Human Stem Cell	40

-I-

I-BAR Bin/Amphiphysin/Rvs.....	19
IGL Inner Granule Layer	120
ILV Intraluminal vesicle	3
IP3 Inositol triphosphate.....	2
IRSp53 Insulin Receptor Tyrosine kinase substrate	21

-L-

LSCM Laser scanning confocal microscopy.....	12
--	----

-M-	
MDCK Madine-Darby canine kidney	12
MEF Mouse Embryonic Fibroblasts.....	21
ML Machine learning	12
mTOR Mammalian target of rapamycin	29
MV Microvesicle	3
MVE Multivesicular endosome	3
-N-	
NEF Negative Regulatory factor	31
NK Natural Killer.....	5
NRK Normal Rat Kidney	5
N-WASP Neural-WASP	21
-P-	
PC12 Pheochromocytoma 12.....	5
PI3K Phosphatidylinositol-3-kinase.....	29
PMC primary mesenchyme cell	38
-R-	
Rab Ras-related proteins in brain	26
Rac1 Ras-related C3 botulinum toxin substrate	21
RASSF1A Ras association domain family 1 isoform A	27
RC Ring Canal	39
REF52 Rat Embryonic Fibroblasts 52.....	12
-S-	
Shh Sonic hedgehog	39
SMC Secondary mesenchyme cell	38
-T-	
TM Tumor microtube.....	7
TNF Tumor Necrosis Factor.....	3
TNFAIP2 TNF- α induced protein 2	29
TNT Tunneling Nanotube	5
-V-	
VAMP3 v-SNARE Vesicle-associated membrane protein 3	26
VASP Vasodilator-stimulated phosphoprotein	19
-W-	
WASP Wiskott-Aldrich syndrome protein.....	21
WAVE WASP-family verprolin homologous protein	21
WAVE2 WASP family verprolin-homologous 2	26
WGA Wheat Germ Agglutinin	5
Wnt Wingless-related integration site.....	39

List of Figures

Figure 1. Modes of Inter-cellular Communication.	4
Figure 2. Topological Architecture of Tunneling Nanotubes.....	6
Figure 3. Properties that define Tunneling Nanotubes.....	10
Figure 4. Mechanisms of Tunneling Nanotube Biogenesis.	16
Figure 5. Examples of filopodia.	18
Figure 6. Arp2/3 and Formins: two major actin-nucleating machineries.....	20
Figure 7. Filopodia formation by CDC42, IRSp53, and VASP.	22
Figure 8. Ultra-structure Architecture of filopodia.	24
Figure 9. Regulation of Tunneling Nanotubes by Rab11a-Rab8a-VAMP3 cascade.	28
Figure 10. TNT formation and induction.	35
Figure 11. Ultra-structural analyses of Tunneling Nanotubes.....	40
Figure 12. Examples of TNT-like structures in vivo.	45
Figure 13. Model of prion-like protein aggregate–induced formation of TNTs.	47
Figure 16. Connectomics by serial-sectioning scanning electron microscopy.	126
Figure 17. Cerebellar granule cell migration during development.	129
Figure 18. Granule cell progenitor morphology characterization.....	131
Figure 19. Datasets produced by Serial-Sectioning Scanning Electron Microscopy.....	133
Figure 20. ssSEM Reveals TNT-like connections between GCPs.	135
Figure 21. Skeletonization of TNT-like connections.	137
Figure 22. Connected GCPs exhibit perpendicular orientation.....	140
Figure 23. Identification of GCPs undergoing division.	142
Figure 24. Quantification of PH3+ cells in the Developing Cerebellum.	145
Figure 25. Dye-coupling between GCPs in the EGL reveal TNT-like structures.....	149

Chapter 1

1 Tunneling Nanotube-mediated Cellular Connectivity & Communication

1.1 Introduction to Cell to Cell Communication

From the discovery of the cell by English polymath, Robert Hooke, in 1665 (Hooke, 1665), humans have embarked on the quest to better understand the building blocks that sustain life, and ultimately allow us to feel and think. This 354-year old ongoing voyage has revealed that cells interact in a vast universe in elegant harmony (Cajal, 1888; de Duve, 1984; Golgi, 1885). Animal and plant life rely on this essential interaction; constant and effective cell-to-cell communication orchestrates all normal physiological functions but can give rise to diseases under certain conditions (Virchow, 1858).

Cell-to-cell communication occurs through a variety of mechanisms that enable an extraordinarily diverse collection of biological messages to be shared between cells. Messages range from small molecules that maintain intra- and extra- cellular ion concentrations at normal physiological levels, such as potassium (Kozoriz et al., 2006), to large energy-producing organelles, such as mitochondria (Torralba et al., 2016). In addition to size, two key factors that differentiate how these messages are transported inter-cellularly are (i) specificity and, (ii) the distance they need to reach their target.

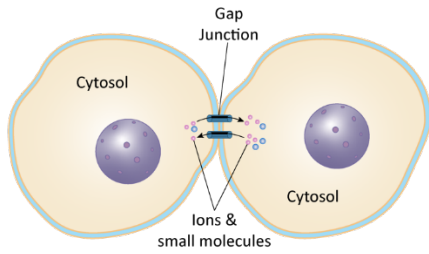
Adjacent cells can communicate via nanoscopic water-filled channels called gap junctions (GJs) (Figure 1), which allow the inter-cellular transport of small (~1kDa) soluble molecules and inorganic ions (e.g. cyclic nucleotides and inositol phosphates) (Bermudez-Fajardo et al., 2007). GJs are formed by two hemichannel connexons (hexameric connexin complexes) that facilitate electrical and metabolic coupling (Donahue et al., 2017). Connexin 43 (Cx43) is the primary component of GJs and it plays a wide variety of functions. For example, it can transport cellular death signals (e.g. Inositol trisphosphate, IP3) during the invasion of breast and lung tumor-derived cancer (Aasen et al., 2019). Cx43 also plays a key role in development by contributing to the proper migration of pyramidal neurons in the cerebral cortex (Liu et al., 2012).

Cells also use various forms of 'signal transmission' for inter-cellular communication: *Paracrine signaling* is used by cells in close proximity, where messages (paracrine ligand molecules) are secreted into the extracellular matrix (ECM) where they bind to a neighboring's cell receptor (Saxen et al., 1976). Endocrine signaling is a slow and passive cell-to-cell signaling process in

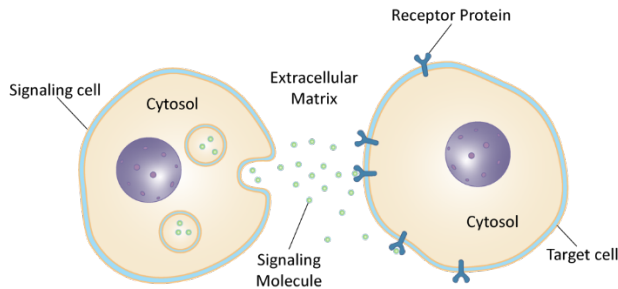
which hormones (small, 5-20 kDa soluble factors) are secreted by stimulatory cells in endocrine tissue (e.g. adrenal glands), and travel through the bloodstream until they reach a specific receptor on a distant target cell in the body (**Figure 1**) (Starling, 1905). Physiological examples of these processes include neurotransmitters that cross a synaptic cleft to reach the postsynaptic terminal, as a paracrine signal; and as endocrine signal, insulin, a hormone that controls glucose and lipid metabolism. Other forms of signaling modes of communication include autocrine and Juxtacrine signaling. During autocrine signaling, cells 'self-communicate' by secreting soluble ligands that bind to receptors on their own surface (Dođaner et al., 2016). Depending on the type of signal, ligands can also bind to receptors within the cell. Common examples of autocrine signaling include interleukin-1, a soluble protein involved in immune response to antigens and mitogens (Youk and Lim, 2014). Juxtacrine signaling is a contact-dependent class of signaling in which membrane ligands from one cell bind to cell surface receptors located on another cell, initiating an intracellular signaling cascade (Zimmerman et al., 1993). One of the best characterized examples of Juxtacrine signaling is the Notch signaling pathway, in which the ligand of the signaling cell, *Delta*, binds to the receptor *Notch*, activating cascades that affect a wide variety of functions that include cell fate, death, and proliferation (Lai, 2004).

Other modes of cellular communication involve extracellular vesicles (EVs), which gained popularity as avenues for the inter-cellular exchange of genetic material, lipids, and proteins (van Niel et al., 2018). EVs are classified into two categories, microvesicles (MVs) and exosomes (**Figure 1**). MVs are 100 – 1,000 nm plasma membrane-derived particles that form from outward blebbing of the plasma membrane; exosomes are intraluminal vesicles (ILVs) of 30 – 100 nm in diameter of endocytic origin that get exocytosed when the multivesicular endosomes (MVEs) containing them fuses with the plasma membrane (Keller et al., 2006). EVs are highly heterogeneous in size, composition, morphology and biogenesis. Although their precise biological role and presence *in vivo* remains to be defined, there is substantial evidence that links EVs to numerous physiological and pathological roles (Buzas et al., 2014).

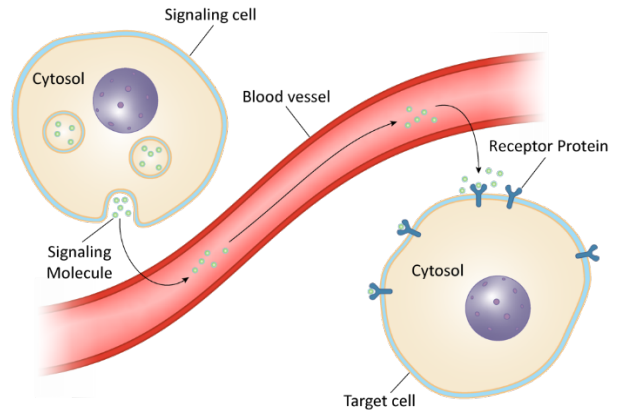
(A) Gap Junctions



(B) Paracrine Signaling



(C) Endocrine Signaling



(D) Extracellular Vesicles

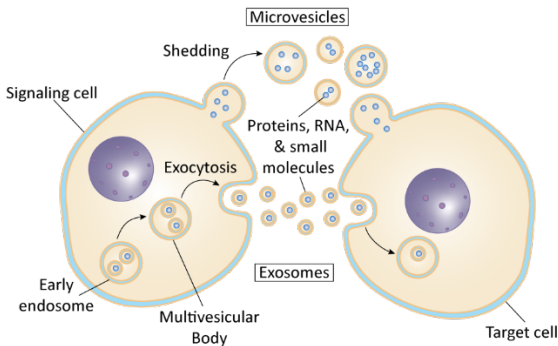


Figure 1. Modes of Inter-cellular Communication.

Schematic diagram depicting: **(A)** Cells coupled by gap junctions, which allow various small (5-20 kDa) molecules, (e.g. ions, secondary messenger molecules, and electrical impulses) to directly pass through a regulated gate. **(B)** Paracrine signaling is mediated by the secretion of soluble signaling molecules that bind to specific receptors on neighboring cells. **(C)** Endocrine signaling is mediated by signaling molecules that travel through the blood stream before binding to a receptor on a distant cell; **(D)** Extracellular vesicles, which enable the transport of small particles (e.g. Proteins, RNA, and small molecules) through Microvesicles and Exosomes. Microvesicles (100 nm – 1,000nm in diameter) arise from the budding of the plasma membrane. Exosomes (30 – 100nm in diameter) originate from the exocytosis of intraluminal vesicle contained within a multivesicular body.

1.2 Introduction to Tunneling Nanotubes

The quest to discover novel modes of cell-to-cell communication didn't stop with the identification of exosomes. 15 years ago, Hans-Hermann Gerdes and colleagues observed membranous tubes forming in cell cultures of rat kidney pheochromocytoma 12 (PC12), human embryonic kidney (HEK), and normal rat kidney (NRK) cells which they called *Tunneling Nanotubes* (TNTs) (**Figure 2**) ([Rustom et al., 2004](#)). Stained with fluorescently conjugated Wheat Germ Agglutinin (WGA), cells connected by TNTs created an inter-connected cellular network. Using structural approaches (discussed in further detail in later sections of this chapter), the authors found that these 50 to 200 nm-thick, several μm -long actin-bearing membranous threads permitted the inter-cellular transport of synaptophysin-marked endosomes, small synaptic-like microvesicles, and lysotracker-labeled organelles. That same year, Davis and colleagues identified similar (30 to 140 μm -long) structures forming in various immune cells, including macrophages, B lymphocytes, and blood natural killer (NK) cells ([Onfelt et al., 2004](#)). In the same study, the authors discovered that TNTs could form upon disassembly of the immunological synapse (discussed in later sections of this chapter), and, like the connections described by Rustom et al., can also facilitate the trafficking of membrane components.

Further studies from our group and others shed light on TNTs connecting numerous other cell types, along with the detection of a long list of TNT-mediated cargo trafficking that includes ions, organelles, viruses, bacteria, apoptotic signals, genetic material, and proteins. TNTs were found to connect cells of the same- (homotypic) and different- (heterotypic) type and allow both uni- and bi- directional cargo transport. Numerous review articles have described how these findings link TNTs to both physiological and pathological conditions, which range from tissue repair to tumor progression; bacterial to virus infection; and stem cell differentiation to progression of neurodegenerative diseases ([Abounit and Zurzolo, 2012](#); [Ariazi et al., 2017](#); [Austefjord et al., 2014](#); [Drab et al., 2019](#); [Jash et al., 2018](#); [Marzo et al., 2012](#); [Mittal et al., 2019](#); [Venkatesh and Lou, 2019](#); [Vignais et al., 2017](#); [Yamashita et al., 2018](#)).

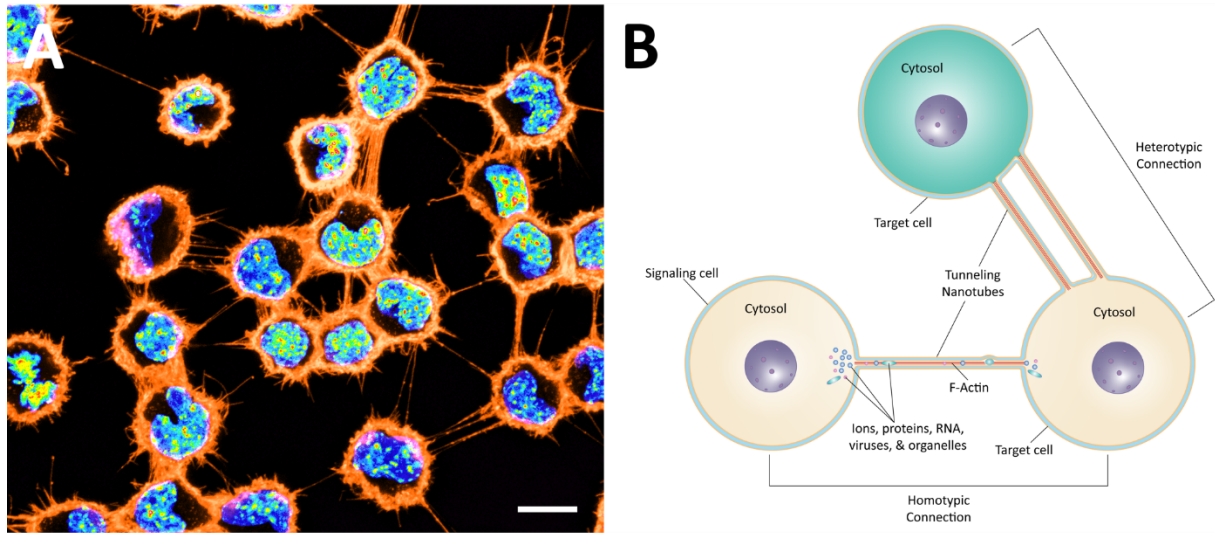


Figure 2. Topological Architecture of Tunneling Nanotubes.

(A) TNTs connecting Cath.a-differentiated (CAD) neuronal cells stained with Wheat Germ Agglutinin-Alexa Fluor (Orange), to label the membrane of cells, and DAPI (16-color Lookup table, *Fiji*), to label nuclei. Cells can connect by one or numerous TNTs, as seen in **A**. (B) Schematic diagram depicting Tunneling Nanotube-mediated communication between cells. Tunneling Nanotubes create direct conduits filled with actin filaments, which allow the transport of cargo (e.g. ions, proteins, RNA, viruses, and organelles). TNTs can form between cells of the same- (homotypic) and different- (heterotypic) type. As shown in **A**, cells can form one or numerous TNTs. Scale bar: **A**, 10 μm .

Particular morphological and functional differences (e.g. cell type, TNT length and thickness, open- vs. close- ended tip, nature of cargo transport, and relationship to a given disease), resulted in TNTs acquiring disparate names. For example, “nanoscale channels” connect metastatic cancer and endothelial cells (Connor et al., 2015); “T-cell nanotubes”, connect Jurkat T cells (Sowinski et al., 2008); “membrane nanotubes” connect human NK cells (Chauveau et al., 2010); “bridging conduits”, or ‘thick TNTs’ contain actin and microtubules (Kadiu and Gendelman, 2011); “intercellular bridges”, connect epiblast cells in the developing zebrafish (Caneparo et al., 2011); “epithelial bridges” (EBs) connect primary human bronchial epithelial cells (Zani et al., 2010); “tumor microtubes” (TMs) connect astrocytoma cells (Osswald et al., 2015a); and “membrane fronds” connect baby hamster kidney 21 (BHK-21) cells, 293 T cells, and NIH-3T3 fibroblasts (Gill et al., 2008); etc.

The heterogeneity of TNT-like structures justifies nomenclature diversity. After all, numerous studies describing similar organelles (e.g. thin filopodia during sea urchin gastrulation, (Miller et al., 1995)) were published prior to the work by Rustom et al., and it is conceivable that plenty others were also reported but never mentioned in any of our field’s bibliography. However, the number of names increased for structures that could simply be one structure— an open-ended membranous connection that, through a contiguous cytoplasmic tunnel containing actin cytoskeletal railways, permit the transport of cellular cargo— or, entirely distinct structures which only share essential properties (e.g. enclosure by a membrane and extending between two distant cells), has been subject of much debate in our field (Baker, 2017).

The lack of a TNT-specific marker and limitations in optical microscopy resolution have hampered our ability to catalog TNTs accurately and address the ambiguous heterogeneity described above. In order to better understand these structures and move the field forward, we will need the answers to pivotal questions, such as: how do TNTs form? How do TNTs function; that is, what cytoskeletal filaments and motor proteins work together to enable cargo transport? Are TNTs open-ended tunnels or tip-close-ended protrusions? Do TNTs exist in animals? Do TNTs play the essential roles they demonstrate *in vitro*, in living organisms? If so, how do they compete with other modes of cell-to-cell communication?

In the remaining sections of this chapter, I will present a synthesized review of the advances our group and others have made in the field of TNTs and point to specific biological questions that drove the direction of my doctoral dissertation, while also highlighting how my efforts have contributed to a better understanding of the unanswered points above. Specifically, I will describe the tools, methods, and criteria employed to study TNTs, as well as findings on TNT biogenesis, mechanisms of formation, structure, presence *in vivo*, pathological implications, and therapeutic applications. Throughout these sub-sections, I will also emphasize published and preliminary data from our group that served as the foundation for the projects I worked on during my doctoral work.

1.3 Methods and Criteria used for the study of Tunneling Nanotubes

1.3.1 Tunneling Nanotubes: Denotation *In Vitro*

Today, the properties that make up the criteria used by us and others to label TNTs as ‘*TNTs*’ are the following: (i) a cell protrusion with a surrounding plasma membrane that extends between two cells, (ii) the presence of of actin cytoskeletal filaments, and (iii) ability to transport cargo, which also serves as a strong indicator of (iiii) cytoplasmic continuity through open-ended cell-TNT-cell contact sites (**Figure 3**) ([Dupont et al., 2018](#)). Other protrusions, which share some or most of these features are often called TNT-like structures; however, for simplicity, I will use the term *TNT* for the remaining sections of this chapter unless stated otherwise.

1.3.2 Preservation of Tunneling Nanotubes

The long and thin topological features that characterize TNTs make them fragile and vulnerable to shearing forces. The preservation of TNTs through classical fixation methods has met obstacles along the way, as TNTs’ susceptibility to low-concentrated chemical fixatives (e.g. paraformaldehyde) and long-light exposures often break or crook them. To circumvent this obstacle, we and others employ a two-step fixation protocol that leverages extensive cross-linking via glutaraldehyde prior to paraformaldehyde fixation ([Abounit et al., 2015](#)).

The fragility of TNTs impairs investigations involving membrane permeabilization experimentally cumbersome, as pores on the membrane weaken the scaffolding structure that builds TNTs. Presently, access to the inside of TNTs has been achieved with the use of milder membrane detergents (e.g. Saponin) at low concentrations ([Costanzo et al., 2013](#); [Rupp et al., 2011](#); [Zhu et al., 2018](#)); however, the identification of components within TNTs by this method remains inefficient and unsatisfactory.

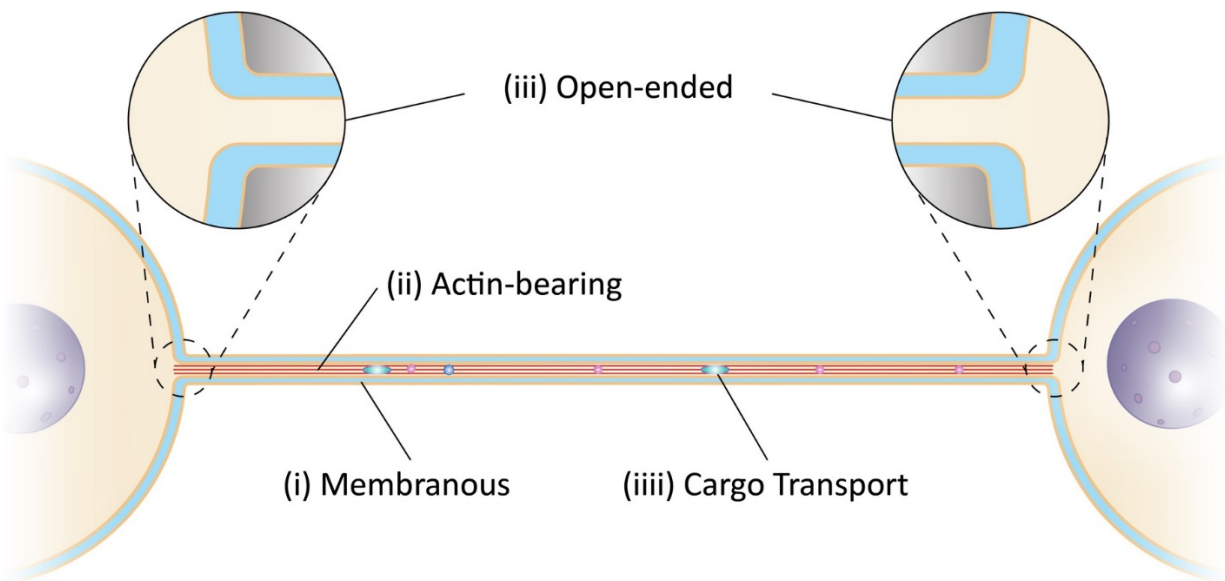


Figure 3. Properties that define Tunneling Nanotubes.

Schematic diagram depicting a TNT connecting two cells superimposed with labels that indicate the four underlying topological properties that make up TNTs: (i) a membranous extension of the plasma membrane from the cells connected; (ii) an actin cytoskeletal backbone; (iii) open-ended cell-TNT-cell contact sites, (iiii) functional ability to transfer cargo.

1.3.3 Labeling of Tunneling Nanotubes and Actin Backbone

A TNT-specific marker hasn't been identified yet. However, recent efforts to obtain molecular markers specific for labeling TNTs by using micro-proteomic approaches highlighted several unexpected candidate proteins, (e.g. Grk5 and Hist1h3b), which have yet to be investigated (Gousset et al., 2019). At the present time, the method applied to label TNTs is to stain the entire plasma membrane of cells with fluorescently-conjugated proteins that bind to glycolipids and glycoproteins, such as WGA (Abounit et al., 2015), FM1-43 (McCoy-Simandle et al., 2016), and MemBright (Collot et al., 2019), or by genetic over-expressing proteins associated to the plasma membrane, such as H-Ras and CAAX (Hanna et al., 2019; Rainy et al., 2013).

The actin backbone composition of TNTs is labeled with fluorescently-conjugated Phalloidin (Abounit et al., 2015) or by genetic over-expressing the small F-actin peptide dye, *Lifeact* (Riedl et al., 2008) fused to GFP or mCherry (Sáenz-de-Santa-María et al., 2017). A new report shed light on a novel approach to simultaneously label actin-, intermediate-, and microtubule-filaments of TNTs of urothelial cells (Resnik et al., 2019), with promising application for co-cytoskeletal-distribution studies. The reproducibility of this approach in TNTs of other cells has yet to be determined.

1.3.4 Detection by Microscopy

The detection of TNTs by microscopy requires high-magnification differential interference contrast (DIC) imaging and/or laser scanning confocal microscopy (LSCM), as TNTs, unlike peripheral filopodia (substrate-adherent filopodia), hover over the substrate and, in some cases, over other cells. To discriminate TNTs from dorsal filopodia, (filopodia located near or toward the upper surface of cells in culture), TNTs must not touch the substratum, extend towards the medium, and be sufficiently long and stable to connect at least two cells (Abounit et al., 2015).

The identification of TNTs *in vitro* is contingent upon adequate signal-to-noise ratio, which requires that cells in culture be seeded in a medium-confluent monolayer ecosystem that warrants sufficient physical space between cells to visualize TNTs. A recent study found that this paradigm could be avoided with treatment of proteases. In their study, Rustom and colleagues

singularized cells by turning them spherical and cleared the way for TNTs to become visible. The authors confirmed this phenomena in various cell lines, including Rat Embryonic Fibroblasts 52 (REF52), NRK, Henrietta Lacks (HeLa), Madine-Darby canine kidney (MDCK), endothelial, adenocarcinoma, and HEK cells (Staufer et al., 2018); however, it is currently unknown whether protease treatment could also be inducing the formation of TNT (via a stress response, which will be discussed later in this chapter), and if the observable connections are capable of inter-cellular cargo transport.

1.3.5 Quantitative Assessment

Unfortunately, a method to quantify individual TNTs does not exist but new artificial intelligence (AI) approaches and machine learning (ML) have been proposed (Valdebenito et al., 2018). For now, our group and others extrapolate relevant biological information from experiments by quantifying the number of cells connected via TNTs using a computer-assisted manual approach in *Fiji/ImageJ* or *ICY* (TNT-Annotator plugin) (Delage et al., 2016).

These analyses are informative but in order to definitively identify TNTs with accuracy they must be accompanied by functional assays (i.e. transport of cargo). Cargo transfer is assessed by observing organelles (e.g. lysosomes), vesicles (or endosomes) labeled with fluorescent lipophilic cationic indocarbocyanine dyes (e.g. Dil and DiD) transfer between cells in a donor-and-acceptor cell co-culture system (Abounit et al., 2015; Sharma and Subramaniam, 2019). The amount of transfer is assessed by (i) live imaging microscopy or in fixed conditions by (ii) LSCM or Fluorescence Activated Cell Sorting (FACS) (Abounit et al., 2015). In order to examine if the inter-cellular transport of vesicles in these functional assays is TNT-dependent and not, via long-range EV mediated mechanisms, experiments must be accompanied by three controls: (i) a transwell filter that reduces (or eliminates) cell-to-cell contact; (ii) assessment of supernatant transferred from donor- to acceptor cells; and (iii) a mixture of non- co-cultured cells to obtain *background noise* threshold (Gousset et al., 2009; Thayanithy et al., 2017). Integrating these assays into a controlled device where the position of cells and growth-direction of TNTs are confined to microchannels in a micro-fluidic chip (similarly to those routinely used for axonal growth studies

(Neto et al., 2016)), could significantly increase the 'control', throughput, and versatility of our studies but have only been employed once, previously (Yang et al., 2016).

The metrics described above hold a stringent enough criterion to identify TNTs in culture. However, new challenges arise from cell type and model organism complexity. These technical and biological obstacles will continue to be discussed throughout this chapter in order to pinpoint the areas in which our field is lacking, and my dissertation work contributes to.

1.4 Tunneling Nanotubes: Biogenesis

TNTs emerge from two physico-mechanical origins: a 'cell dislodgement mechanism' and an 'actin-driven protrusion mechanism. In order to further understand these models, I will take a deeper look at each one of them over the next sub-sections.

1.4.1 Cell dislodgement mechanism

The cell dislodgement mechanism of TNT formation occurs when two adjacent cells fuse transiently and as they move apart, a thin actin-bearing membranous tube remains (**Figure 4**). It accounts for 100% of TNTs in squamous cell carcinomas (SCC), neuronal crest cells (NCCs), and NRK cells; 82% in HEK 293 cells ([Sáenz-de-Santa-María et al., 2017](#); [Wang et al., 2010](#)), and the vast majority in human primary, hematopoietic progenitors, and leukemic KG1a cells ([Reichert et al., 2016](#)). In neuronal cells such as PC12, only 7% of TNTs are formed by dislodgment ([Bukoreshtliev et al., 2009](#)), suggesting that this biogenesis mechanism is cell specific. Interestingly, some of the TNTs derived from dislodgement were shown to be electrically coupled by Cx43 GJs ([Wang et al., 2010](#)). This observation agrees with the findings of several other groups, in which immune-cells, which are known to interact by immune synapses when they are in close proximity ([Finetti et al., 2017](#)), form closed-tip TNT-like protrusions ([Davis and Sowinski, 2008](#); [Dustin et al., 2010](#); [Onfelt et al., 2004, 2006](#); [Watkins and Salter, 2005](#)). Whether TNTs in immune cells require adhesion molecules (e.g. Cadherins) to establish dislodged TNTs is currently unknown. The precise mechanism by which cells incorporate an actin backbone into TNTs formed by dislodgement is another unexplored question. However, recent studies provided new insights after finding that Fascin, an actin-bundling protein found in numerous membranous protrusions, is absent in the cell dislodgment- based formation of TNTs in epithelial lung cells ([Dubois et al., 2018](#)). This finding is consistent with one of our previous reports in which we showed a decrease in TNT formation and increase in filopodial protrusions upon over-expression of Fascin in neuronal CAD cells ([Gousset et al., 2013](#)). Together, this data suggests significant variations amongst TNTs of distinct cell types formed by cell dislodgment and raises new directions for future studies.

1.4.2 Actin-driven protrusion mechanism

The actin-driven protrusion mechanism of TNT biogenesis occurs when the tip of a filopodium-like structure extrudes from one cell and fuses with another, onto either the cell body or the tip of a filopodium emanating from it (**Figure 4**). Differently from dislodgement, the actin-driven protrusion mechanism is typical of relatively immobile cells (e.g. neurons and epithelial cells) ([Gousset et al., 2013](#)).

With the exception of a select group of “thick” (>0.7 μm), microtubule-bearing TNTs in macrophages and urothelial cells ([Onfelt et al., 2006](#); [Resnik et al., 2018](#); [Veranic et al., 2008](#)), all TNTs contain only actin. This premise was demonstrated by two key findings: (i) microtubule-disrupting and microtubule-stabilizing agents (nocodazole and paclitaxel, respectively) do not alter induction of TNTs ([Wang et al., 2011](#)), and (ii) F-actin depolymerizing toxins, (*latrunculin*, *cytochalasin B*, and *cytochalasin D*) block TNT formation ([Bukoreshtliev et al., 2009](#); [Dupont et al., 2018, 2018](#); [Schiller et al., 2013](#); [Takahashi et al., 2013](#)). These findings propose that TNTs form by the interaction of actin protein networks that also give rise to other actin-based protrusions such as filopodia, or filopodia-like structures. Live-imaging assays showing that 93% of TNTs in HeLa cells originate from filopodia like protrusion interplay ([Bukoreshtliev et al., 2009](#)) support this notion, and underscore the importance to investigate the cellular and molecular players involved in the formation of filopodia, which I will describe in the sub-sections below.

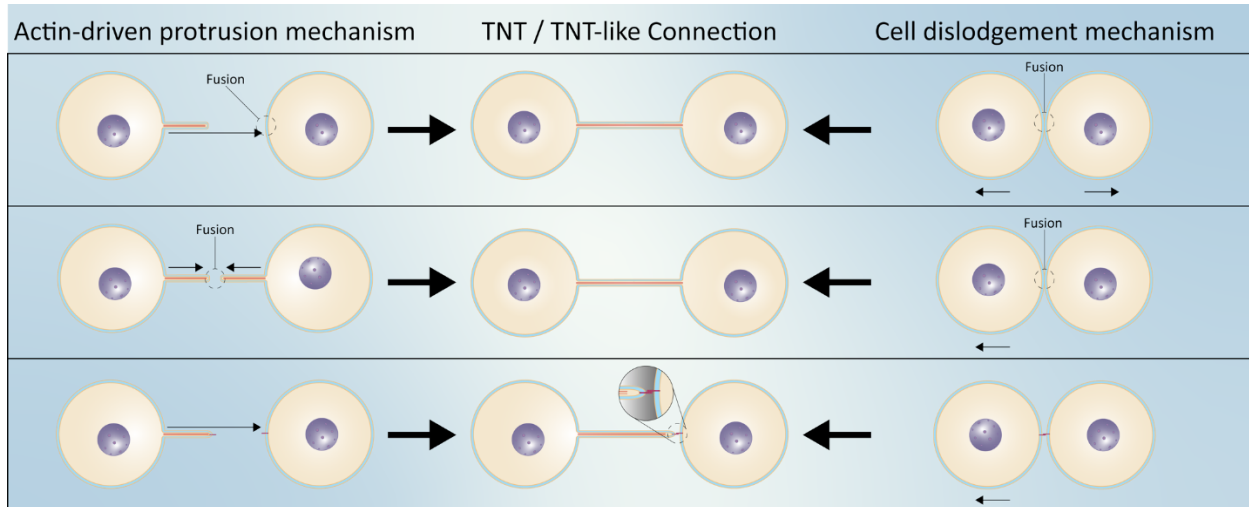


Figure 4. Mechanisms of Tunneling Nanotube Biogenesis.

Schematic diagram depicting the two physico-mechanical origins of TNTs and TNT-like connections (middle). The Actin-driven protrusion mechanism (left), in which one or both cells extend filopodia-like protrusions towards the target cell (or towards each other). Upon contact with the target cell, the tip of the protruding process fuses spontaneously or via fusion molecules leading to open-ended TNTs. The cell dislodgement mechanism (right) occurs when cells that are in sufficient proximity with each other fuse spontaneously and migrate away from each other, leaving behind membrane tethers that lead to TNTs. Cells interacting via adhesion molecules or electrically coupled with GJs can also lead to the formation of TNT-like structures (middle, bottom).

1.4.2.1 Filopodia: Introduction

In 1907, Ross Granville Harrison discovered that upon isolating and culturing embryonic tissue from adult frogs, thin “hyaline protoplasm” filaments of 25 μm in length and 1.5 – 3 μm in thickness, extended from the end of growing nerve fibers (Harrison, 1907). Over 100 years later, we now know that Harrison’s “rhizopod”-resembling nerve protrusions drive several major neuronal events, which include axonal guidance, dendritic spine formation, and synaptic connectivity (Gallo, 2013), and represent only one of various kinds of membranous protrusions classified under the umbrella of *filopodia* (Figure 5).

Today, filopodia are defined as thin (100 – 300 nm), close-ended actin-rich finger-like protrusions at the leading edge of cells. Their ‘antenna’-like ability to sense the extracellular environment has granted them roles in vital processes such as cell-to-cell adhesion and migration (Gardel et al., 2010; Jacquemet et al., 2015). As with TNTs, variations in length, thickness, dynamicity, and cellular localization make filopodia largely heterogenous. These variations could be due to organism- or cell type specific signaling proteins, actin-cross-linking proteins, nucleators, motor proteins, and actin-to-plasma membrane Bin/Amphiphysin/Rvs (I-BAR) linking proteins (Mattila and Lappalainen, 2008). Studies by the group of Giorgio Scita and others have made seminal findings that will be described below, and which served as preliminary data for Chapter 2 of my work.

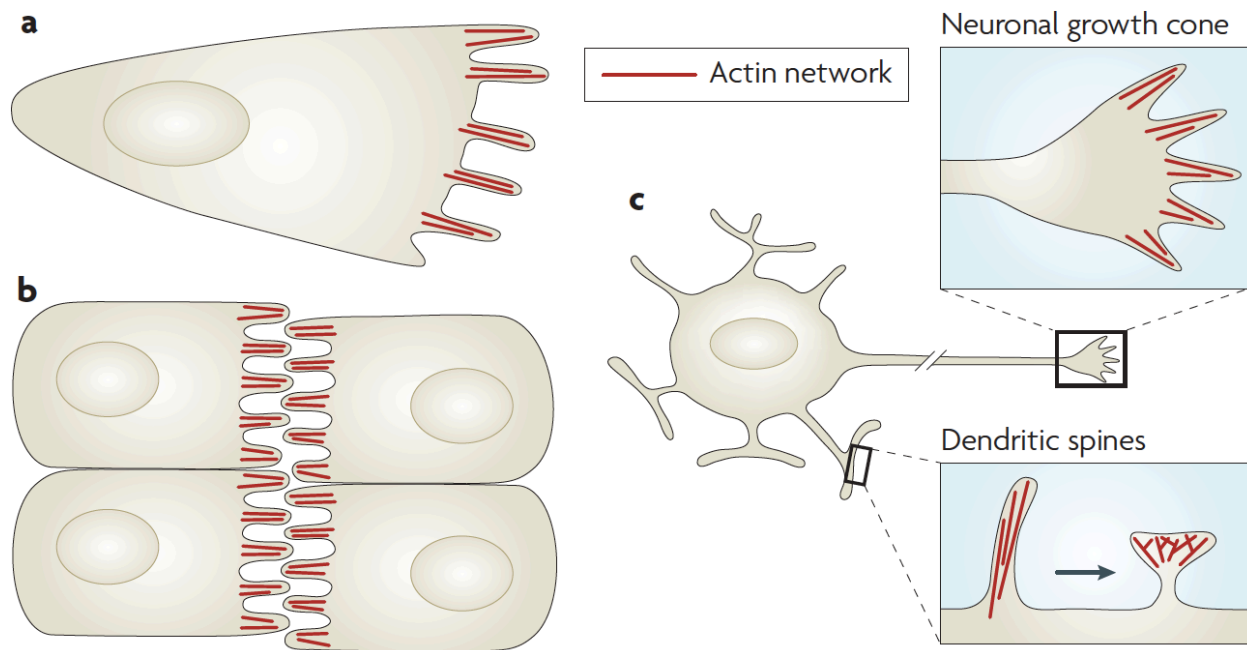


Figure 5. Examples of filopodia.

Schematic diagram depicting several examples of different types of filopodia, (obtained from [Mattila and Lappalainen, 2008](#)). **(A)** Filopodia localized at the leading edge of cells probe the microenvironment during cellular migration. **(B)** Filopodia of epithelial sheets, which protrude from opposing cells, help the sheets of cells to align and adhere together. **(C)** In neurons, filopodia participate in the guidance and migration of neuronal growth cones (top inset) and are precursors of dendritic spines (bottom inset).

1.4.2.2 Filopodia: Mechanisms of Formation

The formation of filopodia requires a highly dynamic actin cytoskeleton structure that forms by two models, a 'convergent elongation model' in which filopodia arise from the Lamellipodium dynamic actin filament meshwork assembled by the Actin-related protein 2/3 (Arp2/3), and a '*de novo* filament nucleation model', in which the actin of filopodia is nucleated at the tips by the vasodilator-stimulated phosphoprotein (VASP) and the actin polymerizer, *formin* (Mattila and Lappalainen, 2008) (Figure 6).

Small GTPases of the Ras and *Rho* superfamily lie at the heart of the '*convergent elongation model*' (Bishop and Hall, 2000; Nobes and Hall, 1995), where the Cell Division Control Protein 42 (CDC42) and Ras-related C3 botulinum toxin substrate (Rac1) play key roles in the activation of Arp2/3. Specifically, CDC42 acts on the Wiskott-Aldrich syndrome protein (WASP), or neural-WASP (N-WASP), to initiate the nucleation of new actin filaments through the activation of Arp2/3 (Carlier et al., 1999), whereas Rac1 (Heasman and Ridley, 2008) acts on its downstream interactor, WASP-family verprolin homologous (WAVE) protein, before activating Arp2/3 (Kurusu and Takenawa, 2009). Importantly, CDC42 is involved in filopodia formation while Rac1 in lamellipodia formation (Nobes and Hall, 1995).

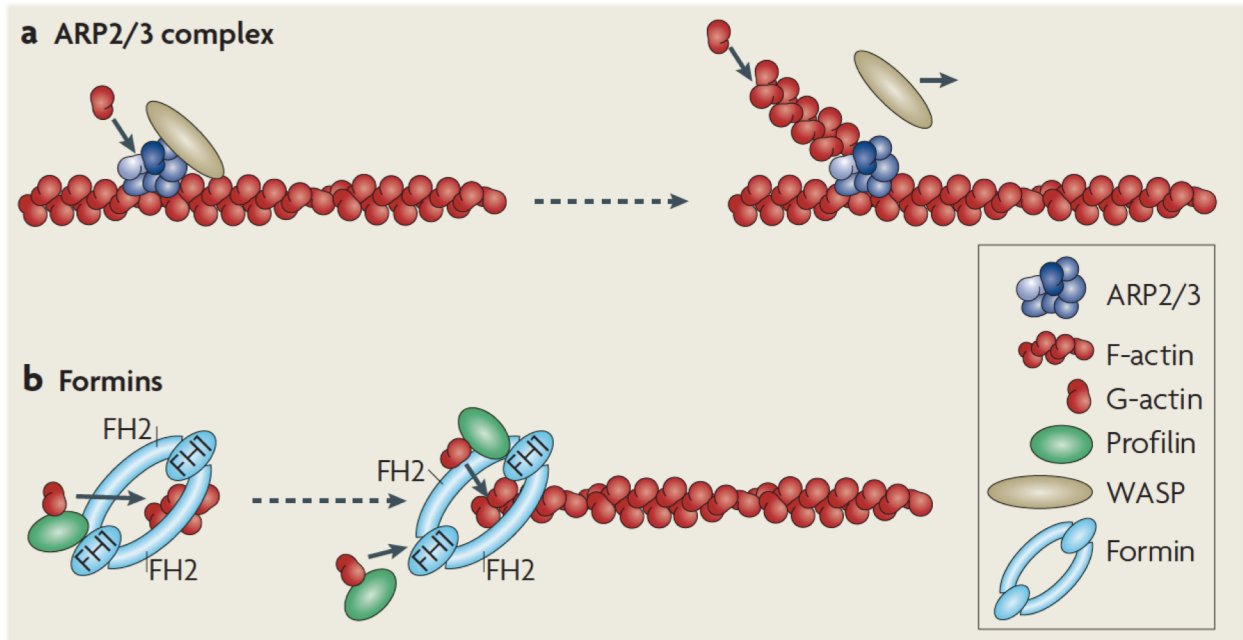


Figure 6. Arp2/3 and Formins: two major actin-nucleating machineries.

Schematic diagram depicting the molecular assembly of Arp2/3 (**A**) and Formins (**B**), (obtained from [Mattila and Lappalainen, 2008](#)). (**A**) The Arp2/3 complex is made up of seven subunits, two actin-related proteins and five other proteins. When Arp2/3 binds to pre-existing actin filaments, the actin-related subunits form a ‘seed’ that nucleates actin polymerization. The activation of the ARP2/3 complex is induced by binding to nucleation-promoting factors, such as WASP/WAVE-family proteins, which dissociate from the ARP2/3 complex after filament nucleation. (**B**) Formins are multi-domain proteins that nucleate polymerization of unbranched actin filaments. The formin homology-2 (FH2) domain initiates filament assembly and remains persistently associated with the fast-growing barbed end, enabling insertion of actin subunits while protecting the end from capping proteins. Formins can contain a profilin binding formin homology-1 (FH1) domain, which recruits profilin–G-actin complexes to the barbed ends of the growing filament.

An alternative mechanism to the CDC42–WASP–Arp2/3-dependent filopodia formation pathway involves the interaction of CDC42 and VASP with the I-BAR-domain, Insulin Receptor Tyrosine kinase substrate (IRSp53), an actin crosslinking protein involved in the formation of filopodia-like protrusions such as neurites (Govind et al., 2001). Using quantitative binding assays and Mouse Embryonic Fibroblasts (MEF) cells, Scita and colleagues demonstrated that filopodia-inducing stimulus ensues the binding of CDC42 to IRSp53, and subsequently promotes the growth of a filopodial filament through the formation of a CDC42–IRSp53–VASP complex (Disanza et al., 2013). In the same study, the authors also observed a reduction in filopodia filament formation upon the interaction between IRSp53 with the Epidermal growth factor receptor kinase substrate 8 (Eps8), a GTPase which had previously been associated with actin dynamics through its barbed-end capping activity (Di Fiore and Scita, 2002), and strong synergy with IRSp53 in mediating actin bundling (Disanza et al., 2006) (Figure 7).

Using a mouse neuronal cell line of catecholaminergic origin, Cath.a-differentiated (CAD) (Qi et al., 1997), which our group previously identified as a robust *in vitro* model for the study of TNTs *in vitro* (Abounit et al., 2015; Gousset et al., 2009, 2013; Zhu et al., 2018), we previously demonstrated that overexpression of VASP reduce TNT formation. Our more recent results (detailed in Chapter 2) reinforce these findings and reveal that, contrary to their role in filopodia, (i) CDC42–VASP–IRSp53 network serve as negative regulators of TNTs and inter-cellular vesicle transport, while (ii) Eps8, induces TNT formation and increases cargo transfer (Delage et al., 2016).

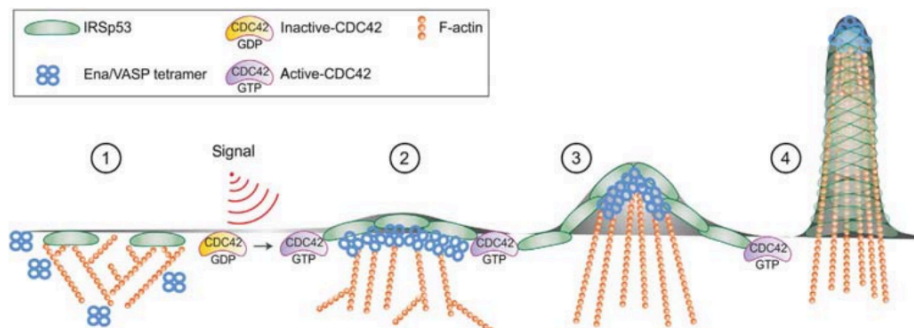


Figure 7. Filopodia formation by CDC42, IRSp53, and VASP.

Schematic diagram depicting how, during filopodia formation, CDC42 switches IRSp53 from inhibition of actin assembly to filament elongation by clustering of VASP (obtained from [Disanza et al., 2013](#)). **(1)** in the absence of stimuli, IRSp53 binds to the plasma membrane and slows down barbed-end elongation. **(2)** Upon stimuli, activated CDC42 binds to IRSp53, relieving IRSp53-mediated inhibition of filament growth. This promotes the formation of a CDC42-IRSp53-VASP complex and reduces the formation of the IRSp53-EPS8 complex. **(3)** Binding to CDC42 facilitates the formation of IRSp53 and VASP at the leading edge of the plasma membrane, in which the clustering of VASP allows processive actin filament elongation. **(4)** Membrane deforming activity of IRSp53 and processive filament elongation by VASP work together to extend actin filaments beyond the x, y plane of the membrane.

1.4.2.3 Filopodia: Ultra-Structure

Cryo-electron microscopy and vitrification of specimens have revolutionized structural analyses of biological samples (Murata and Wolf, 2018). Cryo-transmission electron microscopy (cryo-TEM) and cryo-electron tomography (cryo-ET) of vitrified *Dictyostelium discoideum* amoeba revealed the intracellular ultrastructure of *de novo* filopodia with sufficient detail to elucidate several key topological features about their cytoskeletal architecture: actin filaments that make the shaft of the filopodia appear fragmented; at the close-ended tip, the “terminal cone”, is built of short branched actin filaments that anchor to the tip of the filopodium on one end and flank on the other (Medalia et al., 2007).

Using similar imaging approaches, Yasunaga and colleagues observed over 30 filopodial filaments emanating from the neuronal cell line, NG108-15, and unveiled their cytoskeletal architecture by revealed that actin filaments (of 2.7 nm in thickness) are bundled by Fascin in a hexagonal shape (Aramaki et al., 2014, 2016). Fast Fourier transformation analyses confirmed that the bundles observed within the filopodial filament were in fact actin.

As part of one of my projects (described in detail in *Chapter 3*), I studied TNTs using cryo-TEM and cryo-ET in two neuronal cell models, CAD and SH-SY5Y cells (Kovalevich and Langford, 2013), in which we and others had observed functional TNTs (Dieriks et al., 2017; Dilsizoglu Senol et al., 2019; Epperla et al., 2015). In these cells, our observations indicate that TNTs are comprised of numerous individual TNTs (iTNTs), whereas filopodia are not; TNTs contain cargo (e.g. vesicles and organelles) within, filopodia do not (Sartori-Rupp et al., 2019).

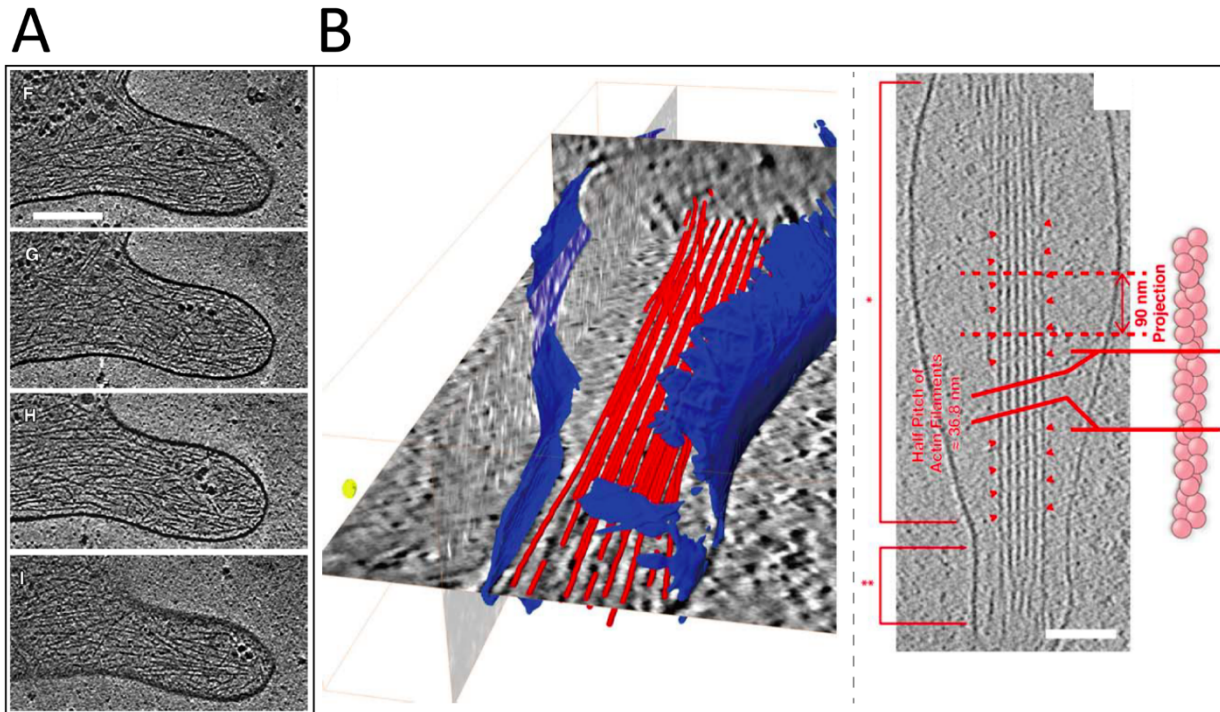


Figure 8. Ultra-structure Architecture of filopodia.

Electron micrographs showing the ultra-structure of filopodia, (obtained from [Medalia et al., 2007](#) and [Aramaki et al., 2016](#), respectively). **(A)** Four consecutive sections through the reconstructed volume of a wild-type *Dictyostelium* cell filopod shows clear branching of actin filaments that reaches the growth cone. **(B)** 3D structure of a filopodium and intracellular filaments of a (NG108-15) neuronal cell by cryo-ET. Segmentation shows filamentous structures, cell membrane, and a 10-nm gold marker in red, blue, and yellow, respectively. A highly ordered bundled filamentous structure can be clearly observed. (right) The periodicity of the bundled filamentous structure is shown using “>” and “<” with 36-nm helical repeats. The diameter of the filopodium is 100 nm at its thinnest region (**) and 250 nm at its thickest region (*).

1.5 Tunneling Nanotubes: Molecular Formation

In an attempt to identify the molecular pathways involved in the two biogenesis mechanisms described above, our group and others have focused on investigating a series of proteins and signaling pathways linked to actin networks that play a role in the formation and regulation of other common membranous protrusions, including those of filopodia.

1.5.1 Role of Actin Cytoskeleton and Actin Protein Regulators

CDC42 and Rac, whose roles in Arp2/3-dependent actin polymerization were mentioned above and previously studied in filopodia and lamellipodia formation (Heasman and Ridley, 2008), were first observed at the base of TNTs connecting immune Jurkat T cells (Lachambre et al., 2014). Its role in TNTs was revealed by the inhibition of CDC42 using *Secramine A*, which blocked TNT formation (Arkwright et al., 2010). In the cervical cancer HeLa cell, inhibition of CDC42 by transfecting a dominant negative construct decreased the formation of TNTs. Conversely, inhibition of Rac1 by overexpression of its dominant negative form had no significant effect (Hase et al., 2009). By treating macrophages with specific inhibitors for CDC42 and Rac1, ML-141 and 6-Thio-GTP, respectively, Hanna and colleagues confirmed that TNTs in immune cells require both CDC42 and Rac GTPases for their formation (Hanna et al., 2017).

A portion of my dissertation was devoted to studying the role of these GTPases on TNTs connecting neuronal CAD cells. Interestingly, as will be described in more detail in *Section 2*, our observations indicate that inhibition of CDC42 and Rac1 by transfecting CAD neuronal cells with dominant negative forms, significantly increases the number of cells connected by TNTs (Delage et al., 2016).

Downstream effectors of CDC42, WASP localize throughout macrophage TNTs. Silencing WASP by short hairpin (sh) RNA (shWASP) resulted in a 90% reduction of cells connected by TNTs and blocking of DiI-labeled cargo. Similar results were observed with macrophages depleted of Rac's downstream effector, *WASP family verprolin-homologous 2* (WAVE2) by transient silencing (Hanna et al., 2017).

Direct inhibition of the common downstream effector of WASP and WAVE2, Arp2/3, with CK-666, that blocks movement of the Arp 2 and Arp 3 subunits into the activated filament-like conformation (Hetrick et al., 2013), resulted in a decrease in the formation of TNTs in bone marrow-derived macrophage (Hanna et al., 2017). On the contrary, as described in detail in my results, inhibition of the Arp2/3 complex in neuronal CAD cells induces the formation of TNTs and significantly increases inter-cellular DiD-labeled vesicle transfer (Sartori-Rupp et al., 2019).

1.5.2 Rab Cascades

Ras-related proteins in brain (Rabs), are peripheral membrane-anchored proteins best known for their essential roles in endo- and exocytic membrane trafficking, including vesicle formation and vesicle movement along cytoskeletal networks (Stenmark, 2009). Through various pathways, Rabs also regulate ciliary axoneme extension (Blacque et al., 2018), dendritic growth cones, and dendritic filopodia and spines (Mori et al., 2012).

Through a high-content screening in which 41 Rab GTPase subfamilies were studied in CAD neuronal cells, our group found that Rab8a and Rab11a increased TNT formation and promoted contact-dependent inter-cellular vesicle transfer (Zhu et al., 2018). On the contrary, the activation of Rabin8, a major Guanine nucleotide Exchange Factor (GEF) of Rab8 and important for ciliogenesis and filopodia elongation (Homma and Fukuda, 2016; Westlake et al., 2011), increased the generation of filopodia but did not affect TNT formation. In the same study, the v-SNARE Vesicle-associated membrane protein 3 (VAMP3) was identified as an effector of Rab11a- and Rab8- TNT formation, but not of filopodia. This study indicates that Rab11 and Rab8 act in a signaling cascade through VAMP3 to induce TNT formation. This study corroborates another finding in which knockdown of Rab8a or Rab11a in neuronal Schwann cells inhibited the formation of TNTs and reduced inter-cellular vesicle transfer (Zhu et al., 2016). By overexpressing Rab8 in HeLa cells, Gerdes and colleagues found an increase in TNT formation and transport of Transferrin (Tf) and Tf- receptor, suggesting that Rab8-dependent TNT formation mechanism plays a role in cancer cell lines as well (Burtey et al., 2015). The authors confirmed this notion after observing that significantly less cargo transfer occurred between non-cancer NRK cells. In agreement with these observations, we found that blocking the Tf recycling pathway inhibits TNT

formation ([Zhu et al., 2018](#)). Finally, in other cancer cells, bronchial epithelial and pleural mesothelial cells, recent reports by Levallet and colleagues identified the Ras association domain family 1 isoform A (RASSF1A) as a regulator of TNTs formation through induction of GEF-H1 and upregulation of Rab11 ([Dubois et al., 2018](#)).

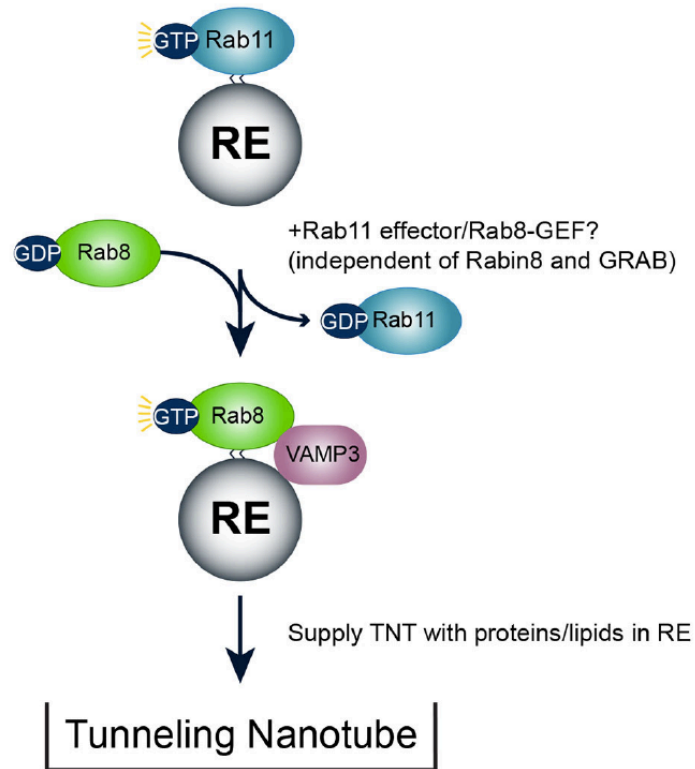


Figure 9. Regulation of Tunneling Nanotubes by Rab11a-Rab8a-VAMP3 cascade.

Schematic diagram depicting neuronal TNT formation by Rab cascade, (obtained from [Zhu et al., 2018](#)). GTP-bound Rab11a acts upstream of Rab8a, while VAMP3 acts downstream of Rab8a in regulating TNT formation. Rab11a-induced activation of Rab8a is independent of Rabin8 and GRAB. One possibility is that Rab11a is released from the recycling endosome when Rab8a is activated. GTP-bound Rab8a interacts with VAMP3, which functions as a Rab8a effector and facilitates the fusion of recycling endosome-derived vesicle to supply lipids and specific proteins needed for TNT formation.

Together, these studies shed light on the formation of TNTs via Rab GTPases and supports our group's hypothesis that TNTs and filopodia harness distinct protein modulators underlying the regulation of their formation. However, it is currently unclear whether Rabs could affect TNT formation by modulating actin cytoskeletal dynamics or/in addition to regulating membrane supply and specific lipids and proteins through activation of the recycling pathway.

1.5.3 PI3K/AKT/mTOR Signaling Pathway

The Phosphatidylinositol-3-kinase (PI3K) and its downstream mediators Akt and the mammalian target of rapamycin (mTOR) constitute a crucial signaling pathway for the regulation of the cell cycle, cellular proliferation, metabolism, and survival (Yu and Cui, 2016). The pathway is also involved in the morphogenesis of filopodial structures such as dendrites (Kumar et al., 2005).

Several studies have also revealed the importance of this signaling pathway in the formation of TNTs. Using a dominant negative mutant for Akt, Wang and colleagues found a significant reduction in TNT formation of PC12 cells. Similarly, inhibition of PI3K with specific inhibitors (*ly294002* and *wortmannin*) also reduced TNT formation. Inhibition of mTOR via rapamycin had a similar effect (Wang et al., 2011). Using the mTOR-specific inhibitors *everolimus* and *metformin*, studies in mesothelioma and ovarian cancer cells also observed a suppression of TNT formation (Desir et al., 2016; Lou et al., 2012).

Together, these studies indicate that the PI3K/AKT/mTOR signaling pathway plays a role in the formation of TNTs, and postulate the notion that TNTs might be inter-cellular mechanisms that aid cells under stress (Figure 10) (Wang et al., 2011).

1.5.4 M-Sec/TNFaip2/B94

Downstream of the PI3K/AKT/mTOR Signaling Pathway lies M-Sec, a cytosolic protein homolog of *Sec6* that was first detected in specialized epithelial enterocytes called *M* cells. Originally known as 'TNF- α induced protein 2' (TNFaip2) (or B94) for exerting various proinflammatory and catabolic effects as a pleiotropic cytokine, M-Sec was one of the earliest markers found to be involved in the formation of TNTs (Hase et al., 2009). The depletion of M-Sec by RNA interference

in Raw264.7 macrophages significantly decreases TNT formation and inter-cellular propagation of calcium flux. Conversely, its overexpression has the opposite effect, (i.e. it induces TNT formation). In HeLa, M-Sec's induction activity involves the interaction with the Ras-related A (RalA) GTPase and the Exocyst complex (**Figure 10**).

In other studies carried out in both HeLa and HEK-293 cells, M-Sec was shown to also depend on the transmembrane major histocompatibility complex (MHC) class III protein leucocyte specific transcript 1 (LST1) (Schiller et al., 2013). The authors propose that LST1 recruits RalA to the plasma membrane, where RalA then interacts with the Exocyst complex (**Figure 10**). This suggests that M-Sec activates a molecular assembly machinery that could be responsible for supplying the membrane required for TNT formation (Hanna et al., 2017).

A recent proteome interactomic analyses for M-Sec in human osteosarcoma-origin U2OS cells revealed an important upstream interactor of M-Sec, the endoplasmic reticulum chaperone ERp29 (Pergu et al., 2019). After depleting M-Sec by siRNA, while simultaneously over-expressing exogenous ERp29, the authors observed a significant reduction in TNT formation, indicating that ERp29 can only induce TNTs in the presence of M-Sec.

Interestingly, M-Sec does not appear to play the same role in all of immune cells. For example, M-Sec was not found, nor did it increase, TNT formation in immune Jurkat T cells (Lachambre et al., 2014). Furthermore, M-Sec doesn't appear to be expressed in neuronal cells either (Gousset et al., 2013), which could suggest that its role in TNT formation is restricted to myeloid lineages only.

1.5.5 MyosinX

The myosins are a superfamily of actin-based motor proteins that “walk” on actin filaments. Of all the myosins, MyoX is the most broadly distributed one in cells, inducing the formation of filopodia (Sousa and Cheney, 2005). Studies from our group showed that MyoX is involved in TNT formation after findings revealed that its deletion inhibited TNT formation. Intriguingly, different domains of MyoX are essential for TNTs, and some for filopodia (Gousset et al., 2013). We demonstrated that neuronal TNT formation requires the motor and tail domains of MyoX, and, specifically, identified the F2 lobe of the tail protein-ezrin-radixin-moesin (FERM) domain. Given

that MyoX increases the formation of adherent- and dorsal filopodia, we postulated that neuronal TNTs can arise from a subset of MyoX-driven dorsal filopodia, independent of integrins, transmembrane receptors required for the formation of adherent filopodia. Consistent with our hypothesis and subsequent data shown in *Chapter 2* (Delage et al., 2016), MyoX acts downstream of CDC42 and is independent of VASP, another potent inducer of dorsal filopodia formation (Bohil et al., 2006). Together, these findings demonstrate the existence of different mechanisms for dorsal filopodia formation.

In macrophages, recent studies showed that MyoX expression depends on the Immunodeficiency Virus Type 1 (HIV-1) Negative Regulatory factor (NEF) (Uhl et al., 2019), indicating, for the first time, that MyoX-dependent TNT formation is not restricted to neuronal cells.

1.6 Tunneling Nanotubes: Intrinsic and Extrinsic Induction

There are several physiological factors that can affect the molecular machineries described above (Rustom, 2016) and which indicate that stressful stimuli induce TNT formation. Some studies have postulated that TNTs arise from stress responses to conditions that favor metabolic dysregulation (Lou et al., 2012; Victoria and Zurzolo, 2017; Wang and Gerdes, 2012). The effectors known to date are described below.

1.6.1 Reactive Oxygen Species

Reactive Oxygen Species (ROS), whose free radicals have been long known to pose a threat to cellular integrity and viability (Dixon and Stockwell, 2014), were found to be effective inducers of TNTs via the major form of endogenous ROS, hydrogen peroxide (H₂O₂) (Liang, 2018). In rat hippocampal astrocytes, neurons, and HEK293 cells, H₂O₂ significantly increased the number of (homotypic and heterotypic) cells connected by TNT-like protrusions compared to untreated cells (Wang et al., 2011). Notably, upon co-culturing non-stressed and stressed cells, the authors observed that H₂O₂-treated cells were the initiators of TNT formation. Subsequent studies from our group showed that H₂O₂-induced stress increases TNT formation of neuronal CAD cells by 70% (Gousset et al., 2013). In one of our group's prior reviews (Victoria and Zurzolo, 2017), we proposed that, based on (i) the strict correlation between neurodegeneration-associated proteins and increased ROS production and oxidative stress (Kim et al., 2015), and (ii) our findings showing an increase in neuronal TNTs through intercellular aggregate buildup, ROS generated as a consequence of prion-like protein aggregation may stimulate TNT formation.

The mechanism leading to ROS-mediated TNT induction is not well understood; however, a study on TNTs in astrocytes indicates that H₂O₂ triggers the phosphorylation of the p38 mitogen-activated protein kinase (MAPK) (Zhu et al., 2005), a kinase responsive to stress stimuli previously shown to induce actin cytoskeletal remodeling in fibroblasts (Hoffman et al., 2017). Together, these observations support the established notion that H₂O₂ affects the actin cytoskeletal organization and induces the formation of actin-rich protrusions (Huot et al., 1998).

1.6.2 Hypoxia

Decreased oxygen availability (hypoxia) has been well acknowledged as a cellular state that severely affects the balance between ROS and antioxidant defenses, making cells vulnerable to oxidant damage that negatively impacts organ structure and function. Pathological conditions, such as tumor aggression and metastasis and cerebral and heart ischemia have been associated to the deleterious side-effects of hypoxia (Michiels, 2004). In order to investigate if TNTs found in chemoresistant mammalian cancer cells were affected by hypoxia, Lou and colleagues cultured A2780, C200, and SKOV3 ovarian cancer cells in a chamber containing 2% oxygen and tested the expression of a factor known to maintain cellular homeostasis in low oxygen levels, hypoxia inducible factor-1 α (HIF-1 α). By 24 hrs, the authors observed an increase in HIF-1 α expression and a 6-, 10-, and 11-fold increase in TNT formation compared to normoxic conditions, respectively (Desir et al., 2016). Similarly, in another study examining the prevalence of hypoxia in other carcinoma cells, Lou et al. discovered that hypoxia also induced TNT formation in three different colon cancer cell lines, SW480, HCT-116, and DLD-1 (Lou et al., 2018). Stress-induced TNT formation by hypoxia has also recently been observed in prostate cancer PC3 and LNCaP cells (Kretschmer et al., 2019). Taken together, these studies present convincing evidence that the tumor microenvironment, which is known to benefit from hypoxic conditions (Petrova et al., 2018), benefits from an inter-cellular TNT-mediated network that can yield cancer spreading (TNTs and Cancers explored in more detail below).

1.6.3 Apoptosis Signaling

p53, Bax, and caspases play important roles in cell apoptosis. Wang and colleagues tested the role of each one and found that the overexpression of p53 increased the number of TNT-connected cells, while its depletion using a dominant negative mutant had the opposite effect. In support of this finding, the authors silencing p53 (p53-1 & p53-2) by siRNA and observed similar results (Wang et al., 2011).

The apoptosis antigen 1, FAS receptor (also called APO-1 or CD95), is a type II transmembrane protein receptor that belongs to the TNF family that induces apoptosis when ligands bind to it (Strasser et al., 2009). Esposti and colleagues observed that the activation of FAS in immune

Jurkat T cells induced 20-fold increase in the number of TNT-connected cells ([Arkwright et al., 2010](#)). Transfer of vesicles and fluorescent cytosolic proteins was also observed upon activation of Fas. Lastly, upon observing that Secramine A and actin Rho-GTPase inhibitor, toxin B, blocked FAS-stimulated TNT formation, the authors indicate that the role of FAS on TNT induction is mediated by Rho GTPases. Whether other immune cells, or cell types of other origins, behave similarly upon the activation of FAS is not currently known.

1.6.4 Stressful Environment

Low-serum, hyperglycemic, acidic growth medium stimulate TNT formation. In a study of TNTs connecting Mesothelioma cells, Lou and colleagues demonstrated that low Hyperglycemic low-serum medium (pH 6.6, 50mM glucose, 2.5% fetal calf serum) or hyperglycemic, low-serum medium with cytokines added to stimulate epithelial-to-mesenchymal transition (EMT), increased TNT formation in mesothelioma ([Lou et al., 2012](#)). Serum depletion in Schwann cells, described in more detail above, also increased TNT formation and TNT-mediated transport of GTPases, Rab8a and Rab11a ([Zhu et al., 2016](#)).

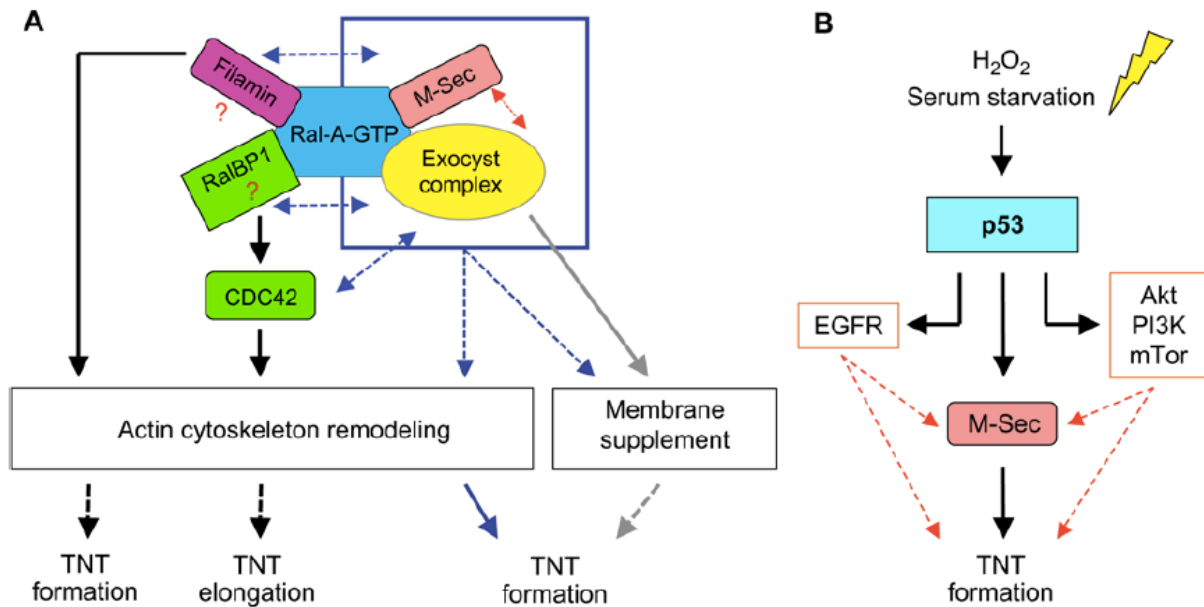


Figure 10. TNT formation and induction.

(A) Schematic diagram depicting the induction of TNT formation through the binding of M-Sec to the active form of Ral-A, an event dependent on the interaction between Ral-A and its downstream effector, the exocyst complex, whose function is to target secretory vesicles for membrane expansion. Through its interaction with Ral binding protein 1 (RalBP1), Ral-A is able to activate CDC42, which leads to actin remodeling. Given the role Ral-A plays in actin remodeling and the role of the exocyst complex, it is likely that M-Sec induces TNT formation by actin cytoskeleton remodeling and the supply of membrane. The association of Ral-A with filamin, an actin-filament crosslinking protein implicated in the regulation of actin remodeling in filopodia, may also be a candidate protein involved in TNT formation. (B) Stress conditions (H_2O_2 and serum starvation) induce TNT formation through the activation of the transcription factor p53, the EGF receptor (EGFR), and the Akt–PI3K–mTor pathway. M-Sec is also induced by the activation of p53. Black arrows indicate pathways previously described whereas dotted lines show hypothesized pathways. Blue colored arrows indicate interactions with the M-Sec–Ral-A–exocyst complex (blue square). Grey colored arrows show the exocyst-complex-mediated pathway. Single arrows indicate pathways, double arrows depict putative interactions. Both schematics and content were obtained from [Abounit and Zurzolo, 2012](#).

1.7 Tunneling Nanotube: Ultra-Structure

Specialized cellular membranous protrusions are defined by a strict structure and function relationship. For example, lamellipodia are membranous sheet projections that play a vital role in steering the migration of neuronal precursors during early brain cerebral and cerebellar development (Krause and Gautreau, 2014). They owe this function to Arp2/3, which by promoting branched actin polymerization, it enables cells to propel across large distances (Innocenti, 2018).

Unfortunately, little is known about the structure of TNTs. In-depth ultrastructural analyses of TNTs have been scarce due to the transient and fragile nature of TNTs discussed at the beginning of this chapter. Only a small number of studies have been able to successfully examine the ultrastructure of TNTs using structural imaging approaches such as Scanning Electron Microscopy (SEM) and Transmission Electron Microscopy (TEM). Unfortunately, the information provided by these studies lack (i) quantitative analysis of the number, prevalence, and significance of the connections presented, and (ii) answers to several key anatomical questions, such as: what does the cytoskeletal backbone of TNTs contain: actin, microtubules, or both? Does the cargo described as 'being transferred' by light microscopy get shuttled within TNTs, or on the outside of the membrane? Are TNTs open at both ends of the structure, or are they closed, filopodia-like protrusions that mediate cargo transport via trogocytosis-like event (in which an entire patch of plasma membrane gets engulfed by another cell) (Dance, 2019)?

Classic SEM analyses revealed that TNTs create a "seamless" membranous transition between the surface of PC12-connected cells (Rustom et al., 2004) (Figure 10) By serial sectioning-TEM (ssTEM) at 80nm/section, accurate diameter measurements were found in the range of 50 – 200 nm (Figure 10). ssTEM micrographs also indicated cytoplasmic continuity between two cells connected. However, the example of a TNT provided by the authors is significantly shorter in length than the ones obtained by SEM or light microscopy, making comparisons between these two observations difficult. For example, the connection contained 'kinks' along its length, presumably from mechanical stress during sample preparation, as suggested by the authors. Examples showing similar aberrations were shown in TNTs connecting SEP AS583 cells (Miyazawa

et al., 2010). Whether these connections are representative of TNTs, or a sub-class of TNTs seen by light microscopy was not discussed in either report.

Another study using ssTEM at 60 nm found that HIV-1-transporting-TNTs (of 180–380 nm in diameter) in Jurkat lymphocyte T cells consisted of either a single protrusion invaginating into the opposing cell, or of two filopodia-like protrusions touching each other (**Figure 10**) (Sowinski et al., 2008). Both observations explain how membrane dyes of two cell populations connected by TNTs do not mix and suggest that TNTs observed by light microscopy (at least in Jurkat T cells) are derived solely from one of the cells that appeared connected. Moreover, the authors suggest that TNTs in T cells function through a receptor-dependent manner, indicating that TNTs in immune cells are unique compared to TNTs in other cells, such as neuronal cells (Rustom et al., 2004). Finally, to distinguish Jurkat T cell connections to other connections formed by homotypic cells, the authors also presented an example of an intercellular bridge derived from cytokinesis with dense microtubule bundles making up a midbody (Skop et al., 2004; Sowinski et al., 2008).

More recently, Eugenin and colleagues employed SEM and TEM on HIV-infected (and non-infected) human monocyte-derived macrophages and observed two distinct types of connections: open-ended structures that presumably allow cargo transport, and “non-fused”, close-ended, synapse-like protrusions (**Figure 10**) (Okafo et al., 2017). TEM revealed that the connection identified contained actin and numerous mitochondria within the connection but no viral particles in/outside. This finding is consistent with the cytoskeletal composition of TNT-like structures described by Sowinski et al., in Jurkat T cells– TNTs in immune cells are often close-ended protrusions (Sowinski et al., 2008). In MDCK and lung epithelial cells (A549), SEM analysis underscored the detrimental impact that sample preparation steps can have on the integrity of TNTs, most often affecting their ‘straightness’. By SEM, the authors found that TNTs of A549 cells vary in diameter, from 250 nm – 1.37 μm (**Figure 10**) (Kumar et al., 2017). TEM analysis showed an electron-dense bundle of fibers (presumably microtubules) running along the length of the inside of the expansion-processed connection, which wasn’t expected based on the tubulin-lacking TNTs previously reported for T lymphocytes (Sowinski et al., 2008). The presence of mitochondria and ribosomes within the connections observed was also reported. Bladder cancer T24 and RT4 cells by SEM were measured at 100 – 200 nm in diameter, with lengths that spanned

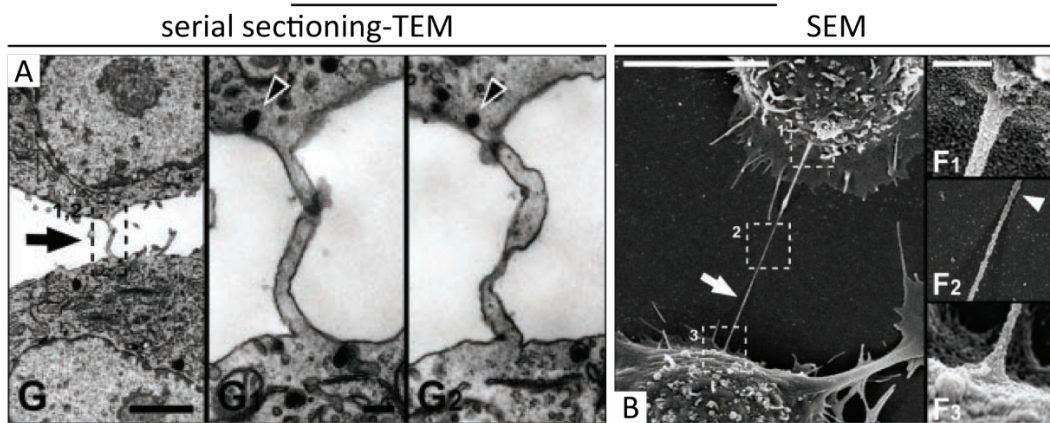
from 20 μm to 1 mm. The electron micrographs showing TNTs connecting T24-to-RT4 appeared to be single connection with branches (Lu et al., 2017). It is not clear whether the branches stemming from these TNTs were ever connections that snapped during sample preparation. Other examples presented by the authors lacked a contiguous plasma membrane connecting both cells; that is, appeared as filopodia-like structures.

In another study, Corbeil and colleagues explored the ultra-structure of TNTs connecting human primary CD34+ hematopoietic stem and progenitor cells (HSPCs). Using SEM, the authors found that TNTs had a diameter of 100 nm, a length that reached $> 100 \mu\text{m}$, and importantly, appeared to create membrane continuity between the cells at both ends (**Figure 10**) (Reichert et al., 2016). In contrast, KG1a cells, an immature hematopoietic cell line displayed a clear junction half-way along the length of their TNTs, indicating a close-ended connection, which the authors confirmed upon the observation of fluorescent membrane probes and covalently labeled long-lived intracellular molecules not flowing seamlessly between cells.

In spite of the technical obstacles encountered, previous structural studies in neuronal, immune, and epithelial cells propose a variety of topologically different TNTs within and between cell types. Unfortunately, the resolution and sample quality based on the images provided does not provide sufficient detail to definitively distinguish whether the connections found contained actin, microtubules, or both. Moreover, only a couple of studies provide examples of cargo-bearing TNTs, and neither of these reports obtained any convincing evidence proving TNTs' open-endedness. The lack of these pivotal pieces of information led to an ongoing debate regarding the structural identity and the mechanisms TNTs use to transport cargo (Baker, 2017).

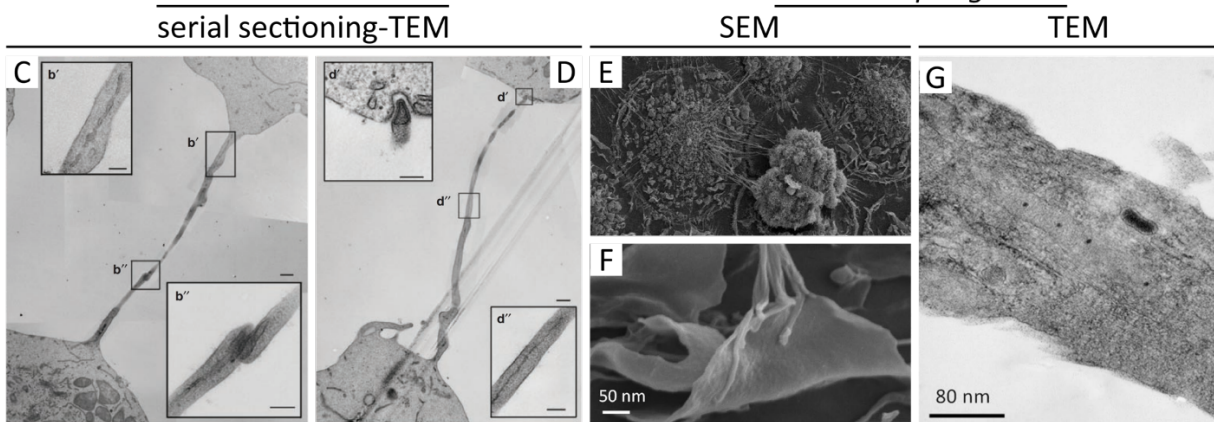
A significant portion of my dissertation dealt with the optimization and application of a correlative- cryo electron-microscopy-based pipeline to address these questions. Using these strategies, which will be described in detail in *Chapter 3*, we were able to observe TNTs connecting cells in culture under native conditions and discover that most TNTs, classically defined as single connections, were comprised of several individual TNTs. We also demonstrated that cargo (e.g. vesicles and mitochondria) get transported through the inside of the TNT, using actin. Our work also proves that TNTs, at least in neuronal cells, create cytoplasmic continuity.

PC12



Jurkat T

Macrophages



A549 cells

HSPC

SEM / TEM

SEM

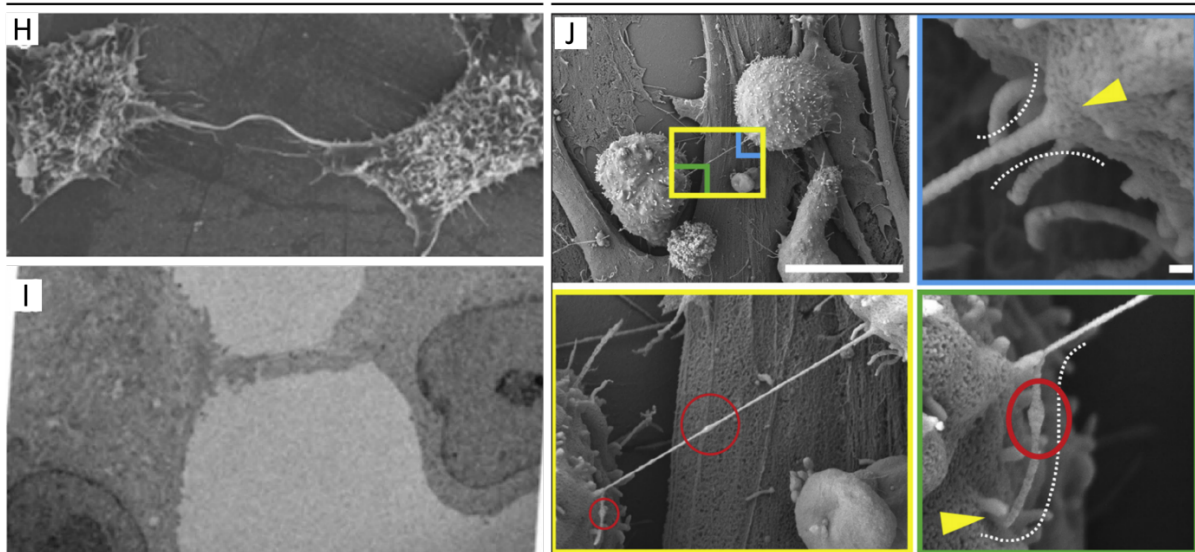


Figure 11. Ultra-structural analyses of Tunneling Nanotubes.

(A-B) TNTs connecting PC12 cells seen by Serial-sectioning TEM (A) and SEM (B), obtained from [Rustom et al., 2004](#). Scale bar: Left (G), 2 μ m, Middle (G1), Right (G2), 200 nm. (C-D) TNTs connecting Jurkat T cells seen by Serial-sectioning TEM (C) and SEM (D). Scale bar, C, D, 500 nm; insets (*b'*, *b''*, *d'*, and *d''*), 200 nm. Images were obtained from [Sowinski et al., 2008](#). (E-G) Representative image of HIV infected cultures after 3 days post infection shown by SEM (E-F) and TEM (G). (F) High magnification electron micrograph of the end of the TNT process in HIV infected conditions. Images were obtained from [Okafo et al., 2017](#). Scale bar: F, 50nm; G, 80nm. (H-I) Lung epithelial A549 cells seen by SEM (H) and TEM (I) show TNTs after expansion microscopy. Images obtained from [Kumar et al., 2017](#). (J) TNT connecting Human primary CD34+ hematopoietic stem and progenitor cells (HSPC) as seen by SEM. Specific regions highlighted with green and blue boxes in are shown at high magnification as insets. Red circles indicate membrane bulges along TNTs. Dotted white lines and yellow arrowheads indicate the apparent membrane continuity of TNT ending points. Dotted white lines and yellow arrowheads indicate the apparent membrane continuity of TNT contact sites with HSPC body. Scale bar, 10 μ m; Insets, 100 nm. Image obtained from [Reichert et al., 2016](#).

1.8 Tunneling Nanotube-like structures *In Vivo*

Definitive evidence that TNTs exist in the complex biological contexts where *in vitro* observations point to is currently missing. However, numerous studies have reported the presence of membranous protrusions with signaling roles in several classes of tissues at embryonic and early stages of post-natal development.

During gastrulation of marine animals such as Sea Urchins, 200 – 400 nm thick, and up to 80 μm -long actin- and microtubule-containing filopodial protrusions extend from ectodermal cells, and between primary and secondary mesenchyme cells (PMCs and SMCs, respectively) (**Figure 12**) (Miller et al., 1995). Although sightings of thin filopodia were previously made in Sea Urchins and hypothesized to play a role in locomotion (Gustafson and Wolpert, 1963), McClay and colleagues suggest that the developmental timing, location, and rich cytoskeletal apparatus of filopodia formed by PMCs and SMCs point their function role towards signaling organelles that enable the communication of migratory cues (McClay, 1999).

During zebrafish gastrulation, long (up to 350 μm), actin-rich Intercellular Bridges (IBs) generate from dividing epiblast cells (Caneparo et al., 2011) that do not separate by abscission as daughter cells normally do during cytokinesis, (the final step of cell division) (**Figure 12**). The observation of membrane-linked Dendra2 moving along IBs at a rate that would only be possible through an active process led the authors to hypothesize that IBs could function as TNTs for inter-cellular signaling during embryonic patterning and development. However, recently published studies described similar protrusions as ‘retraction fiber projections’ that host *Migrasomes* (**Figure 12**) (Jiang et al., 2019), vesicular structures at the tips of projections emanating from migrating cells that release contents into the environment through an EV-like mechanism called ‘migracytosis’ (Huang et al., 2019; Ma et al., 2015; Tavano and Heisenberg, 2019). Although IBs and migrasome-carrying fibers resemble each other topologically, it is currently unclear whether migrasomes are derived from IBs, or whether these two structures coexist in the complex zebrafish gastrular micro-environment as two separate processes.

The formation of stable IBs formed by incomplete cytokinesis was also shown in various germline and somatic tissues (Haglund et al., 2011). For example, actin-rich germline bridges

called *Ring Canals* (RCs), are 500 nm – 10 µm-thick rims that connect germ cells in cysts of *Xenopus laevis* (Kloc et al., 2004), *Drosophila* (Haglund et al., 2010), mice (Pepling and Spradling, 1998), and several others (Haglund et al., 2011). The function of these connections remains unknown; however, numerous reports have proposed that they promote the exchange of cytoplasm and organelles, in a similar fashion as TNTs, as TNTs do not form from cell division. Whether ring canals or other IBs, such as those suggested by Caneparo et al., in zebrafish represent specialized TNT-like protrusions that enable inter-cellular communication and synchronization of cell division and differentiation requires future investigation.

During development of the Imaginal disc of *Drosophila*, 200 nm-thick and up to 700 µm in length, specialized filopodia called *Cytonemes* were identified, and are sometimes erroneously classified as the first demonstration of TNT-like structures *in vivo* (Figure 12) (Ramírez-Weber and Kornberg, 1999). Differently from TNTs, cytonemes are close-ended, specialized filopodia (Kornberg and Roy, 2014), that play an important role in signaling of morphogens, (e.g. Bone morphogenetic protein, BMP; Sonic hedgehog, Shh; Wingless-related integration site, Wnt, and Fibroblast growth factor, Fgf), through ligands and receptors that are currently under investigation (Huang and Kornberg, 2016; Zhang and Scholpp, 2019). Interestingly, recent evidence from our group indicates that Wnt signaling is involved in the regulation of TNT formation of primary neurons (Vargas et al., *EMBO in press*). However, Wnt-dependent TNT formation is mediated by the activation of the downstream Calcium-Calmodulin signaling pathway, while the formation of cytonemes is mediated by the downstream activation of beta catenin (Mattes et al., 2018). Thus, while activation of the Wnt receptor is involved in both cytoneme and TNT formation, their downstream pathways differ, suggesting that cytonemes and TNTs are different structures with different functions during development.

In other studies, major histocompatibility complex (MHC) class II+ cells in the mouse cornea were observed to connect via TNT-like structures called membrane nanotubes (MNTs), of <800 nm in thickness and > 300 µm in length (Chinnery et al., 2008; Seyed-Razavi et al., 2013). The authors hypothesize that isolated (dendritic) cells might use TNTs to communicate and form an immunological syncytium, however, this hypothesis has yet to be explored.

Intervascular bridges are actin-bearing fibrous strands that connect neighboring capillaries in the retina of humans and mice (**Figure 12**) ([Mendes-Jorge et al., 2012](#)). The expression of common pericyte markers (NG2 and PDGFR-b) led the authors to hypothesize that they are of pericytic nature. Interestingly, these bridges express Cx43, suggesting that these connections allow inter-cellular communication. However, the precise signals transported between cells via these bridges has not been explored yet.

Various malignant tumors, including those of lung cancer, ovarian cancer, laryngeal cancer, mesothelioma, and neuroblastoma were shown to form TNT-like connections ([Ady et al., 2016](#); [Antanavičiūtė et al., 2014a, 2015](#); [Desir et al., 2016](#)). Mesothelioma cells forming TNTs of > 70 μm in length contained microvesicles labeled with MitoTracker ([Lou et al., 2012](#)). Human glioblastoma tumors labeled with an astrocytoma cell GFP reporter and implanted into a mouse brain form long (>500 μm) connections called Tumor Microtube (TMs) between glioblastoma cells (**Figure 12**) ([Osswald et al., 2015a](#)).

Stephanie Cherqui and colleagues identified human stem cells (HSCs) grafted to cystinotic kidneys also generated TNT-like, nanotubular extensions that crossed the dense basement membranes that delivered cystinosin into diseased proximal tubular cells (**Figure 12**) ([Cherqui and Courtoy, 2017](#); [Naphade et al., 2015](#)).

Collectively, these findings show that TNT-like structures exist *in vivo* under certain physiological and/or pathological conditions. Future studies will need to demonstrate whether these different structures feature the TNT criteria described above.

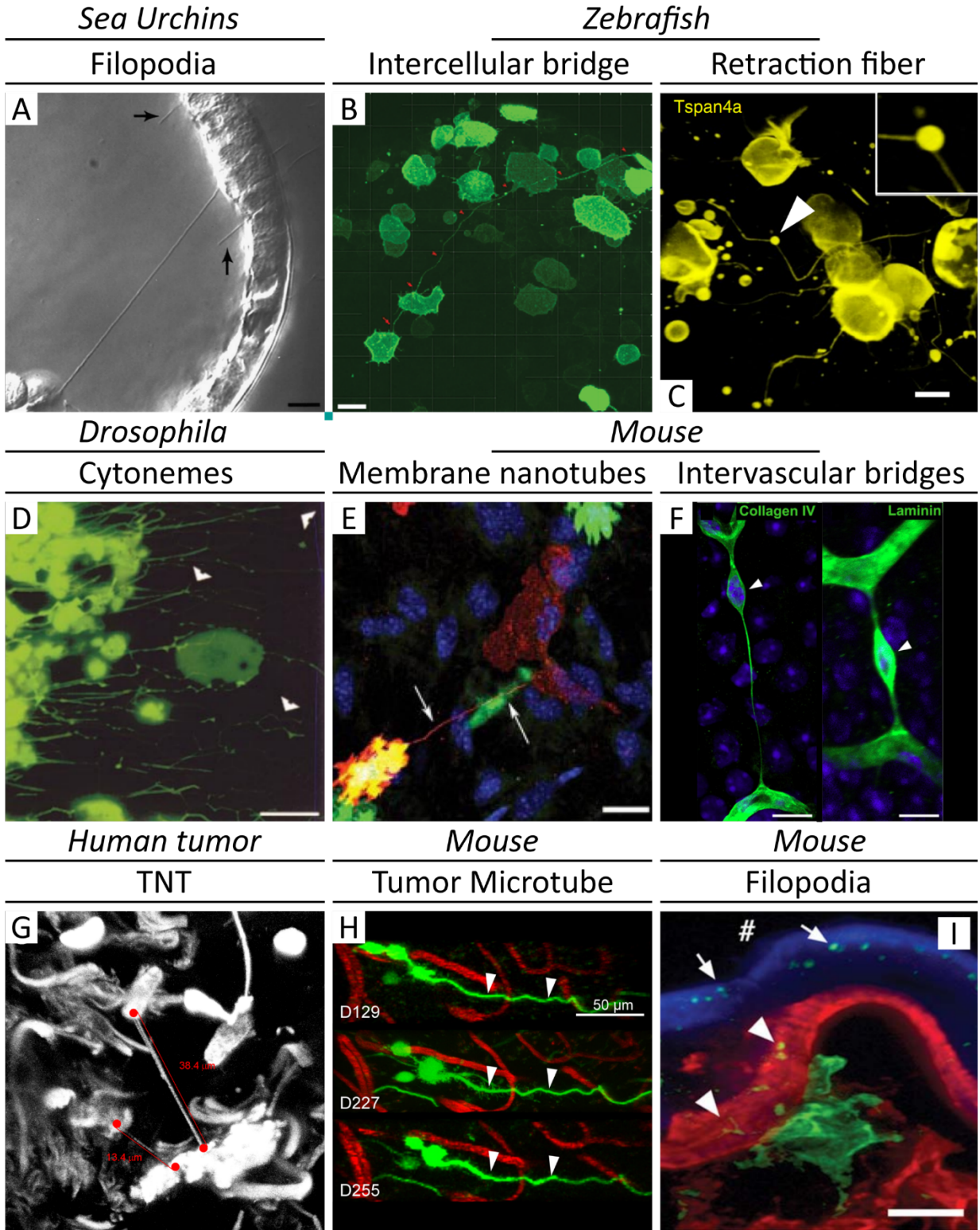


Figure 12. Examples of TNT-like structures in vivo.

Gallery of examples displaying Tunneling Nanotube-like structures *In Vivo* with the respective names given and model organisms in which they were identified. **(A)** Videomicrograph displaying a long, thin (200-400 nm in diameter) filopodium extending from a primary mesenchyme cell to the wall of the ectoderm ~80 μm away. The image also displays thin filopodia extending from ectoderm cells into the blastocoel (arrows). Scale bar, 10 μm . Image obtained from [Miller et al., 1995](#). **(B)** Confocal micrograph displaying an intercellular bridge (red arrows) formed between epiblast cells, acquired in a sub-region of a mosaic zebrafish embryo expressing mDendra2 at the onset of gastrulation. Scale bar, 20 μm . Image obtained from [Caneparo et al., 2011](#). **(C)** Confocal image of retraction fibers containing migrasomes, acquired on a single blastomere of an eight-cell stage embryo injected with tspan4a-GFP mRNA. The arrow indicates an enlarged, process-connected vesicle. Scale bar, 10 μm . Image obtained from [Jiang et al., 2019](#). **(D)** Cells from the late third instar drosophila wing disks extending long processes containing GFP. **(E)** Confocal micrograph of Chimeric mouse corneal whole mount reveals a donor-derived (GFP+/green) MHC class II+ (red) and double positive (yellow) cell connecting via a fine membrane nanotube (arrows) to a resident MHC class II+ GFP+ cell (red only). Scale bar = 10 μm . Image obtained from [Chinnery et al., 2008](#). **(F)** Differential chromatin distribution in mouse intervascular bridge cells (IBCs). Mouse IBCs were surrounded by a basement membrane stained by PAS reaction and containing collagen IV (left) and laminin (right). Image obtained from [Mendes-Jorge et al., 2012](#). **(G)** Lung adenocarcinoma tumor specimen with multiple mitotracker-labeled nanotubes of various lengths. **(H)** Example of a very stable T325 GBMSC tumor microtube (TM) (arrowheads), followed over 126 days in vivo. Scale bar, 50 μm . Image obtained from [Osswald et al., 2015](#). **(I)** Z-stack projections over 7 mm of confocal optical sections from an 8-month-old Ctns2/2 mouse kidney, transplanted at 2 months with eGFP-expressing wild-type hematopoietic stem cell (HSC). Green, immunolabeled eGFP; red, laminin immunolabeling provides a grazing view of basement lamina; blue, proximal tubular cell (PTC) brush border-specific sugars labeling by Lotus Tetragonolobus (LT)-lectin defines PTCs (lumen, #). Scale bar, 10 μm . Image obtained from [Naphade et al., 2015](#).

1.9 Roles in Disease

A growing body of literature suggests that TNTs play a role in a wide variety of diseases, including neurodegenerative diseases (NDs), viral diseases, bacterial infection, and cancer.

1.9.1 Neurodegenerative Diseases

Major NDs, such as Parkinson's disease (PD), Alzheimer's disease (AD), Huntington's disease (HD), and amyotrophic lateral sclerosis (ALS) share the defining feature of proteinaceous aggregates that accumulate in the central nervous system (CNS) (Jucker and Walker, 2013). A growing body of evidence suggests the notion that the progression of these diseases is the consequence of prion-like propagation of amyloid-like pathologies (Zhang et al., 2018). Our group demonstrated that the infectious form of prions (PrP^{Sc}) are able to spread to other cells by hijacking TNTs (Gousset et al., 2009). The fact that amyloid proteins behave like prions, in their ability to induce misfolding of normal proteins, led our group to propose TNTs as one of the avenues for the spreading of neurodegenerative diseases in the CNS (Baker, 2017; Gousset and Zurzolo, 2009; Gousset et al., 2009). Over the last decade, our group and others confirmed this notion by demonstrating that in addition to prions (Gousset et al., 2009; Victoria and Zurzolo, 2017; Victoria et al., 2016; Zhu et al., 2015), other aggregates of misfolded proteins get transported inter-cellularly via TNTs. These misfolded proteins include tau and amyloid beta (A β), the main components of amyloid plaques found in the brains of Alzheimer disease patients (Abounit et al., 2016a; Tardivel et al., 2016; Wang et al., 2011). α -synuclein, the presynaptic neuronal protein genetically linked to Parkinson's disease, was also found transmitted across other cells via TNTs (Abounit et al., 2016b; Dieriks et al., 2017; Rostami et al., 2017; Vargas et al., 2019). Mutant Huntingtin (mHtt), the unstable protein associated to Huntington's disease was no exception. Our lab first observed aggregate spreading of polyglutamine and mHtt in TNTs connecting CAD cells (Costanzo et al., 2013). Recently published reports identified a brain-enriched GTPase, Rhes, as a key factor in the biogenesis of TNTs and enhanced intercellular transfer of mHtt between donor and acceptor cell populations (Sharma and Subramaniam, 2019).

1. Prion/ prion-like protein-infected cell

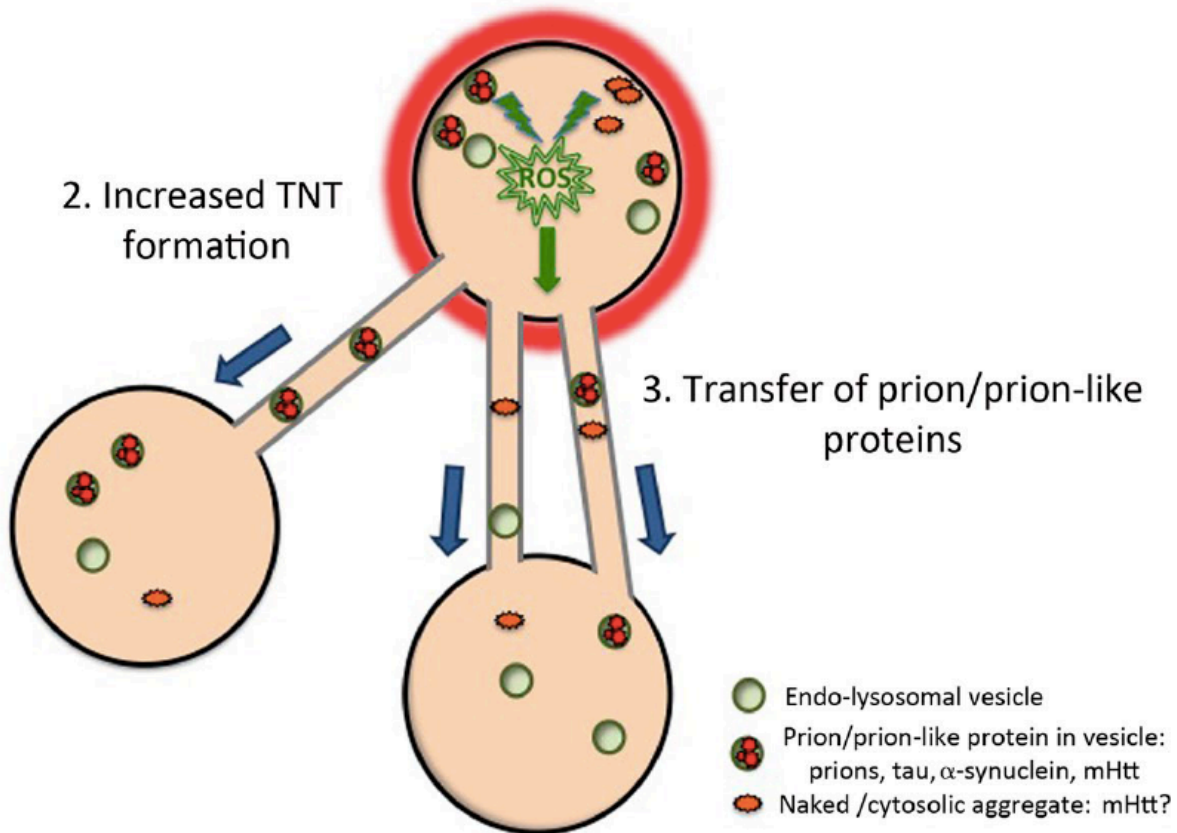


Figure 13. Model of prion-like protein aggregate–induced formation of TNTs.

Model of prion-like protein aggregate–induced formation of TNTs and intercellular spreading, (Obtained from [Victoria and Zurzolo., 2017](#)). The aggregation and accumulation of prions or prion-like proteins in an “infected” cell (1) induces an increase in TNT number via an unknown mechanism, (e.g. via ROS-induced stress pathway) (2). The prion/prion-like aggregates may then be propagated via TNTs from infected cells to naive cells (3), wherein they effect the conversion and seeding of naive self-protein molecules.

1.9.2 Viral Diseases

Viruses are inert pathogens that rely on host cellular mechanisms to transmit and propagate effectively to non-infected cells in order to thrive. Numerous reports have shown that viral particles can also utilize TNTs to transport inter-cellularly ([Sattentau, 2010](#)).

The earliest detection of viral particles associated to TNT-like connections dates back to 2005, when Favoreel and colleagues found that a protein kinase of the pseudorabies virus induced the formation of “cell projections” in swine testicle and rabbit kidney cells. Viral particles used these projections to propagate onto non-infected cells ([Favoreel et al., 2005](#); [La Boissière et al., 2004](#)). Other members of the Herpes virus family, such as the Herpes Simplex Virus (HSV), NV1066 ([Ady et al., 2016](#)), and the Murine gamma-herpesvirus-68 (MHV-68), were also found in TNTs of distinct cells, including primary embryonic fibroblasts, MHV-68, NIH-3T3, BHK-21 cells, NMuMG cells and mesothelioma-infected cells ([Gill et al., 2008](#)). In bovine primary fibroblasts and oropharynx cells infected with the bovine herpesvirus 1 (BoHV-1), TNTs can transport mitochondria and the viral proteins glycoprotein E and capsid VP26 ([Panasiuk et al., 2018](#)). Other studies have also linked TNTs to T cell leukemia virus type I (HTLV-1) ([Van Prooyen et al., 2010](#)), murine leukemia virus ([Sherer et al., 2007](#)); influenza A virus ([Kumar et al., 2017](#); [Roberts et al., 2015](#)); and human immunodeficiency virus type 1 (HIV-1), the most studied TNT-mediated virus ([Aggarwal et al., 2012](#); [Eugenin et al., 2009](#); [Hashimoto et al., 2016, 2016](#); [Okafo et al., 2017](#); [Shrivastava et al., 2015](#); [Sowinski et al., 2008](#); [Xu et al., 2009](#)).

In spite of the numerous findings describing TNTs in the transport of viruses, there is evidence that, as they do in filopodia, most viruses move on the outer surface of the protrusion and not through the inside ([Sherer et al., 2007](#)). This suggests that many of the TNTs described during viral infection may not be open-ended connections.

1.9.3 Bacterial Infection

Even though initial sightings of contact-dependent bacterial cell-to-cell transport in macrophages date back to 1989 ([Tilney and Portnoy, 1989](#)), bacteria spreading between macrophages derived from human monocytes along the membrane of TNTs was never shown prior to the study by Davis and colleagues ([Onfelt et al., 2006](#)). In their study, Onfelt et al.,

demonstrated that bacteria “surf” along the tubes from the outside until they reach the cell at the other end, where they get phagocytosed. It is likely that these structures exhibit distinct structural characteristics from classical TNTs, however that is not an avenue that has been pursued.

Bacteria can also communicate amongst themselves via TNT-like connections. For example, *Bacillus subtilis* form open-ended TNT-like connections that form in the course of minutes (Dubey et al., 2016). Other studies in the same bacteria indicate that TNT-like connections can form extensive networks known as biofilms (Sretenovic et al., 2017); however the function of these tubes has yet to be defined.

1.9.4 Cancer

Cancer is a disease characterized by a deleterious ability to proliferate, spread, and invade organisms. Inter-cellular transfer of chemical signals and materials responsible for stimulating cellular growth and proliferation, and the coordination of tumor invasion. The classical paradigm of inter-cellular communication between cancer cells is via diffusion of chemical signals, GJs, MVs, and exosomes. However, over the last decade, evidence from several groups have detected TNTs forming between cancer cells, as well as between cancer and non-cancer stromal cells.

It is hypothesized that heterotypic connections could contribute to the formation of cancer microenvironments and stem cell niches that support tumor growth. These studies include TNTs in mesothelioma cell lines and primary human mesothelioma cells capable of transporting mitochondria, vesicles, and proteins (Lou et al., 2012). In their study, Lou and colleagues also identified mitotracker-labeled structures in surgical specimens that resembled TNTs. The identification of TNTs capable of transporting mitochondria between primary human laryngeal SCC cells also linked TNTs to laryngeal cancer (Antanavičiūtė et al., 2014b). Later studies reinforced these findings and added other TNT-mediated cargo transport (vesicles, lysosomes, and autophagosomes) to the list of SCC-derived TNTs (Sáenz-de-Santa-María et al., 2017). Other reports examining micro RNAs getting transported via TNTs in metastatic cancer cells and the endothelium linked TNTs to breast cancer (Connor et al., 2015; Parker et al., 2017). GJ-bearing thick TNTs, TM, that transport calcium between astrocytoma cells have also linked TNTs to

Astrocytoma ([Osswald et al., 2015b](#)). Bladder cancer cell models can also form TNTs and share mitochondria ([Lu et al., 2017](#)). MSC and Leukemic cell TNTs that transport autophagosomes and mitochondria have also linked TNTs to Leukemia ([Polak et al., 2015](#); [de Rooij et al., 2017](#)). A better understanding of how these *in vitro* findings could reproduce in real-life tumors are still in progress. The development of artificial 3D model systems (e.g. organoids) could be more representative of complex and heterogenous tumor microenvironments and are described in more detail in a review by Venkatesh and Lou ([Venkatesh and Lou, 2019](#)).

1.10 References

- Aasen, T., Leithe, E., Graham, S.V., Kameritsch, P., Mayán, M.D., Mesnil, M., Pogoda, K., and Tabernero, A. (2019). Connexins in cancer: bridging the gap to the clinic. *Oncogene* 38, 4429–4451.
- Abounit, S., and Zurzolo, C. (2012). Wiring through tunneling nanotubes--from electrical signals to organelle transfer. *J. Cell. Sci.* 125, 1089–1098.
- Abounit, S., Delage, E., and Zurzolo, C. (2015). Identification and Characterization of Tunneling Nanotubes for Intercellular Trafficking. *Curr Protoc Cell Biol* 67, 12.10.1-21.
- Abounit, S., Wu, J.W., Duff, K., Victoria, G.S., and Zurzolo, C. (2016a). Tunneling nanotubes: A possible highway in the spreading of tau and other prion-like proteins in neurodegenerative diseases. *Prion* 10, 344–351.
- Abounit, S., Bousset, L., Loria, F., Zhu, S., de Chaumont, F., Pieri, L., Olivo-Marin, J.-C., Melki, R., and Zurzolo, C. (2016b). Tunneling nanotubes spread fibrillar α -synuclein by intercellular trafficking of lysosomes. *EMBO J.* 35, 2120–2138.
- Ady, J., Thayanithy, V., Mojica, K., Wong, P., Carson, J., Rao, P., Fong, Y., and Lou, E. (2016). Tunneling nanotubes: an alternate route for propagation of the bystander effect following oncolytic viral infection. *Mol Ther Oncolytics* 3, 16029.
- Aggarwal, A., Iemma, T.L., Shih, I., Newsome, T.P., McAllery, S., Cunningham, A.L., and Turville, S.G. (2012). Mobilization of HIV spread by diaphanous 2 dependent filopodia in infected dendritic cells. *PLoS Pathog.* 8, e1002762.
- Antanavičiūtė, I., Rysevaitė, K., Liutkevičius, V., Marandykina, A., Rimkutė, L., Sveikatiėnė, R., Uloza, V., and Skeberdis, V.A. (2014a). Long-distance communication between laryngeal carcinoma cells. *PLoS ONE* 9, e99196.
- Antanavičiūtė, I., Rysevaitė, K., Liutkevičius, V., Marandykina, A., Rimkutė, L., Sveikatiėnė, R., Uloza, V., and Skeberdis, V.A. (2014b). Long-distance communication between laryngeal carcinoma cells. *PLoS ONE* 9, e99196.
- Antanavičiūtė, I., Ereminienė, E., Vysockas, V., Račkauskas, M., Skipskis, V., Rysevaitė, K., Treinys, R., Benetis, R., Jurevičius, J., and Skeberdis, V.A. (2015). Exogenous connexin43-expressing autologous skeletal myoblasts ameliorate mechanical function and electrical activity of the rabbit heart after experimental infarction. *Int J Exp Pathol* 96, 42–53.
- Aramaki, S., Mayanagi, K., Aoyama, K., and Yasunaga, T. (2014). Revealing the intracellular ultrastructure of filopodia with cryo-electron tomography. *Microscopy (Oxf)* 63 Suppl 1, i33–i34.
- Aramaki, S., Mayanagi, K., Jin, M., Aoyama, K., and Yasunaga, T. (2016). Filopodia formation by crosslinking of F-actin with fascin in two different binding manners. *Cytoskeleton (Hoboken)* 73, 365–374.
- Ariazi, J., Benowitz, A., De Biasi, V., Den Boer, M.L., Cherqui, S., Cui, H., Douillet, N., Eugenin, E.A., Favre, D., Goodman, S., et al. (2017). Tunneling Nanotubes and Gap Junctions-Their Role in Long-Range

Intercellular Communication during Development, Health, and Disease Conditions. *Front Mol Neurosci* *10*, 333.

Arkwright, P.D., Luchetti, F., Tour, J., Roberts, C., Ayub, R., Morales, A.P., Rodríguez, J.J., Gilmore, A., Canonico, B., Papa, S., et al. (2010). Fas stimulation of T lymphocytes promotes rapid intercellular exchange of death signals via membrane nanotubes. *Cell Res.* *20*, 72–88.

Austefjord, M.W., Gerdes, H.-H., and Wang, X. (2014). Tunneling nanotubes: Diversity in morphology and structure. *Commun Integr Biol* *7*, e27934.

Baker, M. (2017). How the Internet of cells has biologists buzzing. *Nature* *549*, 322–324.

Bermudez-Fajardo, A., Ylihärsilä, M., Evans, W.H., Newby, A.C., and Oviedo-Orta, E. (2007). CD4+ T lymphocyte subsets express connexin 43 and establish gap junction channel communication with macrophages in vitro. *J. Leukoc. Biol.* *82*, 608–612.

Bishop, A.L., and Hall, A. (2000). Rho GTPases and their effector proteins. *Biochem. J.* *348 Pt 2*, 241–255.

Blacque, O.E., Scheidel, N., and Kuhns, S. (2018). Rab GTPases in cilium formation and function. *Small GTPases* *9*, 76–94.

Bohil, A.B., Robertson, B.W., and Cheney, R.E. (2006). Myosin-X is a molecular motor that functions in filopodia formation. *Proc. Natl. Acad. Sci. U.S.A.* *103*, 12411–12416.

Bukoreshtliev, N.V., Wang, X., Hodneland, E., Gurke, S., Barroso, J.F.V., and Gerdes, H.-H. (2009). Selective block of tunneling nanotube (TNT) formation inhibits intercellular organelle transfer between PC12 cells. *FEBS Lett.* *583*, 1481–1488.

Burtey, A., Wagner, M., Hodneland, E., Skaftnesmo, K.O., Schoelermann, J., Mondragon, I.R., Espedal, H., Golebiewska, A., Niclou, S.P., Bjerkvig, R., et al. (2015). Intercellular transfer of transferrin receptor by a contact-, Rab8-dependent mechanism involving tunneling nanotubes. *FASEB J.* *29*, 4695–4712.

Buzas, E.I., György, B., Nagy, G., Falus, A., and Gay, S. (2014). Emerging role of extracellular vesicles in inflammatory diseases. *Nat Rev Rheumatol* *10*, 356–364.

Cajal, S.R. (1888). Estructura de los centros nerviosos de las aves (Rev. Trim. Histol. Norm. Pat.).

Caneparo, L., Pantazis, P., Dempsey, W., and Fraser, S.E. (2011). Intercellular bridges in vertebrate gastrulation. *PLoS ONE* *6*, e20230.

Carlier, M.F., Ducruix, A., and Pantaloni, D. (1999). Signalling to actin: the Cdc42-N-WASP-Arp2/3 connection. *Chem. Biol.* *6*, R235-240.

Chauveau, A., Aucher, A., Eissmann, P., Vivier, E., and Davis, D.M. (2010). Membrane nanotubes facilitate long-distance interactions between natural killer cells and target cells. *Proc. Natl. Acad. Sci. U.S.A.* *107*, 5545–5550.

Cherqui, S., and Courtoy, P.J. (2017). The renal Fanconi syndrome in cystinosis: pathogenic insights and therapeutic perspectives. *Nat Rev Nephrol* *13*, 115–131.

- Chinnery, H.R., Pearlman, E., and McMenamin, P.G. (2008). Cutting edge: Membrane nanotubes in vivo: a feature of MHC class II+ cells in the mouse cornea. *J. Immunol.* *180*, 5779–5783.
- Collot, M., Ashokkumar, P., Anton, H., Boutant, E., Faklaris, O., Galli, T., Mély, Y., Danglot, L., and Klymchenko, A.S. (2019). MemBright: A Family of Fluorescent Membrane Probes for Advanced Cellular Imaging and Neuroscience. *Cell Chem Biol* *26*, 600-614.e7.
- Connor, Y., Tekleab, S., Nandakumar, S., Walls, C., Tekleab, Y., Husain, A., Gadish, O., Sabbisetti, V., Kaushik, S., Sehrawat, S., et al. (2015). Physical nanoscale conduit-mediated communication between tumour cells and the endothelium modulates endothelial phenotype. *Nat Commun* *6*, 8671.
- Costanzo, M., Abounit, S., Marzo, L., Danckaert, A., Chamoun, Z., Roux, P., and Zurzolo, C. (2013). Transfer of polyglutamine aggregates in neuronal cells occurs in tunneling nanotubes. *J. Cell. Sci.* *126*, 3678–3685.
- Dance, A. (2019). Core Concept: Cells nibble one another via the under-appreciated process of trogocytosis. *Proc. Natl. Acad. Sci. U.S.A.* *116*, 17608–17610.
- Davis, D.M., and Sowinski, S. (2008). Membrane nanotubes: dynamic long-distance connections between animal cells. *Nat. Rev. Mol. Cell Biol.* *9*, 431–436.
- Delage, E., Cervantes, D.C., Pénard, E., Schmitt, C., Syan, S., Disanza, A., Scita, G., and Zurzolo, C. (2016). Differential identity of Filopodia and Tunneling Nanotubes revealed by the opposite functions of actin regulatory complexes. *Sci Rep* *6*, 39632.
- Desir, S., Dickson, E.L., Vogel, R.I., Thayanithy, V., Wong, P., Teoh, D., Geller, M.A., Steer, C.J., Subramanian, S., and Lou, E. (2016). Tunneling nanotube formation is stimulated by hypoxia in ovarian cancer cells. *Oncotarget* *7*, 43150–43161.
- Di Fiore, P.P., and Scita, G. (2002). Eps8 in the midst of GTPases. *Int. J. Biochem. Cell Biol.* *34*, 1178–1183.
- Dieriks, B.V., Park, T.I.-H., Fourie, C., Faull, R.L.M., Dragunow, M., and Curtis, M.A. (2017). α -synuclein transfer through tunneling nanotubes occurs in SH-SY5Y cells and primary brain pericytes from Parkinson's disease patients. *Sci Rep* *7*, 42984.
- Dilsizoglu Senol, A., Pepe, A., Grudina, C., Sassoon, N., Reiko, U., Bousset, L., Melki, R., Piel, J., Gugger, M., and Zurzolo, C. (2019). Effect of tolytoxin on tunneling nanotube formation and function. *Sci Rep* *9*, 5741.
- Disanza, A., Mantoani, S., Hertzog, M., Gerboth, S., Frittoli, E., Steffen, A., Berhoerster, K., Kreienkamp, H.-J., Milanesi, F., Di Fiore, P.P., et al. (2006). Regulation of cell shape by Cdc42 is mediated by the synergic actin-bundling activity of the Eps8-IRSp53 complex. *Nat. Cell Biol.* *8*, 1337–1347.
- Disanza, A., Bisi, S., Winterhoff, M., Milanesi, F., Ushakov, D.S., Kast, D., Marighetti, P., Romet-Lemonne, G., Müller, H.-M., Nickel, W., et al. (2013). CDC42 switches IRSp53 from inhibition of actin growth to elongation by clustering of VASP. *EMBO J.* *32*, 2735–2750.

- Dixon, S.J., and Stockwell, B.R. (2014). The role of iron and reactive oxygen species in cell death. *Nat. Chem. Biol.* *10*, 9–17.
- Dođaner, B.A., Yan, L.K.Q., and Youk, H. (2016). Autocrine Signaling and Quorum Sensing: Extreme Ends of a Common Spectrum. *Trends Cell Biol.* *26*, 262–271.
- Donahue, H.J., Qu, R.W., and Genetos, D.C. (2017). Joint diseases: from connexins to gap junctions. *Nat Rev Rheumatol* *14*, 42–51.
- Drab, M., Stopar, D., Kralj-Iglič, V., and Iglič, A. (2019). Inception Mechanisms of Tunneling Nanotubes. *Cells* *8*.
- Dubey, G.P., Malli Mohan, G.B., Dubrovsky, A., Amen, T., Tsipshtein, S., Rouvinski, A., Rosenberg, A., Kaganovich, D., Sherman, E., Medalia, O., et al. (2016). Architecture and Characteristics of Bacterial Nanotubes. *Dev. Cell* *36*, 453–461.
- Dubois, F., Jean-Jacques, B., Roberge, H., Bénard, M., Galas, L., Schapman, D., Elie, N., Goux, D., Keller, M., Maille, E., et al. (2018). A role for RASSF1A in tunneling nanotube formation between cells through GEFH1/Rab11 pathway control. *Cell Commun. Signal* *16*, 66.
- Dupont, M., Souriant, S., Lugo-Villarino, G., Maridonneau-Parini, I., and Vérollet, C. (2018). Tunneling Nanotubes: Intimate Communication between Myeloid Cells. *Front Immunol* *9*, 43.
- Dustin, M.L., Chakraborty, A.K., and Shaw, A.S. (2010). Understanding the structure and function of the immunological synapse. *Cold Spring Harb Perspect Biol* *2*, a002311.
- de Duve, C. (1984). *A Guided Tour of the Living Cell* (Scientific American Books).
- Epperla, C.P., Mohan, N., Chang, C.-W., Chen, C.-C., and Chang, H.-C. (2015). Nanodiamond-Mediated Intercellular Transport of Proteins through Membrane Tunneling Nanotubes. *Small* *11*, 6097–6105.
- Eugenin, E.A., Gaskill, P.J., and Berman, J.W. (2009). Tunneling nanotubes (TNT) are induced by HIV-infection of macrophages: a potential mechanism for intercellular HIV trafficking. *Cell. Immunol.* *254*, 142–148.
- Favoreel, H.W., Van Minnebruggen, G., Adriaensen, D., and Nauwynck, H.J. (2005). Cytoskeletal rearrangements and cell extensions induced by the US3 kinase of an alphaherpesvirus are associated with enhanced spread. *Proc. Natl. Acad. Sci. U.S.A.* *102*, 8990–8995.
- Finetti, F., Cassioli, C., and Baldari, C.T. (2017). Transcellular communication at the immunological synapse: a vesicular traffic-mediated mutual exchange. *F1000Res* *6*, 1880.
- Gallo, G. (2013). Mechanisms underlying the initiation and dynamics of neuronal filopodia: from neurite formation to synaptogenesis. *Int Rev Cell Mol Biol* *301*, 95–156.
- Gardel, M.L., Schneider, I.C., Aratyn-Schaus, Y., and Waterman, C.M. (2010). Mechanical integration of actin and adhesion dynamics in cell migration. *Annu. Rev. Cell Dev. Biol.* *26*, 315–333.

Gill, M.B., Edgar, R., May, J.S., and Stevenson, P.G. (2008). A gamma-herpesvirus glycoprotein complex manipulates actin to promote viral spread. *PLoS ONE* 3, e1808.

Golgi, C. (1885). *Sulla Fina Anatomia degli Organi Centrali del Sistema Nervoso* (Reggio-Emilia: Stefano Calderini e Figlio).

Gousset, K., and Zurzolo, C. (2009). Tunnelling nanotubes: a highway for prion spreading? *Prion* 3, 94–98.

Gousset, K., Schiff, E., Langevin, C., Marijanovic, Z., Caputo, A., Browman, D.T., Chenouard, N., de Chaumont, F., Martino, A., Enninga, J., et al. (2009). Prions hijack tunnelling nanotubes for intercellular spread. *Nat. Cell Biol.* 11, 328–336.

Gousset, K., Marzo, L., Commere, P.-H., and Zurzolo, C. (2013). Myo10 is a key regulator of TNT formation in neuronal cells. *J. Cell. Sci.* 126, 4424–4435.

Gousset, K., Gordon, A., Kumar Kannan, S., and Tovar, J. (2019). A novel Microproteomic Approach Using Laser Capture Microdissection to Study Cellular Protrusions. *Int J Mol Sci* 20.

Govind, S., Kozma, R., Monfries, C., Lim, L., and Ahmed, S. (2001). Cdc42Hs facilitates cytoskeletal reorganization and neurite outgrowth by localizing the 58-kD insulin receptor substrate to filamentous actin. *J. Cell Biol.* 152, 579–594.

Gustafson, T., and Wolpert, L. (1963). THE CELLULAR BASIS OF MORPHOGENESIS AND SEA URCHIN DEVELOPMENT. *Int. Rev. Cytol.* 15, 139–214.

Haglund, K., Nezis, I.P., Lemus, D., Grabbe, C., Wesche, J., Liestøl, K., Dikic, I., Palmer, R., and Stenmark, H. (2010). Cindr interacts with anillin to control cytokinesis in *Drosophila melanogaster*. *Curr. Biol.* 20, 944–950.

Haglund, K., Nezis, I.P., and Stenmark, H. (2011). Structure and functions of stable intercellular bridges formed by incomplete cytokinesis during development. *Commun Integr Biol* 4, 1–9.

Hanna, S.J., McCoy-Simandle, K., Miskolci, V., Guo, P., Cammer, M., Hodgson, L., and Cox, D. (2017). The Role of Rho-GTPases and actin polymerization during Macrophage Tunneling Nanotube Biogenesis. *Sci Rep* 7, 8547.

Hanna, S.J., McCoy-Simandle, K., Leung, E., Genna, A., Condeelis, J., and Cox, D. (2019). Tunneling nanotubes, a novel mode of tumor cell-macrophage communication in tumor cell invasion. *J. Cell. Sci.* 132.

Harrison, R.G. (1907). Observations of the living developing nerve fiber. *Anat Rec.* 1:116–118.

Hase, K., Kimura, S., Takatsu, H., Ohmae, M., Kawano, S., Kitamura, H., Ito, M., Watarai, H., Hazelett, C.C., Yeaman, C., et al. (2009). M-Sec promotes membrane nanotube formation by interacting with Ral and the exocyst complex. *Nat. Cell Biol.* 11, 1427–1432.

Hashimoto, M., Bhuyan, F., Hiyoshi, M., Noyori, O., Nasser, H., Miyazaki, M., Saito, T., Kondoh, Y., Osada, H., Kimura, S., et al. (2016). Potential Role of the Formation of Tunneling Nanotubes in HIV-1 Spread in Macrophages. *J. Immunol.* *196*, 1832–1841.

Heasman, S.J., and Ridley, A.J. (2008). Mammalian Rho GTPases: new insights into their functions from in vivo studies. *Nat. Rev. Mol. Cell Biol.* *9*, 690–701.

Hetrick, B., Han, M.S., Helgeson, L.A., and Nolen, B.J. (2013). Small molecules CK-666 and CK-869 inhibit actin-related protein 2/3 complex by blocking an activating conformational change. *Chem. Biol.* *20*, 701–712.

Hoffman, L., Jensen, C.C., Yoshigi, M., and Beckerle, M. (2017). Mechanical signals activate p38 MAPK pathway-dependent reinforcement of actin via mechanosensitive HspB1. *Mol. Biol. Cell* *28*, 2661–2675.

Homma, Y., and Fukuda, M. (2016). Rabin8 regulates neurite outgrowth in both GEF activity-dependent and -independent manners. *Mol. Biol. Cell* *27*, 2107–2118.

Hooke, R. (1665). *Micrographia : or some physiological descriptions of minute bodies made by magnifying glasses. With observations and inquiries thereupon* (London: Printed by J. Martyn and J. Allestry).

Huang, H., and Kornberg, T.B. (2016). Cells must express components of the planar cell polarity system and extracellular matrix to support cytonemes. *Elife* *5*.

Huang, Y., Zucker, B., Zhang, S., Elias, S., Zhu, Y., Chen, H., Ding, T., Li, Y., Sun, Y., Lou, J., et al. (2019). Migrasome formation is mediated by assembly of micron-scale tetraspanin macrodomains. *Nat. Cell Biol.* *21*, 991–1002.

Huot, J., Houle, F., Rousseau, S., Deschesnes, R.G., Shah, G.M., and Landry, J. (1998). SAPK2/p38-dependent F-actin reorganization regulates early membrane blebbing during stress-induced apoptosis. *J. Cell Biol.* *143*, 1361–1373.

Innocenti, M. (2018). New insights into the formation and the function of lamellipodia and ruffles in mesenchymal cell migration. *Cell Adh Migr* *12*, 401–416.

Jacquemet, G., Hamidi, H., and Ivaska, J. (2015). Filopodia in cell adhesion, 3D migration and cancer cell invasion. *Curr. Opin. Cell Biol.* *36*, 23–31.

Jash, E., Prasad, P., Kumar, N., Sharma, T., Goldman, A., and Sehrawat, S. (2018). Perspective on nanochannels as cellular mediators in different disease conditions. *Cell Commun Signal* *16*, 76.

Jiang, D., Jiang, Z., Lu, D., Wang, X., Liang, H., Zhang, J., Meng, Y., Li, Y., Wu, D., Huang, Y., et al. (2019). Migrasomes provide regional cues for organ morphogenesis during zebrafish gastrulation. *Nat. Cell Biol.* *21*, 966–977.

Jucker, M., and Walker, L.C. (2013). Self-propagation of pathogenic protein aggregates in neurodegenerative diseases. *Nature* *501*, 45–51.

Kadiu, I., and Gendelman, H.E. (2011). Macrophage bridging conduit trafficking of HIV-1 through the endoplasmic reticulum and Golgi network. *J. Proteome Res.* *10*, 3225–3238.

Keller, S., Sanderson, M.P., Stoeck, A., and Altevogt, P. (2006). Exosomes: from biogenesis and secretion to biological function. *Immunol. Lett.* *107*, 102–108.

Kloc, M., Bilinski, S., Dougherty, M.T., Brey, E.M., and Etkin, L.D. (2004). Formation, architecture and polarity of female germline cyst in *Xenopus*. *Dev. Biol.* *266*, 43–61.

Kornberg, T.B., and Roy, S. (2014). Cytonemes as specialized signaling filopodia. *Development* *141*, 729–736.

Kovalevich, J., and Langford, D. (2013). Considerations for the use of SH-SY5Y neuroblastoma cells in neurobiology. *Methods Mol. Biol.* *1078*, 9–21.

Kozoriz, M.G., Bates, D.C., Bond, S.R., Lai, C.P.K., and Moniz, D.M. (2006). Passing potassium with and without gap junctions. *J. Neurosci.* *26*, 8023–8024.

Krause, M., and Gautreau, A. (2014). Steering cell migration: lamellipodium dynamics and the regulation of directional persistence. *Nat. Rev. Mol. Cell Biol.* *15*, 577–590.

Kretschmer, A., Zhang, F., Somasekharan, S.P., Tse, C., Leachman, L., Gleave, A., Li, B., Asmaro, I., Huang, T., Kotula, L., et al. (2019). Stress-induced tunneling nanotubes support treatment adaptation in prostate cancer. *Sci Rep* *9*, 7826.

Kumar, A., Kim, J.H., Ranjan, P., Metcalfe, M.G., Cao, W., Mishina, M., Gangappa, S., Guo, Z., Boyden, E.S., Zaki, S., et al. (2017). Influenza virus exploits tunneling nanotubes for cell-to-cell spread. *Sci Rep* *7*, 40360.

Kumar, V., Zhang, M.-X., Swank, M.W., Kunz, J., and Wu, G.-Y. (2005). Regulation of dendritic morphogenesis by Ras-PI3K-Akt-mTOR and Ras-MAPK signaling pathways. *J. Neurosci.* *25*, 11288–11299.

Kurusu, S., and Takenawa, T. (2009). The WASP and WAVE family proteins. *Genome Biol.* *10*, 226.

La Boissière, S., Izeta, A., Malcomber, S., and O’Hare, P. (2004). Compartmentalization of VP16 in cells infected with recombinant herpes simplex virus expressing VP16-green fluorescent protein fusion proteins. *J. Virol.* *78*, 8002–8014.

Lachambre, S., Chopard, C., and Beaumelle, B. (2014). Preliminary characterisation of nanotubes connecting T-cells and their use by HIV-1. *Biol. Cell* *106*, 394–404.

Lai, E.C. (2004). Notch signaling: control of cell communication and cell fate. *Development* *131*, 965–973.

Liang, D. (2018). A Salutary Role of Reactive Oxygen Species in Intercellular Tunnel-Mediated Communication. *Front Cell Dev Biol* *6*, 2.

Liu, X., Sun, L., Torii, M., and Rakic, P. (2012). Connexin 43 controls the multipolar phase of neuronal migration to the cerebral cortex. *Proc. Natl. Acad. Sci. U.S.A.* *109*, 8280–8285.

- Lou, E., Fujisawa, S., Morozov, A., Barlas, A., Romin, Y., Dogan, Y., Gholami, S., Moreira, A.L., Manova-Todorova, K., and Moore, M.A.S. (2012). Tunneling nanotubes provide a unique conduit for intercellular transfer of cellular contents in human malignant pleural mesothelioma. *PLoS ONE* 7, e33093.
- Lou, E., Zhai, E., Sarkari, A., Desir, S., Wong, P., Iizuka, Y., Yang, J., Subramanian, S., McCarthy, J., Bazzaro, M., et al. (2018). Cellular and Molecular Networking Within the Ecosystem of Cancer Cell Communication via Tunneling Nanotubes. *Front Cell Dev Biol* 6, 95.
- Lu, J., Zheng, X., Li, F., Yu, Y., Chen, Z., Liu, Z., Wang, Z., Xu, H., and Yang, W. (2017). Tunneling nanotubes promote intercellular mitochondria transfer followed by increased invasiveness in bladder cancer cells. *Oncotarget* 8, 15539–15552.
- Ma, L., Li, Y., Peng, J., Wu, D., Zhao, X., Cui, Y., Chen, L., Yan, X., Du, Y., and Yu, L. (2015). Discovery of the migrasome, an organelle mediating release of cytoplasmic contents during cell migration. *Cell Res.* 25, 24–38.
- Marzo, L., Gousset, K., and Zurzolo, C. (2012). Multifaceted roles of tunneling nanotubes in intercellular communication. *Front Physiol* 3, 72.
- Mattes, B., Dang, Y., Greicius, G., Kaufmann, L.T., Prunsche, B., Rosenbauer, J., Stegmaier, J., Mikut, R., Özbek, S., Nienhaus, G.U., et al. (2018). Wnt/PCP controls spreading of Wnt/ β -catenin signals by cytonemes in vertebrates. *Elife* 7.
- Mattila, P.K., and Lappalainen, P. (2008). Filopodia: molecular architecture and cellular functions. *Nat. Rev. Mol. Cell Biol.* 9, 446–454.
- McCoy-Simandle, K., Hanna, S.J., and Cox, D. (2016). Exosomes and nanotubes: Control of immune cell communication. *Int. J. Biochem. Cell Biol.* 71, 44–54.
- Medalia, O., Beck, M., Ecke, M., Weber, I., Neujahr, R., Baumeister, W., and Gerisch, G. (2007). Organization of actin networks in intact filopodia. *Curr. Biol.* 17, 79–84.
- Mendes-Jorge, L., Llobart, C., Ramos, D., López-Luppo, M., Valença, A., Nacher, V., Navarro, M., Carretero, A., Méndez-Ferrer, S., Rodríguez-Baeza, A., et al. (2012). Intercapillary bridging cells: immunocytochemical characteristics of cells that connect blood vessels in the retina. *Exp. Eye Res.* 98, 79–87.
- Michiels, C. (2004). Physiological and pathological responses to hypoxia. *Am. J. Pathol.* 164, 1875–1882.
- Miller, J., Fraser, S.E., and McClay, D. (1995). Dynamics of thin filopodia during sea urchin gastrulation. *Development* 121, 2501–2511.
- Mittal, R., Karhu, E., Wang, J.-S., Delgado, S., Zukerman, R., Mittal, J., and Jhaveri, V.M. (2019). Cell communication by tunneling nanotubes: Implications in disease and therapeutic applications. *J. Cell. Physiol.* 234, 1130–1146.
- Miyazawa, K., Emmerling, K., and Manuelidis, L. (2010). Proliferative arrest of neural cells induces prion protein synthesis, nanotube formation, and cell-to-cell contacts. *J. Cell. Biochem.* 111, 239–247.

- Mori, Y., Matsui, T., Furutani, Y., Yoshihara, Y., and Fukuda, M. (2012). Small GTPase Rab17 regulates dendritic morphogenesis and postsynaptic development of hippocampal neurons. *J. Biol. Chem.* *287*, 8963–8973.
- Murata, K., and Wolf, M. (2018). Cryo-electron microscopy for structural analysis of dynamic biological macromolecules. *Biochim Biophys Acta Gen Subj* *1862*, 324–334.
- Naphade, S., Sharma, J., Gaide Chevronnay, H.P., Shook, M.A., Yeagy, B.A., Rocca, C.J., Ur, S.N., Lau, A.J., Courtoy, P.J., and Cherqui, S. (2015). Brief reports: Lysosomal cross-correction by hematopoietic stem cell-derived macrophages via tunneling nanotubes. *Stem Cells* *33*, 301–309.
- Neto, E., Leitão, L., Sousa, D.M., Alves, C.J., Alencastre, I.S., Aguiar, P., and Lamghari, M. (2016). Compartmentalized Microfluidic Platforms: The Unrivaled Breakthrough of In Vitro Tools for Neurobiological Research. *J. Neurosci.* *36*, 11573–11584.
- van Niel, G., D'Angelo, G., and Raposo, G. (2018). Shedding light on the cell biology of extracellular vesicles. *Nat. Rev. Mol. Cell Biol.* *19*, 213–228.
- Nobes, C.D., and Hall, A. (1995). Rho, rac, and cdc42 GTPases regulate the assembly of multimolecular focal complexes associated with actin stress fibers, lamellipodia, and filopodia. *Cell* *81*, 53–62.
- Okafo, G., Prevedel, L., and Eugenin, E. (2017). Tunneling nanotubes (TNT) mediate long-range gap junctional communication: Implications for HIV cell to cell spread. *Sci Rep* *7*, 16660.
- Onfelt, B., Nedvetzki, S., Yanagi, K., and Davis, D.M. (2004). Cutting edge: Membrane nanotubes connect immune cells. *J. Immunol.* *173*, 1511–1513.
- Onfelt, B., Nedvetzki, S., Benninger, R.K.P., Purbhoo, M.A., Sowinski, S., Hume, A.N., Seabra, M.C., Neil, M.A.A., French, P.M.W., and Davis, D.M. (2006). Structurally distinct membrane nanotubes between human macrophages support long-distance vesicular traffic or surfing of bacteria. *J. Immunol.* *177*, 8476–8483.
- Osswald, M., Jung, E., Sahm, F., Solecki, G., Venkataramani, V., Blaes, J., Weil, S., Horstmann, H., Wiestler, B., Syed, M., et al. (2015a). Brain tumour cells interconnect to a functional and resistant network. *Nature* *528*, 93–98.
- Osswald, M., Jung, E., Sahm, F., Solecki, G., Venkataramani, V., Blaes, J., Weil, S., Horstmann, H., Wiestler, B., Syed, M., et al. (2015b). Brain tumour cells interconnect to a functional and resistant network. *Nature* *528*, 93–98.
- Panasiuk, M., Rychłowski, M., Derewońko, N., and Bieńkowska-Szewczyk, K. (2018). Tunneling Nanotubes as a Novel Route of Cell-to-Cell Spread of Herpesviruses. *J. Virol.* *92*.
- Parker, I., Evans, K.T., Ellefsen, K., Lawson, D.A., and Smith, I.F. (2017). Lattice light sheet imaging of membrane nanotubes between human breast cancer cells in culture and in brain metastases. *Sci Rep* *7*, 11029.
- Pepling, M.E., and Spradling, A.C. (1998). Female mouse germ cells form synchronously dividing cysts. *Development* *125*, 3323–3328.

- Pergu, R., Dagar, S., Kumar, H., Kumar, R., Bhattacharya, J., and Mylavarapu, S.V.S. (2019). The chaperone ERp29 is required for tunneling nanotube formation by stabilizing MSec. *J. Biol. Chem.* *294*, 7177–7193.
- Petrova, V., Annicchiarico-Petruzzelli, M., Melino, G., and Amelio, I. (2018). The hypoxic tumour microenvironment. *Oncogenesis* *7*, 10.
- Polak, R., de Rooij, B., Pieters, R., and den Boer, M.L. (2015). B-cell precursor acute lymphoblastic leukemia cells use tunneling nanotubes to orchestrate their microenvironment. *Blood* *126*, 2404–2414.
- Qi, Y., Wang, J.K., McMillian, M., and Chikaraishi, D.M. (1997). Characterization of a CNS cell line, CAD, in which morphological differentiation is initiated by serum deprivation. *J. Neurosci.* *17*, 1217–1225.
- Rainy, N., Chetrit, D., Rouger, V., Vernitsky, H., Rechavi, O., Marguet, D., Goldstein, I., Ehrlich, M., and Kloog, Y. (2013). H-Ras transfers from B to T cells via tunneling nanotubes. *Cell Death Dis* *4*, e726.
- Ramírez-Weber, F.A., and Kornberg, T.B. (1999). Cytonemes: cellular processes that project to the principal signaling center in *Drosophila* imaginal discs. *Cell* *97*, 599–607.
- Reichert, D., Scheinpflug, J., Karbanová, J., Freund, D., Bornhäuser, M., and Corbeil, D. (2016). Tunneling nanotubes mediate the transfer of stem cell marker CD133 between hematopoietic progenitor cells. *Exp. Hematol.* *44*, 1092-1112.e2.
- Resnik, N., Prezelj, T., De Luca, G.M.R., Manders, E., Polishchuk, R., Veranič, P., and Kreft, M.E. (2018). Helical organization of microtubules occurs in a minority of tunneling membrane nanotubes in normal and cancer urothelial cells. *Sci Rep* *8*, 17133.
- Resnik, N., Erman, A., Veranič, P., and Kreft, M.E. (2019). Triple labelling of actin filaments, intermediate filaments and microtubules for broad application in cell biology: uncovering the cytoskeletal composition in tunneling nanotubes. *Histochem. Cell Biol.*
- Riedl, J., Crevenna, A.H., Kessenbrock, K., Yu, J.H., Neukirchen, D., Bista, M., Bradke, F., Jenne, D., Holak, T.A., Werb, Z., et al. (2008). Lifeact: a versatile marker to visualize F-actin. *Nat. Methods* *5*, 605–607.
- Roberts, K.L., Manicassamy, B., and Lamb, R.A. (2015). Influenza A virus uses intercellular connections to spread to neighboring cells. *J. Virol.* *89*, 1537–1549.
- de Rooij, B., Polak, R., Stalpers, F., Pieters, R., and den Boer, M.L. (2017). Tunneling nanotubes facilitate autophagosome transfer in the leukemic niche. *Leukemia* *31*, 1651–1654.
- Rostami, J., Holmqvist, S., Lindström, V., Sigvardson, J., Westermarck, G.T., Ingelsson, M., Bergström, J., Roybon, L., and Erlandsson, A. (2017). Human Astrocytes Transfer Aggregated Alpha-Synuclein via Tunneling Nanotubes. *J. Neurosci.* *37*, 11835–11853.
- Rupp, I., Sologub, L., Williamson, K.C., Scheuermayer, M., Reininger, L., Doerig, C., Eksi, S., Kombila, D.U., Frank, M., and Pradel, G. (2011). Malaria parasites form filamentous cell-to-cell connections during reproduction in the mosquito midgut. *Cell Res.* *21*, 683–696.

- Rustom, A. (2016). The missing link: does tunnelling nanotube-based supercellularity provide a new understanding of chronic and lifestyle diseases? *Open Biol* 6.
- Rustom, A., Saffrich, R., Markovic, I., Walther, P., and Gerdes, H.-H. (2004). Nanotubular highways for intercellular organelle transport. *Science* 303, 1007–1010.
- Sáenz-de-Santa-María, I., Bernardo-Castiñeira, C., Enciso, E., García-Moreno, I., Chiara, J.L., Suarez, C., and Chiara, M.-D. (2017). Control of long-distance cell-to-cell communication and autophagosome transfer in squamous cell carcinoma via tunneling nanotubes. *Oncotarget* 8, 20939–20960.
- Sartori-Rupp, A., Cordero Cervantes, D., Pepe, A., Gousset, K., Delage, E., Corroyer-Dulmont, S., Schmitt, C., Krijnse-Locker, J., and Zurzolo, C. (2019). Correlative cryo-electron microscopy reveals the structure of TNTs in neuronal cells. *Nat Commun* 10, 342.
- Sattentau, Q.J. (2010). Cell-to-Cell Spread of Retroviruses. *Viruses* 2, 1306–1321.
- Saxen, L., Lehtonen, E., Karkinen-Jääskeläinen, M., Nordling, S., and Wartiovaara, J. (1976). Are morphogenetic tissue interactions mediated by transmissible signal substances or through cell contacts? *Nature* 259, 662–663.
- Schiller, C., Diakopoulos, K.N., Rohwedder, I., Kremmer, E., von Toerne, C., Ueffing, M., Weidle, U.H., Ohno, H., and Weiss, E.H. (2013). LST1 promotes the assembly of a molecular machinery responsible for tunneling nanotube formation. *J. Cell. Sci.* 126, 767–777.
- Seyed-Razavi, Y., Hickey, M.J., Kuffová, L., McMenamin, P.G., and Chinnery, H.R. (2013). Membrane nanotubes in myeloid cells in the adult mouse cornea represent a novel mode of immune cell interaction. *Immunol. Cell Biol.* 91, 89–95.
- Sharma, M., and Subramaniam, S. (2019). Rhes travels from cell to cell and transports Huntington disease protein via TNT-like protrusion. *J. Cell Biol.* 218, 1972–1993.
- Sherer, N.M., Lehmann, M.J., Jimenez-Soto, L.F., Horensavitz, C., Pypaert, M., and Mothes, W. (2007). Retroviruses can establish filopodial bridges for efficient cell-to-cell transmission. *Nat. Cell Biol.* 9, 310–315.
- Shrivastava, A., Prasad, A., Kuzontkoski, P.M., Yu, J., and Groopman, J.E. (2015). Slit2N Inhibits Transmission of HIV-1 from Dendritic Cells to T-cells by Modulating Novel Cytoskeletal Elements. *Sci Rep* 5, 16833.
- Skop, A.R., Liu, H., Yates, J., Meyer, B.J., and Heald, R. (2004). Dissection of the mammalian midbody proteome reveals conserved cytokinesis mechanisms. *Science* 305, 61–66.
- Sousa, A.D., and Cheney, R.E. (2005). Myosin-X: a molecular motor at the cell's fingertips. *Trends Cell Biol.* 15, 533–539.
- Sowinski, S., Jolly, C., Berninghausen, O., Purbhoo, M.A., Chauveau, A., Köhler, K., Oddos, S., Eissmann, P., Brodsky, F.M., Hopkins, C., et al. (2008). Membrane nanotubes physically connect T cells over long distances presenting a novel route for HIV-1 transmission. *Nat. Cell Biol.* 10, 211–219.

- Sretenovic, S., Stojković, B., Dogsa, I., Kostanjšek, R., Poberaj, I., and Stopar, D. (2017). An early mechanical coupling of planktonic bacteria in dilute suspensions. *Nat Commun* 8, 213.
- Starling, E.H. (1905). On the chemical correlation of the functions of the body. (*Lancet*), pp. 166: 339–341.
- Staufer, O., Hernandez B, J.E., and Rustom, A. (2018). Protease-resistant cell meshworks: An indication of membrane nanotube-based syncytia formation. *Exp. Cell Res.* 372, 85–91.
- Stenmark, H. (2009). Rab GTPases as coordinators of vesicle traffic. *Nat. Rev. Mol. Cell Biol.* 10, 513–525.
- Strasser, A., Jost, P.J., and Nagata, S. (2009). The many roles of FAS receptor signaling in the immune system. *Immunity* 30, 180–192.
- Takahashi, A., Kukita, A., Li, Y., Zhang, J., Nomiya, H., Yamaza, T., Ayukawa, Y., Koyano, K., and Kukita, T. (2013). Tunneling nanotube formation is essential for the regulation of osteoclastogenesis. *J. Cell. Biochem.* 114, 1238–1247.
- Tardivel, M., Bégard, S., Bousset, L., Dujardin, S., Coens, A., Melki, R., Buée, L., and Colin, M. (2016). Tunneling nanotube (TNT)-mediated neuron-to neuron transfer of pathological Tau protein assemblies. *Acta Neuropathol Commun* 4, 117.
- Tavano, S., and Heisenberg, C.-P. (2019). Migrasomes take center stage. *Nat. Cell Biol.* 21, 918–920.
- Thayanithy, V., O’Hare, P., Wong, P., Zhao, X., Steer, C.J., Subramanian, S., and Lou, E. (2017). A transwell assay that excludes exosomes for assessment of tunneling nanotube-mediated intercellular communication. *Cell Commun. Signal* 15, 46.
- Tilney, L.G., and Portnoy, D.A. (1989). Actin filaments and the growth, movement, and spread of the intracellular bacterial parasite, *Listeria monocytogenes*. *J. Cell Biol.* 109, 1597–1608.
- Torralba, D., Baixauli, F., and Sánchez-Madrid, F. (2016). Mitochondria Know No Boundaries: Mechanisms and Functions of Intercellular Mitochondrial Transfer. *Front Cell Dev Biol* 4, 107.
- Uhl, J., Gujarathi, S., Waheed, A.A., Gordon, A., Freed, E.O., and Gousset, K. (2019). Myosin-X is essential to the intercellular spread of HIV-1 Nef through tunneling nanotubes. *J Cell Commun Signal* 13, 209–224.
- Valdebenito, S., Lou, E., Baldoni, J., Okafo, G., and Eugenin, E. (2018). The Novel Roles of Connexin Channels and Tunneling Nanotubes in Cancer Pathogenesis. *Int J Mol Sci* 19.
- Van Prooyen, N., Gold, H., Andresen, V., Schwartz, O., Jones, K., Ruscetti, F., Lockett, S., Gudla, P., Venzon, D., and Franchini, G. (2010). Human T-cell leukemia virus type 1 p8 protein increases cellular conduits and virus transmission. *Proc. Natl. Acad. Sci. U.S.A.* 107, 20738–20743.
- Vargas, J.Y., Grudina, C., and Zurzolo, C. (2019). The prion-like spreading of α -synuclein: From in vitro to in vivo models of Parkinson’s disease. *Ageing Res. Rev.* 50, 89–101.
- Venkatesh, V.S., and Lou, E. (2019). Tunneling nanotubes: A bridge for heterogeneity in glioblastoma and a new therapeutic target? *Cancer Reports* e1185.

- Veranic, P., Lokar, M., Schütz, G.J., Weghuber, J., Wieser, S., Hägerstrand, H., Kralj-Iglic, V., and Iglic, A. (2008). Different types of cell-to-cell connections mediated by nanotubular structures. *Biophys. J.* *95*, 4416–4425.
- Victoria, G.S., and Zurzolo, C. (2017). The spread of prion-like proteins by lysosomes and tunneling nanotubes: Implications for neurodegenerative diseases. *J. Cell Biol.* *216*, 2633–2644.
- Victoria, G.S., Arkhipenko, A., Zhu, S., Syan, S., and Zurzolo, C. (2016). Astrocyte-to-neuron intercellular prion transfer is mediated by cell-cell contact. *Sci Rep* *6*, 20762.
- Vignais, M.-L., Caicedo, A., Brondello, J.-M., and Jorgensen, C. (2017). Cell Connections by Tunneling Nanotubes: Effects of Mitochondrial Trafficking on Target Cell Metabolism, Homeostasis, and Response to Therapy. *Stem Cells Int* *2017*, 6917941.
- Virchow, R.L.K. (1858). *Die cellularpathologie in ihrer begründung auf physiologische und pathologische gewebelehre* (A. Hirschwald, Berlin).
- Wang, X., and Gerdes, H.-H. (2012). Long-distance electrical coupling via tunneling nanotubes. *Biochim. Biophys. Acta* *1818*, 2082–2086.
- Wang, X., Veruki, M.L., Bukoreshtliev, N.V., Hartveit, E., and Gerdes, H.-H. (2010). Animal cells connected by nanotubes can be electrically coupled through interposed gap-junction channels. *Proc. Natl. Acad. Sci. U.S.A.* *107*, 17194–17199.
- Wang, Y., Cui, J., Sun, X., and Zhang, Y. (2011). Tunneling-nanotube development in astrocytes depends on p53 activation. *Cell Death Differ.* *18*, 732–742.
- Watkins, S.C., and Salter, R.D. (2005). Functional connectivity between immune cells mediated by tunneling nanotubules. *Immunity* *23*, 309–318.
- Westlake, C.J., Baye, L.M., Nachury, M.V., Wright, K.J., Ervin, K.E., Phu, L., Chalouni, C., Beck, J.S., Kirkpatrick, D.S., Slusarski, D.C., et al. (2011). Primary cilia membrane assembly is initiated by Rab11 and transport protein particle II (TRAPPII) complex-dependent trafficking of Rabin8 to the centrosome. *Proceedings of the National Academy of Sciences* *108*, 2759–2764.
- Xu, W., Santini, P.A., Sullivan, J.S., He, B., Shan, M., Ball, S.C., Dyer, W.B., Ketas, T.J., Chadburn, A., Cohen-Gould, L., et al. (2009). HIV-1 evades virus-specific IgG2 and IgA responses by targeting systemic and intestinal B cells via long-range intercellular conduits. *Nat. Immunol.* *10*, 1008–1017.
- Yamashita, Y.M., Inaba, M., and Buszczak, M. (2018). Specialized Intercellular Communications via Cytosomes and Nanotubes. *Annu. Rev. Cell Dev. Biol.* *34*, 59–84.
- Yang, H., Borg, T.K., Ma, Z., Xu, M., Wetzel, G., Saraf, L.V., Markwald, R., Runyan, R.B., and Gao, B.Z. (2016). Biochip-based study of unidirectional mitochondrial transfer from stem cells to myocytes via tunneling nanotubes. *Biofabrication* *8*, 015012.
- Youk, H., and Lim, W.A. (2014). Secreting and sensing the same molecule allows cells to achieve versatile social behaviors. *Science* *343*, 1242782.

Yu, J.S.L., and Cui, W. (2016). Proliferation, survival and metabolism: the role of PI3K/AKT/mTOR signalling in pluripotency and cell fate determination. *Development* *143*, 3050–3060.

Zani, B.G., Indolfi, L., and Edelman, E.R. (2010). Tubular bridges for bronchial epithelial cell migration and communication. *PLoS ONE* *5*, e8930.

Zhang, C., and Scholpp, S. (2019). Cytonemes in development. *Curr. Opin. Genet. Dev.* *57*, 25–30.

Zhang, Z., Nie, S., and Chen, L. (2018). Targeting prion-like protein spreading in neurodegenerative diseases. *Neural Regen Res* *13*, 1875–1878.

Zhu, D., Tan, K.S., Zhang, X., Sun, A.Y., Sun, G.Y., and Lee, J.C.-M. (2005). Hydrogen peroxide alters membrane and cytoskeleton properties and increases intercellular connections in astrocytes. *J. Cell. Sci.* *118*, 3695–3703.

Zhu, H., Xue, C., Xu, X., Guo, Y., Li, X., Lu, J., Ju, S., Wang, Y., Cao, Z., and Gu, X. (2016). Rab8a/Rab11a regulate intercellular communications between neural cells via tunneling nanotubes. *Cell Death Dis* *7*, e2523.

Zhu, S., Victoria, G.S., Marzo, L., Ghosh, R., and Zurzolo, C. (2015). Prion aggregates transfer through tunneling nanotubes in endocytic vesicles. *Prion* *9*, 125–135.

Zhu, S., Bhat, S., Syan, S., Kuchitsu, Y., Fukuda, M., and Zurzolo, C. (2018). Rab11a-Rab8a cascade regulates the formation of tunneling nanotubes through vesicle recycling. *J. Cell. Sci.* *131*.

Zimmerman, G.A., Lorant, D.E., McIntyre, T.M., and Prescott, S.M. (1993). Juxtacrine intercellular signaling: another way to do it. *Am. J. Respir. Cell Mol. Biol.* *9*, 573–577.

Chapter 2

2 Role of Actin Regulatory Networks in Neuronal Tunneling Nanotube Formation

2.1 Results

2.1.1 Summary

Filopodia are tip-closed membranous protrusions containing polymerized actin filaments, which have not been shown to transport cargo between cells. TNTs on the other hand share many similarities with filopodia but allow the long-range inter-cellular transport of cargo through open-ended contact sites. In this project, we studied different regulatory complexes of actin, which play a role in the formation of filopodia and asked whether they also played a role in TNT formation. To this end, we tested the role CDC42, IRSp5, and VASP play in the formation and function of neuronal TNTs through the ectopic expression of constitutively active- and dominant negative forms of each protein. Our analyses elucidated new insights on the cytoskeletal architecture and mechanisms underlying TNT formation and intercellular vesicle transfer in neuronal CAD cells. Specifically, our results show that the filopodia-promoting CDC42/IRSp53/VASP network negatively regulates TNT formation and impairs TNT-mediated intercellular vesicle transfer. We further found that these proteins act in concert to inhibit TNT formation. Conversely, elevation of Eps8, an actin regulatory protein that inhibits the extension of filopodia in neurons, increases TNT formation. Notably, Eps8-mediated TNT induction requires Eps8 bundling but not its capping activity. Thus, despite their structural similarities, filopodia and TNTs form through distinct molecular mechanisms. Taken together, our results suggest that a switch in the molecular composition in common actin regulatory complexes is critical in driving the formation of either type of membrane protrusion.

2.1.2 Aims of the project

- Examine the molecular relationship between filopodia and TNTs.
- Test the role of the CDC42/IRSp53/VASP network in TNT formation and functionality.
- Examine the role of Eps8 in TNT formation and functionality.
- Test if Eps8-mediated TNT induction requires its bundling and/or capping activity.

2.1.3 Contribution

In this project, in which I contributed equally as a second author when the study was well-advanced, we addressed the role of specific actin modifiers in the formation of TNTs in contrast to filopodia. I studied the role of Rac1 in the formation of neuronal TNTs by ectopic expression of the dominant negative- and constitutively active- form of the protein. Specifically, I performed the experiments, acquired the images, and manually analyzed the data collected to prepare Supplementary Figure 2. By Western Blotting, I also evaluated the expression of Eps8 in CAD and CHO cells, as well as brain (hippocampus and striatum) lysates, (see Supplementary Figure 6a). In addition, I examined the mRNA expression of Eps8 by RT-PCR in the cell lines above, (see Supplementary Figure 6b). I integrated my results and figures into the manuscript and replaced panels in Figure 1 and 5 with more representative, re-processed images. Finally, I updated several sections of the manuscript, including the Introduction, Results, Discussion, Methods, and Bibliography, and rephrased several key points throughout these sections. This work was carried out during the two-revision, peer-review process of the manuscript, which I handled all-throughout until publication of the article.

2.1.4 Article 1: Differential identity of Filopodia and Tunneling Nanotubes revealed by the opposite functions of actin regulatory complexes

SCIENTIFIC REPORTS



OPEN

Differential identity of Filopodia and Tunneling Nanotubes revealed by the opposite functions of actin regulatory complexes

Received: 06 June 2016

Accepted: 25 November 2016

Published: 23 December 2016

Elise Delage¹, Diégo Cordero Cervantes^{1,*}, Esthel Pénard^{1,*}, Christine Schmitt², Sylvie Syan¹, Andrea Disanza³, Giorgio Scita^{3,4} & Chiara Zurzolo¹

Tunneling Nanotubes (TNTs) are actin enriched filopodia-like protrusions that play a pivotal role in long-range intercellular communication. Different pathogens use TNT-like structures as “freeways” to propagate across cells. TNTs are also implicated in cancer and neurodegenerative diseases, making them promising therapeutic targets. Understanding the mechanism of their formation, and their relation with filopodia is of fundamental importance to uncover their physiological function, particularly since filopodia, differently from TNTs, are not able to mediate transfer of cargo between distant cells. Here we studied different regulatory complexes of actin, which play a role in the formation of both these structures. We demonstrate that the filopodia-promoting CDC42/IRSp53/VASP network negatively regulates TNT formation and impairs TNT-mediated intercellular vesicle transfer. Conversely, elevation of Eps8, an actin regulatory protein that inhibits the extension of filopodia in neurons, increases TNT formation. Notably, Eps8-mediated TNT induction requires Eps8 bundling but not its capping activity. Thus, despite their structural similarities, filopodia and TNTs form through distinct molecular mechanisms. Our results further suggest that a switch in the molecular composition in common actin regulatory complexes is critical in driving the formation of either type of membrane protrusion.

Tunneling Nanotubes (TNTs) are cellular protrusions that represent a mechanism for direct, long-range intercellular communication¹. They constitute a membranous and cytoplasmic continuity between remote cells supported by the actin cytoskeleton and in some cases microtubules^{1,2}. TNTs are fragile and dynamic structures with a small diameter (20–500 nm) and a length up to 100 μm, which hover freely in the medium without touching the substrate in culture. They have been shown to mediate the cell-to-cell transfer of many different cellular components including: membrane proteins, soluble molecules, vesicles derived from various organelles, and mitochondria³. TNT-like structures have been observed in a wide variety of cell types *in vitro*² as well as *in vivo* models^{4–7}. Even though the precise physiological function of TNTs remains enigmatic, their involvement in essential processes like signal transduction, apoptosis, development, and immune response has been postulated^{2,8}. Various pathogens, such as viruses^{9,10} and bacteria¹¹, can use TNT-like structures to travel from one cell to another. TNTs are also emerging as an important player in cancer development^{5,6,12,13}. We have previously demonstrated that TNTs can mediate the intercellular transfer of infectious prions between neuronal cells, dendritic cells to neurons, and between astrocytes^{14–17}. Interestingly, other “prion-like” amyloidogenic proteins like misfolded huntingtin¹⁸, amyloid β¹⁹, α-synuclein²⁰, and tau²¹ can also be transferred between distant cells through TNTs, thus underscoring the important role of TNTs in the progression of neurodegenerative diseases, and their potential use as therapeutic targets²².

Two mechanisms for TNT formation have been proposed²³. The first one, which is commonly referred to as the “cell dislodgment mechanism”, describes two cells closely apposed to each other fusing transiently and

¹Unité Trafic Membranaire et Pathogénèse, Institut Pasteur, 25–28 Rue du Docteur Roux, 75724 Paris CEDEX 15, France. ²Ultrapole, Institut Pasteur, 25–28 Rue du Docteur Roux, 75724 Paris CEDEX 15, France. ³FIRC Institute of Molecular Oncology, 20139 Milan, Italy. ⁴Dipartimento di Scienze della Salute, Università degli Studi di Milano, 20122 Milan, Italy. *These authors contributed equally to this work. Correspondence and requests for materials should be addressed to C.Z. (email: chiara.zurzolo@pasteur.fr)

subsequently retaining a thin thread of membrane while they move apart¹¹. An alternative mechanism, known as the actin driven protrusion mechanism, proposes an active process based on the extension of a filopodium-like protrusion from one cell to another, followed by membrane fusion of the tip upon physical contact¹. In both cases, the application of actin depolymerizing drugs strongly reduces TNT formation, suggesting that actin plays a critical role^{1,24,25}. However the molecular mechanism(s) underlying TNT formation is still ill defined. The role of endogenously and exogenously expressed M-Sec, a protein sharing homology with Sec6, a component of the exocyst complex, as a positive regulator of TNT formation has been shown in multiple cell types^{9,26,28}. M-Sec induction of TNT formation involves its interaction with the GTPase Ras-related A protein (RalA) and the exocyst complex²⁶. Furthermore, the transmembrane major histocompatibility complex (MHC) class III protein leucocyte specific transcript 1 (LST1) interacts with M-Sec and mediates the recruitment of RalA to the plasma membrane, promoting its interaction with the exocyst complex²⁷. This multi-molecular complex can contribute to the remodeling of the actin cytoskeleton and to the delivery of membrane at the site of TNT formation. The protein p53 was recently found to play a crucial role in the formation of TNTs in astrocytes via the epidermal growth factor and the Akt/mammalian target of rapamycin (mTor)/phosphatidylinositol 3-kinase (PI3K) pathway¹⁹. However, cells that do not express M-Sec, such as the mouse neuronal CAD cell line and neurons, are still capable of forming TNTs²⁹. Furthermore, p53-independent TNT formation was observed in rat pheochromocytoma PC12 cells and in acute myeloid leukemia cells²⁹, suggesting that different molecular mechanisms may be at play. Whether different formation mechanisms lead to intercellular connections having distinct functions remains to be determined³⁰.

Another important observation is that TNTs share structural similarities with filopodia, particularly in their small diameter and requirement of actin for the protrusion³¹. We have previously observed that the expression of two known filopodia inducers, the vasodilator-stimulated phosphoprotein (VASP) and fascin³², decreases the number of TNT-connected cells³⁰ while Myosin X, another filopodial inducer, stimulates the formation of TNTs and intercellular transfer of vesicles in CAD cells³³. We further demonstrated that TNT induction requires the F2 lobe of Myosin X “band 4.1, ezrin, radixin, moesin” (FERM) domain³⁰, but not the F3 lobe (both needed for filopodia adherence to the substrate^{34,35}, suggesting that dorsal filopodia might be a TNT precursor. However, these findings and other data in the literature did not reveal whether TNTs and filopodia are identical or structurally related structures, and whether they share the same machinery for their formation.

To address this issue we studied the role of a subset of different actin remodeling complexes in TNT formation previously shown to be involved in filopodial protrusion. Specifically, up-regulation of filopodia elongation was shown to depend on VASP recruitment and clustering by the Insulin Receptor Substrate of 53 kDa (IRSp53)³⁶. IRSp53 has been implicated in the formation of filopodia via its dual function: it can deform the plasma membrane through its “Inverted Bin-Amphiphysin-Rvs” (I-BAR) domain, thus generating a membrane protrusion, and it interacts with several actin regulators via its “Src homology 3” (SH3) domain^{37,38}. IRSp53 is synergistically activated by the binding of effectors to its SH3 domain and by the binding of the RhoGTPase CDC42 to its “CDC42 and Rac interactive binding” (CRIB) domain³⁹. Thus, we investigated the possible role of IRSp53 and CDC42 in the formation of TNTs and intercellular transfer of vesicles. We found that CDC42, IRSp53, and VASP act as negative regulators of TNT formation and vesicle transfer function. We further show that these proteins act in concert to inhibit TNT formation. We also demonstrated that epidermal growth factor receptor pathway 8 (Eps8), another actin regulator that has been shown to inhibit filopodia formation in neurons^{38,40}, is a positive regulator of TNT formation and transfer. In addition, by expressing mutant forms of Eps8 which were impaired in either the capping or bundling activity of the protein, we showed that TNT induction requires Eps8 bundling but not capping activity. To our knowledge, this is the first molecular demonstration that TNTs and filopodia are different cellular structures that form through different mechanisms, paving the way to further study their physiological function(s).

Results

CDC42, IRSp53, and VASP negatively regulate TNT formation. In order to understand the relationship between filopodia and TNTs, and to dissect the molecular players involved in TNT generation, we investigated the role of actin regulators known to be involved in filopodia formation. We first transfected neuronal CAD cells^{18,20,30} with plasmids encoding fluorescently-tagged versions of these proteins and evaluated the ratio of TNT-connected cells in sub-confluent cultures by confocal microscopy. Around 65% of the control cells transfected with an empty vector encoding a fluorescent tag were connected by TNTs. Interestingly, the ectopic expression of GFP-CDC42 V12, a constitutively active form of CDC42, reduced the number of TNT-connected cells by approximately 40%, while GFP-CDC42 T17N, a dominant-negative form of the protein, significantly increased TNT formation (Fig. 1a and b, Supplementary Fig. 1). This suggests that, contrary to what has been reported in other cell lines^{26,27,41}, CDC42 may negatively regulate TNT formation in neuronal CAD cells.

A significant reduction of TNT-connected cells was also observed upon ectopic expression of RFP-IRSp53 while expression of RFP-IRS-FP/AA, an IRSp53 mutant impaired in its binding to downstream effectors through the SH3 domain, did not affect TNT formation (Fig. 1a and b, Supplementary Fig. 1). This result points to the potential role of IRSp53 in the negative regulation of TNTs via its interaction with protein partners. Consistently, ectopic expression of GFP-VASP, an interactor of IRSp53, also leads to less cells connected via TNTs compared to the control (Fig. 1a and b, Supplementary Fig. 1).

The Ras-related C3 botulinum toxin substrate 1 (Rac1), a member of the ras-related superfamily of small GTPases has been shown to share the same signaling pathway with and be activated by CDC42⁴². To test if Rac1 has a similar effect on TNT formation as CDC42 in CADs, we tested Myc-Rac1 V12, a constitutively active form of Rac1, and Myc-Rac1 17 N, a dominant negative form of Rac1. We evaluated any changes in TNT formation and discovered that the active form of Rac1 decreases the percentage of cells connected via TNTs while its dominant negative form increases TNT formation, similar to the effect of the active and negative forms of CDC42,

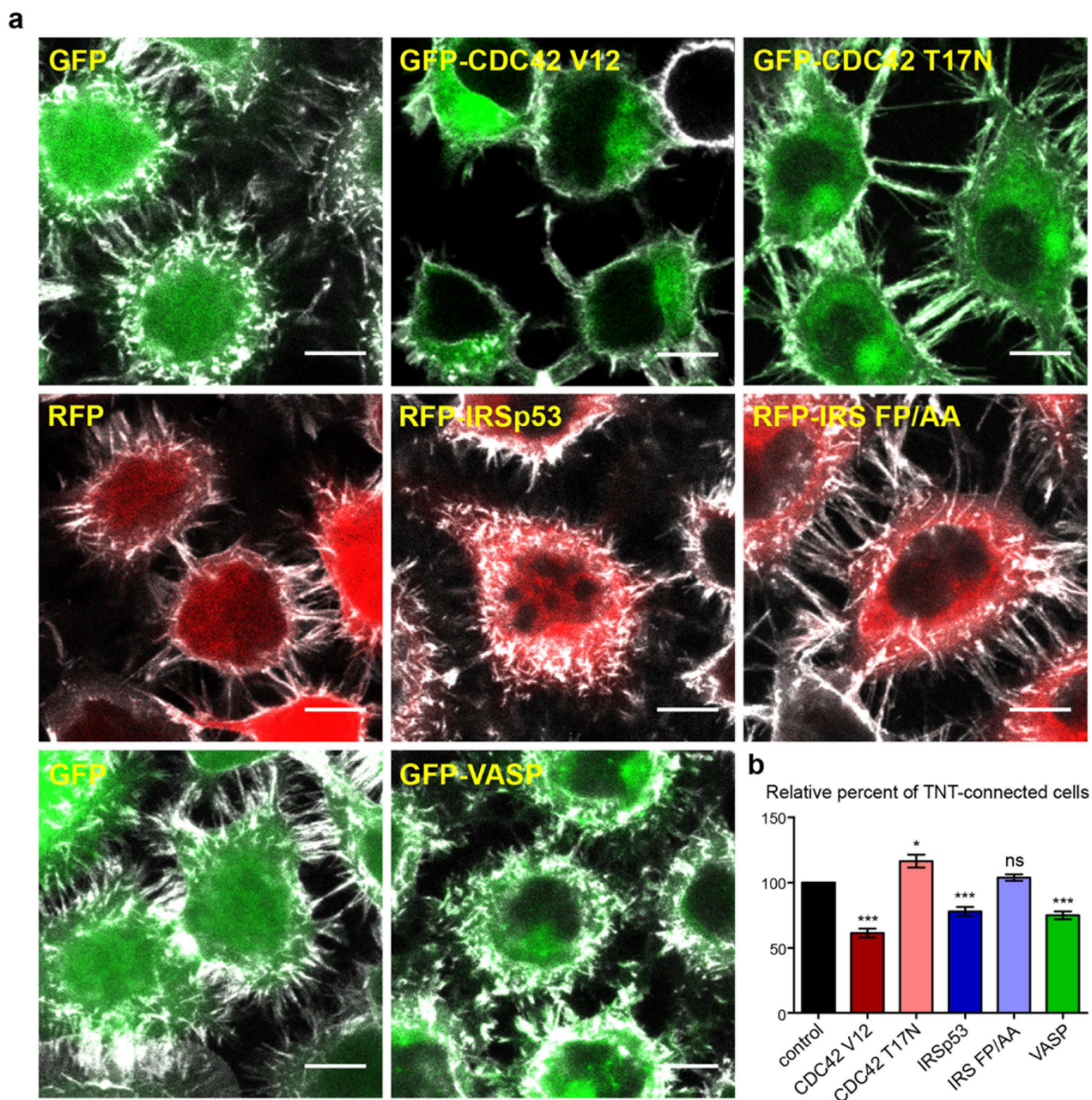


Figure 1. VASP, CDC42, and IRSp53 negatively regulate the number of TNT-connected cells. (a) Representative confocal images showing intercellular connections upon ectopic expression of GFP-CDC42 V12 (constitutively active form), GFP-CDC42 T17N (dominant negative form), RFP-IRSp53, RFP-IRS FP/AA (an IRSp53 SH3-mutant defective in its binding to ligands), or GFP-VASP. Cells were fixed 14 hrs post-transfection, labeled with WGA-Alexa Fluor[®]-647 nm (grey) in order to detect TNTs and observed by confocal microscopy. Scale bar = 10 μ M. (b) Quantification of TNT-connected cells upon ectopic expression of GFP-CDC42 V12, GFP-CDC42 T17N, RFP-IRSp53, RFP-IRS FP/AA, or GFP-VASP. The ratio of TNT-forming transfected cells/number of transfected cells was evaluated. Data represent the mean (\pm SEM), normalized to control cells (GFP or RFP transfected cells) arbitrarily set at 100%, of at least 6 independent experiments. * $P < 0.05$; ** $P < 0.01$; *** $P < 0.001$; ns = not significant.

respectively (Supplementary Fig. 2). Thus, the combined use of Rac1 and CDC42 mutants provide evidence that inducers of filopodia and lamellipodia have an opposite effect (i.e. decrease) on TNT formation.

CDC42, IRSp53, and VASP negatively regulate intercellular vesicle transfer. To address the functional relevance of CDC42, IRSp53, and VASP action on TNT formation, we investigated their effects on TNT-mediated vesicle transfer. We used a well-established protocol that allows the evaluation of cell-contact dependent intercellular vesicle transfer^{24,30,43}. This protocol is based on the co-culture of two cell populations with a 1:1 ratio: a “donor population”, whose internal vesicles are labeled with the non-specific membrane dye DiD, and an “acceptor population”, transfected with a different fluorescent marker (H2B-mCherry or H2B-GFP). After

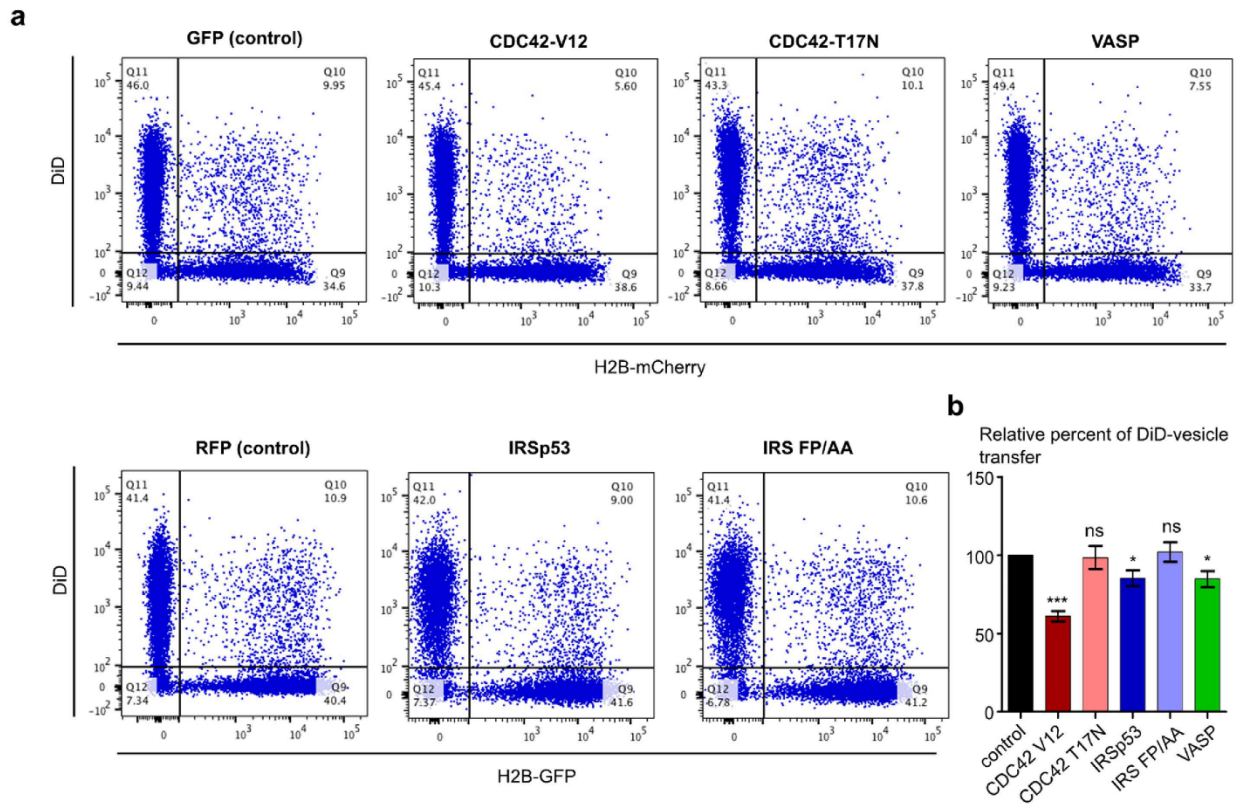


Figure 2. CDC42, IRSp53, and VASP negatively regulate intercellular vesicle transfer. (a) Raw data (dot plots) from a representative experiment showing the transfer of DiD-labeled vesicles to the acceptor population (H2B-mCherry) upon ectopic expression of GFP-CDC42 V12, GFP-CDC42 T17N, RFP-IRSp53, RFP-IRS FP/AA, or GFP-VASP in the donor population. A population of CAD cells was transiently transfected with the different fluorescently-tagged constructs (donor population) and another population was transiently transfected with either H2B-GFP or H2B-mCherry (acceptor population). Internal vesicles of donor cells were labeled with the membrane dye Vybrant DiD as described in the ‘Material and Methods’ section. Donor and acceptor cells were co-cultured for 16 hrs. Cells were then fixed and analyzed by flow cytometry. (b) Quantification by flow cytometry of DiD-positive acceptor cells upon ectopic expression of GFP-CDC42 V12, GFP-CDC42 T17N, RFP-IRSp53, RFP-IRS FP/AA, or GFP-VASP in the donor population. The percentage of DiD-positive acceptor cells in the total cell population was evaluated. Data represent the mean (\pm SEM), normalized to control cells arbitrarily set at 100%, of at least 4 independent experiments. * $P < 0.05$; ** $P < 0.01$; *** $P < 0.001$; ns = not significant.

16h of co-culture, the cells are fixed and the number of acceptor cells having received DiD-labeled vesicles from the donor population is evaluated by flow cytometry. The cell-contact requirement of this transfer was assessed by using a filter to physically separate the two cell populations while allowing the transfer of exosomes and soluble molecules or by applying the conditioned medium from the donor cells onto the acceptor population for the same duration as the co-culture, as we previously showed³⁰. After transfecting the donor population with GFP-CDC42 V12, RFP-IRSp53, and GFP-VASP, we observed a significant reduction in intercellular vesicle transfer (40%, 15% and 20% on average, respectively) (Fig. 2a and b, Supplementary Fig. 3). On the other hand, we observed no significant difference in comparison to control group upon overexpression of GFP-CDC42 T17N or RFP-IRS FP/AA (Fig. 2a and b, Supplementary Fig. 3). These effects on vesicle transfer paralleled those seen on the number of TNT-connected cells indicating that CDC42, IRSp53, and VASP act as negative regulators of both TNT formation and transfer function.

CDC42, IRSp53, and VASP act as a network to inhibit TNT formation. Next, we investigated whether the mechanism by which CDC42, IRSp53, and VASP inhibit TNT formation involved them acting independently or in concert. We co-transfected cells with either CDC42/IRSp53, IRSp53/VASP or CDC42/VASP couples of different constructs described above, and evaluated the number of TNT-forming cells by immunofluorescence. Interestingly, co-transfection of the dominant negative form of CDC42, (GFP-CDC42-T17N), Myc-CDC42 T17N), RFP-IRSp53, or GFP-VASP reverted the decrease in TNT-connected cells observed upon transfection of either RFP-IRSp53 or GFP-VASP alone. Notably, this finding indicates that CDC42 activity is required for IRSp53 and VASP inhibition of TNT formation (Fig. 3, Supplementary Fig. 4). On the other hand, the IRSp53 mutant (RFP-IRS FP/AA) reverted the decrease in TNT-connected cells induced by GFP-CDC42 V12 overexpression, suggesting that CDC42 negative regulation of TNT formation requires IRSp53 capacity to recruit its protein partners (Fig. 3, Supplementary Fig. 4). Upon co-expression of GFP-VASP and RFP-IRSp53,

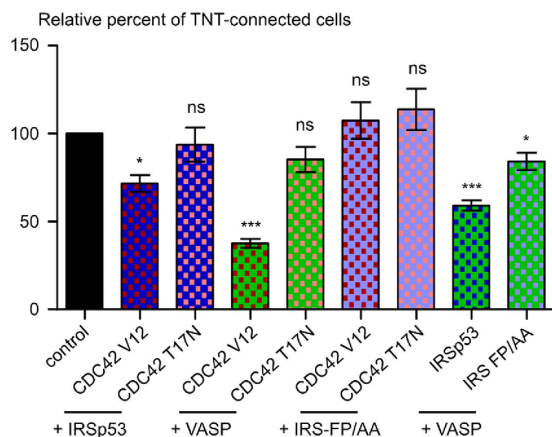


Figure 3. CDC42, IRSp53, and VASP act as a network to negatively regulate the number of TNT-connected cells. CAD cells were transiently co-transfected as indicated under the graph. Cells were fixed 14 hrs post-transfection, labeled with fluorescent WGA in order to detect TNTs and observed by confocal microscopy. The ratio of TNT-forming cotransfected cells/number of cotransfected cells was evaluated. Data represent the mean (\pm SEM), normalized to control cells arbitrarily set at 100%, of at least 4 independent experiments. * $P < 0.05$; ** $P < 0.01$; *** $P < 0.001$; ns = not significant.

we observed a significantly higher reduction in the number of TNT-connected cells compared to the decrease observed after the expression of either GFP-VASP or RFP-IRSp53 alone (Fig. 3, Supplementary Fig. 4). Collectively, these results indicate that CDC42, IRSp53, and VASP act as a network which negatively regulates TNT formation.

VASP positively regulates filopodia formation. Because the CDC42/IRSp53/VASP network was shown to act as a positive regulator in filopodia formation in neuronal cells^{36,38,44}, we analyzed whether it plays a similar role in CAD cells. However, since CDC42 and IRSp53 can also reduce the formation of membrane ruffles and lamellipodia that can mask filopodia formation we focused on VASP. VASP was shown to act downstream of IRSp53 for filopodia induction, but is not involved in IRSp53-mediated lamellipodia formation^{38,44}. The formation of filopodia was qualitatively assessed by both correlative-scanning electron microscopy (CL-SEM) (Fig. 4a) and super resolution structured illumination microscopy (SR-SIM) imaging (Fig. 4b) of transfected cells. In most cases, VASP transfected cells exhibited an increase in the number of actin-positive, filopodia-like dorsal protrusions with respect to GFP transfected control cells, suggesting that VASP also exerts a positive regulation of filopodia formation in CAD cells. Contrary to TNTs and dorsal filopodia, attached filopodia display vinculin-positive focal adhesions at their tips^{33,45}. We used this specificity to automatically detect and count vinculin-positive peripheral cellular protrusions, in order to obtain more quantitative data on the role of VASP in attached filopodia formation (see methods)⁴⁶. We demonstrated an enrichment of peripheral focal adhesions in GFP-VASP transfected cells compared to the control, confirming the involvement of VASP in promoting filopodia formation in our cell line model (Supplementary Fig. 5).

Eps8 positively regulates TNT formation and function via its bundling activity. The results presented above show that positive regulators of filopodia formation can inhibit TNT formation and function. This suggests that TNTs and filopodia might be distinct structures oppositely regulated by the same signaling pathways. To further investigate this hypothesis, we decided to look at the role in TNT formation of Eps8, another actin regulator shown to negatively regulate the formation of filopodia in neuronal cells⁴⁰. First, the endogenous levels of Eps8 were analyzed in CAD cells (Supplementary Fig. 6). We found that CAD cells express very low amounts of Eps8 mRNA, compared to brain tissue and CHO cells, and the protein was not detectable, thus the role of this actin regulator was studied by its overexpression. Consistent with data present in the literature in other cell models, we observed a nearly complete disappearance of dorsal and peripheral filopodia like protrusions in CAD cells overexpressing GFP-Eps8 (Fig. 4a and b). Indeed the CL-SEM (Fig. 4a) and SR-SIM (Fig. 4b) images showed tiny actin-positive protrusions, reminiscent to the club-like protrusions previously described in neurons overexpressing this construct⁴⁰.

Intriguingly, ectopic expression of GFP-Eps8 in CAD cells induced a significant increase in the number of TNT-connected cells (Fig. 5a and b, Supplementary Fig. 7). To dissect the mechanism of Eps8 action, we assessed the effect on TNT formation of its actin-capping and -bundling activity. We transfected CAD cells with GFP-Eps8 Δ capping and GFP-Eps8 Δ bundling, (constructs encoding Eps8 mutants impaired in their actin-capping and -bundling activity respectively)⁴⁷. The expression of GFP-Eps8 Δ capping-mutant, likewise of Eps8, increased TNT-connected cells. Conversely, no increase upon the expression of GFP-Eps8 Δ bundling-mutant was observed (Fig. 5a and b, Supplementary Fig. 7). This finding indicates that Eps8 exerts a positive regulation on TNT formation via its bundling activity. We, then, evaluated whether Eps8 had any functional consequences by looking at the effect on intercellular vesicle transfer. We observed a significant increase of DiD-positive acceptor cells upon expression of GFP-Eps8 or GFP-Eps8 Δ capping compared to the control, whereas no significant change

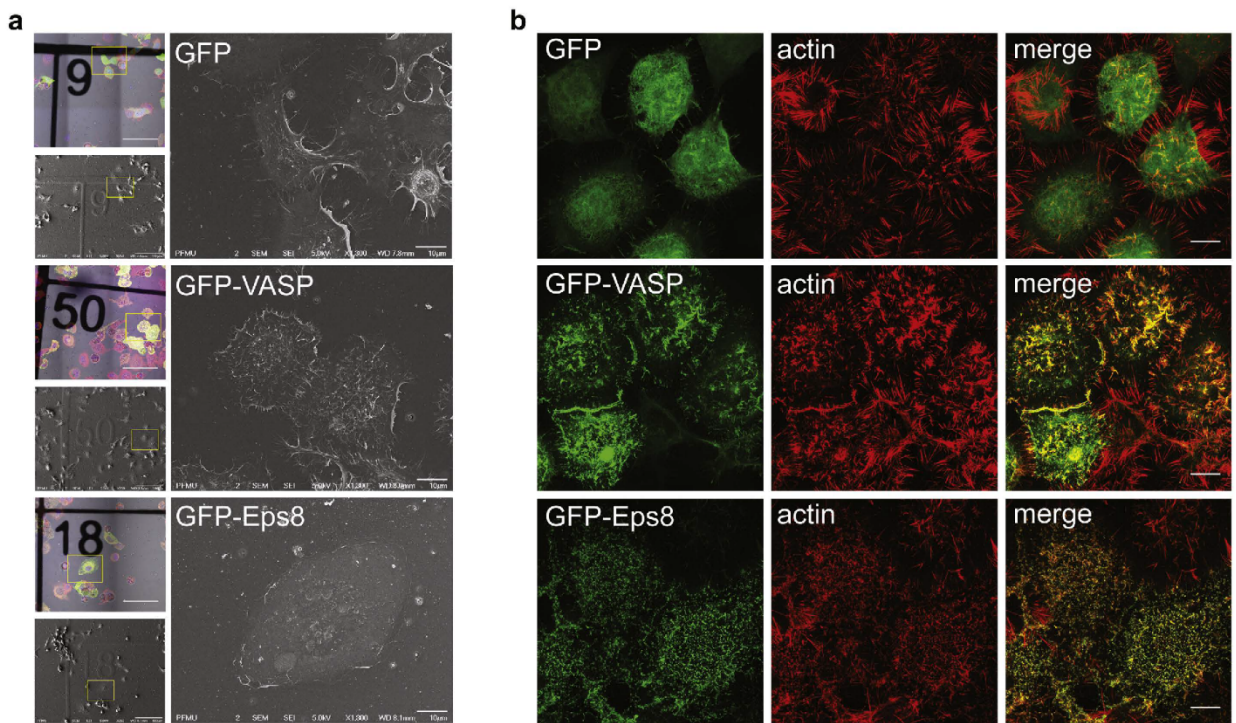


Figure 4. VASP and Eps8 ectopic expression have opposite effect on filopodia formation. (a) Morphology of CAD cells expressing GFP-VASP or GFP-Eps8 characterized by CL-SEM. Cells were transiently transfected with GFP-VASP, GFP-Eps8 or GFP as a control. Cells were plated for 6 hrs on correlative microscopy coverslips, fixed and stained with WGA Alexa Fluor[®]-594 nm. Coverslips were first imaged by confocal microscopy, then prepared for SEM and imaged with a JEOL JSM 6700 F field emission scanning electron microscope. Scale bar = 10 μ M. (b) Morphology of CAD cells transfected with GFP-VASP or GFP-Eps8 characterized by SR-SIM. Cells were fixed after 14 hrs. Actin was stained using rhodamine-phalloidin. Cells were imaged by SR-SIM using an Elyra P.S.1 microscope. Scale bar = 10 μ M.

was monitored for GFP-Eps8 Δ bundling (Fig. 5c, Supplementary Fig. 7). Overall this data indicates that Eps8 is a positive regulator of functionally active TNTs and that its actin-bundling activity is required.

Discussion

The data presented here provides new insights on the cytoskeleton architecture and mechanisms underlying TNT formation and intercellular vesicle transfer in neuronal CAD cells. Our results show that CDC42, IRSp53, and VASP act in concert to inhibit TNT formation while concomitantly promoting the extension of filopodia (Fig. 6). We previously observed a drastic reduction of TNT-connected cells upon overexpression of GFP-VASP in CAD cells³⁰. Here, we demonstrate that VASP expression also reduces contact-dependent intercellular vesicle transfer, supporting a negative role of VASP on functional TNTs. Our data also points to IRSp53 as another negative regulator of TNT formation and transfer. To exert this function, IRSp53 must interact with downstream partners since no decrease in TNT-connected cells nor vesicle transfer were observed upon overexpression of a mutant form of IRSp53 impaired in binding its downstream partners (eg, VASP, N-WASP, Wave, mDia and Eps8³²). Nevertheless, we observed a stronger inhibition of TNT formation upon co-expression of IRSp53 and VASP compared to the expression of one or the other alone. This indicates that VASP might cooperate with IRSp53 (perhaps by acting downstream as proposed in filopodia³⁶), although we cannot exclude that IRSp53 inhibition of TNT formation and function also involves additional interacting partners. More importantly, we showed that activation of CDC42 negatively regulates TNT formation and transfer function. Indeed, while the constitutively active form of the GTPase strongly reduces the number of cells connected via TNTs and intercellular vesicle transfer, overexpression of the dominant-negative form increases TNT formation without a significant effect on vesicle transfer. This latter observation suggests that the formation of functional TNTs requires additional limiting factors. It is important to note that both IRSp53- and VASP-mediated inhibition of TNT formation and transfer appears to require CDC42 activity, suggesting that an active CDC42-IRSp53-VASP complex is needed to counteract TNT formation and activity.

Our data contradicts prior work showing a decrease in TNT formation and elongation upon inhibition of CDC42^{26,27,41}. The contact-dependent intercellular transfer was also shown to require CDC42 activity^{48,49}. However, all of these studies were performed in non-neuronal cells (Hela, Jurkat and NK cells). Thus, this apparent discrepancy could simply reflect cell type-dependent mechanisms of TNT formation, as it has been reported for M-Sec and p53-dependent mechanisms^{29,30}. It is also worth pointing out that IRSp53, VASP, and Eps8 display

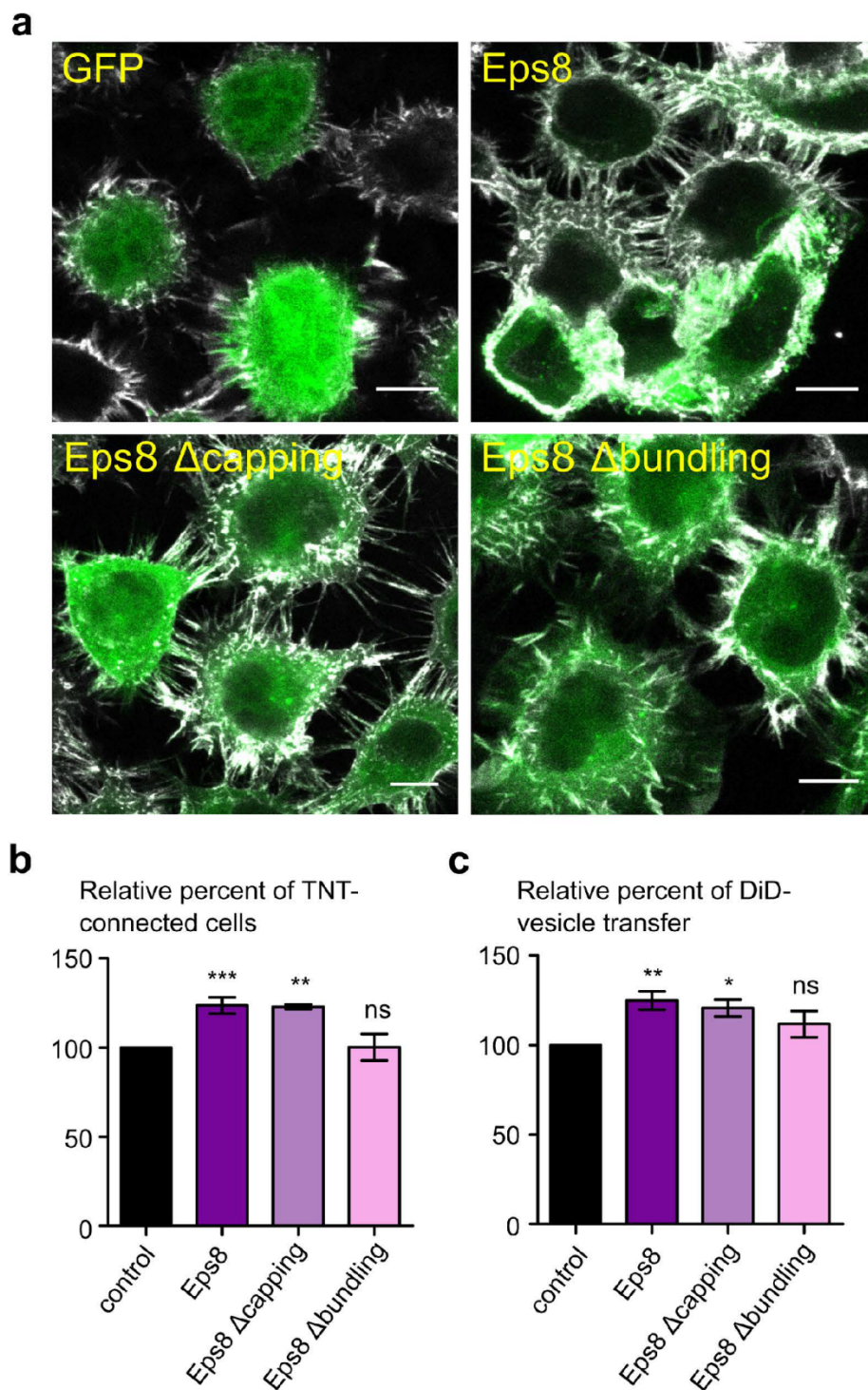


Figure 5. Eps8 positively regulates TNT formation and intercellular vesicle transfer via its bundling activity. (a) Representative confocal images showing intercellular connections upon ectopic expression of GFP-Eps8, GFP-Eps8 Δ capping or GFP-Eps8 Δ bundling. Cells were fixed 14 hrs post-transfection, labeled with WGA-Alexa Fluor[®]-647 nm (grey) in order to detect TNTs and observed by confocal microscopy. Scale bar = 10 μ m. (b) Quantification of TNT-connected cells upon ectopic expression of GFP-Eps8, GFP-Eps8 Δ capping or GFP-Eps8 Δ bundling. The ratio of TNT-forming transfected cells/number of transfected cells was evaluated. (c) The donor population of CAD cells was transfected with either GFP-Eps8, GFP-Eps8 Δ capping or GFP-Eps8 Δ bundling, and the acceptor population was transfected with H2B-mCherry. The co-culture was prepared as described in Fig. 3. Cells were analyzed by flow cytometry to quantify the percentage of acceptor cells having received DiD-labeled vesicles from the donor population. Data represent the mean (\pm SEM), normalized to control cells arbitrarily set at 100%, of at least 3 independent experiments. (b,c) Data represent the mean (\pm SEM), normalized to control cells (GFP-vector transfected cells) arbitrarily set at 100%, of at least 3 independent experiments. *P < 0.05; **P < 0.01; ***P < 0.001; ns = not significant.

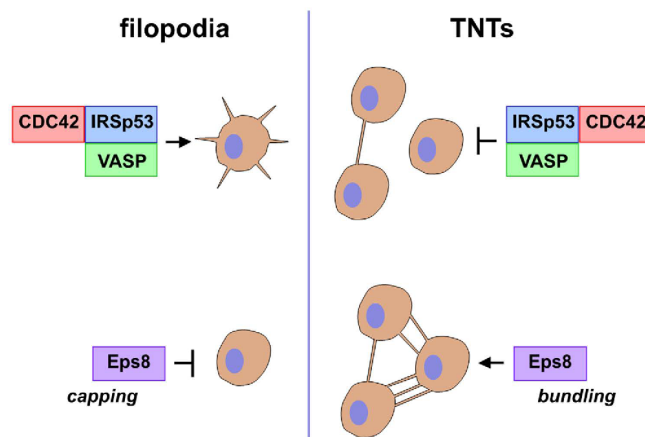


Figure 6. TNT and filopodia formation involve the same actin regulatory complexes acting in opposite ways.

context-dependent effects on filopodia formation that may be directly relevant in the context of TNT formation and could account, in part, to an specific cell activity of this actin regulatory signaling axis (see below)^{36,38}.

The CDC42/IRSp53/VASP network has previously been identified as a positive regulator of filopodia formation^{36,38}. In CAD cells, we observed an increase of actin-rich dorsal protrusions and peripheral vinculin-positive focal adhesions upon overexpression of GFP-VASP. This indicates that VASP also positively regulates filopodia formation in our cellular model. On the other hand, the inhibitory role of the CDC42/IRSp53/VASP network in TNT formation reported here suggests that filopodia and TNTs are distinct structures that utilize different mechanisms for their formation (Fig. 6). In order to investigate this hypothesis, we study the role of Eps8. Eps8 can coordinate and integrate multiple signaling pathways via the formation of distinct macromolecular complexes^{50,51}. It is involved in the endocytosis of receptor tyrosine kinases and can transduce signals from Ras to Rac, leading to actin remodeling⁵¹. Eps8 directly interacts with actin and is capable of capping and bundling actin filaments depending on its downstream ligands⁴⁷. In keeping with the latter notion, Eps8 was shown to play a complex role in filopodia regulation³⁸. It acts as a positive regulator of filopodia formation in non-neuronal cells (Hela and epithelial cells), where it was shown to synergize with IRSp53 in bundling actin filaments^{38,52}. On the other hand, the genetic removal of Eps8 increases the formation of filopodia in primary hippocampal neurons^{38,40}. This inhibitory function is exerted, instead, through the capping activity of Eps8 triggered by the interaction with Abi1/2, and by its competition with VASP-family proteins for IRSp53 binding. In CAD cells, we observed a striking remodeling of cellular protrusions upon overexpression of GFP-Eps8. Instead of the abundant peripheral and dorsal filopodia-like protrusions observed in control cells, GFP-Eps8-transfected cells harbor tiny and curved actin-rich protrusions. This phenotype may correspond to the thick club-like protrusions observed along axon and dendrites in primary neurons upon ectopic expression of Eps8⁴⁰. These observations suggest that Eps8 negatively regulates filopodia formation in our cellular model as well as in primary neurons. Interestingly, Eps8 overexpression induced a significant increase in TNT-connected cells and intercellular vesicle transfer, indicating that it may act as a positive regulator of TNT formation. Our data also indicates that Eps8-mediated TNT induction involves the bundling activity of the protein, while the capping activity does not seem to be required. However, it was previously shown that capping activity of Eps8 is regulated by MAPK-dependent phosphorylation, suggesting that modulation of this latter activity rather than an on/off switch may be important in controlling actin-based structures in filopodia as well as in TNTs⁵³. Most of the data published in the literature so far points to a synergy with IRSp53, driving Eps8 bundling activity^{38,52}. However, IRSp53 is unlikely to contribute to Eps8-dependent TNT induction in CAD cells as it is a negative regulator of TNT formation. Further work will have to focus on the identification of Eps8 partners in this context.

In summary, our results represent the first molecular evidence that TNTs and filopodia may be completely different structures, which invalidates the hypothesis that TNTs could arise from a subset of filopodia. In fact, our data rather suggests that TNT precursors are different structures from the beginning. Furthermore, the observation that the same actin regulators may be involved in filopodia and TNT formation, but acting in opposite ways, raises the intriguing possibility of a “switch” between the two structures. Interestingly, our laboratory previously reported that when a growing TNT-like protrusion attaches to a distant cell, the filopodia of this cell subsequently retracts³⁰. This constitutes an additional hint for a regulated balance between TNTs and filopodia. Whether this balance results from a signaling pathway having a physiological relevance, or if it is the consequence of a limiting factor, remains to be determined but nevertheless calls for further studies both at the molecular and ultrastructural level.

Methods

Cell culture, transfection and DNA constructs. Mouse neuronal CAD cells were kindly given by Hubert Laude (Institut National de la Recherche Agronomique, Jouy-en-Josas, France) and were cultured in Gibco™ Opti-MEM® (Invitrogen) supplemented with 10% fetal bovine serum and 1% penicillin/streptomycin. Transient transfections were performed with Lipofectamine 2000 (Invitrogen) in accordance with the manufacturer's

instructions. The various GFP-tagged Eps8 constructs were previously described^{47,52}. RFP-IRSp53 and RFP-IRSp53/AA were a kind gift from Sohail Ahmed (IMB, Singapore). GFP-CDC42 V12 and GFP-CDC42 T17N were a gift from Roberto Mayor (University College London, UK) and GFP-VASP was a gift from Sandrine Etienne-Manneville (Pasteur Institute, Paris, France). Myc-CDC42 V12 and Myc-CDC42 T17N were obtained from Nathalie Sauvonnnet (Pasteur Institute, Paris, France). H2B-GFP was a gift from Geoff Wahl (Addgene plasmid # 11680⁵⁴), and H2B-mCherry was a gift from Robert Benezra (Addgene plasmid # 20972⁵⁵). Myc-tagged mouse Rac1 17 N and Rac1 V12 were a kind gift from Dr. A Hall from the University College London, UK. Visualization of Rac1-Myc-tagged cells was performed using a c-Myc mouse monoclonal antibody (Santa Cruz) in a 1:100 dilution, followed by a goat anti-mouse secondary antibody Alexa Fluor®-546 in a 1:500 dilution, both dissolved in a 2% BSA in PBS solution.

Quantification of TNT-connected cells. Confluent CAD cells were mechanically detached and counted, and 100,000 cells were plated for 24 hrs on Ibidi μ -dishes (Biovalley, France). Cells were transfected as described above, with the appropriate plasmids. At 14 hrs post-transfection, cells were fixed for 15 min at 37 °C in 2% PFA, 0.05% glutaraldehyde and 0.2 M HEPES in PBS, and then additionally fixed for 15 min in 4% PFA and 0.2 M HEPES in PBS. Cells were carefully washed in PBS, labeled for 20 min at RT with a 3.3 $\mu\text{g}\cdot\mu\text{L}^{-1}$ solution of Wheat Germ Agglutinin (WGA) Alexa Fluor®-647 nm conjugate (Invitrogen) in PBS, washed again and sealed with Aqua-Poly/Mount (Polysciences, Inc.). The whole cellular volume was imaged by acquiring 0.5 μm Z-stacks with an inverted confocal microscope (Zeiss LSM 700) controlled by ZEN software. TNT-connected cells, *i.e.* cells connected by straight WGA-labeled structures that do not touch the substrate and have a diameter smaller than 1 μm were manually counted by experimenters blind to the condition in the same manner as previously described^{20,23,30}. Displayed images correspond to stack projections. Only linear corrections were applied using the software ImageJ.

Quantification of vinculin-positive peripheral focal adhesion. For indirect immunofluorescence labeling of vinculin, 90,000 cells were plated for 16 hrs on Ibidi μ -dishes and then fixed in 4% PFA in PBS for 15 min at 37 °C. Samples were quenched with 50 mM NH_4Cl for 15 min, then cells were permeabilized with 0.01% saponin in PBS containing 2% BSA (w/v) for 20 min at 37 °C. After a first 1 hr incubation with mouse anti-vinculin antibody (V9264, Sigma) diluted 1:500 in PBS containing 0.01% saponin and 2% BSA (w/v), cells were thoroughly washed and incubated for 40 min with goat anti-mouse AlexaFluor®-488 (Invitrogen) diluted 1:500 in PBS containing 0.01% saponin and 2% BSA (w/v). Cells were washed and sequentially stained for 20 min with a 3.3 $\mu\text{g}\cdot\mu\text{L}^{-1}$ solution of WGA Alexa Fluor®-647 nm conjugate, for 30 min with a 1 $\mu\text{g}\cdot\text{mL}^{-1}$ solution of HCS CellMask™ Blue, which stains the entire cell volume (*i.e.* cytoplasm and nucleus), and for 5 min with a 0.2 $\mu\text{g}\cdot\mu\text{L}^{-1}$ solution of DAPI. Samples were washed and sealed with Aqua-Poly/Mount (Polysciences, Inc.). The bottom of the cell (in contact with the plastic dish) was imaged with an inverted confocal microscope (Zeiss LSM700) controlled by ZEN software. Displayed images correspond to stack projections. Only linear corrections were applied, using the software ImageJ. Vinculin-positive peripheral focal adhesion were automatically detected and counted using ICY software (<http://icy.bioimageanalysis.org/>).

Quantification of vesicle intercellular transfer. CAD cells were separately transfected in T25 flasks with the appropriate constructs (donor cells) and H2B-mCherry or H2B-GFP (acceptor cells) for 3 hrs in serum-free medium and incubated for one additional hour in complete medium. Donor cells were detached, counted and labeled with a 333 nM solution of the lipophilic tracer Vybrant™ DiD (long-chain dialkylcarbocyanine) in complete medium for 30 min at 37 °C. Cells were pelleted at 1000 rpm for 4 min to remove the DiD solution, resuspended in complete medium and incubated for 45 min at 37 °C in order to internalize the dye. Cells were then pelleted once more to wash away any remaining dye and resuspended in complete medium. The labeled donor cells were mixed in a 1:1 ratio with H2B-transfected acceptor cells and plated at subconfluence (120,000 cells per well) on 24-well plates for 16 hrs at 37 °C. Each independent co-culture was performed in triplicate. Cells were then washed with PBS to remove any dead cells, mechanically detached from the dish by pipetting up and down with 500 μL PBS, and passed through sterile 40-mm nylon cell strainers (BD Falcon™) in order to obtain single-cell suspensions. Cell suspensions were fixed with 500 μL of 4% PFA (2% final solution). Flow cytometry data were acquired using a LSR Fortessa flow cytometer (BD Biosciences). GFP fluorescence was analyzed at 488 nm excitation wavelength, RFP and mCherry fluorescence were analyzed at 561 nm excitation wavelength, and DiD fluorescence was analyzed at 640 nm excitation wavelength. Samples were analyzed at high flow rate, corresponding to 200–400 events per second and 10,000 events were acquired for each condition. The data were analyzed using FlowJo analysis software.

Correlative scanning electron microscopy. CADs were transfected as described above with GFP, GFP-VASP or GFP-Eps8 and 500,000 cells were plated on sterile (UV sterilization) plastic Correlative Microscopy Coverslips® (10 \times 10 grids of 1 mm squares, 66108-03, EMS). After 6 hrs at 37 °C, cells were fixed for 20 min at 37 °C in 2% PFA, 0.05% GA and 0.2 M HEPES in PBS, then additionally fixed for 20 min in 4% PFA and 0.2 M HEPES in PBS. Cells were carefully washed in PBS, labeled for 20 min at RT with a 3.3 $\mu\text{g}\cdot\mu\text{L}^{-1}$ solution of WGA Alexa Fluor®-594 nm or -488 nm conjugate (Invitrogen) in PBS, then washed again. Samples were imaged in PBS using an upright LSM700 confocal microscope (Zeiss) with an immersed long-distance working 40X objective. Cells were then fixed a second time in 2.5% GA in PHEM (pH 6.9). They were washed three times with 0.2 M cacodylate buffer (pH 7.2), post-fixed for 1 hr in 1% (w/v) osmium tetroxide in 0.1 M cacodylate buffer (pH 7.2), and then rinsed with distilled water. Samples were dehydrated through a graded series of 25, 50, 17 and 95% ethanol solution for 5 min each time. Samples were then dehydrated for 10 min in 100% ethanol, followed by critical point drying with CO_2 . Dried specimens were sputtered with 10 nm gold palladium, with a GATAN Ion

Beam Coater and were examined and photographed with a JEOL JSM 6700 F field emission scanning electron microscope operating at 5Kv. Images were acquired with the upper SE detector (SEI). Only linear corrections were applied, using Image J software.

Super Resolution Structured Illumination Microscopy (SR-SIM). Cells were prepared as described for the quantification of TNT-connected cells. Samples were imaged with an Elyra P.S.1 microscope controlled by ZEN software, using a 63×1.4 NA plan-apo objective lens. Data sets were collected with five grating phases, three rotations and 300 nm Z-stacks. SIM post-processing was performed using the ZEN software in manual mode to optimize noise filtering and sectioning parameters for each channel. Reconstructed images were then corrected for spatial misalignment between spectrally distinct channels (variations in the dichroic mirrors) with the Channel Alignment method of the ZEN software. Polystyrene beads coated with multiple fluorophores were used for calibration. Displayed images correspond to stack projections. Only linear corrections were applied, using Image J software.

Statistical analysis. Mean comparisons were calculated on the raw data by two-tailed paired Student's t-test using the software Prism. Normal distributions were assumed but not formally tested. All experiments were repeated at least three times and no issues in reproducibility were encountered.

Western blot. Mouse brain tissue and cells were lysed in NP-40 lysis buffer (25 mM Tris pH 7.5, 150 mM NaCl, 1% NP-40), and protein concentration in the cell lysate was quantified using a Bradford protein assay (Bio-Rad). Protein samples were incubated at 100 °C for 5 min and electrophoresed on 10% SDS-polyacrylamide gels. Proteins were transferred onto PVDF membranes (GE Healthcare Life sciences). Membranes were blocked in 5% nonfat milk in Tris-buffered saline with 0.1% Tween 20 (TBS-T) for 1 h. Membranes were then incubated at 4 °C with a primary antibody mouse anti-Eps8 (BD Transduction) and mouse anti-GAPDH (Millipore) diluted in 5% nonfat milk overnight (1:500 and 1:10,000, respectively) then washed several times with TBS-T. After 1 h incubation with horseradish peroxidase-conjugated anti-mouse IgG secondary antibody (1:10,000) (GE Healthcare Life sciences), membranes were washed with TBS-T and protein bands on the membrane were detected using an ECL-Plus immunoblotting chemiluminescence system (GE Healthcare Life sciences). Membranes were imaged using ImageQuant LAS 500TM camera (GE Healthcare Life sciences).

RNA preparation and Reverse Transcription PCR. Total RNA was prepared from CAD and CHO cells in 25-mm dishes with an RNeasy Plus Micro Kit (QIAGEN Cat: 74034) according to the manufacturer's instructions. Reverse transcription-PCR was performed using random hexamer primers, and using a SuperScript II Reverse Transcriptase kit (Invitrogen). The following primers were used for Eps8: a forward primer sequence: 5'- caatgtgtccgactatcctc -3', and a reverse primer sequence: 5'- tcagtggctgctcctcat -3'. A total of 2 µL of the product was used to amplify a fragment of Eps8 cDNA for 30 cycles.

References

- Rustom, A., Saffrich, R., Markovic, I., Walther, P. & Gerdes, H. H. Nanotubular highways for intercellular organelle transport. *Science* **303**, 1007–1010, doi: 10.1126/science.1093133 (2004).
- Aboutin, S. & Zurzolo, C. Wiring through tunneling nanotubes—from electrical signals to organelle transfer. *Journal of cell science* **125**, 1089–1098, doi: 10.1242/jcs.083279 (2012).
- Marzo, L., Gousset, K. & Zurzolo, C. Multifaceted roles of tunneling nanotubes in intercellular communication. *Frontiers in physiology* **3**, 72, doi: 10.3389/fphys.2012.00072 (2012).
- Chinnery, H. R., Pearlman, E. & McMenamin, P. G. Cutting edge: Membrane nanotubes *in vivo*: a feature of MHC class II+ cells in the mouse cornea. *Journal of immunology* **180**, 5779–5783 (2008).
- Lou, E. *et al.* Tunneling nanotubes provide a unique conduit for intercellular transfer of cellular contents in human malignant pleural mesothelioma. *PloS one* **7**, e33093, doi: 10.1371/journal.pone.0033093 (2012).
- Pasquier, J. *et al.* Preferential transfer of mitochondria from endothelial to cancer cells through tunneling nanotubes modulates chemoresistance. *Journal of translational medicine* **11**, 94, doi: 10.1186/1479-5876-11-94 (2013).
- Seyed-Razavi, Y., Hickey, M. J., Kuffova, L., McMenamin, P. G. & Chinnery, H. R. Membrane nanotubes in myeloid cells in the adult mouse cornea represent a novel mode of immune cell interaction. *Immunology and cell biology* **91**, 89–95, doi: 10.1038/icb.2012.52 (2013).
- Gerdes, H. H., Rustom, A. & Wang, X. Tunneling nanotubes, an emerging intercellular communication route in development. *Mechanisms of development* **130**, 381–387, doi: 10.1016/j.mod.2012.11.006 (2013).
- Hashimoto, M. *et al.* Potential Role of the Formation of Tunneling Nanotubes in HIV-1 Spread in Macrophages. *Journal of immunology* **196**, 1832–1841, doi: 10.4049/jimmunol.1500845 (2016).
- Sowinski, S. *et al.* Membrane nanotubes physically connect T cells over long distances presenting a novel route for HIV-1 transmission. *Nature cell biology* **10**, 211–219, doi: 10.1038/ncb1682 (2008).
- Onfelt, B. *et al.* Structurally distinct membrane nanotubes between human macrophages support long-distance vesicular traffic or surfing of bacteria. *Journal of immunology* **177**, 8476–8483 (2006).
- Lou, E. Intercellular conduits in tumours: the new social network. *Trends in cancer* **2**, 3–5, doi: 10.1016/j.trecan.2015.12.004 (2016).
- Ware, M. J. *et al.* Radiofrequency treatment alters cancer cell phenotype. *Scientific reports* **5**, 12083, doi: 10.1038/srep12083 (2015).
- Gousset, K. & Zurzolo, C. Tunneling nanotubes: a highway for prion spreading? *Prion* **3**, 94–98 (2009).
- Langevin, C., Gousset, K., Costanzo, M., Richard-Le Goff, O. & Zurzolo, C. Characterization of the role of dendritic cells in prion transfer to primary neurons. *The Biochemical journal* **431**, 189–198, doi: 10.1042/BJ20100698 (2010).
- Victoria, G. S., Arkhipenko, A., Zhu, S., Syan, S. & Zurzolo, C. Astrocyte-to-neuron intercellular prion transfer is mediated by cell-cell contact. *Scientific reports* **6**, 20762, doi: 10.1038/srep20762 (2016).
- Zhu, S., Victoria, G. S., Marzo, L., Ghosh, R. & Zurzolo, C. Prion aggregates transfer through tunneling nanotubes in endocytic vesicles. *Prion* **9**, 125–135, doi: 10.1080/19336896.2015.1025189 (2015).
- Costanzo, M. *et al.* Transfer of polyglutamine aggregates in neuronal cells occurs in tunneling nanotubes. *Journal of cell science* **126**, 3678–3685, doi: 10.1242/jcs.126086 (2013).
- Wang, Y., Cui, J., Sun, X. & Zhang, Y. Tunneling-nanotube development in astrocytes depends on p53 activation. *Cell death and differentiation* **18**, 732–742, doi: 10.1038/cdd.2010.147 (2011).

20. Abounit, S. *et al.* Tunneling nanotubes spread fibrillar alpha-synuclein by intercellular trafficking of lysosomes. *The EMBO journal* **35**, 2120–2138, doi: 10.15252/embj.201593411 (2016).
21. Abounit, S., Wu, J. W., Victoria, G. S. & Zurzolo, C. Tunneling nanotubes: A possible highway in the spreading of tau and other prion-like proteins in neurodegenerative diseases. *Prion* **0**, doi: 10.1080/19336896.2016.1223003 (2016).
22. Costanzo, M. & Zurzolo, C. The cell biology of prion-like spread of protein aggregates: mechanisms and implication in neurodegeneration. *The Biochemical journal* **452**, 1–17, doi: 10.1042/BJ20121898 (2013).
23. Abounit, S., Delage, E. & Zurzolo, C. Identification and Characterization of Tunneling Nanotubes for Intercellular Trafficking. *Current protocols in cell biology/ editorial board, Juan S. Bonifacino ... [et al.]* **67**, 12 10 11–21, doi: 10.1002/0471143030.cb1210s67 (2015).
24. Bukoreshtliev, N. V. *et al.* Selective block of tunneling nanotube (TNT) formation inhibits intercellular organelle transfer between PC12 cells. *FEBS letters* **583**, 1481–1488, doi: 10.1016/j.febslet.2009.03.065 (2009).
25. Gousset, K. *et al.* Prions hijack tunnelling nanotubes for intercellular spread. *Nature cell biology* **11**, 328–336, doi: 10.1038/ncb1841 (2009).
26. Hase, K. *et al.* M-Sec promotes membrane nanotube formation by interacting with Ral and the exocyst complex. *Nature cell biology* **11**, 1427–1432, doi: 10.1038/ncb1990 (2009).
27. Schiller, C. *et al.* LST1 promotes the assembly of a molecular machinery responsible for tunneling nanotube formation. *Journal of cell science* **126**, 767–777, doi: 10.1242/jcs.114033 (2013).
28. Takahashi, A. *et al.* Tunneling nanotube formation is essential for the regulation of osteoclastogenesis. *Journal of cellular biochemistry* **114**, 1238–1247, doi: 10.1002/jcb.24433 (2013).
29. Andresen, V. *et al.* Tunneling nanotube (TNT) formation is independent of p53 expression. *Cell death and differentiation* **20**, 1124, doi: 10.1038/cdd.2013.61 (2013).
30. Gousset, K., Marzo, L., Commere, P. H. & Zurzolo, C. Myo10 is a key regulator of TNT formation in neuronal cells. *Journal of cell science* **126**, 4424–4435, doi: 10.1242/jcs.129239 (2013).
31. Lokar, M., Igljic, A. & Veranic, P. Protruding membrane nanotubes: attachment of tubular protrusions to adjacent cells by several anchoring junctions. *Protoplasma* **246**, 81–87, doi: 10.1007/s00709-010-0143-7 (2010).
32. Arjonen, A., Kaukonen, R. & Ivaska, J. Filopodia and adhesion in cancer cell motility. *Cell adhesion & migration* **5**, 421–430, doi: 10.4161/cam.5.5.17723 (2011).
33. Bohil, A. B., Robertson, B. W. & Cheney, R. E. Myosin-X is a molecular motor that functions in filopodia formation. *Proceedings of the National Academy of Sciences of the United States of America* **103**, 12411–12416, doi: 10.1073/pnas.0602443103 (2006).
34. Watanabe, T. M., Tokuo, H., Gonda, K., Higuchi, H. & Ikebe, M. Myosin-X induces filopodia by multiple elongation mechanism. *The Journal of biological chemistry* **285**, 19605–19614, doi: 10.1074/jbc.M109.093864 (2010).
35. Zhang, H. *et al.* Myosin-X provides a motor-based link between integrins and the cytoskeleton. *Nature cell biology* **6**, 523–531, doi: 10.1038/ncb1136 (2004).
36. Disanza, A. *et al.* CDC42 switches IRSp53 from inhibition of actin growth to elongation by clustering of VASP. *The EMBO journal* **32**, 2735–2750, doi: 10.1038/emboj.2013.208 (2013).
37. Chou, A. M., Sem, K. P., Wright, G. D., Sudhakaran, T. & Ahmed, S. Dynamin1 is a novel target for IRSp53 protein and works with mammalian enabled (Mena) protein and Eps8 to regulate filopodial dynamics. *The Journal of biological chemistry* **289**, 24383–24396, doi: 10.1074/jbc.M114.553883 (2014).
38. Vaggi, F. *et al.* The Eps8/IRSp53/VASP network differentially controls actin capping and bundling in filopodia formation. *PLoS computational biology* **7**, e1002088, doi: 10.1371/journal.pcbi.1002088 (2011).
39. Kast, D. J. *et al.* Mechanism of IRSp53 inhibition and combinatorial activation by Cdc42 and downstream effectors. *Nature structural & molecular biology* **21**, 413–422, doi: 10.1038/nsmb.2781 (2014).
40. Menna, E. *et al.* Eps8 regulates axonal filopodia in hippocampal neurons in response to brain-derived neurotrophic factor (BDNF). *PLoS biology* **7**, e1000138, doi: 10.1371/journal.pbio.1000138 (2009).
41. Arkwright, P. D. *et al.* Fas stimulation of T lymphocytes promotes rapid intercellular exchange of death signals via membrane nanotubes. *Cell research* **20**, 72–88, doi: 10.1038/cr.2009.112 (2010).
42. Van Aelst, L. & D'Souza-Schorey, C. Rho GTPases and signaling networks. *Genes & development* **11**, 2295–2322 (1997).
43. Gurke, S. *et al.* Tunneling nanotube (TNT)-like structures facilitate a constitutive, actomyosin-dependent exchange of endocytic organelles between normal rat kidney cells. *Experimental cell research* **314**, 3669–3683, doi: 10.1016/j.yexcr.2008.08.022 (2008).
44. Lim, K. B. *et al.* The Cdc42 effector IRSp53 generates filopodia by coupling membrane protrusion with actin dynamics. *The Journal of biological chemistry* **283**, 20454–20472, doi: 10.1074/jbc.M710185200 (2008).
45. Schafer, C. *et al.* The key feature for early migratory processes: Dependence of adhesion, actin bundles, force generation and transmission on filopodia. *Cell adhesion & migration* **4**, 215–225 (2010).
46. Barzik, M., McClain, L. M., Gupton, S. L. & Gertler, F. B. Ena/VASP regulates mDia2-initiated filopodial length, dynamics, and function. *Molecular biology of the cell* **25**, 2604–2619, doi: 10.1091/mbc.E14-02-0712 (2014).
47. Hertzog, M. *et al.* Molecular basis for the dual function of Eps8 on actin dynamics: bundling and capping. *PLoS biology* **8**, e1000387, doi: 10.1371/journal.pbio.1000387 (2010).
48. Biran, A. *et al.* Senescent cells communicate via intercellular protein transfer. *Genes & development* **29**, 791–802, doi: 10.1101/gad.259341.115 (2015).
49. Frei, D. M. *et al.* Novel microscopy-based screening method reveals regulators of contact-dependent intercellular transfer. *Scientific reports* **5**, 12879, doi: 10.1038/srep12879 (2015).
50. Cunningham, D. L. *et al.* Novel binding partners and differentially regulated phosphorylation sites clarify Eps8 as a multi-functional adaptor. *PLoS one* **8**, e61513, doi: 10.1371/journal.pone.0061513 (2013).
51. Di Fiore, P. P. & Scita, G. Eps8 in the midst of GTPases. *The international journal of biochemistry & cell biology* **34**, 1178–1183 (2002).
52. Disanza, A. *et al.* Regulation of cell shape by Cdc42 is mediated by the synergic actin-bundling activity of the Eps8-IRSp53 complex. *Nature cell biology* **8**, 1337–1347, doi: 10.1038/ncb1502 (2006).
53. Logue, J. S. *et al.* Erk regulation of actin capping and bundling by Eps8 promotes cortex tension and leader bleb-based migration. *eLife* **4**, e08314, doi: 10.7554/eLife.08314 (2015).
54. Kanda, T., Sullivan, K. F. & Wahl, G. M. Histone-GFP fusion protein enables sensitive analysis of chromosome dynamics in living mammalian cells. *Current biology: CB* **8**, 377–385 (1998).
55. Nam, H. S. & Benzeval, R. High levels of Id1 expression define B1 type adult neural stem cells. *Cell stem cell* **5**, 515–526, doi: 10.1016/j.stem.2009.08.017 (2009).

Acknowledgements

We thank Jessica Vargas and Yuan-Ju Wu for technical help, and Guiliana Soraya Victoria and Brittany Mayweather for critical manuscript comments. We gratefully acknowledge the kind financial support of the Institut Pasteur (Paris), the France–BioImaging infrastructure network supported by the French National Research Agency (ANR-10-INSB-04, Investments for the future), and the Région Ile-de-France (program DIM-Malinf). We thank Dr. Jean-Yves Tinevez and Dr. Audrey Salles from Imagopole at Institut Pasteur for their help with microscopy imaging. We thank Dr. Sophie Novault from the Flow Cytometry Platform at Institut Pasteur for

her help with flow cytometry experiments. We thank Dr. Fabrice De Chaumont from the Bioimage Analysis Unit at Institut Pasteur for his help with the software: ICY. E.D. is a recipient of the Bourse Carnot-Pasteur Maladies Infectieuses and the Bourse Pasteur-Roux, Institut Pasteur. This work is supported by research grants from the Agence Nationale de la Recherche (ANR-14-JPCD-0002-01 and ANR-16-CE16-0019-Neurotunn), AIC RECH COLLECT CYANOBAC, and Equipe FRM (Fondation Recherche Médicale) 2014 (DEQ20140329557) to C.Z.

Author Contributions

C.Z. and E.D. conceived the project. E.D. designed the experimental plan. E.D., E.P., D.C.C., C.S., and S.S. performed the experiments. E.D., and C.Z. wrote the paper. All authors contributed to data analysis, discussions, and reviewed the paper.

Additional Information

Supplementary information accompanies this paper at <http://www.nature.com/srep>

Competing financial interests: The authors declare no competing financial interests.

How to cite this article: Delage, E. *et al.* Differential identity of Filopodia and Tunneling Nanotubes revealed by the opposite functions of actin regulatory complexes. *Sci. Rep.* **6**, 39632; doi: 10.1038/srep39632 (2016).

Publisher's note: Springer Nature remains neutral with regard to jurisdictional claims in published maps and institutional affiliations.



This work is licensed under a Creative Commons Attribution 4.0 International License. The images or other third party material in this article are included in the article's Creative Commons license, unless indicated otherwise in the credit line; if the material is not included under the Creative Commons license, users will need to obtain permission from the license holder to reproduce the material. To view a copy of this license, visit <http://creativecommons.org/licenses/by/4.0/>

© The Author(s) 2016

Article 1
Supplementary Material

**Differential identity of Filopodia and Tunneling Nanotubes revealed by the
opposite functions of actin regulatory complexes**

AUTHORS :

Elise Delage¹, Diégo Cordero Cervantes^{1,#}, Esthel Pénard^{1,#}, Christine Schmitt², Sylvie Syan¹, Andrea Disanza³, Giorgio Scita^{3,4}, Chiara Zurzolo^{1*}

¹ Unité Trafic Membranaire et Pathogénèse, Institut Pasteur, 25-28 Rue du Docteur Roux, 75724 Paris CEDEX 15, France

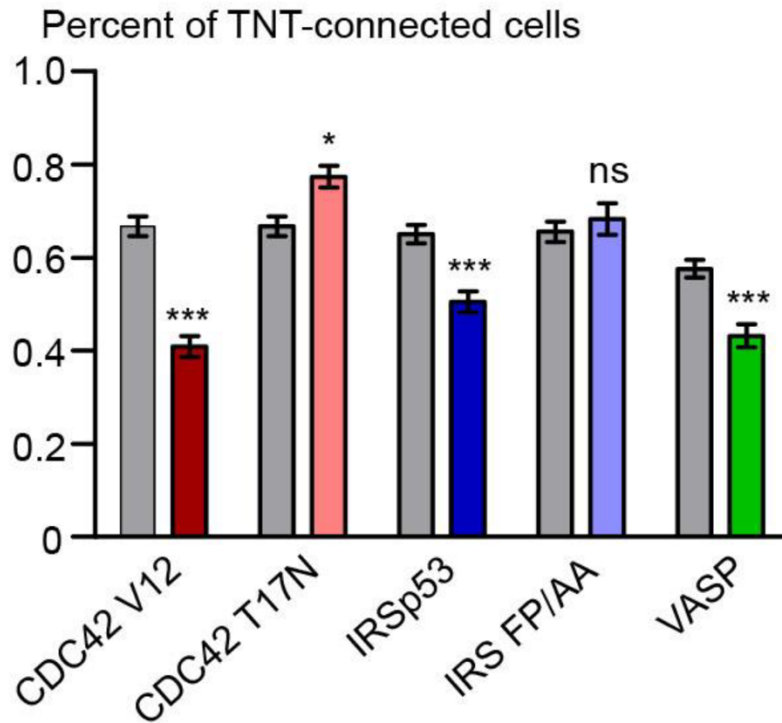
² Utrapole, Institut Pasteur, 25-28 Rue du Docteur Roux, 75724 Paris CEDEX 15, France

³ FIRC Institute of Molecular Oncology, 20139 Milan, Italy

⁴ Dipartimento di Scienze della Salute, Università degli Studi di Milano, 20122 Milan, Italy

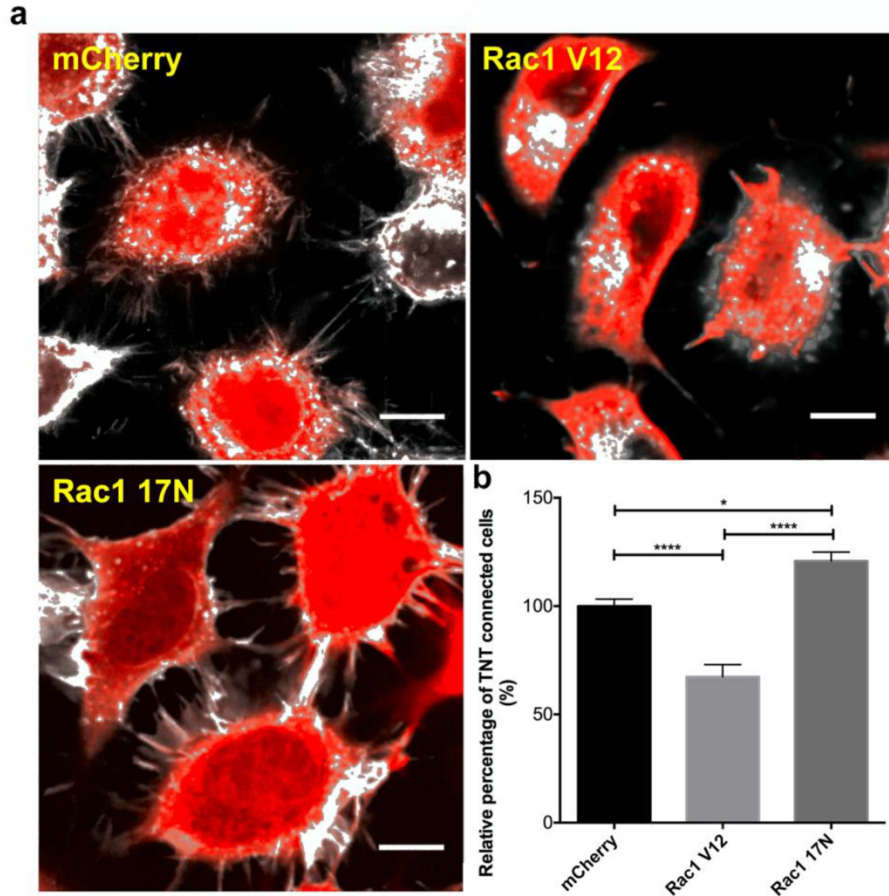
These authors contributed equally to this work

*corresponding author; e-mail: chiara.zurzolo@pasteur.fr



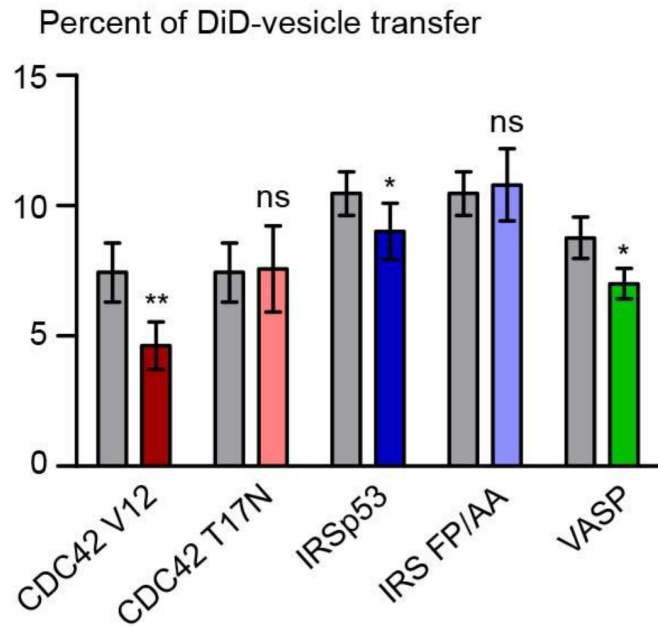
Supplementary Figure 1. CDC42, IRSp53, and VASP negatively regulate the number of TNT-connected cells.

Quantification of TNT-connected cells upon ectopic expression of GFP-CDC42 V12, GFP-CDC42 T17N, RFP-IRSp53, RFP-IRS FP/AA or GFPVASP (colored bars) compared to respective control (i.e. GFP or RFP, grey bars). The ratio of TNT-forming transfected cells/number of transfected cells was evaluated. Data represent the mean (\pm SEM) of at least 6 independent experiments. *P < 0.05; **P < 0.01; ***P < 0.001; ns = not significant.



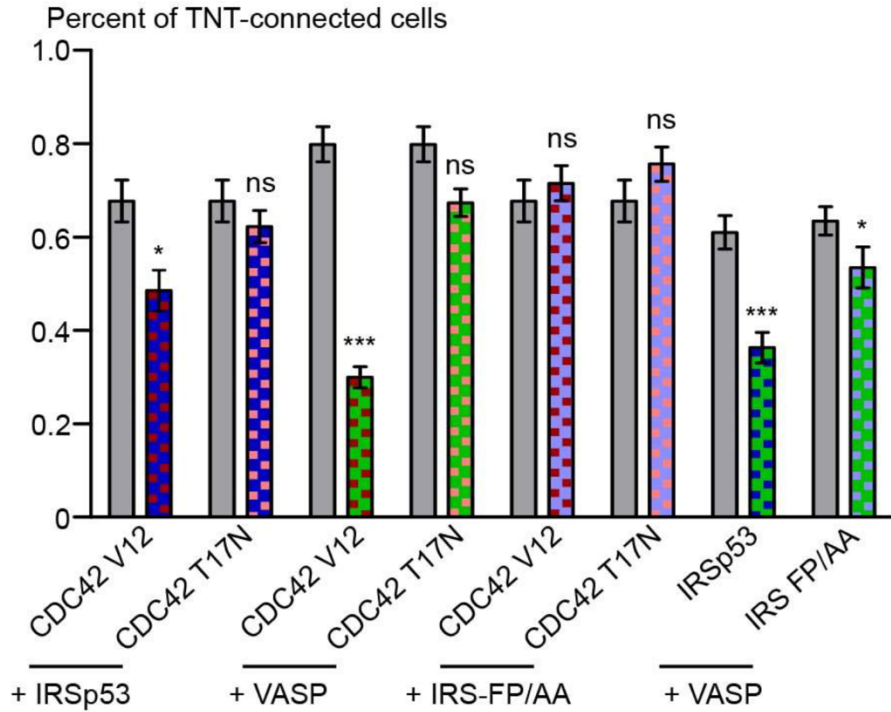
Supplementary Figure 2. Rac1 negatively regulates the number of TNT-connected cells.

a. Representative confocal images showing intercellular connections upon ectopic expression of Myc-Rac1 V12 (constitutively active form), Myc-Rac1 17N (dominant negative form), and their respective control, mCherry (red). Myc was detected by indirect immunofluorescence (red). Cells were observed by confocal microscopy. Scale bar = 10 μ M. b) Quantification of TNT-connected cells upon ectopic expression of mCherry, Myc-Rac1 V12, and Myc-Rac1 17N. The ratio of TNT-forming transfected cells/number of transfected cells was evaluated. Data represents the mean (\pm SEM), normalized to control cells (mCherry transfected cells) arbitrarily set at 100%, of 3 independent experiments. *P < 0.05; **P < 0.01; ***P < 0.001; ns = not significant.



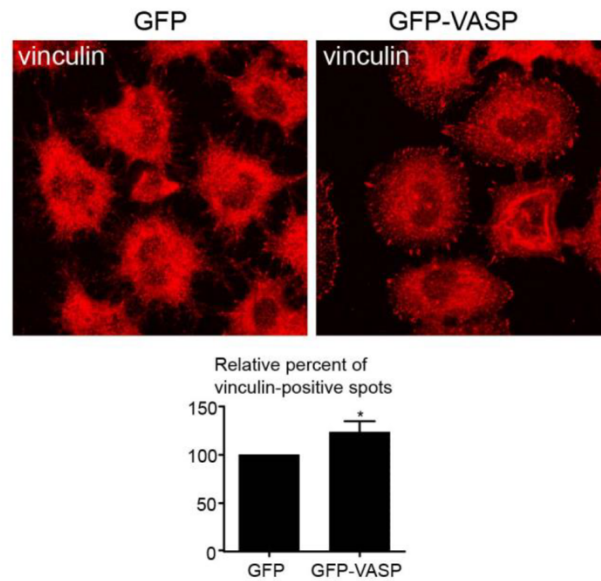
Supplementary Figure 3. CDC42, IRSp53, and VASP negatively regulate intercellular vesicle transfer.

Quantification by flow cytometry of DiD-positive acceptor cells upon ectopic expression of GFP-CDC42 V12, GFP-CDC42 T17N, RFP-IRSp53, RFP-IRS FP/AA or GFP-VASP (colored bars) in the donor population, compared to respective control (i.e. GFP or RFP, grey bars). The percentage of DiD-positive acceptor cells in the total cell population was evaluated. Data represent the mean (\pm SEM) of at least 4 independent experiments. *P < 0.05; **P < 0.01; ***P < 0.001; ns = not significant.



Supplementary Figure 4. CDC42, IRSp53, and VASP act as a network to negatively regulate the number of TNT-connected cells.

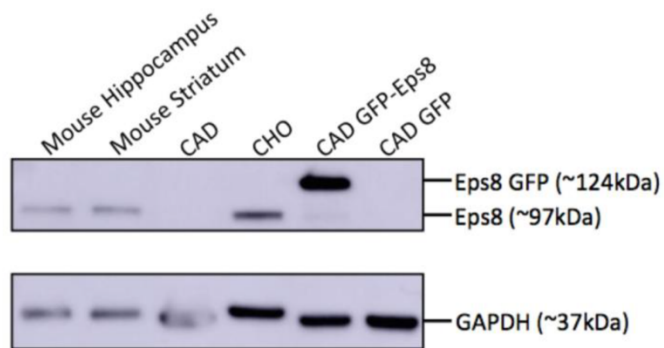
Quantification of TNT-connected cells upon co-transfection as indicated under the graph (colored bars) compared to respective controls (grey bars). Data represent the mean (\pm SEM) of at least 4 independent experiments. *P < 0.05; **P < 0.01; ***P < 0.001; ns = not significant.



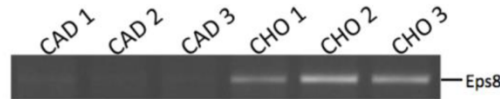
Supplementary Figure 5. Ectopic expression of VASP increases the number of vinculin-positive cellular protrusions

Cells were transiently transfected with GFP-VASP or GFP as a control. Cells were fixed 16 hrs post-plating and vinculin was detected by indirect immunofluorescence. The number of vinculin-positive peripheral focal adhesions was quantified using ICY. Data represent the mean (\pm SEM), normalized to control cells arbitrarily set at 100%, of at least 4 independent experiments. *P < 0.05.

a Western blot

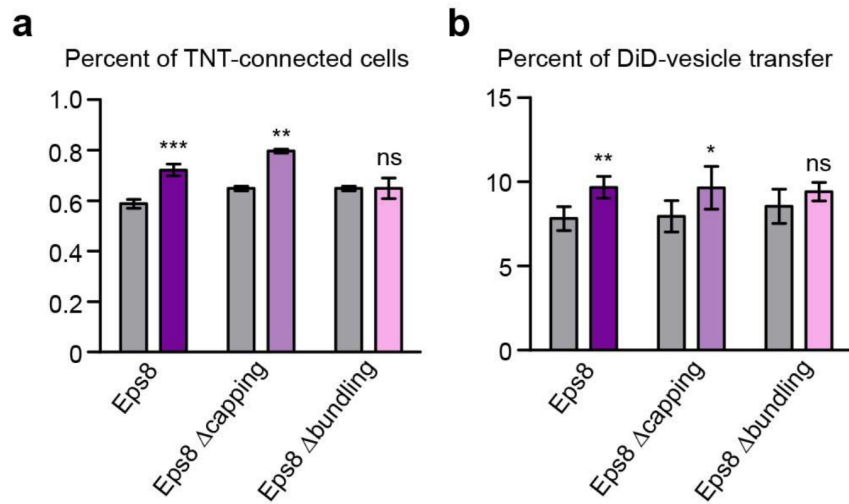


b RT-PCR



Supplementary Figure 6. Endogenous expression of Eps8 via western blotting and RT-PCR

a. Protein lysates from hippocampi and striata from mice at postnatal 21 days, CAD, CHO, CAD overexpressing GFP-Eps8, and CAD overexpressing GFP cells were immunoblotted for Eps8. 50 μ g of protein per lane. b. RT-PCR analysis of Eps8 mRNA in CAD and CHO cells.



Supplementary Figure 7. Eps8 positively regulates TNT formation and intercellular vesicle transfer via its bundling activity.

a. Quantification of TNT-connected cells upon ectopic expression of GFP-Eps8, GFP-Eps8 Δ capping or GFP-Eps8 Δ bundling (colored bars), compared to their respective control (grey bars). b. Quantification by flow cytometry of DiD-positive acceptor cells upon ectopic expression of GFP-Eps8, GFP-Eps8 Δ capping or GFP-Eps8 Δ bundling (colored bars) in the donor population, compared to respective control (grey bars). Data represent the mean (\pm SEM) of at least 3 independent experiments. *P < 0.05; **P < 0.01; ***P < 0.001; ns = not significant.

Chapter 3

3 Tunneling Nanotubes: Ultra-Structural Identity Missing Links

3.1 Results

Summary

For over a decade, TNTs have gained substantial attention as an inter-cellular communication mechanism, allowing the transport of cargo between distant cells. Since their discovery, studies have focused on their functional role but information regarding their ultrastructure and the differences between them and other cellular protrusions such as filopodia is still lacking.

Here, we report on the structural characterization of TNTs in neuronal cells of different species, using correlative light- and cryo-electron tomography approaches. We contrast their structural identity with that of filopodia by showing that most TNTs – shown by fluorescence microscopy to be single connections – are in fact made up of multiple, smaller, individual tunneling nanotubes (iTNTs), all of which contain long, parallel actin filaments, presumably serving as railways for the transport of vesicles and organelles also observed within iTNTs. Our electron tomograms suggest the existence of thin filaments and coils that connect iTNTs, which could serve to increase the mechanical stability of the overall bundle. We demonstrated the functionality of these structures by showing that nanotubes transported mitochondria using live confocal imaging, which we validated by observations of mitochondria within iTNTs by cryo-electron tomography. Furthermore, we employed FIB-SEM to produce 3D electron micrograph volumes with sufficient resolution to clearly identify that TNTs are ‘open’ at both ends (contact sites) and thus form a continuous cytoplasmic bridge between two cells.

Collectively, our findings provide the first structural description of TNTs, support published fluorescence microscopy evidence suggesting bi-directional TNT-mediated transport of cargo, and demonstrate that TNTs are distinct from other actin-containing cellular protrusions such as filopodia. We also employ an imaging workflow that improves upon, and avoids, previous limitations of tools used to study the anatomy of TNTs, such as classic SEM and TEM. Our strategy better preserves these fragile structures in native conditions, which may be useful for studying the role TNTs play in other cell types and physio/pathological models. This work is an essential step toward understanding TNT-mediated cell-to-cell communication and lays the groundwork for investigations into the spreading of pathogens such as viruses and misfolded proteins.

3.1.1 Aims of the project

- Design a strategy to study TNTs at the structural level by combining a series of EM approaches.
- Validate strategy in two neuronal cell lines, CAD (mouse) and SH-SY5Y (human) cells.
- Test the functionality of TNTs connecting SH-SY5Y cells by live-image analysis.
- Examine the F-actin cytoskeletal architecture of TNTs.
- Investigate whether cargo observed by light microscopy is present in/outside of TNTs.
- Identify similarities and differences in the structure of TNTs vs. filopodia.
- Examine whether TNTs are open-ended at each contact site via FIB-SEM.

3.1.2 Contribution

In this project, we designed and optimized a cryo-correlative electron microscopy (cryo-CLEM) approach to characterize the structure of TNTs at the nanometer resolution. I participated and contributed equally with the other two first authors in different aspects of the study. Specifically, I studied the role of Arp2/3 in the formation of neuronal TNTs by testing an Arp2/3 specific inhibitor (CK-666) in CAD cells. To this end, I performed the experiments, acquired the images, and manually analyzed the data collected to prepare Supplementary Figure 3c-3d. Setting up these experiments was fundamental for this project as CK-666 treatment of cells was used to increase the yield of TNTs on cryo-EM grids. I also labeled-, imaged-, and identified regions of interest (filopodia emanating from CAD cells) for the cryo-CLEM/cryo-electron tomography micrographs shown in Figure 5. I also obtained the cryo-TEM micrographs shown in Supplementary Figure 6, performed all the live-imaging experiments in the manuscript and implemented a plugin to analyze the speed of mitochondrial transport via TNTs (see Figure 6 and Supplementary Figure 5). I assisted with the manual analysis of cryo-ET images by computing plot profiles and fast Fourier transforms described in the manuscript and shown in Figure 4 and 5. Moreover, I contributed to the manual segmentation of TNTs in FIB-SEM volumes and re-processing electron micrographs throughout the manuscript for the preparation of figures (i.e. image stitching, alignment, enhancement, and addition of overlays and tracings). I designed and created the schematic diagrams found in Figure 1a and Figure 8. My role also included teaching

one of the co-first authors (i) the protocols employed to study the effect of CK-666 in CAD cells' adherent filopodia and TNT function (see Supplementary Figure 3a-3b and 3e-3f); and (ii) the methods used to prepare samples for cryo-TEM and identification of TNTs on EM grids. Finally, I wrote the manuscript, assembled all the main and Supplementary Figures, as well as Supplementary Movies. I assembled, revised, submitted, and handled the manuscript throughout the three rounds of peer revision until publication of the article.


3.1.3 Article 2: Correlative cryo-electron microscopy reveals the structure of TNTs in neuronal cells

ARTICLE

<https://doi.org/10.1038/s41467-018-08178-7>

OPEN

Correlative cryo-electron microscopy reveals the structure of TNTs in neuronal cells

Anna Sartori-Rupp¹, Diégo Cordero Cervantes², Anna Pepe², Karine Gousset ^{2,3}, Elise Delage², Simon Corroyer-Dulmont¹, Christine Schmitt¹, Jacomina Krijnse-Locker¹ & Chiara Zurzolo²

The orchestration of intercellular communication is essential for multicellular organisms. One mechanism by which cells communicate is through long, actin-rich membranous protrusions called tunneling nanotubes (TNTs), which allow the intercellular transport of various cargoes, between the cytoplasm of distant cells *in vitro* and *in vivo*. With most studies failing to establish their structural identity and examine whether they are truly open-ended organelles, there is a need to study the anatomy of TNTs at the nanometer resolution. Here, we use correlative FIB-SEM, light- and cryo-electron microscopy approaches to elucidate the structural organization of neuronal TNTs. Our data indicate that they are composed of a bundle of open-ended individual tunneling nanotubes (iTNTs) that are held together by threads labeled with anti-N-Cadherin antibodies. iTNTs are filled with parallel actin bundles on which different membrane-bound compartments and mitochondria appear to transfer. These results provide evidence that neuronal TNTs have distinct structural features compared to other cell protrusions.

¹Institut Pasteur, Unit of Technology and Service Ultra-structural Bio-Imaging, 28 rue du Docteur Roux, 75015 Paris, France. ²Institut Pasteur, Membrane Traffic and Pathogenesis, 28 rue du Docteur Roux, 75015 Paris, France. ³Present address: Department of Biology, College of Science and Math, California State University, Fresno, 2555 East San Ramon Avenue M/S SB73, Fresno, CA 93740-8034, USA. These authors contributed equally: Anna Sartori-Rupp, Diégo Cordero Cervantes, Anna Pepe. Correspondence and requests for materials should be addressed to C.Z. (email: chiara.zurzolo@pasteur.fr)

Tunneling nanotubes (TNTs) have been defined as long, thin, non-adherent membranous structures that form contiguous cytoplasmic bridges between cells over long and short distances ranging from several hundred nm up to 100 μm ^{1–4}. Over the last decade, scientific research has effectively improved our understanding of these structures and underscored their role in cell-to-cell communication, facilitating the bi- and unidirectional transfer of compounds between cells, including: organelles, pathogens, ions, genetic material, and misfolded proteins⁵. Altogether, *in vitro* and *in vivo* evidence has shown that TNTs can be involved in many different processes such as stem cell differentiation, tissue regeneration, neurodegenerative diseases, immune response, and cancer^{2,6–10}.

Although these *in vitro* and *in vivo* studies have been informative, the structural complexity of TNTs remains largely unknown. One of the major issues in this field is that many types of TNT-like connections have been described using mainly low-resolution imaging methods such as fluorescence microscopy (FM). As a result, information regarding their structural identity and if or how they differ among each other and with other cellular protrusions such as filopodia, is still lacking. As a result, TNTs have been regarded with skepticism by one part of the scientific community^{5,11}.

Two outstanding questions are whether these protrusions are different from other previously studied cellular processes such as filopodia¹² and whether their function in allowing the exchange of cargos between distant cells is due to direct communication between the cytoplasm of distant cells or to a classic exocytosis process or a trogocytosis event^{13,14}.

Addressing these questions has been difficult due to considerable technical challenges in preserving the ultrastructure of TNTs for electron microscopy (EM) studies. To date, only a handful of articles have examined the ultrastructure of TNTs using scanning and transmission EM (SEM and TEM, respectively)^{1,15–18}, and no correlative studies have been performed to ensure that the structures identified by TEM/SEM represent the functional units observed by FM.

Although very similar by FM, TNT formation appears to be oppositely regulated by the same actin modifiers that act on filopodia¹⁹. Furthermore, filopodia have not been shown to allow cargo transfer^{12,20,21}. Thus, we hypothesize that TNTs are different organelles from filopodia and might display structural differences in morphology and actin architecture.

In order to compare the ultrastructure and actin architecture of TNTs and filopodia at the nanometer resolution we employed a combination of live imaging, correlative light- and cryo-electron tomography (ET) approaches on TNTs of two different neuronal cell models, (mouse catecholaminergic CAD cells and human neuroblastoma SH-SY5Y cells)^{19,22–25}. We found that single TNTs observed by FM are in most cases made up of a bundle of individual TNTs (iTNTs), each surrounded by a plasma membrane and connected to each other by bridging threads containing N-Cadherin. Each iTNTs appeared filled by one highly organized parallel actin bundle on which vesicles, mitochondria, and other membranous compartments appear to be traveling. Finally, by using correlative focused-ion beam SEM (FIB-SEM) we show that TNTs can be open on both ends, thus challenging the dogma of a cell as an individual unit²⁶.

Collectively, our data demonstrates that TNTs connecting neuronal cells are different cellular structures from other membrane protrusions, identifies the structural features that characterize this specific organelle, and supports their role in allowing direct communication between the cytosol of distant cells and cargo transfer.

Results

Ultrastructural analysis of TNTs reveals individual TNTs. TNTs connections reported between different cells in culture appear to be very heterogeneous at the resolution of FM²², therefore their structural identity is unclear. The elective method to study the ultrastructure of organelles and cellular features is correlative light- and electron microscopy. However initial attempts to analyze TNTs in neuronal CAD cells (Supplementary Fig. 1a)^{19,22} by most routinely used correlative SEM showed that most TNTs broke during sample preparation (Supplementary Fig. 1b–e, g, h). Only few, thick, more robust TNTs were preserved (Supplementary Fig. 1f)^{1,15,16}. Intriguingly, some of the broken structures appeared to be comprised of multiple smaller tubes (yellow arrowheads, Supplementary Fig. 1e, h).

To better preserve these fragile structures, we established correlative assays by combining cryo-FM with cryo-electron microscopy (cryo-EM) and cryo-electron tomography (cryo-ET) (see workflow in Fig. 1a). FM was used to screen for long ($\geq 10 \mu\text{m}$) and direct cell-to-cell connections labeled with wheat-germ agglutinin (WGA) hovering over the substrate, a phenotypic criterium used to identify TNTs^{1,2,19,23,27}. Two correlative light and electron microscopy (CLEM) approaches were employed to image cells grown on EM grids: i-CLEM and ii-CLEM (see material and methods, Fig. 1a). By i-CLEM, we found that most TNTs which appeared as one tube under FM and low-magnification cryo-TEM (Fig. 1b–c) were comprised of a bundle of individual tunneling nanotubes (iTNTs) (Fig. 1d–h), each delimited by its own plasma membrane, as suggested by our SEM images (Supplementary Fig. 1d, e). iTNTs contained actin filaments and ran mostly parallel to and occasionally braided over each other (Fig. 1e, g). We also observed that their tips originated from opposite directions, suggesting that they were in the process of extending to other cells or retracting from opposite cells (red stars, Fig. 1f, h). Single thicker TNTs (600–900 nm in diameter), were rarely observed (Supplementary Fig. 1i–l).

TNTs have previously been reported to transfer vesicles, organelles, and various cargoes between cells by FM and live imaging^{2,4,5,22} however, whether these cargoes were transported through the TNT lumen or by surfing on the limiting membrane, as shown for viruses on filopodial bridges²⁸, could not be shown due to the resolution limitations of FM. By cryo-EM, we were able to observe vesicular membrane compartments located inside and between iTNTs. Inside TNTs, vesicles were heterogeneous in size and shape, spanning from single-membrane spherical vesicles (yellow arrowheads, Fig. 1g, h and Supplementary Fig. 2a–e, 2g) with an average diameter of 109 nm (SD = 25 nm) (Supplementary Fig. 2i), to multi-vesicular compartments (blue arrowheads, Supplementary Fig. 2f, h). This observation supports our previous FM-based studies in CAD cells showing TNT-mediated transfer of DiD-labeled vesicles, lysosomes, and aggregated proteins between cells^{7,22,27}, and indicates that transfer occurs through the iTNT lumen. Intriguingly, we also observed vesicles inside iTNTs with tips having opposite orientations (green arrowheads indicate vesicles, and red stars show the tips of tubes, Fig. 1h). This finding suggests that transport is unidirectional within each iTNT having an antiparallel orientation (see discussion). Vesicles found externally were enclosed by a double membrane (turquoise arrowheads, Fig. 1g and Supplementary Fig. 2e, h), suggesting that they resulted from single-membrane vesicles budding off the plasma membrane of an iTNT. Several vesicles coupled together surrounded by an outer membrane were also observed outside iTNTs (pink arrowheads, Fig. 1h and Supplementary Fig. 2b, c), which might be explained by a membrane pinch-off or a break of the iTNT containing them.

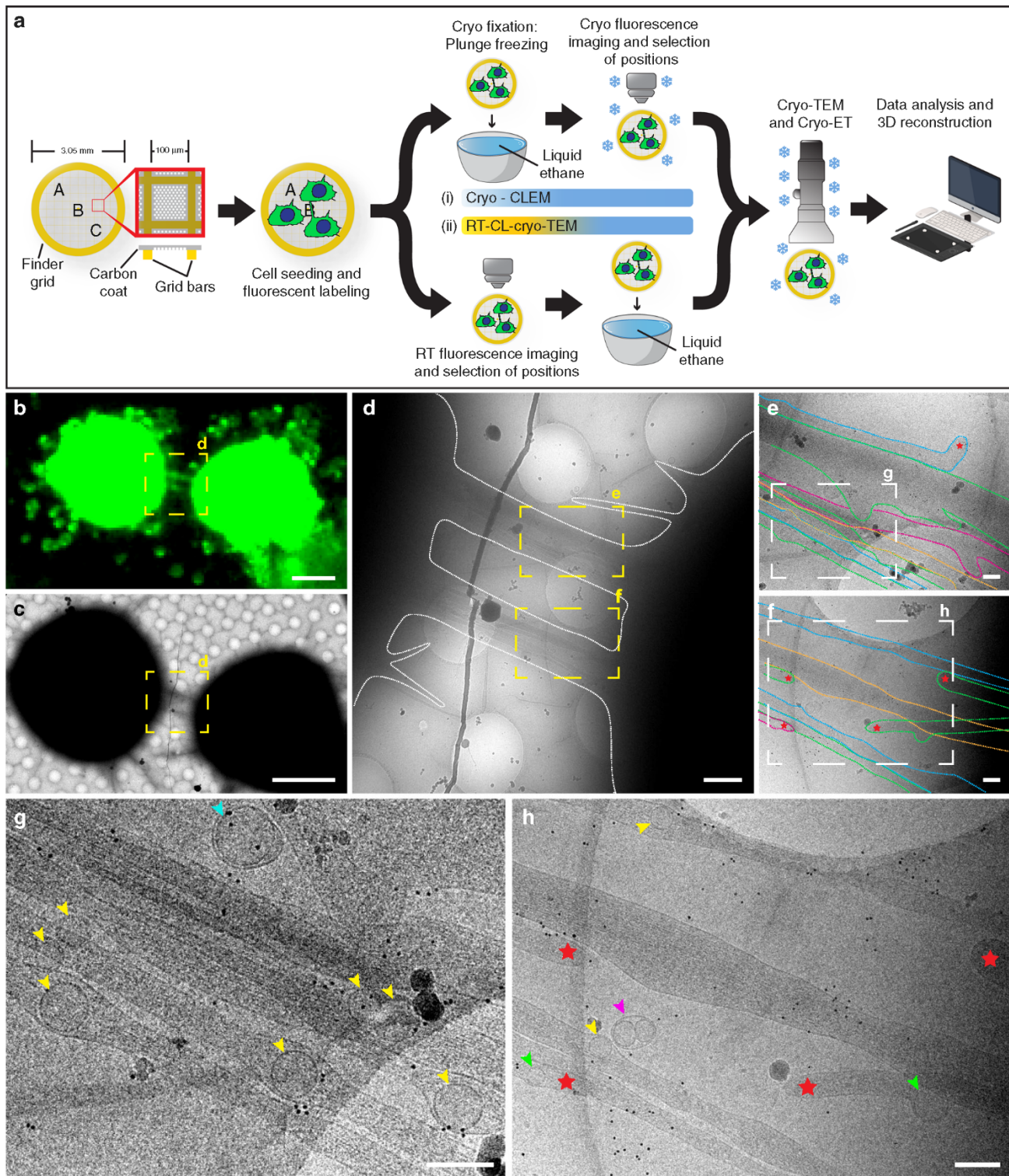


Fig. 1 Correlated light and cryo-electron microscopy strategies reveal individual TNTs. **a** A schematic diagram of the experimental workflow and approaches used to observe TNT-connected CAD cells by cryo-TEM. **b** Cryo-FM image of two CAD cells connected by a TNT stained with WGA (green). **c** Cells in **b** observed in cryo-TEM at low magnification. Yellow dashed squares in **b**, **c** are shown at intermediate magnification in **d**. Yellow dashed rectangles in **d** are shown at high magnification in **e** and **f**, respectively. The plasma membrane of individual TNTs (iTNTs) were drawn with dotted colored lines in **e** and **f** to show membrane boundaries. Enlargements of white dashed rectangles in **e** and **f** are shown in **g** and **h**, respectively. **g**, **h** Various vesicular compartments were observed within and between iTNTs: yellow arrowheads show single vesicles; pink arrowheads show vesicles surrounded by an outer membrane; turquoise arrowheads show vesicles enclosed by a double membrane. Red stars in **e**, **f**, and **h** show tips of iTNTs extending/retracting from neighboring cells. Green arrows indicate vesicles inside extending/retracting iTNT tips observed in **h**. Scale bars: **b**, **c**, 10 µm; **d**, 1 µm; **e**–**h**, 200 nm

Overall, these data support that iTNTs correspond to the FM definition of TNTs. However, the number of TNTs imaged by cryo-CLEM was not sufficient for quantitative analysis, therefore we established a variant workflow by chemically fixing CAD cells and imaging them by FM at room temperature prior to rapid freezing and cryo-TEM (ii-CLEM) (Fig. 1a). Importantly, cryo- and chemically fixed samples (i.e., i-CLEM vs. ii-CLEM) (Supplementary Fig. 1m–1p)²⁹ structural details looked indistinguishable.

N-Cadherin decorates threads holding iTNTs in a bundle. Our previous data demonstrated that TNTs and filopodia in CAD cells are regulated by the same actin modifiers but in an opposite manner¹⁹. Thus, to further increase the number of TNTs on TEM grids, we used CK-666, an Arp 2/3 complex inhibitor previously shown to inhibit filopodia³⁰, which, based on our hypothesis, should increase TNTs. Indeed, our quantitation of adherent filopodia and TNT-connected cells^{19,31} showed that CK-666 inhibits the formation of adherent filopodia (Supplementary Fig. 3a, b), and increased the number of cells connected via TNTs (Supplementary Fig. 3c, d). TNTs in CK-666-treated CAD cells showed no detectable structural differences in cryo-TEM compared to the untreated control (Supplementary Fig. 3g–j). Importantly, we also show that CK-666-induced TNTs are functional (i.e., able to support transfer) by using an assay which consists of monitoring the transfer of DiD-labeled vesicles between a donor-acceptor cell co-culture^{19,23,27} (Supplementary Fig. 3e, f).

Therefore, we used these conditions and cryo-ET to elucidate (i) the spatial and structural arrangement of iTNTs with respect to each other, (ii) the actin organization inside tubes, and (iii) better characterize the vesicular compartments located inside iTNTs. TNTs were comprised of 2 to 11 iTNTs with a bundle diameter between 145 and 700 nm (305 nm on average). Each iTNT had an average diameter of 123 nm (SD = 66 nm). While the majority of iTNTs (~95%) had a diameter of less than 200 nm (Fig. 2a), thicker iTNTs (up to 550 nm) were occasionally observed as part of a bundle of two or more iTNTs. The spacing between individual tubes ranged between 8 and 90 nm for parallel iTNTs, while for less parallel iTNTs the spacing increased to 200 nm. Ninety percent of these distances in parallel iTNTs ranged between 8 and 60 nm (Fig. 2b).

This peculiar arrangement prompted us to ask the question of how individual iTNTs (Fig. 2c–f and Supplementary Movie 1) could be held together and remain bundled to form this unique TNT structure. Along the regions imaged by cryo-ET, we observed thin structures connecting the plasma membrane of two or more iTNTs (turquoise arrows, Fig. 2g, h, and Supplementary Movies 2 and 3). We speculate that N-Cadherin, a transmembrane adhesion protein previously observed inside the TNTs of other cell types³², could be responsible for the formation of these linkers. To test this hypothesis, we first confirmed the presence of N-Cadherin in TNTs of CAD cells using FM (Supplementary Fig. 4a). Next, we employed cryo-ET on N-Cadherin immunogold-labeled samples (Supplementary Movie 4). Interestingly, we observed that the thin linkers connecting iTNTs were positively labeled for N-Cadherin (green arrowheads, Fig. 3a–c and Supplementary Fig. 4b, c).

Furthermore, tomograms slices shown in Fig. 2g, i–k also suggested that iTNTs were held together by long threads that coiled around them (green arrows, Fig. 2g, k, (right), and Supplementary Movie 5). These threads were also observed in native frozen conditions, excluding the possibility they were merely chemical fixation artifacts. Of interest, we found N-Cadherin gold labeling at the contact points between these threads and the iTNT surface (Fig. 3b). Taken together, our data

suggests that N-Cadherin holds iTNTs together and presumably provides stability for the overall bundle of iTNTs.

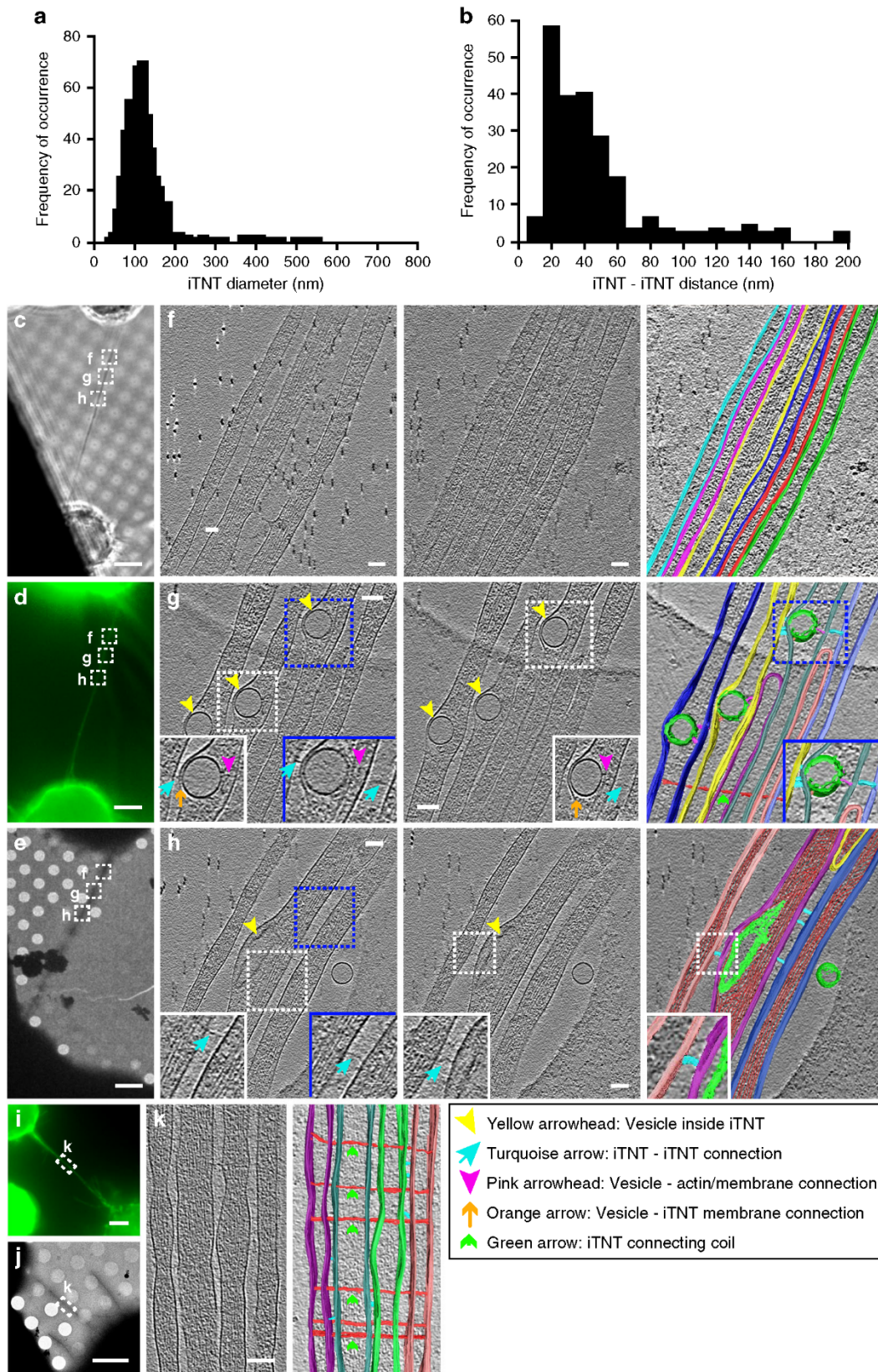
Another open question in the field is how cargo moves inside TNTs. Vesicles inside iTNTs were typically located between the plasma membrane and the actin bundle of parallel filaments, which filled the entire volume of the tube. Because the vesicle size often exceeded the diameter of the individual tube, they frequently bulged out from the plasma membrane, squeezing the actin filaments (Figs. 1g, h, 2g, h, and Supplementary Fig. 2a–f). By cryo-ET, we observed thin electron-dense structures that presumably connected intracellular vesicles to actin filaments (pink arrowheads, Fig. 2g), and short (~10 nm) spike-like structures that seemed to link vesicles to the plasma membrane on the opposite side of the actin bundle (orange arrows, Fig. 2g).

These observations are consistent with the hypothesis that vesicles move inside TNTs on actin filaments using myosin motors^{1,27} and with the fact that different myosin motors have been found in TNTs by FM^{1,5,33–35}. We decided to investigate the localization of one unconventional myosin motor, Myo10, as it was shown to increase TNT number and transfer of vesicles when overexpressed in CAD cells²⁷. By applying our correlative approach (ii-CLEM) on GFP-Myo10-transfected cells, (Fig. 3d), we located Myo10 inside TNTs and associated to vesicular compartments. (Fig. 3e–h and Supplementary Movies 6 and 7). While the mechanism by which Myo10 increases TNT formation needs to be further investigated, the co-localization of Myo10 with vesicular structures inside iTNTs supports its role in motoring cargo on actin filaments inside TNTs²⁷.

Another related question is whether transfer of vesicles is unidirectional or bidirectional. Within iTNTs, actin was organized in long bundles of filaments running parallel to each other (Figs. 2f–h, k, 3b, c, f, g, and Supplementary Movies 1–7). Due to beam damage, an inherent technical limitation of cryo-TEM, we were not able to image the actin bundle along the entire length of iTNTs. However, by imaging non-consecutive 1.2–1.5 μm -long regions of iTNTs, each iTNT contained an uninterrupted parallel actin bundle extending along the whole length of the area imaged. This strongly suggests that each iTNT contains a single continuous bundle of parallel actin filaments. Actin bundles filled the entire lumen of iTNTs with a diameter of <300 nm (Figs. 1g, h, 2f–h, k, and 4a) and although we could not address the polarity of the filaments we speculate that the actin bundle polarity remains the same within each iTNT but could feature opposite polarities in different, parallel, iTNTs (as shown in Fig. 1h). Tracing plot profiles and performing Fourier power spectra analysis on our cryo-CL-ET estimated the average distance between the center of adjacent actin filaments in bundles at 10 nm (SD = 0.8 nm) and 4.7 nm (SD = 1.1 nm) between their surfaces (Fig. 4a–f and Supplementary Movie 8).

We further examined cross-sections of iTNTs and found that actin filaments inside iTNTs were arranged in hexagonal arrays, with a 9.9 nm distance between the center of adjacent actin filaments (SD = 1.6 nm), and 5.1 nm (SD = 1.4) between their surfaces (Fig. 4g, h).

Filopodia show different structural features compared to TNTs. The structures we described above as TNTs appeared different compared to filopodia previously studied by cryo-ET^{36,37} for two main reasons: (i) filopodia are usually isolated and do not run in inter-connected bundles; (ii) filopodia do not contain vesicular structures or organelles. However, filopodia were never studied in CAD cells at the ultrastructural level. Thus, we decided to use our cryo-EM approach to analyze the structure of filopodia in CAD cells to directly compare them with TNTs. To increase filopodia number on TEM grids, CAD cells were transfected with the vasodilator-stimulated phosphoprotein



(VASP), a protein previously shown to be an effective inducer of filopodia in different cells^{12,19,27}. Importantly, filopodia induced by VASP looked indistinguishable from those of untreated cells at the ultrastructural level (Fig. 5a–i).

As previously reported for other cell types^{36,37} we did not observe vesicles or other organelles inside the filopodia of CAD cells. Furthermore, unlike TNTs, filopodia in CAD cells were never in bundles. Instead, they were single isolated protrusions,

Fig. 2 Imaging iTNTs in 3D using correlated light and cryo-electron tomography. **a** iTNT diameter distribution in nm. **b** Distribution of the distance between parallel and non-parallel iTNTs in nm. CAD cells connected by a TNT stained with WGA (green) imaged by phase contrast (**c**), epifluorescence (**d**), and low-magnification TEM (**e**). Dashed squares over the TNT in **c–e**, denoted **f–h**, correspond to non-consecutive high-magnification cryo-ET slices (**f–h**, left, middle, and Supplementary Movies 1–3). **f–h** (right) Rendering of tomograms (Supplementary Movies 1–3, respectively). Turquoise arrows in **g** and **h**, left, middle show filaments connecting iTNTs. Vesicles within iTNTs (yellow arrowheads, **g** and **h**, left, middle) use thin filaments to connect to the plasma membrane on one side (orange arrows, **g** left, middle) and actin on the other (pink arrowheads, **g** left, middle). Additional example of cells connected by a TNT is shown in **i** (epifluorescence) and **j** (low-magnification TEM). Region denoted by a white dashed rectangle in **i–j** is shown at high-magnification cryo-TEM in **k** left. **k** right, rendering of **k**, left (Supplementary Movie 5). Thin filaments connect the bundle of iTNTs by coiling around them (green arrows, **g** and **k** (rendering)). Source data for **a, b** are provided as a Source Data file. Scale bars: **c–e, i–j**, 5 μm ; **f–h, k**, 100 nm

(straight, bent, or twisted around other single filopodia (Fig. 5b, c, e, f, h, i, k–m and Supplementary Movie 9–12)) with an average diameter of 174.9 nm, ranging between 118.3 and 285.5 nm.

As previously described for other neuronal cell lines³⁷, actin filaments were mostly organized in tight parallel bundles that extended into the tip of the filopodium (Fig. 5b, c, e, f, h, i, k–o, and Supplementary Movies 9–12). Although the average diameter of filopodia is within the range of the average diameter of iTNTs (i.e., 174 vs. 123 nm, respectively), differently from TNTs, filopodia's actin filaments did not run uninterrupted along the whole length of the area imaged (1.2–1.5 μm). Instead, they were organized in bundles comprised of shorter filaments with a length varying between 300 and 1100 nm, with only 15% having a length longer than 1 μm (Fig. 5k–m). Alternatively, filopodia also displayed short parallel actin bundles (Fig. 5b, k–l, and Supplementary Movies 9 and 12) that intermingled with short-branched filaments (red arrowheads, Fig. 5b, h, and Supplementary Movies 9 and 11). This latter arrangement was never observed in TNTs, but was similar to what was previously shown for filopodial conformations in *Dyctostelium discoideum* amoebae³⁶.

In agreement with results reported by Aramaki et al.³⁷, in a different neuronal cell line, the average distance between the centers of adjacent actin filaments in bundles was 10.4 nm (SD = 0.4 nm) and 4.7 nm (SD = 0.7 nm) between their surfaces (Fig. 5o–r). This is similar to the estimate obtained for actin bundles within iTNTs (Fig. 4c–e), suggesting that although the overall actin configuration is different in iTNTs, the distance between parallel actin filaments in both structures is maintained. By observing cross-sections of filopodia, the actin bundle diameter ranged between 80 and 170 nm and the number of filaments per bundle ranged between 38 and 150. Moreover, actin filaments in filopodia were bundled by cross-linkers arranged in hexagonal arrays comprised of 12–30 filaments, with a ~4.7 nm distance between their surfaces (Fig. 5 k–s). A similar actin-bundling hexagonal pattern was previously shown to be mediated by the actin-binding protein fascin³⁷.

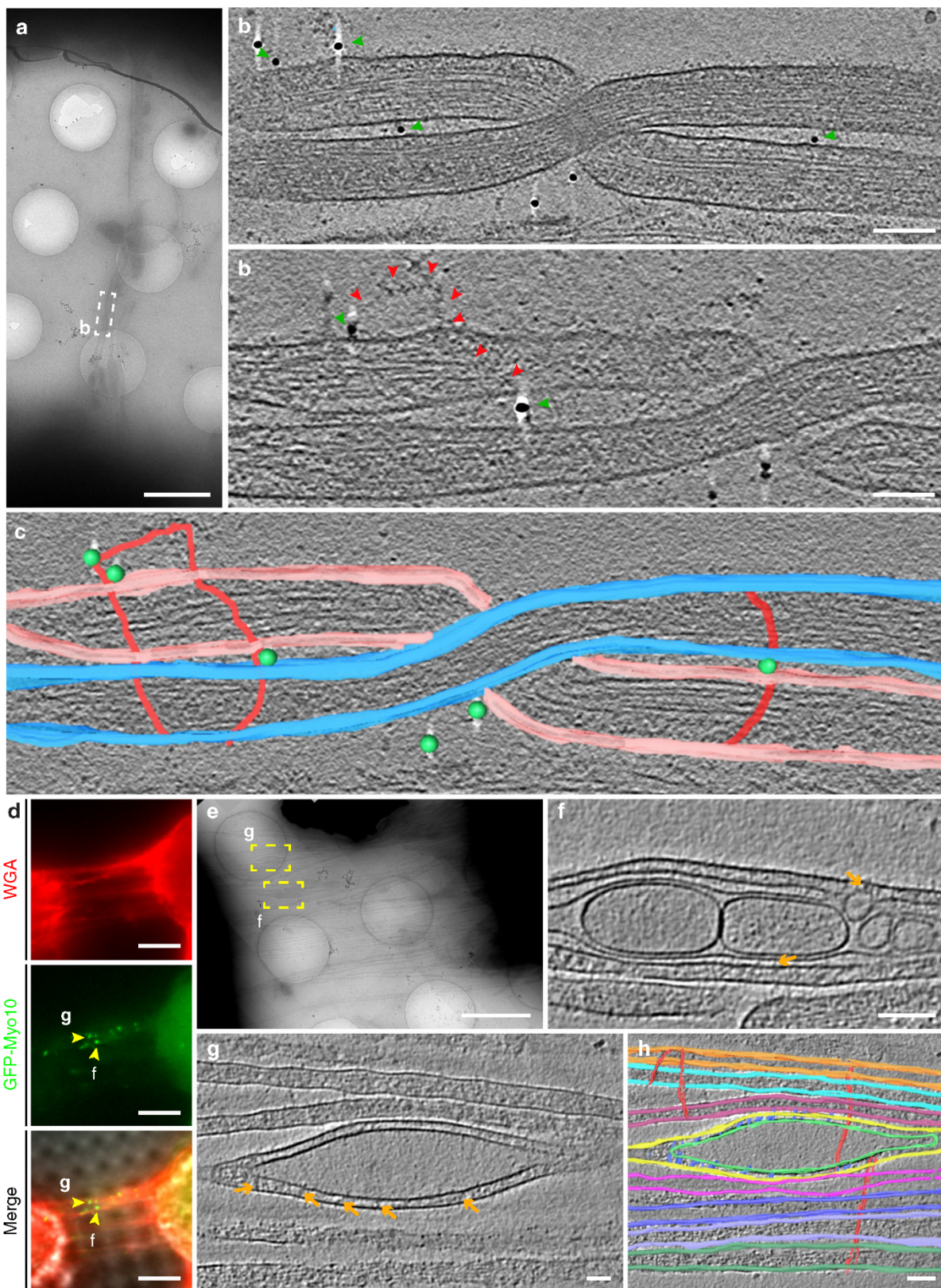
TNTs in SH-SY5Y cells are made of functional iTNTs. While the data presented above unequivocally demonstrates that TNTs are specialized structures in CAD cells, one of the issues in the field of TNTs is the heterogeneity of TNT-like structures observed in different cell types. Due to the diffraction limit of resolution in FM, it is not clear whether the heterogeneity in TNTs reflects a real ultrastructural difference, or whether different cellular features are being reported and are all named TNTs, although possibly referring to different structures. To confirm that the structural characteristics of TNTs described above are not cell-type specific, a neuronal cell model of human origin, SH-SY5Y cells, previously shown to connect via TNTs using FM, was investigated next^{4,24,25} (Supplementary Fig. 5a). To investigate the nature of TNTs connecting SH-SY5Y cells we first analyzed them by SEM. Similar to CAD cells, thicker TNTs appeared to endure harsh classic EM sample preparation steps (red

arrowhead, Supplementary Fig. 5b), while thinner structures would often break (yellow arrowheads, Supplementary Fig. 5c, d, e). Compared to CAD cells, however, more thin structures connecting SH-SY5Y cells survived classical embedding conditions (blue arrowheads, Supplementary Fig. 5e). By employing CLEM approaches on this cell model, TNTs connecting SH-SY5Y cells were also comprised of bundles of two or more iTNTs (Fig. 6a–e) while single thick connections were occasionally observed (Supplementary Fig. 5f–i). iTNTs connecting SH-SY5Y cells had an average diameter of 120.7 nm (SD = 71.4 nm) (Fig. 6f) and contained vesicular compartments (yellow arrowheads, Figs. 6d–e), with an average diameter of 104 nm (SD = 57.8 nm) (Fig. 6g). Importantly, control experiments demonstrated that iTNTs connecting SH-SY5Y cells fixed by rapid freezing were virtually identical to those chemically fixed, as in CAD cells (Supplementary Fig. 5j–m).

In order to demonstrate that the structures identified by cryo-CLEM in SH-SY5Y cells were functional, we examined whether they also transferred cargoes. In addition to vesicles, TNTs are able to transfer mitochondria between connected cells^{4,38–40}. Compared to DiD-labeled vesicles, mitochondria are particularly bright when fluorescently labeled and, therefore, well suited to be imaged by live microscopy^{41,42}. When cells labeled with WGA (green) and MitoTracker (red) were recorded by live cell imaging, mitoTracker-positive puncta moved inside a TNT in a unidirectional fashion at an average velocity of 0.05 $\mu\text{m}/\text{s}$ (SD = 0.03 $\mu\text{m}/\text{s}$) (Fig. 6h and Supplementary Movie 13). As previously reported for PC12 cells⁴¹, mitochondria did not move through the TNT at a uniform speed and seemed to accelerate in segments where the TNT appeared to be completely straight. As exemplified in Supplementary Movie 14, labeled mitochondria traveled all along an iTNT and accumulated in the cytoplasm of the neighboring cell (blue arrowhead, Supplementary Fig. 5n and Supplementary Movie 14).

The presence of mitochondria inside iTNTs was confirmed at the ultrastructural level by ii-CLEM and cryo-ET. By cryo-ET, the mitotracker labeled structures seen by FM (Fig. 6i–k) were mitochondrial cristae based on their size, shape, and presence of mitochondrial cristae (Figs. 6m–o and Supplementary Movie 15). Intriguingly, mitochondria were only observed in one of the iTNTs. As with vesicles, mitochondria also created a bulge in the iTNT containing it (Fig. 6l, n, o, and Supplementary Fig. 5o–s). Altogether, this data demonstrates that the structure of functional TNTs (i.e., allowing transfer of cargoes inside their lumen) is similar between CAD and SH-SY5Y cells, two different neuronal cell models from different origins and species.

Open-ended-TNTs connect the cytoplasm of cells. Given that vesicles and larger organelles such as lysosomes and mitochondria can transfer via TNTs^{4,5,7}, it is conceivable that TNTs are required to be open at the cell contact site. This notion, however, remains controversial, as it has not been sufficiently supported by ultrastructural data^{1,11,15}. Cryo-ET was not suitable to address



this question as the connecting regions between TNTs and cell bodies were too thick (>500 nm in thickness) to be investigated by TEM (Supplementary Fig. 6a–c). To generate 3D EM images that enable the analysis of TNT-to-cell contact sites we therefore employed correlative focus ion beam SEM (FIB-SEM) tomography on both CAD and SH-SY5Y cells.

TNTs connecting CAD cells were first identified by FM (Fig. 7a) and subsequently imaged by FIB-SEM. Under the imaging conditions used, the resolution of our tomograms was sufficient to discern plasma membrane boundaries of cells and TNTs. Manually segmented tomogram renderings (right panel, Fig. 7a) and volume renderings created with the Amira

Fig. 3 Ultrastructural analysis of N-cadherin and Myo10 in iTNTs. **a** Low-magnification electron micrograph displaying N-Cadherin immunogold-labeled CAD cells connected by iTNTs. **(b-top)** White dashed rectangle in **a** correspond to two high-magnification non-consecutive cryo-tomogram slices (25 nm in thickness) shown in **b-top** and **b-bottom** (Supplementary Movie 4). Green arrowheads in **b** and spheres in **c** indicate 10 nm gold particles attached to a polyclonal secondary antibody that binds to an N-Cadherin primary antibody. Red arrows indicate a long thin thread filament surrounding iTNTs anchored to the membrane of iTNTs by N-Cadherin molecules (green arrows). **c** Segmentation rendering of the tomogram described in **b**; N-Cadherin (green beads), thin thread surrounding iTNTs (green arrowheads). **d** Epifluorescence micrographs of CAD cells overexpressing GFP-Myo10 connected by TNTs stained with WGA (red). Yellow arrowheads indicate GFP-Myo10 signal in TNTs. **e** Low-magnification electron micrograph corresponding to TNTs shown in **d**. **f, g** High-magnification cryo-tomography slices corresponding to the yellow dashed squares in **e**. Yellow arrowheads in **d** mark GFP-Myo10 vesicles (Supplementary Movies 6 and 7). Orange arrows indicate vesicle-iTNT connections. **h** Rendering of tomogram shown in **g** (Supplementary Movie 7). Scale bars: **a, e**, 2 μm ; **b, f**, 100 nm; **d**, 5 μm ; **g, h**, 50 nm

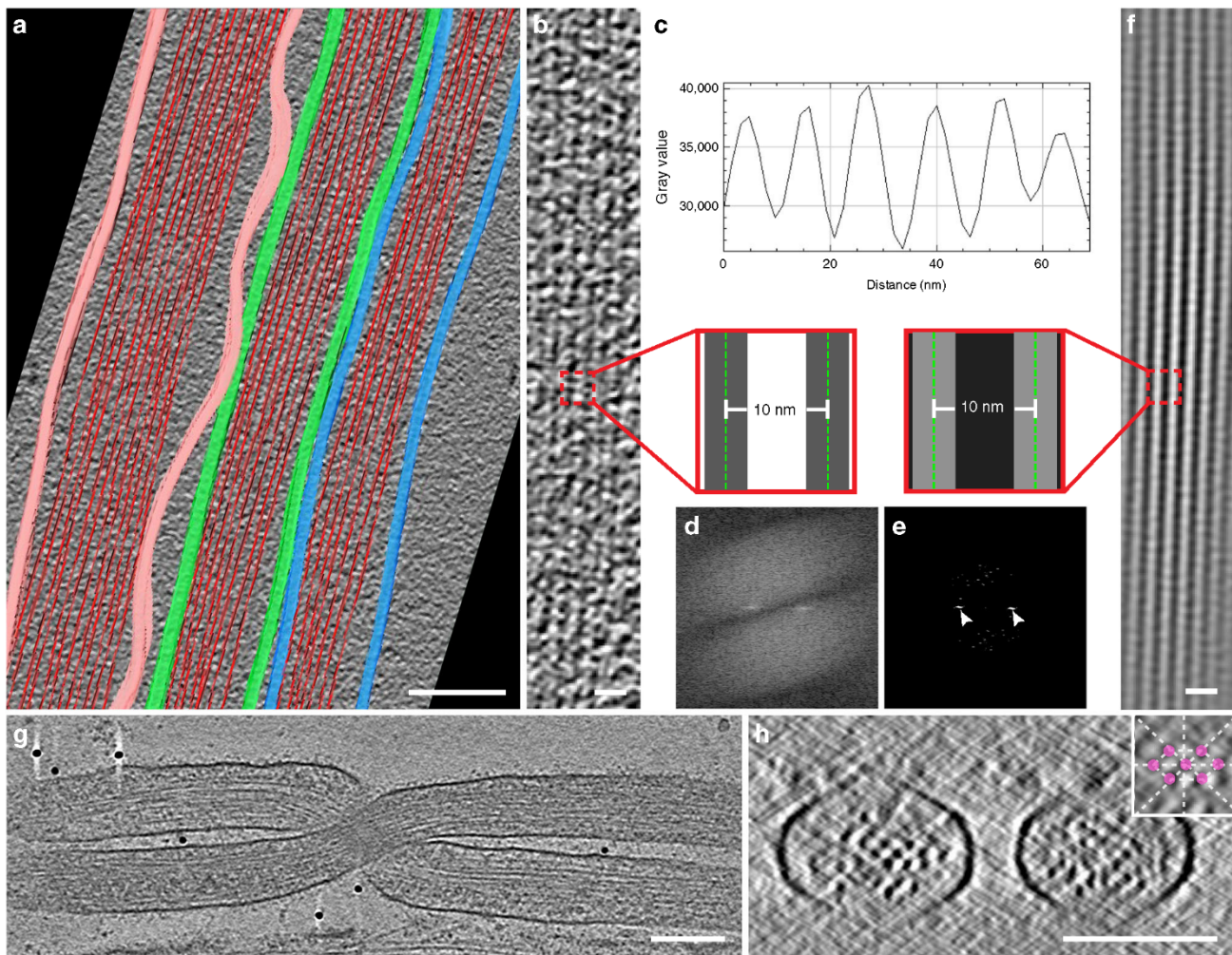
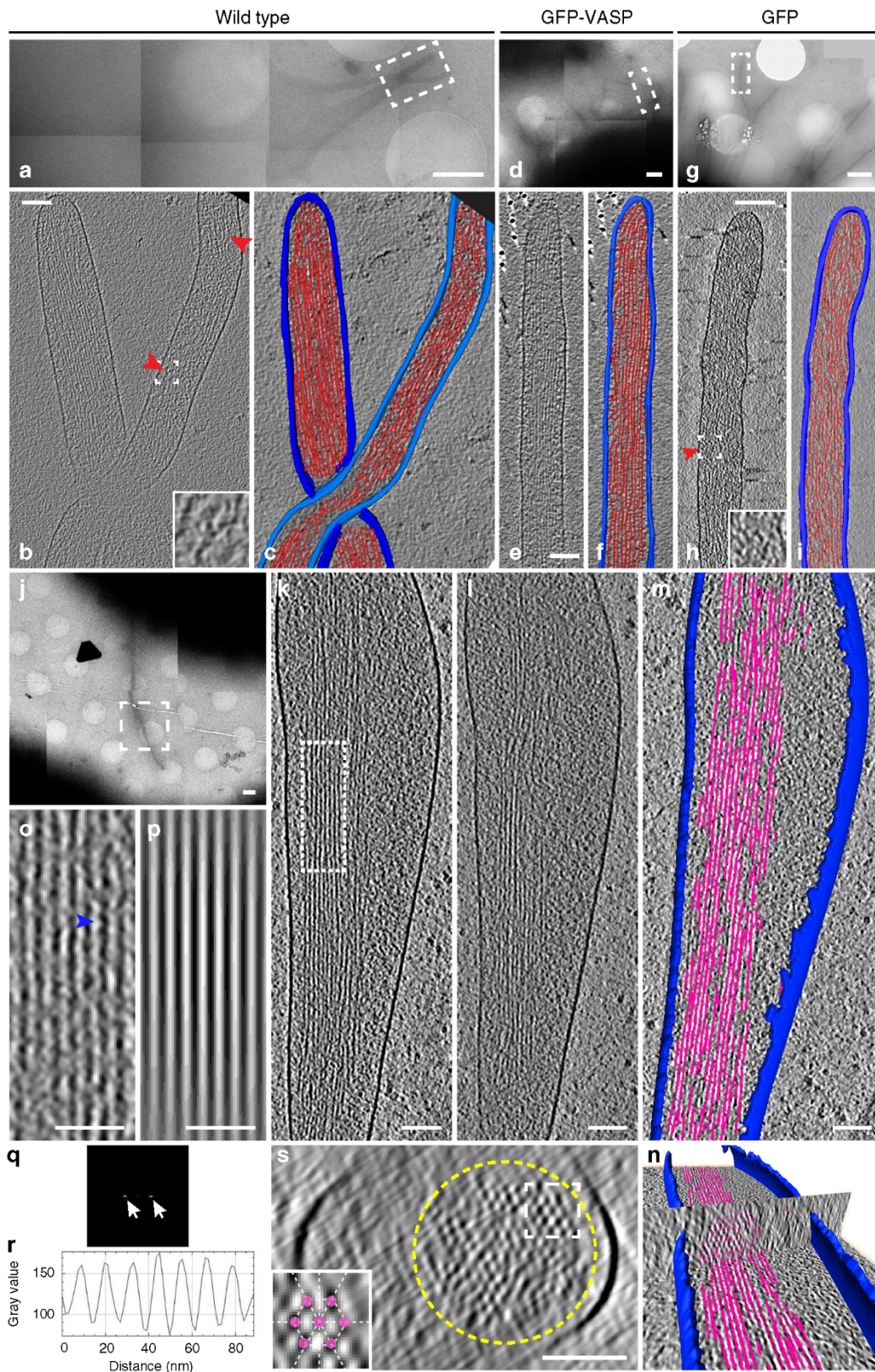


Fig. 4 Cryo-electron tomography reveal F-actin organization in iTNTs. **a** Segmentation rendering obtained from a tomogram showing iTNTs (Supplementary Movie 8). The average size and spacing between filaments of an iTNT shown in **b** were measured by computing the plot profile of actin bundles residing within. **c-e** Filament-to-filament distance measured by extracting peaks in the frequency domain using the fast Fourier transform (white arrowheads, **e**) and by computing plot profiles (**c**). **f** Model of the actin filaments displaying a parallel bundle in iTNTs obtained by retransforming peaks in the frequency domain shown in **e**. Insets in **b** and **f** show distances between the average measurements in nm obtained by the analysis shown in **c** and **d**. **g** High-magnification cryo-tomogram slice of two iTNTs (Fig. 3b and Supplementary Movie 4). **h** Cross-section of the cryo-electron tomogram in **g** displaying the actin arrangement within two iTNTs. Scale bars: **a**, 100 nm; **b, f**, 20 nm; **g, h**, 100 nm

software (Fig. 7b), helped with the visualization of contact sites (Fig. 7c) in 3D (Supplementary Movie 16) showing fusion of TNTs with the membrane of the cell bodies of both connected cells (orange and pink stars, Fig. 7b, c). Three-dimensional tomogram volumes revealed a TNT comprised of three iTNTs with an average diameter of 108 nm, creating a bundle of 388 nm in diameter.

FM-identified TNTs connecting SH-SY5Y cells (Fig. 7d) imaged by FIB-SEM showed similar features as those shown for CAD cells. Three-dimensional segmentation renderings (Fig. 7d), volume renderings (Fig. 7e), and careful observation of contact sites (orange and pink stars, Fig. 7f), revealed an open-ended TNT comprised of two iTNTs with an average diameter of 235 nm (Supplementary Movie 17).



In a separate example, we observed a pair of TNTs of 220 nm in diameter each connecting two SH-SY5Y cells by FM (Supplementary Fig. 7a). One of these tubes was inserted inside the apposing cell and appeared to be closed at its tip (red arrowhead, Supplementary Fig. 7a, b, Supplementary Movie 18).

This invaginating configuration (3D volume reconstruction shown in Supplementary Fig. 7c), could presumably be the result of a pre-TNT fusion event. Alternatively, this observation could indicate that TNTs can either be open- or close-ended at contact sites.

Fig. 5 Cryo-electron tomography reveal actin ultrastructure in filopodia. Representative electron micrographs of filopodial protrusions of untreated (**a–c**, **j–m**), GFP-VASP (**d–f**), and GFP (control) (**g–i**) transfected CAD cells imaged by cryo-TEM at low magnification (**a**, **d**, **g**, **j**). **b**, **e**, **h** Slices from volumes rendered in **c**, **f**, and **i** correspond to white dashed rectangles shown in **a**, **d**, and **g**, respectively. Red arrowheads in **b** and **h** indicate branched actin configuration. **k–l** slices corresponding to white dashed square in **j**. **m–n** Three-dimensional automated rendering of **k–l** and cross-section of the filopodium (**n**). Segmentation of the plasma membrane (blue) and actin (pink). **o** High-magnification view of filaments corresponding to the white dashed rectangle in **k**, where filaments display a wavy periodic pattern (blue arrowhead, **o**). By computing its plot profile (**r**), the average filament size and spacing between filaments was measured. **p** Model of the parallel filament bundle obtained from the peak extraction in the fast Fourier transform (**q**). **s** Cross-section through the cryo-electron tomogram of the white dashed rectangle in **j**. Scale bars: **a**, **d**, **g**, **j**, 1 μm ; **b**, **c**, **e**, **f**, **h**, **i**, **k**, **l**, **m**, **n**, 100 nm, **o**, **p**, 50 nm

It should be noted that TNTs of both CAD and SH-SY5Y cells in our FIB-SEM volumes did not display the straight and smooth morphology typically observed by FM and cryo-EM. We believe tubes can deform during sample preparation or milling. Nonetheless, this demonstrates that TNTs observed by FM can be open-ended at TNT-to-cell contact sites and thus directly link the cytoplasm of two connected cells.

Discussion

TNTs have been shown to play a vital role in the intercellular spreading of various cargos, which include deleterious materials such as amyloidogenic proteins and have therefore been implicated in many different physiological and pathological processes^{2–5,22}.

While the morphological features of TNTs have been extensively described in various cell types using fluorescence microscopy, to date, no reliable EM method has been applied to TNTs that would allow their observation at the nanoscale resolution without jeopardizing their fragile membranous and cytoskeletal composition. Indeed TNTs have only been studied at the ultrastructural level by conventional SEM and TEM methods in a handful of publications^{1,15–18}, and no study has attempted to assess the structure of TNTs in correlative mode.

Here, we set-up a workflow for correlative light- and cryo-ET microscopy that, to the best of our knowledge, is the only approach to identify and characterize the underlying structures behind TNTs observed by FM. By using this approach, we were able to observe TNTs connecting two different neuronal cell models, CAD and SH-SY5Y cells, at the nanometer resolution.

Our results show that most TNTs, which appear as single connections by fluorescence microscopy, are in fact made up of several individual tunneling nanotubes (iTNTs). iTNTs often run together in a parallel fashion but occasionally braid over each other. We speculate that this conformation might greatly increase their stability and elasticity, allowing them to withstand movements between connected cells. In addition, our tomograms suggest the existence of thin linkers that connect adjacent iTNTs (Figs. 2, 3, and 8). We identified N-Cadherin, a transmembrane cell adhesion molecule, as a component of these connections. We speculate that these connections could serve as guidance for growing iTNTs to run on top or beside of one another and therefore be of importance during TNT formation (see below). These contacts could also increase the mechanical stability of the overall bundle by holding iTNTs together. Furthermore, tomogram reconstructions suggested that long threads that coiled around iTNTs held the bundle together. Interestingly, N-Cadherin was also found at the base of these threads, connecting them to the membrane of iTNTs. While pointing to an important role in TNT formation in neuronal cells, our N-Cadherin data paves the way for additional studies required to understand its specific role, and to uncover the nature and assembly of these filaments.

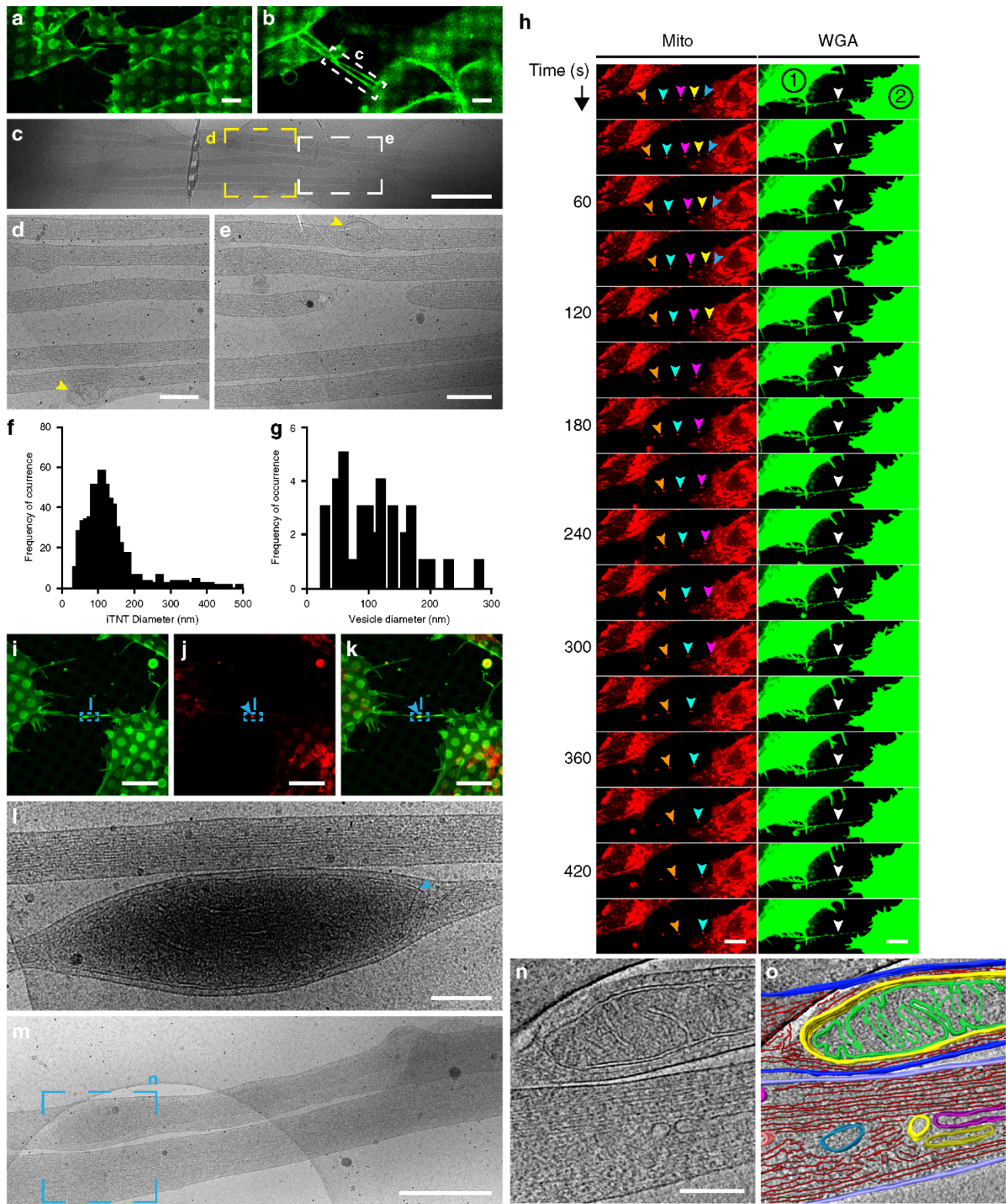
Each iTNT contains one actin bundle organized in a highly ordered fashion and likely extend all along the tube. In most

cases, the actin bundle filled the entire lumen within iTNTs. This suggests the same actin polarity in a single tube. We also observed tips of iTNTs likely in the process of extending to- or retracting from either of the two connected cells (Figs. 1 and 6). We hypothesize that this event could represent a ‘snapshot’ of the mechanism by which TNTs are formed and maintained, a highly dynamic process that involves multiple iTNTs extending and retracting between opposite cells. We also speculate that iTNTs extending from opposing cells would have opposite polarities, thus allowing unidirectional transfer in opposite directions. In support of this hypothesis we could observe vesicles inside distinct iTNTs (within the TNT bundle) that appear to originate from opposite sides (Figs. 1h and 8). This could explain bidirectional vesicular transfer previously observed inside what appeared as a single TNT by FM⁴⁰. Further studies combining live microscopy with cryo-TEM will be required to directly confirm these hypotheses. Alternatively, one could imagine that each iTNT could contain actin filaments with opposite polarity, or both actin and microtubules. While our tomograms are suggestive of a single actin bundle per iTNT, the presence of tubulin has been observed (by FM) in thicker connections, mainly in cells of the immune system, but not inside TNTs connecting neuronal cells^{1,43,44}. We speculate that TNTs containing tubulin might be different from the ones we observe here in neuronal cells. Furthermore, there is no evidence that TNT-like structures in immune cells are open-ended¹⁵, therefore it will be interesting to inquire their ultrastructure by correlative EM.

One distinguishing feature of TNTs is that they allow cargo transfer. We detected vesicular compartments of different shapes and sizes inside the single iTNTs (Supplementary Fig. 2), reinforcing the wealth of literature demonstrating the intercellular transfer of vesicles and organelles via TNTs^{2,4,5}. In addition, we observed extracellular vesicles surrounded by a double membrane, which could have derived from either budding or fission from an iTNT. Exosome markers have been found in TNTs. They have also been proposed to travel inside TNTs and shown to stimulate TNT formation^{45,46}. We found examples of multi-vesicular body-like structures inside iTNTs and external vesicles bearing a single-membrane, which could be exosomes. However, future studies will be necessary to investigate the nature of these structures.

Nonetheless, by correlative cryo-TEM we clearly identified mitochondria inside iTNTs connecting SH-SY5Y cells (Fig. 6). Altogether with live microscopy data showing mitochondria traveling through TNTs, these findings indicate that mitochondria can be transported within iTNTs by a microtubule-independent mechanism (Fig. 6n, o). Interestingly, while microtubules and their motors have been established as important factors for mitochondrial transport⁴⁷, emerging evidence indicates that mitochondria interact with the actin cytoskeleton in many cell types^{48–50}. Although we could track single mitochondria and measure their velocity by live imaging, the motors involved in their transport through iTNTs, remain unidentified.

On the other hand, by overexpressing Myo10, previously shown to increase TNT formation in CAD cells²⁷, we were able to



localize this actin driven motor with vesicular structures inside the lumen of iTNTs. While the mechanism of cargo movements on actin bundles needs to be further enquired, and could involve other motors previously observed in TNTs in FM^{1,27}, these data support a role for Myo10 in this process.

Overall, our data indicate that TNTs are largely different from filopodia. Tomograms revealed that although the average diameter of filopodia is within the range of the average diameter of iTNTs (174 vs. 123 nm), similar to other cells, filopodia in CAD

cells are isolated protrusions, not found in bundles. Importantly, as previously shown in other cell types^{36,37}, filopodia in CAD cells do not appear to contain vesicles. Finally, filopodia displayed various actin arrangements compared to TNTs. While the actin in TNTs was always found in parallel bundles that ran along the entire length of the area imaged (up to 1.5 μm) and continued seemingly uninterrupted in the next (non-consecutive) area imaged; in filopodia, tight parallel bundles were of much shorter length (with only 15% having a length longer than 1 μm),

Fig. 6 Structural analysis and live imaging reveal mitochondrial transport via iTNTs. **a** Confocal micrograph of SH-SY5Y cells stained with WGA (green). **a** Lower and **b** upper optical slices show TNTs hovering over the substrate. **c** Low-magnification electron micrograph corresponding to white dashed rectangle in **b**. **d–e** High-magnification micrographs corresponding to yellow and white dashed squares in **c**. Yellow arrowheads indicate membranous compartments inside iTNTs. **f–g** Diameter distribution of iTNTs (**f**) and vesicles found within them (**g**) in nm. **h** Time-lapse sequence of two SH-SY5Y cells stained with WGA (green) and MitoTracker (red) reveal mitochondrial puncta (orange, cyan, pink, yellow, and blue arrowheads) traveling across a TNT (white arrowhead) entering the apposing cell, (cell #2). **i–k** SH-SY5Y cells stained with WGA (green) and mitotracker (red), (blue arrowheads indicate mitochondria inside the TNT). **l** Micrograph corresponding to blue dashed rectangles in **i–k** reveal mitochondria (blue arrowhead) observed by fluorescence (**i–k**). **m** Micrograph displays two iTNTs, one containing mitochondria. **n** Tomogram slice corresponding to **m** (blue dashed square) reveal mitochondrial cristae, actin, and membranous compartments found inside iTNTs. **o** Rendering of **n**. Source data for **f–g** are provided as a Source Data file. Scale bars: **a–b**, 5 μm ; **c**, 1 μm ; **d, e, l, n**, 200 nm, **h–i**, 10 μm ; **m**, 500 nm

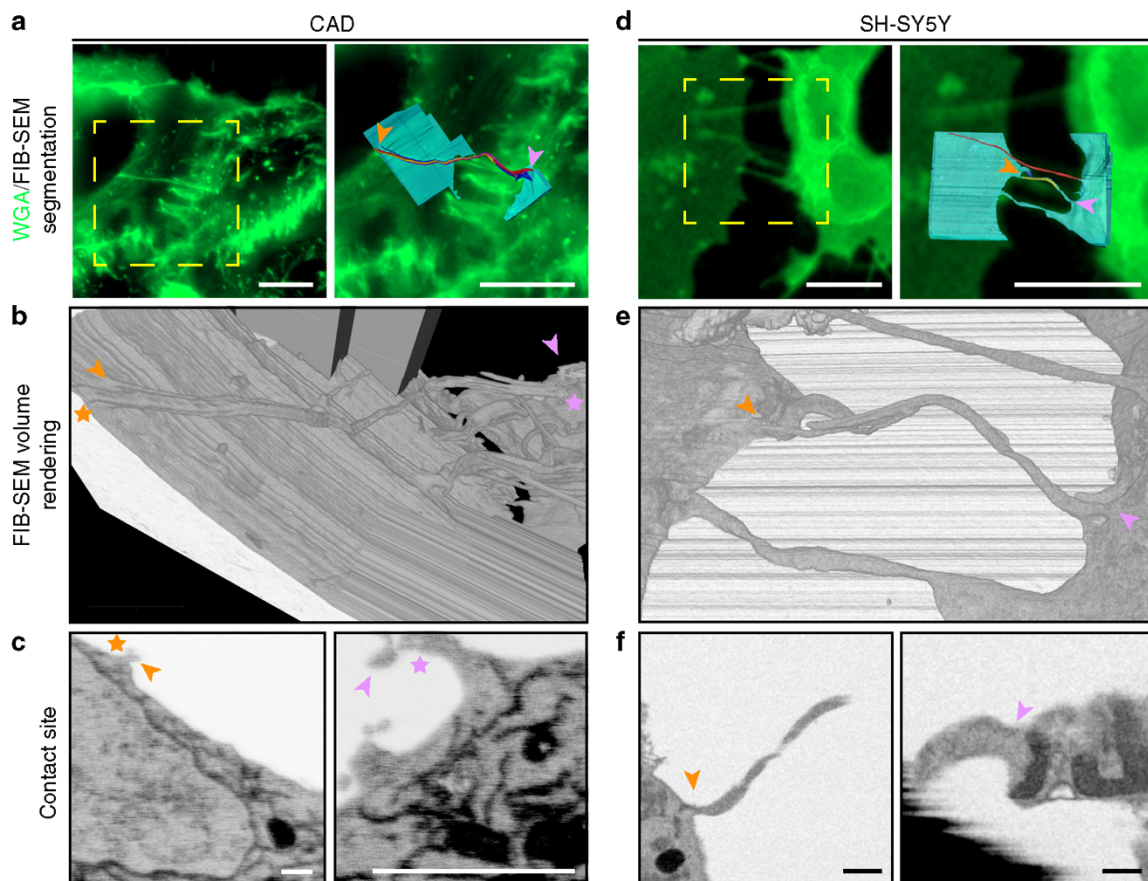


Fig. 7 FIB-SEM of TNTs in CAD and SH-SY5Y cells open-open contact sites. **a, d** Confocal micrographs of TNT-connected CAD (**a**) and SH-SY5Y (**d**) cells stained with WGA (green). Yellow dashed boxes in **a** and **d** (left) show the regions of interest chosen for FIB-SEM volume acquisition. A magnified view of these regions is shown in **a** and **d** (right) overlaid with their FIB-SEM segmented rendering counterpart. Segmented cell bodies and single open-ended connections are shown in cyan. Open-ended iTNTs are shown in blue, yellow, and magenta. Single close-ended protrusions are shown in red. Orange and pink arrowheads indicate contact sites with cells. **b, e** Renderings of FIB-SEM volumes produced by the Amira software are shown for CAD (**b**) and SH-SY5Y (**e**) cells. **c, f** Single frames obtained from the raw FIB-SEM data of CAD cells (**c**), obtained at a pixel size of 2.5 nm and displayed in an x-y orientation, and SH-SY5Y cells (**f**) obtained at a pixel size of 10 nm and displayed in an x-z orientation. Panels show TNT-to-cell contact sites at both ends of the connection: orange arrowhead (left); pink arrowhead (right). Scale bars: **a, d**, 10 μm ; **c, f**, 500 nm

arranged in parallel bundles intermingled with short-branched filaments. Interestingly, when we looked at the arrangement of parallel bundles in TNT and filopodia by cross-section analysis, we revealed similar arrangements, (i.e., similar distance between the center and surface of filaments). In filopodia we also showed a typical actin-bundling hexagonal pattern possibly due to the actin-binding protein Fascin³⁷. A similar hexagonal pattern was observed in TNTs but under the imaging conditions used, the number of filaments per bundle could not be clearly detected for TNTs. This is possibly due to the lack of resolution achievable by our cryo-TEM on thick samples and the considerable technical challenges we faced when imaging iTNT bundles under cryogenic

conditions compared to isolated filopodia. Thus, to further analyze the structural differences and similarities in the actin arrangements within iTNTs, the use of TEMs with improved optics will be required.

To specifically address the controversial question in the TNT field whether TNTs are connecting the cytosol of two cells, we performed FIB-SEM tomography on CAD and SH-SY5Y cells, which allowed us to image the ends (or contact sites) of TNTs. Interestingly, FIB-SEM enabled us to identify TNTs open at both ends, in both cell lines. TNTs appeared to fuse with the membrane of cell bodies at separate locations, while in other cases they seemed to merge into one stem that fused with the cell. This

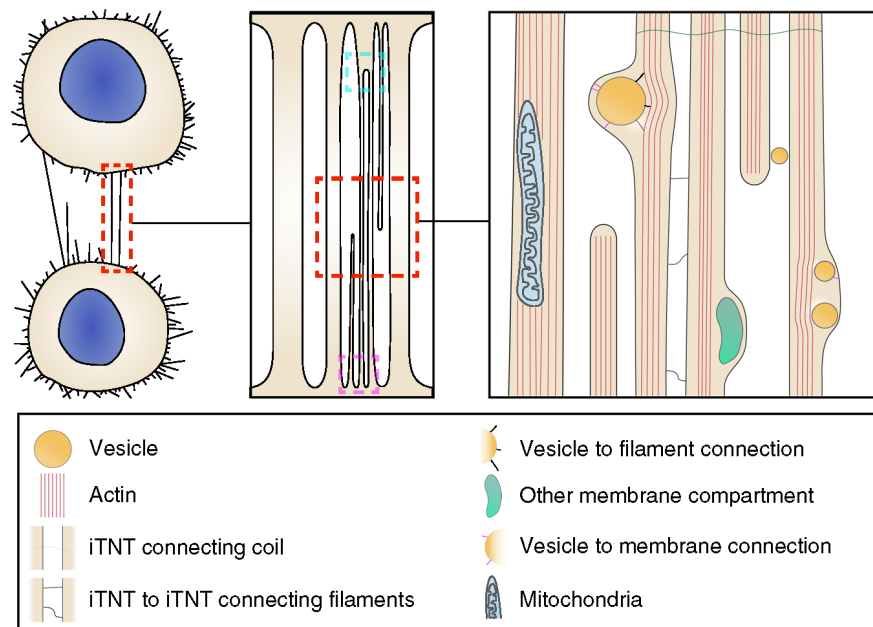


Fig. 8 Schematic diagram depicting how cells connect via TNTs. TNT-connecting cells can either be single thick connections or a bundle of thin individual TNTs (iTNTs). iTNTs contain vesicles and mitochondria. Membranous compartments within iTNTs appear to be connected by thin filaments to actin on one side and to the inner side of the plasma membrane on the other. Thin membrane threads coil between and around several iTNTs. Cyan and magenta dashed squares show two types of contact sites: merging of iTNTs prior to fusion and fusion of iTNTs at separate locations, respectively

observation is particularly interesting as it suggests that iTNTs can also merge. Whether this occurs only at the ends or along their extension, or whether N-Cadherin is involved in this process, is an interesting question that needs to be further addressed.

We also found some close-ended connections and invaginations at contact sites. At this point, we cannot discriminate whether the differences observed are the result of the existence of distinct TNTs or whether it is due to temporal pre or post fusion events. Nonetheless, these data demonstrates that open-ended TNTs exist and could correspond to the functional TNTs structures observed by FM.

Overall, the data presented here provides a structural characterization of functional TNTs previously observed by light microscopy in two different neuronal cell models. They demonstrate their specific identity, highlight the morphological differences with filopodia, show the actin architecture at high resolution and the presence of vesicular structures and mitochondria inside them.

While many more questions remain open these data also guide the establishment of a TNT inducing and imaging platform for investigating the structural mechanism underlying TNTs, as well as for revealing the specific role that membrane and cytoskeleton-associated proteins may play in the formation and function of this important biological process.

Methods

Cell preparation and transfections. CAD (mouse catecholaminergic neuronal cell line, Cath.a-differentiated) cells were kindly given by Hubert Laude (Institut National de la Recherche Agronomique, Jouy-en-Josas, France) and cultured at 37 °C in Gibco Opti-MEM (Invitrogen), plus 10% fetal bovine serum and 1% penicillin/streptomycin²³. SH-SY5Y cells (neuroblasts from human neural tissue) were cultured at 37 °C in RPMI-1640 (Euroclone), plus 10% fetal bovine serum and 1% penicillin/streptomycin. Transient transfections were performed with Lipofectamine 2000 (Invitrogen) in accordance with the manufacturer's instructions. CAD cells were transfected in T25 flasks with the appropriate constructs: GFP-tagged constructs, GFP-VASP, GFP-Myo10, or H2B-mCherry for 3 h in serum-free medium and incubated O/N with complete medium. The following day, transfected cells were plated on grids¹⁹.

Pharmacological treatments. For pharmacological assays, confluent CAD cells were mechanically detached and counted; 100,000 cells were plated for 24 h on Ibidi μ -dishes (Biovalley, France). Cells were then treated with CK-666 (SML0006, Sigma), an Arp 2/3 complex inhibitor, which was made up as 75 mM stock solution in dimethyl sulfoxide (DMSO) and diluted in complete medium to a final concentration of 25 μ M or 50 μ M. DMSO-alone control treatments were performed as part of every experiment involving drug treatment. Cells were treated for 15 min at 37 °C before fixation and fluorescent labeling. Acceptor cells were plated in T25 flasks (Corning, USA) and transiently transfected with an H2B-mcherry vector after 24 h. The following day, donor cells were detached and resuspended in complete medium with 1 μ M of DiD-labeled vesicles and incubated for 30 min at 37 °C. Donor cells were then washed with complete culture medium, mixed with acceptor cells (1:1), and plated on 35 mm Ibidi μ -Dish (Biovalley, France). After an incubation of 1 h at 37 °C, cells were treated with CK-666 (25 μ M and 50 μ M) and DMSO (control) for 6 h. After washing cells with fresh, complete medium they were incubated at 37 °C O/N. The next day, cells were washed with phosphate-buffered saline (PBS), fixed in 2% PFA + 0.05% GA in 0.2 M Hepes for 15 min followed by fixation in 4% PFA in 0.2 M Hepes for 15 min, stained with DAPI (1:1000), and mounted with Aqua-Poly/Mount (Polysciences, Inc.). Images were acquired on an LSM 700 confocal microscope (Zeiss) with a 40X objective. Semi-automated detection and quantification of the number of DiD-labeled puncta was assessed with the open source software, ICY⁷.

Immunofluorescence labeling. CAD cells plated overnight were washed carefully, fixed with 4% paraformaldehyde (PFA) for 15 min at 37 °C, quenched with 50 mM NH₄Cl for 15 min, permeabilized and blocked with 0.075% Saponin in PBS containing 2% BSA (w/v) for 1 h at 37 °C. Cells were then incubated with a mouse anti-vinculin primary antibody (V9264, Sigma) (1:500) in 0.01% saponin and 2% BSA (w/v) in PBS. Cells were thoroughly washed and incubated for 40 min with a goat anti-mouse AlexaFluor 488-conjugated secondary antibody (Invitrogen) at 1:500 in 0.01% saponin and 2% BSA (w/v) in PBS. Cells were then carefully washed in PBS and labeled with WGA-647 (1:300 in PBS) for 5 min at room temperature (RT), and 5 min with Phalloidin-Rhodamine (1:300 in PBS); nuclei were labeled for 5 min with DAPI (1:1000). Cells were washed and mounted with Aqua-Poly mount (Polysciences, Inc.).

Cell preparation for cryo-EM. Carbon-coated gold TEM grids (Quantifoil NH2A R2/2) were glow-discharged at 2 mA and 1.5–1.8 $\times 10^{-1}$ m bar for 1 min in an ELMO (Cordouan) glow discharge system. Grids were sterilized under UV three times for 15 min at RT and incubated at 37 °C in complete culture medium. Grids were carefully washed twice in PBS and coated with 40 μ g/mL of fibronectin for 20 min at 37 °C. After three PBS washes, 250,000 CAD or 700,000 SH-SY5Y cells were seeded on grids and incubated O/N at 37 °C, resulting in 3 to 4 cells per grid square. Prior to chemical or cryo-fixation, cells were labeled with WGA-Alexa-488 (1:300 in PBS) for 5 min at 37 °C. For correlative light- and cryo-electron

microscopy, cells were chemically fixed in 2% PFA + 0.05% GA in 0.2 M Hepes for 15 min followed by fixation in 4% PFA in 0.2 M Hepes for 15 min and kept hydrated in PBS buffer prior to vitrification. For cell vitrification, fluorescently labeled CAD and SH-SY5Y cells were blotted from the back side of the grid for 7 s and rapidly frozen in liquid ethane⁵¹ using a Leica EMGP system.

EM immuno-labeling. CAD cells were plated on grids as described in above. After incubation O/N at 37 °C, cells were treated with 25 μM CK-666 for 15 min at 37 °C and fixed with PFA 4% for 15 min at 37 °C, quenched with 50 mM NH₄Cl for 15 min, and blocked with PBS containing 1% BSA (w/v) for 30 min at 37 °C. Cells were labeled with a rabbit anti-N-Cadherin ABCAM 76057 antibody (1:200), followed by Protein A-gold conjugated to 10 nm colloidal gold particles (CMC, Utrecht, Netherlands). CAD cells were then rapidly frozen in liquid ethane⁵¹ as above.

Myo10 sample preparation. CADs were transfected with GFP-Myo10 as described in the section Cell preparation and transfections and in Goussset et al.²⁷. In all, 250,000 cells were plated on grids, After O/N incubation at 37 °C, chemically fixed in 2% PFA + 0.05% GA in 0.2 M Hepes for 15 min followed by fixation in 4% PFA in 0.2 M Hepes for 15 min and labeled with WGA-546 (1:300 in PBS) for 15 min at RT; Before plunge-freezing, the grids were imaged with an inverted Zeiss Axiovision widefield microscope.

Confocal microscopy and image analysis. Fluorescent images from pharmacological assays were acquired using an inverted Zeiss LSM 700 confocal microscope. For quantification of TNT-connected cells, confluent CAD cells were mechanically detached and counted; 100,000 cells were plated for 24 h on Ibidi μ-dishes (Biovalley, France). Cells were then treated with CK-666 (25 μM or 50 μM, and DMSO-alone control treatments). Cells were treated for 15 min at 37 °C before fixation (15 min at 37 °C in 2% PFA, 0.05% glutaraldehyde and 0.2 M HEPES in PBS, and then additionally fixed for 15 min in 4% PFA and 0.2 M HEPES in PBS). Cells were carefully washed in PBS, labeled for 20 min at RT with a 3.3 μg/μL solution of Wheat-Germ Agglutinin (WGA) Alexa Fluor®-647 nm conjugate (Invitrogen) in PBS, washed again and sealed with Aqua-Poly/Mount (Polysciences, Inc.). The whole cellular volume was imaged by acquiring 0.5 μm Z-stacks with an inverted confocal microscope (Zeiss LSM 700) using ZEN software. TNT-connected cells, i.e., cells connected by straight WGA-labeled structures that do not touch the substrate and have a diameter smaller than 1 μm were manually counted by experimenters blind to the condition in the same manner as previously^{19,23}.

For vinculin-positive focal adhesions, after indirect immunofluorescence labeling of vinculin, described above in the section Immunofluorescence labeling, the bottom of the cell (in contact with the plastic dish) was imaged with an inverted confocal microscope (Zeiss LSM 700) using ZEN software. Displayed images correspond to stack projections Vinculin-positive peripheral focal adhesion were automatically detected and counted using ICY software (<http://icy.bioimageanalysis.org/>)^{19,23}.

Scanning electron microscopy (SEM) and correlative light/SEM. CAD and SH-SY5Y cells were plated overnight on gridded IBIDI dishes, fixed at 37 °C in 0.05% glutaraldehyde, 2% PFA in 0.2 M Hepes for 15 min followed by fixation in 4% PFA in 0.2 M Hepes for 15 min, stained with WGA 488 (1:300) for 15 min at RT. The samples were post-fixed in 2.5% glutaraldehyde in 0.2 M cacodylate buffer (pH 7.2) at 4 °C, washed three times 5 min in 0.2 M cacodylate buffer (pH 7.2), treated for 1 h with 1% osmium tetroxide in 0.2 M cacodylate buffer and then rinsed in distilled water. Samples were dehydrated through a graded series of 25, 50, 75 and 95% ethanol solutions for 5 min and for 10 min in 100% ethanol followed by critical point drying with CO₂. Samples were sputtered with a 10 nm gold/palladium layer and were observed in a JEOL JSM-6700F field emission scanning electron microscope at a voltage of 5 kV.

Focused-ion beam scanning electron microscopy (FIB-SEM). CAD and SH-SY5Y cells were plated on gridded Ibidi μ-dishes (Biovalley, France). Positions of TNTs were recorded by LM after labeling with WGA. Fixation was carried out as described for SEM followed by post-fixation with 1% (w/v) osmium tetroxide and 1.5% (w/v) potassium ferrocyanide for 30 min, incubation with 1% tannic acid for 30 min, followed by another post-fixation with 1% osmium tetroxide for 30 min. Samples were dehydrated in a graded ethanol series (25, 50, 75, 95 and 100%) and embedded in Epon (Agar Scientific, UK) and subsequently placed on a pin stub and covered with silver paint (Agar Scientific, UK). The surfaces were coated with a 10 nm-thick layer of gold/palladium using an ion Beam Coater (Gatan Inc, USA) to avoid charging effect. Three-dimensional tomography was performed with a FIB-SEM Auriga (Zeiss, Germany). An additional 1 μm protective layer of platinum was deposited on the surface of the region of interest using a 500 pA ion beam assisted deposition with a 30 kV acceleration potential. The cross-section was milled using a 10 nA ion beam current. The surface obtained was then polished using a 2 nA ion beam current. Tomographic sections of 10 nm in thickness during acquisition were obtained using a 500 pA ion beam current. SEM images were acquired with a voxel size of 10 × 10 × 10 nm for a frame size window of 2048 × 2048 pixels or with a voxel size of 2.5 × 2.5 × 10 nm with a frame size window of 4096 × 4096 pixels by

using a 1.5 keV acceleration voltage and a 30 μm aperture with an energy selected back-scattered electron detector in a Zeiss system. Alignment of the acquired stack of images was done using ImageJ. Segmentations and measurements were performed using Amira 6.4 (Thermo Fisher Scientific, USA).

Cryo-correlative light and electron microscopy (i-CLEM). Vitrified TEM grids containing fluorescently labeled CAD cells were imaged on an epifluorescent Axiovert 200 M inverted microscope (Zeiss) equipped with a cryo-correlative stage (Cryostage2, FEI), 10 × (NA 0.3), 40 × (NA 0.6) and 63 × (NA 0.75, working distance 1.7 mm) long working distance air objectives and with a 482/18 (Excitation), 520/28 (Emission, green) filter cube. The cryo-correlative stage (MPI Biochemistry, Martinsried⁵²) was mounted on the light microscope motorized stage. Samples were transferred from liquid nitrogen storage only when the temperature of the microscope cryo-correlative stage was below -170 °C. Fluorescent and phase contrast digital images at cryogenic temperatures were recorded with an Axio-camMRm camera (Zeiss). Following cryo-fluorescence imaging, the vitrified samples on grids were stored in liquid nitrogen until they were used for cryo-TEM. In all images, the brightness and contrast were adjusted in order to highlight TNTs.

Correlative light and cryo-electron microscopy (ii-CLEM). CAD and SH-SY5Y cells on TEM finder grids were chemically fixed after fluorescent labeling as described in the cell culture section. The samples on TEM grids were then positioned in glass-bottom dishes (MatTek Corporation, Ashland, USA) in Hepes buffer. Fluorescence and corresponding transmitted light z-stack images of cells were obtained by using the same epifluorescence Axiovert 200 M inverted microscope (Zeiss) equipped with 482/18 (Excitation), 520/28 (Emission, green) and a 546/12 (Excitation), 575–640 nm (Emission, red) filter cubes and a 40 × (NA 1.3, WD 0.21 mm) oil objective. Following fluorescence imaging, the samples on grids were immediately vitrified and stored in liquid nitrogen until they were used for cryo-TEM.

Cryo-electron microscopy. Cryo-electron tomography was performed on a Tecnai 20 equipped with a field emission gun and operated at 200 kV (Thermo Fisher company). Images were recorded using either Explore 3D or SerialEM software on a 4k × 4k camera (Ultrascan from Gatan) and a Falcon II (FEI, Thermo Fisher) direct electron detector, with a 14 μm pixel size. Tilt series of TNTs were acquired covering either an angular range of -52° to +52° (Fig. 4a and Supplementary Movie 8), -51° to 51° (Fig. 2k and Supplementary Movie 5), -30° to +48° (Fig. 3f and Supplementary Movie 6) and tilt range of -28° to +48° (Fig. 3g and Supplementary Movie 7) or in specific cases due to sample physical constraints with a reduced angular range (Fig. 2f–h, and corresponding Supplementary Movies 1, 2, and 3), with 2–4 degrees increment. The defocuses used were -6, -8, and -10 μm. Tilt series of filopodial protrusions were acquired covering a tilt range of -65° to +66° (Fig. 5b, e, h, with corresponding Supplementary Movies 9, 10, 11, and Fig. 5k–i with corresponding Supplementary Movie 12), with 2 degrees increment and defocus of -6 μm. Tilt series of TNTs with mitochondria were acquired covering a tilt range of -51° to +67° (Fig. 6 and Supplementary Movie 15). All tilt series were acquired at magnifications of 25,000× or 29,000×, binning 2, corresponding to a pixel size of 0.742 or 0.634 nm, respectively.

Live-series microscopy. Live time series images were acquired with a 60 × 1.4NA CSU oil immersion objective lens on an inverted Elipse Ti microscope system (Nikon Instruments, Melville, NY, USA). Laser illumination was provided by 488 and 561 nm. Pairs of images were captured in immediate succession with one of two cooled CCD cameras, which enabled time intervals between 20 and 30 s per z-stack. For live cell imaging, the 37 °C temperature was controlled with an Air Stream Stage Incubator, which also controlled humidity. Cells were incubated with 5% CO₂ during image acquisition.

Image analysis and visualization. Tomographic tilt series were processed using version 4.9.2 of IMOD⁵³. Projections were pre-processed by hot pixel removal and rough alignment by cross-correlation. Final alignments were done by using 10 nm fiducial gold particles coated with BSA (BSA Gold Tracer, EMS). The reconstructions were obtained by using a weighted back-projection algorithm⁵⁴. For visualization purposes, the reconstructed volumes were processed by a Gaussian filter. Surface rendering was done with Amira 6.2 software package. The diameter of iTNTs and filopodia was quantified by measuring the diameter of individual structures along the tube every 300 nm. Quantitative measurements of vesicle diameter on TEM micrographs or of TNTs' and actin filaments' distances on 3D tomographic reconstructions were done by using the open source program Fiji. Distances between actin filaments were obtained in two ways: (1) by selecting sub-regions in sections from tomographic reconstructions containing only parallel actin filaments and by extracting peaks in the corresponding Fourier transform; (2) by performing plot profiles of the selected sub-regions and by measuring the peak-to-peak distances and the full width at half maximum.

Statistical analysis. The results of image analysis from pharmacological assays were transferred to Prism (GraphPad). For more than two groups statistical

significance was assessed by a one-way ANOVA with Tukey correction. Differences were considered significant at * $p < 0.05$, ** $p < 0.005$, or *** $p < 0.0005$. Quantifications were done blind. Quantitative data depicted as (\pm SEM) mean standard deviation.

Reporting Summary. Further information on experimental design is available in the Nature Research Reporting Summary linked to this Article.

Data availability

The source data underlying Figs. 2a, 2b, 6f, 6g and Supplementary Figures 2i, 3 are provided as a Source Data file. A Reporting Summary for this Article is available as a Supplementary Information file. All other data that support the findings of this study are available from the corresponding author upon request.

Received: 27 July 2017 Accepted: 18 December 2018

Published online: 21 January 2019

References

- Rustom, A., Saffrich, R., Markovic, I., Walther, P. & Gerdes, H. H. Nanotubular highways for intercellular organelle transport. *Science* **303**, 1007–1010 (2004).
- Abounit, S. & Zurzolo, C. Wiring through tunneling nanotubes—from electrical signals to organelle transfer. *J. Cell Sci.* **125**, 1089–1098 (2012).
- Austefjord, M. W., Gerdes, H. H. & Wang, X. Tunneling nanotubes: Diversity in morphology and structure. *Commun. Integr. Biol.* **7**, e27934 (2014).
- Vignais, M. L., Caicedo, A., Brondello, J. M. & Jorgensen, C. Cell connections by tunneling nanotubes: Effects of mitochondrial trafficking on target cell metabolism, homeostasis, and response to therapy. *Stem Cells Int.* **2017**, 6917941 (2017).
- Ariazi, J. et al. Tunneling nanotubes and gap junctions—their role in long-range intercellular communication during development, health, and disease conditions. *Front. Mol. Neurosci.* **10**, 333 (2017).
- Koyanagi, M., Brandes, R. P., Haendeler, J., Zeiher, A. M. & Dimmeler, S. Cell-to-cell connection of endothelial progenitor cells with cardiac myocytes by nanotubes: a novel mechanism for cell fate changes? *Circ. Res.* **96**, 1039–1041 (2005).
- Abounit, S., Wu, J. W., Duff, K., Victoria, G. S. & Zurzolo, C. Tunneling nanotubes: A possible highway in the spreading of tau and other prion-like proteins in neurodegenerative diseases. *Prion* **10**, 344–351 (2016).
- Chinnery, H. R., Pearlman, E. & McMenamin, P. G. Cutting edge: Membrane nanotubes in vivo: a feature of MHC class II+ cells in the mouse cornea. *J. Immunol.* **180**, 5779–5783 (2008).
- Lou, E. et al. Tunneling nanotubes provide a unique conduit for intercellular transfer of cellular contents in human malignant pleural mesothelioma. *PLoS ONE* **7**, e33093 (2012).
- Osswald, M. et al. Brain tumour cells interconnect to a functional and resistant network. *Nature* **528**, 93–98 (2015).
- Baker, M. How the Internet of cells has biologists buzzing. *Nature* **549**, 322–324 (2017).
- Mattila, P. K. & Lappalainen, P. Filopodia: molecular architecture and cellular functions. *Nat. Rev. Mol. Cell Biol.* **9**, 446–454 (2008).
- Gutierrez-Vazquez, C., Villarroya-Beltri, C., Mittelbrunn, M. & Sanchez-Madrid, F. Transfer of extracellular vesicles during immune cell-cell interactions. *Immunol. Rev.* **251**, 125–142 (2013).
- Nawaz, M. & Fatima, F. Extracellular vesicles, tunneling nanotubes, and cellular interplay: Synergies and missing links. *Front. Mol. Biosci.* **4**, 50 (2017).
- Sowinski, S. et al. Membrane nanotubes physically connect T cells over long distances presenting a novel route for HIV-1 transmission. *Nat. Cell Biol.* **10**, 211–219 (2008).
- Kumar, A. et al. Influenza virus exploits tunneling nanotubes for cell-to-cell spread. *Sci. Rep.* **7**, 40360 (2017).
- Lu, J. et al. Tunneling nanotubes promote intercellular mitochondria transfer followed by increased invasiveness in bladder cancer cells. *Oncotarget* **8**, 15539–15552 (2017).
- Okafo, G., Prevedel, L. & Eugenin, E. Tunneling nanotubes (TNT) mediate long-range gap junctional communication: Implications for HIV cell to cell spread. *Sci. Rep.* **7**, 16660 (2017).
- Delage, E. et al. Differential identity of filopodia and tunneling nanotubes revealed by the opposite functions of actin regulatory complexes. *Sci. Rep.* **6**, 39632 (2016).
- Gallo, G. Mechanisms underlying the initiation and dynamics of neuronal filopodia: from neurite formation to synaptogenesis. *Int. Rev. Cell. Mol. Biol.* **301**, 95–156 (2013).
- Jacquemet, G., Hamidi, H. & Ivaska, J. Filopodia in cell adhesion, 3D migration and cancer cell invasion. *Curr. Opin. Cell Biol.* **36**, 23–31 (2015).
- Gousset, K. et al. Prions hijack tunnelling nanotubes for intercellular spread. *Nat. Cell Biol.* **11**, 328–336 (2009).
- Abounit, S., Delage, E. & Zurzolo, C. Identification and characterization of tunneling nanotubes for intercellular trafficking. *Curr. Protoc. Cell Biol.* **67**, 12.10.11–12.10.21 (2015).
- Smith, I. F., Shuai, J. & Parker, I. Active generation and propagation of Ca²⁺ signals within tunneling membrane nanotubes. *Biophys. J.* **100**, L37–L39 (2011).
- Dieriks, B. V. et al. alpha-synuclein transfer through tunneling nanotubes occurs in SH-SY5Y cells and primary brain pericytes from Parkinson's disease patients. *Sci. Rep.* **7**, 42984 (2017).
- Schultz, M. Rudolf virchow. *Emerg. Infect. Dis.* **14**, 1480–1481 (2008).
- Gousset, K., Marzo, L., Commere, P. H. & Zurzolo, C. Myo10 is a key regulator of TNT formation in neuronal cells. *J. Cell Sci.* **126**, 4424–4435 (2013).
- Sherer, N. M. et al. Retroviruses can establish filopodial bridges for efficient cell-to-cell transmission. *Nat. Cell Biol.* **9**, 310–315 (2007).
- Patla, I. et al. Dissecting the molecular architecture of integrin adhesion sites by cryo-electron tomography. *Nat. Cell Biol.* **12**, 909–915 (2010).
- Korobova, F. & Svitkina, T. Arp2/3 complex is important for filopodia formation, growth cone motility, and neurogenesis in neuronal cells. *Mol. Biol. Cell* **19**, 1561–1574 (2008).
- Barzik, M., McClain, L. M., Gupton, S. L. & Gertler, F. B. Ena/VASP regulates mDia2-initiated filopodial length, dynamics, and function. *Mol. Biol. Cell* **25**, 2604–2619 (2014).
- Lokar, M., Iglie, A. & Veranic, P. Protruding membrane nanotubes: attachment of tubular protrusions to adjacent cells by several anchoring junctions. *Protoplasma* **246**, 81–87 (2010).
- Zhu, D. et al. Hydrogen peroxide alters membrane and cytoskeleton properties and increases intercellular connections in astrocytes. *J. Cell Sci.* **118**, 3695–3703 (2005).
- Schiller, C. et al. LST1 promotes the assembly of a molecular machinery responsible for tunneling nanotube formation. *J. Cell Sci.* **126**, 767–777 (2013).
- Reichert, D. et al. Tunneling nanotubes mediate the transfer of stem cell marker CD133 between hematopoietic progenitor cells. *Exp. Hematol.* **44**, 1092–1112 e1092 (2016).
- Medalia, O. et al. Organization of actin networks in intact filopodia. *Curr. Biol.: CB* **17**, 79–84 (2007).
- Aramaki, S., Mayanagi, K., Jin, M., Aoyama, K. & Yasunaga, T. Filopodia formation by crosslinking of F-actin with fascin in two different binding manners. *Cytoskeleton* **73**, 365–374 (2016).
- Pasquier, J. et al. Preferential transfer of mitochondria from endothelial to cancer cells through tunneling nanotubes modulates chemoresistance. *J. Transl. Med.* **11**, 94 (2013).
- Ady, J. W. et al. Intercellular communication in malignant pleural mesothelioma: properties of tunneling nanotubes. *Front. Physiol.* **5**, 400 (2014).
- Zhu, H. et al. Rab8a/Rab11a regulate intercellular communications between neural cells via tunneling nanotubes. *Cell Death Dis.* **7**, e2523 (2016).
- Wang, X. & Gerdes, H. H. Transfer of mitochondria via tunneling nanotubes rescues apoptotic PC12 cells. *Cell Death Differ.* **22**, 1181–1191 (2015).
- Keller, K. E., Bradley, J. M., Sun, Y. Y., Yang, Y. F. & Acott, T. S. Tunneling nanotubes are novel cellular structures that communicate signals between trabecular meshwork cells. *Invest. Ophthalmol. Vis. Sci.* **58**, 5298–5307 (2017).
- Gurke, S., Barroso, J. F. & Gerdes, H. H. The art of cellular communication: tunneling nanotubes bridge the divide. *Histochem. Cell Biol.* **129**, 539–550 (2008).
- Onfelt, B. et al. Structurally distinct membrane nanotubes between human macrophages support long-distance vesicular traffic or surfing of bacteria. *J. Immunol.* **177**, 8476–8483 (2006).
- McCoy-Simandle, K., Hanna, S. J. & Cox, D. Exosomes and nanotubes: Control of immune cell communication. *Int. J. Biochem. Cell Biol.* **71**, 44–54 (2016).
- Thayanithy, V. et al. Tumor exosomes induce tunneling nanotubes in lipid raft-enriched regions of human mesothelioma cells. *Exp. Cell Res.* **323**, 178–188 (2014).
- Melkov, A. & Abdu, U. Regulation of long-distance transport of mitochondria along microtubules. *Cell. Mol. Life Sci.: CMLS* **75**, 163–176 (2018).
- Morris, R. L. & Hollenbeck, P. J. Axonal transport of mitochondria along microtubules and F-actin in living vertebrate neurons. *J. Cell Biol.* **131**, 1315–1326 (1995).
- Quintero, O. A. et al. Human Myo19 is a novel myosin that associates with mitochondria. *Curr. Biol.: CB* **19**, 2008–2013 (2009).
- Pathak, D., Sepp, K. J. & Hollenbeck, P. J. Evidence that myosin activity opposes microtubule-based axonal transport of mitochondria. *J. Neurosci.: Off. J. Soc. Neurosci.* **30**, 8984–8992 (2010).
- Dubochet, J. et al. Cryo-electron microscopy of vitrified specimens. *Q. Rev. Biophys.* **21**, 129–228 (1988).

52. Rigort, A. et al. Micromachining tools and correlative approaches for cellular cryo-electron tomography. *J. Struct. Biol.* **172**, 169–179 (2010).
53. Kremer, J. R., Mastrorarde, D. N. & McIntosh, J. R. Computer visualization of three-dimensional image data using IMOD. *J. Struct. Biol.* **116**, 71–76 (1996).
54. Hegerl, R. The EM program package: A platform for image processing in biological electron microscopy. *J. Struct. Biol.* **116**, 30–34 (1996).

Acknowledgements

We thank Seng Zhu for image analysis technical expertise and Christel Brou for valuable manuscript comments. We also gratefully acknowledge Gerard Péhau-Arnaudet (Ultrapole, Institut Pasteur) for his help in setting up freezing conditions of CAD cells during early stages of the project, and Remi Blanc from Amira (FEI, Thermo Fischer Scientific) for the automated segmentation of actin in Fig. 6 using the XTracing—Filament detection module. We thank the equipment excellence CACSICE for providing the Falcon II direct electron detector. We acknowledge the Ultrastructural Bio-Imaging facility at Institut Pasteur, member of the national infrastructure France-Bio-Imaging (FBI) supported by the French National Research Agency (ANR-10-INBS-04) and IBISA. This work was supported by grants from the Agence Nationale de Recherche (JPND Neutargets: ANR-14-JPCD-0002-01 and ANR-16 CE160019-01 NEUR0TUNN), and the Equipe FRM (Fondation Recherche Médicale) 2014 (DEQ20140329557) to C.Z. D.C.C. was supported by the Pasteur—Paris University (PPU) International PhD Program. A.P. was supported by fellowships from France Parkinson and the Fondazione Ermenegildo Zegna.

Author contributions

A.S. performed all correlative, cryo-correlative light, and electron microscopy experiments and quantification, wrote the results, and prepared the figures. D.C.C. prepared cells for TEM experiments, performed FM experiments and live imaging, helped with acquisition, prepared figures, and wrote the manuscript. A.P. performed CK-666 pharmacological experiments with D.C.C., set experimental conditions for SH-SY5Y cells, performed N-Cadherin and Myosin 10 experiments in the revised version, performed experiments and helped with the image rendering of TEM tomograms, prepared figures, and wrote results. K.G. and E.D. contributed equally; set-up and prepared CAD cell cultures for TEM and SEM and discussed earlier experiments. S.C.-D. performed FIB-SEM experiments and the corresponding data rendering, C.S. performed

SEM experiments in CAD cells. C.Z. conceived the project, supervised all the work, and wrote the manuscript. A.S., D.C.C., A.P., J.K.-L., and C.Z. discussed the results. All authors commented on the manuscript.

Additional information

Supplementary Information accompanies this paper at <https://doi.org/10.1038/s41467-018-08178-7>.

Competing interests: The authors declare no competing interests.

Reprints and permission information is available online at <http://npg.nature.com/reprintsandpermissions/>

Journal peer review information: *Nature Communications* thanks Martin Schorb and the other anonymous reviewers for their contribution to the peer review of this work. Peer reviewer reports are available.

Publisher's note: Springer Nature remains neutral with regard to jurisdictional claims in published maps and institutional affiliations.

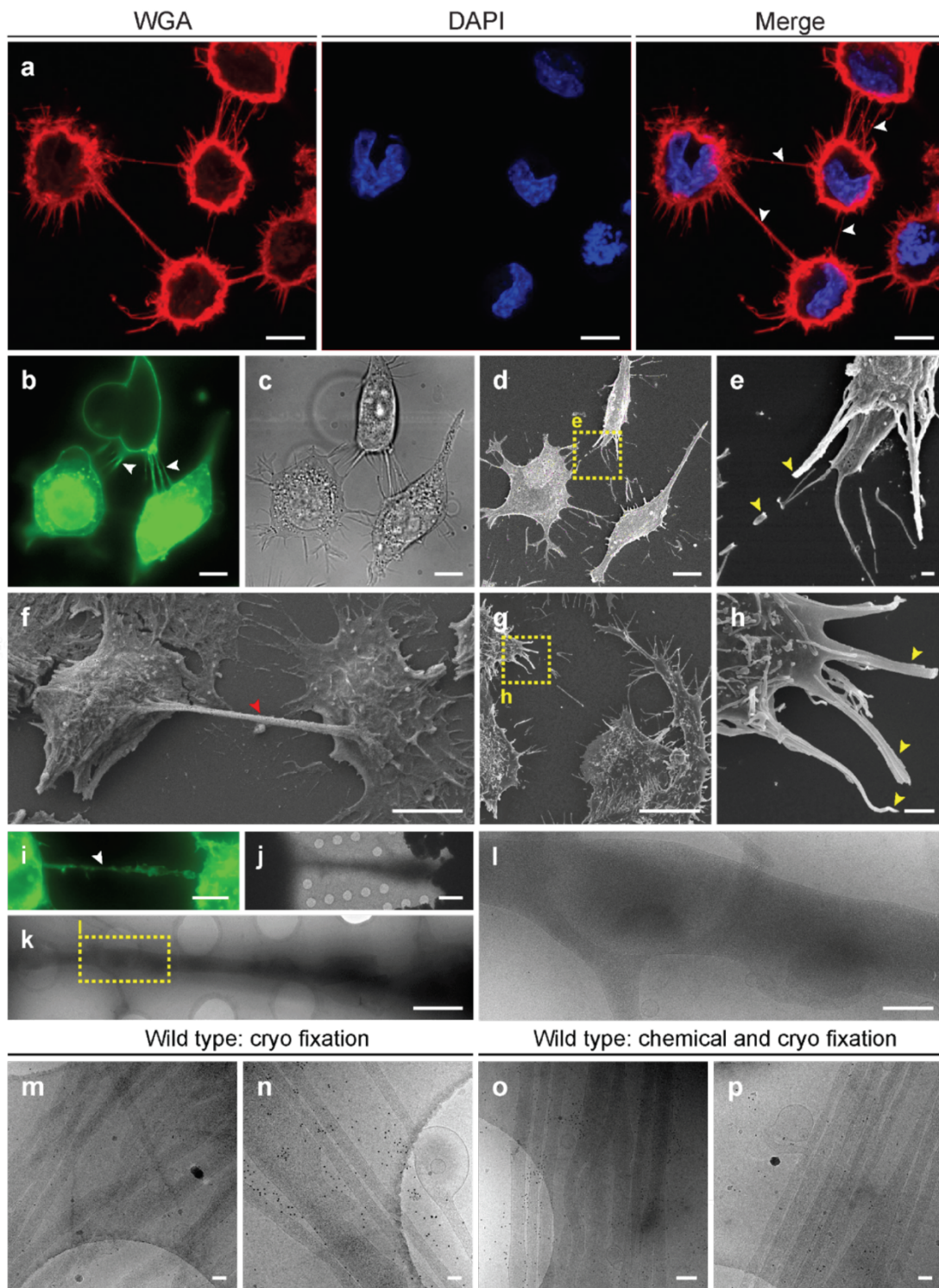


Open Access This article is licensed under a Creative Commons Attribution 4.0 International License, which permits use, sharing, adaptation, distribution and reproduction in any medium or format, as long as you give appropriate credit to the original author(s) and the source, provide a link to the Creative Commons license, and indicate if changes were made. The images or other third party material in this article are included in the article's Creative Commons license, unless indicated otherwise in a credit line to the material. If material is not included in the article's Creative Commons license and your intended use is not permitted by statutory regulation or exceeds the permitted use, you will need to obtain permission directly from the copyright holder. To view a copy of this license, visit <http://creativecommons.org/licenses/by/4.0/>.

© The Author(s) 2019

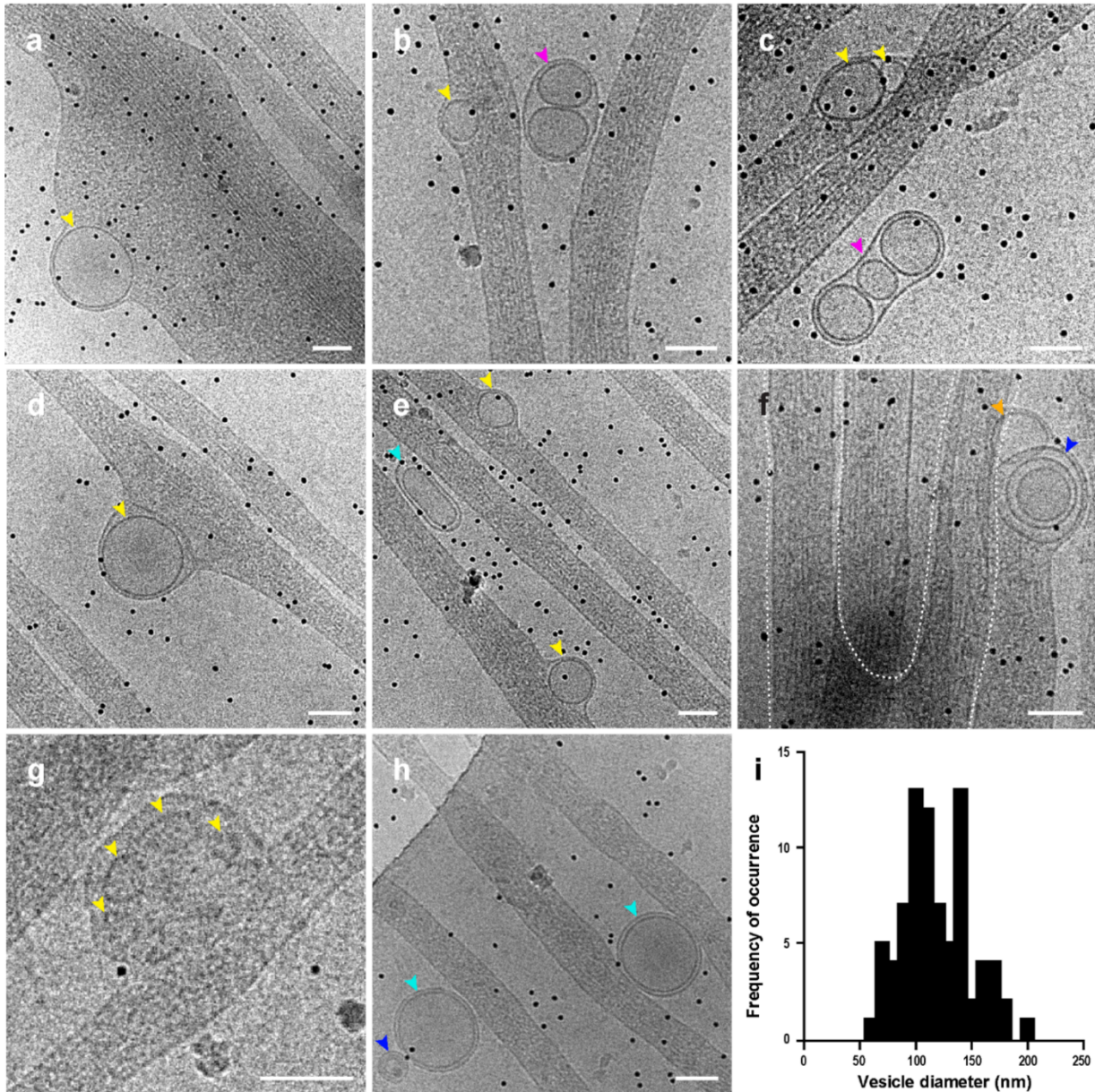
Article 2
Supplementary Material

Supplementary Material



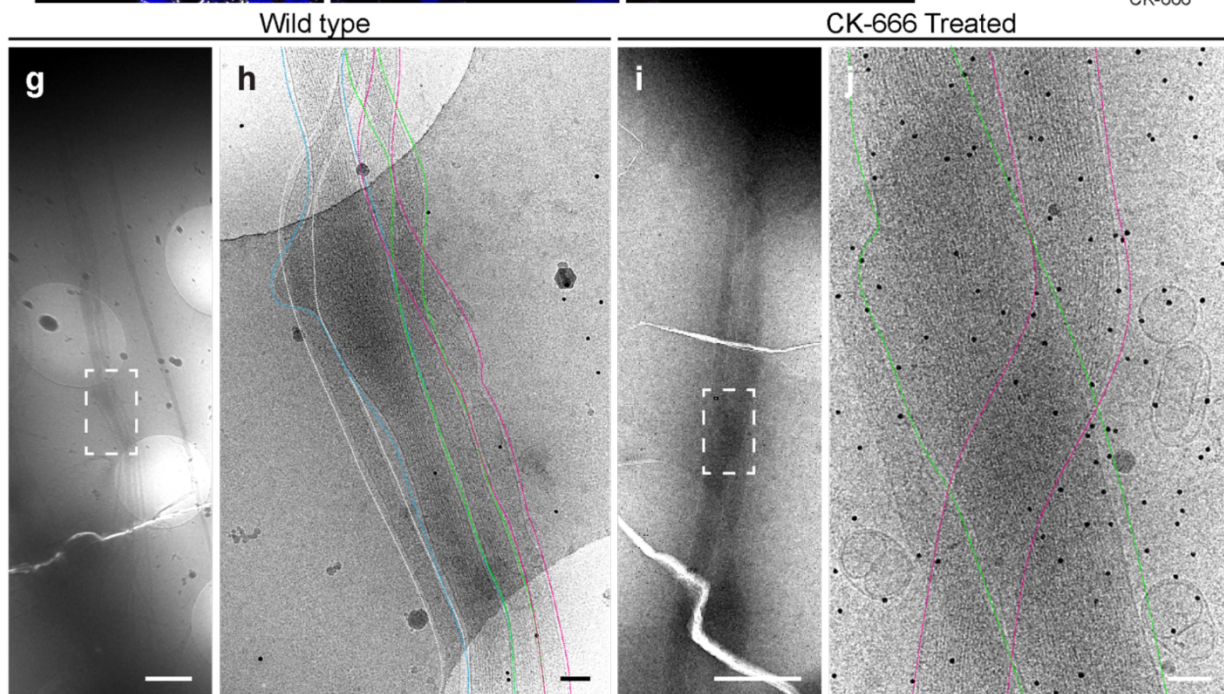
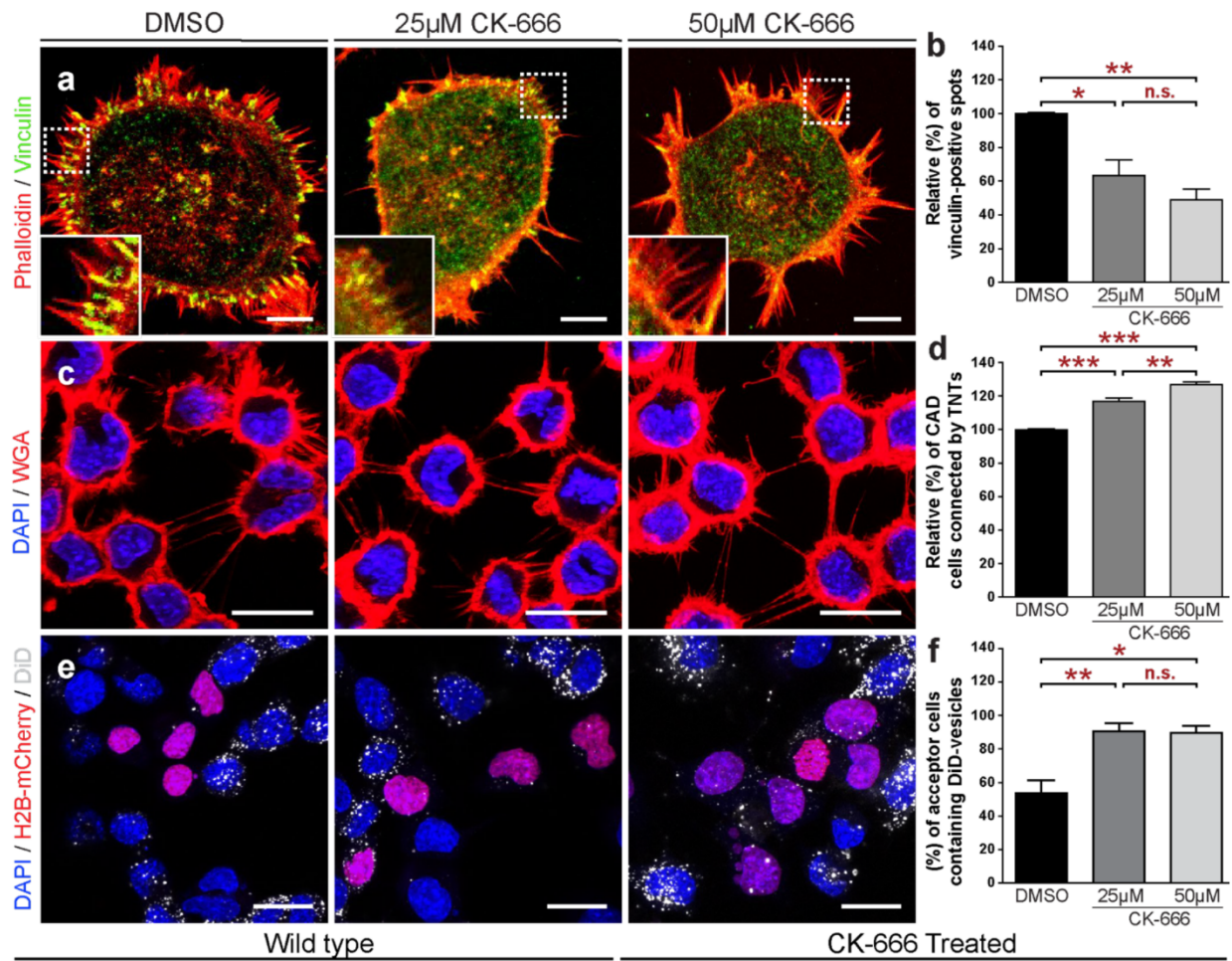
Supplementary Figure 1. Morphology of TNTs in CAD Cells using Fluorescence, Scanning-, and Cryo- Electron Microscopy

(a) Representative confocal micrographs displaying CAD cells stained with WGA (red) to label the plasma membrane and TNTs, and DAPI (blue) to label the nuclei. CAD cells connected via TNTs stained with WGA (green) and imaged by fluorescence (b) and phase contrast (c) microscopy. (d–e) Ultrastructure of CAD cells connected by TNTs in b–c analyzed by SEM at low- (d) and high- (e, yellow dashed box in d) magnification reveals that TNTs break during EM sample preparation. (f) SEM micrograph of CAD cells reveals that only thick TNTs endure EM sample preparation. (g–h) Representative SEM micrographs of CAD cells obtained at low- (g) and high- (h, yellow dashed box in g) magnification reveals that broken TNTs are comprised of single cylindrical units bundled together. (i–l) TNTs in CAD cells imaged by fluorescence (i), low- (j), intermediate (k), and high- (l, yellow dashed boxes in k) magnification cryo-TEM images reveal single, thick TNTs connecting cells. White arrowhead shows TNTs connecting cells by fluorescence microscopy. (m–p) Representative electron micrographs displaying iTNTs connecting CAD cells fixed by cryo fixation (rapid freezing) (m–n), and chemical fixation (o–p), show no differences in structural characteristics, in particular, the presence of parallel actin filaments and vesicular compartments within iTNTs. White arrowheads show TNTs connecting cells by confocal (a) and fluorescence microscopy (b, i). Yellow arrowheads show thin TNTs that break during EM sample preparation (e, h). Red arrowhead shows thick TNTs that endure EM sample preparation (f). Scale bars: a–c, f–g, 10 μm ; d, e, i–j, 500 nm; h, 1 μm ; k, 2 μm ; m–p, 100 nm.



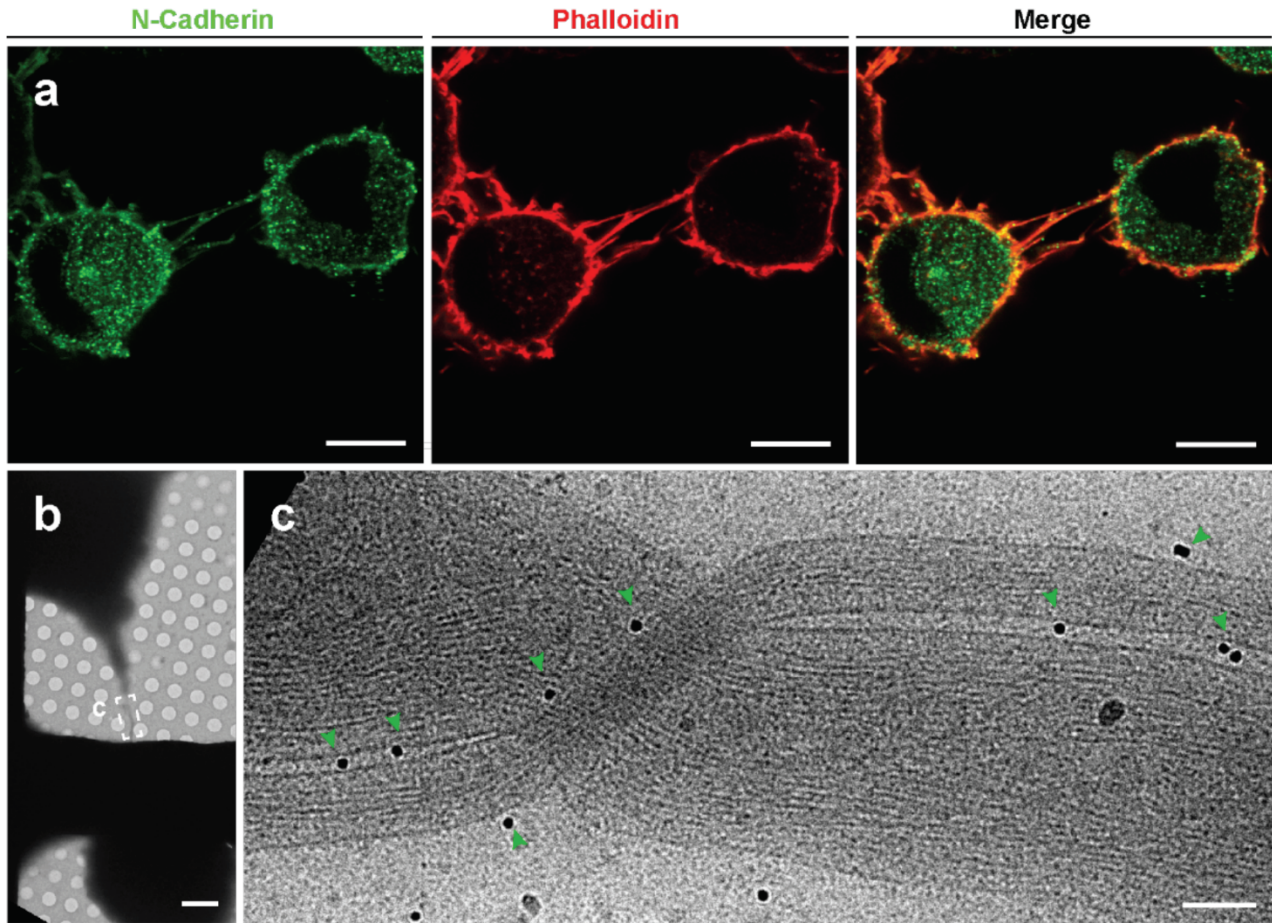
Supplementary Figure 2. Gallery of Different Membrane Compartments Observed Outside and Within iTNTs

(a–h) Representative cryo-electron micrographs of membrane compartments and vesicular structures associated with iTNTs. Blue arrowheads in **f** and **h** indicate vesicles with a multi-lamellar appearance. Yellow arrowheads in **a–g** show single vesicular compartments. Turquoise arrowheads in **e–h** show extracellular vesicles with a double membrane. Pink arrowheads in **b–c** show groups of vesicles surrounded by a secondary membrane. Vesicles squeeze actin bundles together and create a bump on the plasma membrane (**a–g**). (**i**) Distribution of the diameter of vesicles in nm. Scale bars: **a–h**, 100nm.



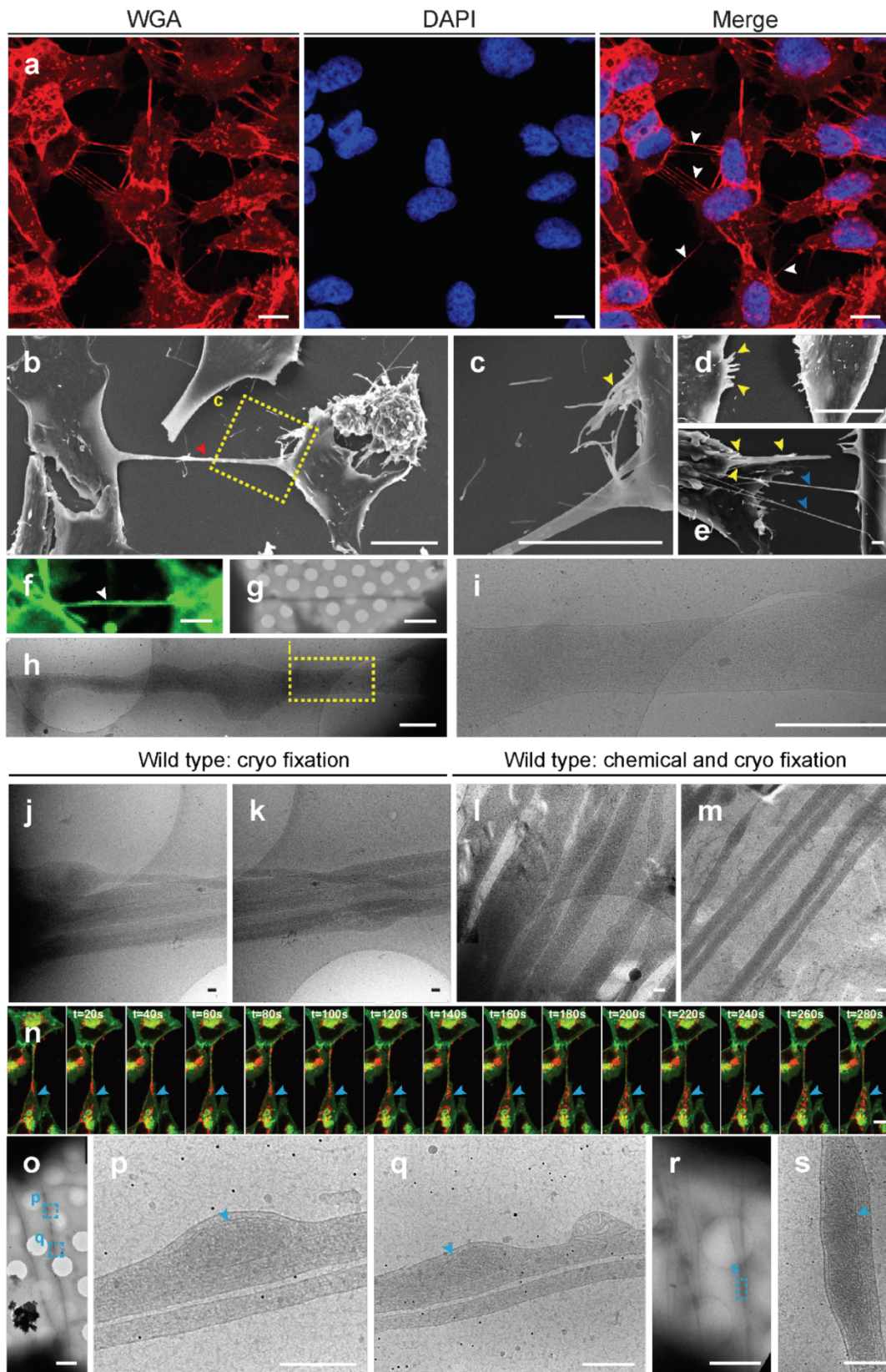
Supplementary Figure 3. Effect of Arp 2/3 Complex Inhibition on TNTs

(a) Representative confocal micrographs displaying CAD cells immunostained with anti-vinculin (green) to label peripheral focal adhesions, and phalloidin (red) to label actin. (b) Statistical analysis of vinculin positive spots after treatment with DMSO and CK-666 (25 μ M and 50 μ M), respectively. Only peripheral focal adherent spots located at the base of the protrusion (insets, a), and found in low focal planes of the projection, were quantified as adherent filopodia. (c) Confocal micrographs showing cells stained with DAPI (blue) and WGA (red) to label the plasma membrane and TNTs. (d) Statistical analysis showing the relative percentage of cells connected by TNTs. TNTs were detected in high focal planes of the projection. (e) Confocal micrographs of the co-culture between cells stained with DAPI (donor and acceptor) (blue), WGA (donor and acceptor) (not shown), DiD (donor) (grey), and transfected with H2B-mCherry (acceptor cells) (red). (f) Statistical analysis showing the percentage of acceptor cells containing DiD-labeled vesicles transferred from donor cells. (g–j) Representative electron micrographs show wild-type (g–h) and CK-666 treated (i–j) iTNTs connecting CAD cells. (g, i) Low magnification cryo-TEM images of TNTs. (h, j) High-magnification electron micrographs correspond to white dashed rectangles in g and i, respectively. (g–j) CK-666 treated TNTs look indistinguishable from untreated controls, which display a bundled and twisted phenotype with actin arranged in a parallel fashion. The plasma membrane of iTNTs were drawn with colored dotted lines in h and j to show membrane boundaries. Scale bars: a, e, 20 μ m; c, 10 μ m; g, i, 1 μ m; h, j, 100nm. Data is represented as mean (\pm SEM), normalized to control cells arbitrarily set at 100% of at least 3 independent experiments. *p < 0.05, **p < 0.005, ***p < 0.0005, n.s. = not significant, according to one-way ANOVA test with Tukey correction.



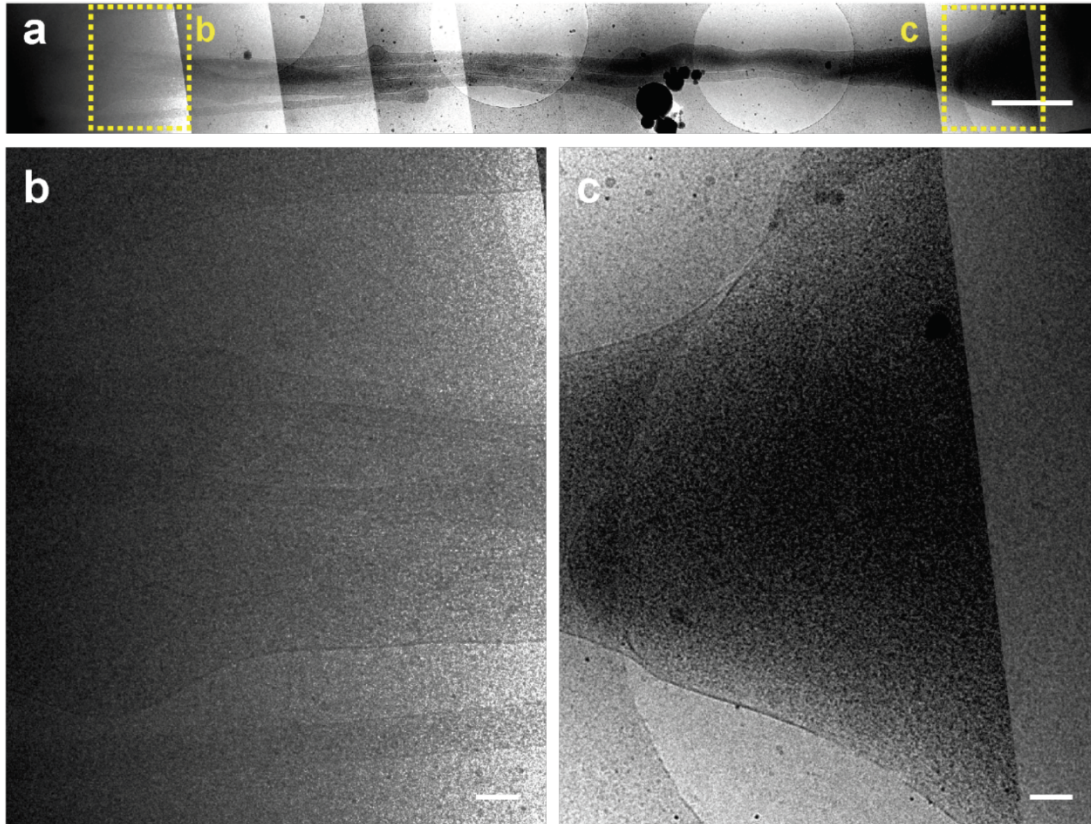
Supplementary Figure 4. N-Cadherin detection on TNTs using CLEM

(a) Confocal micrographs displaying CAD cells connected by TNTs labeled with an anti-N-Cadherin antibody (green) and Phalloidin (red). (b) low magnification electron micrograph of TNT-connected CAD cells immunolabeled with an anti-N-Cadherin primary antibody, followed by a secondary antibody coupled to 10nm gold particles. (c) High magnification cryo-ET slice corresponding to the white dashed rectangle in b. Green arrowheads indicate N-Cadherin gold particles at the surface and between iTNTs. Scale bars: a, 10 μ m; b, 5 μ m; c, 100 nm.



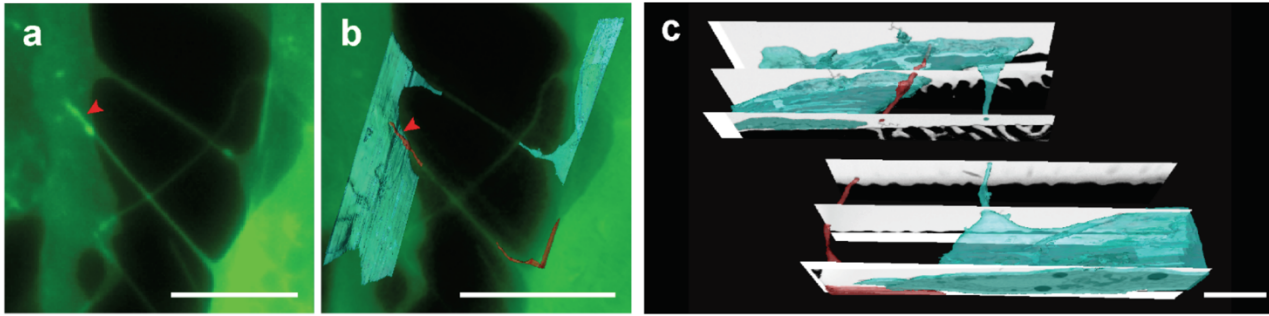
Supplementary Figure 5. Structural and Functional Analysis of TNTs in SH-SY5Y Cells

(a) Representative confocal micrographs displaying SH-SY5Y cells stained with WGA (red) to label the plasma membrane and TNTs, and DAPI (blue) to label the nuclei. (b–e) SEM micrograph of SH-SY5Y cells obtained at low- (b) and high- (c, yellow dashed box in b) magnification reveals that single thick TNTs endure EM sample preparation, while thin ones bundled together break. White arrowheads show TNTs connecting cells by fluorescence microscopy (a). Yellow arrowheads show thin TNTs that break during EM sample preparation (c, d, e). Red arrowheads show thick TNTs that endure EM sample preparation (b). Blue arrowheads show an example of thin TNTs in SH-SY5Y cells enduring EM sample preparation (e). (e–i) TNTs in SH-SY5Y cells imaged by fluorescence (f), low- (g), intermediate- (h), and high- (i), yellow dashed boxes in h magnification cryo-TEM images reveal single, thick TNTs connecting cells. White arrowheads in f show TNTs connecting cells by fluorescence microscopy. (j–m) Representative electron micrographs displaying iTNTs connecting SH-SY5Y cells fixed by cryo fixation (rapid freezing) (j, k), and chemical fixation (l, m), show no differences in structural characteristics. (n) Time-lapse images of wild-type SH-SY5Y cells stained with WGA (green) and MitoTracker (red) show mitochondria traveling across a TNT unidirectionally and accumulating in the cytoplasm of the neighboring cell (blue arrowhead). Image intensity was increased to better visualize (thin) TNT connecting the two cells. (o, r) Low magnification cryo-TEM micrographs of SH-SY5Y cells connected by iTNTs. (p, q, s) High magnification cryo TEM images of TNTs shown in o, r, containing mitochondria (blue arrowheads) within tubes. Images reveal mitochondria stretched inside tubes, surrounded by actin filaments. Scale bars: a–d, n, 10 μm ; e, 1 μm , f, g, 5 μm ; o, r, 2 μm ; h, i, 500 nm, j–m, p, q, s, 100 nm.



Supplementary Figure 6. iTNT Contact Sites by cryo-TEM

(a) Collage of high magnification cryo-TEM micrographs of SH-SY5Y cells connected by iTNTs. (b–c) High magnification cryo TEM micrographs of TNT contact zones shown in a (yellow dashed rectangles). Images reveal that the ice formed around the periphery of cells, including the ends of iTNTs, is too thick for the electron beam to go through. Scale bars: a, 1 μ m; b, c, 100nm.



Supplementary Figure 7. FIB-SEM of TNTs in SH-SY5Y Cells Reveal Open-Ended Contact Sites

(a) Confocal micrograph of SH-SY5Y cells stained with WGA (green). (b) Overlay of 3D rendering of FIB-SEM tomogram segmentations over fluorescent counterpart reveal two connections: one open-ended TNT, and one invaginating inside the cytoplasm of the opposing cell (red arrowhead). (c) 3D rendering of FIB-SEM tomogram segmentation shown in b. Scale bars: a–b, 10µm; c, 3µm.

Chapter 4

4 Mapping of Tunneling Nanotube-Like Structures In the Developing Cerebellum

4.1 Introduction

Identifying TNTs in complex organisms is one of the most outstanding challenges in the field of TNT-based cell-to-cell communication research. As described in *Chapter 1*, the lack of specific markers or antibodies that label TNTs and limitations in resolution of optical microscopy have hampered our ability to address this question, and therefore, to test whether the function of TNTs *in vitro* translate *in vivo*. In order to circumvent these limitations, I sought out to investigate the existence of TNTs in wild-type tissue using a “label everything, see everything” structural approach known as *Connectomics*, a method designed to study connectomes, (comprehensive maps of connections within the CNS).

In the remaining sections of this chapter, I will give an overview of the neurobiology field of Connectomics, with an emphasis on structural (nanoscale) connectomics. I will then discuss how this type of connectomic approach can be utilized for the identification of TNT-like structures in tissue, and specifically, between progenitor cells in postnatal mouse development. In my results, I will describe the connectomic datasets used, the identification of TNT-like structures in these datasets, and immunohistological and dye-coupling experiments that corroborate my structural findings. Thereafter, I will explain all of the experimental methods used throughout this project. Finally, I will discuss the main results of this work and consider possible directions for future studies based on these results.

4.1.1 Connectomics

The first classical map of the human brain connectome dates back to 1909 ([Zilles, 2018](#)), a map widely used today. Presently, the connectome is studied at several orders of magnitudes; structural connections (physical wires and synaptic pathways), functional connections (macroscale interactions between brain regions), and in between the two, connections visible by optical microscopy.

4.1.1.1 Nano-Connectomics: Wiring Diagrams

Understanding how the complex wiring of the brain is structured gave birth to the neuroscience field of *Connectomics*. Structural wires are acquired from EM, which can image specimens down to the level of individual ion channels and synaptic vesicles. With the development of 3D, serial-sectioning SEM (ssSEM), specific subcellular components and complete arborization of specific neurons can be unambiguously identified. Entire volume datasets are now publicly available for brain tissues of the adult fruit fly brain (Zheng et al., 2018), larval fish (Hildebrand et al., 2017), and some regions of the mouse, such as the neocortex (Kasthuri et al., 2015), and primary visual cortex (Bock et al., 2011). These “wiring diagrams” have proved extremely useful for understanding circuit function (Lichtman and Sanes, 2008) and intra-cellular connectivity (Figure 16) (Kasthuri et al., 2015; Schmidt et al., 2017; Zonouzi et al., 2019).

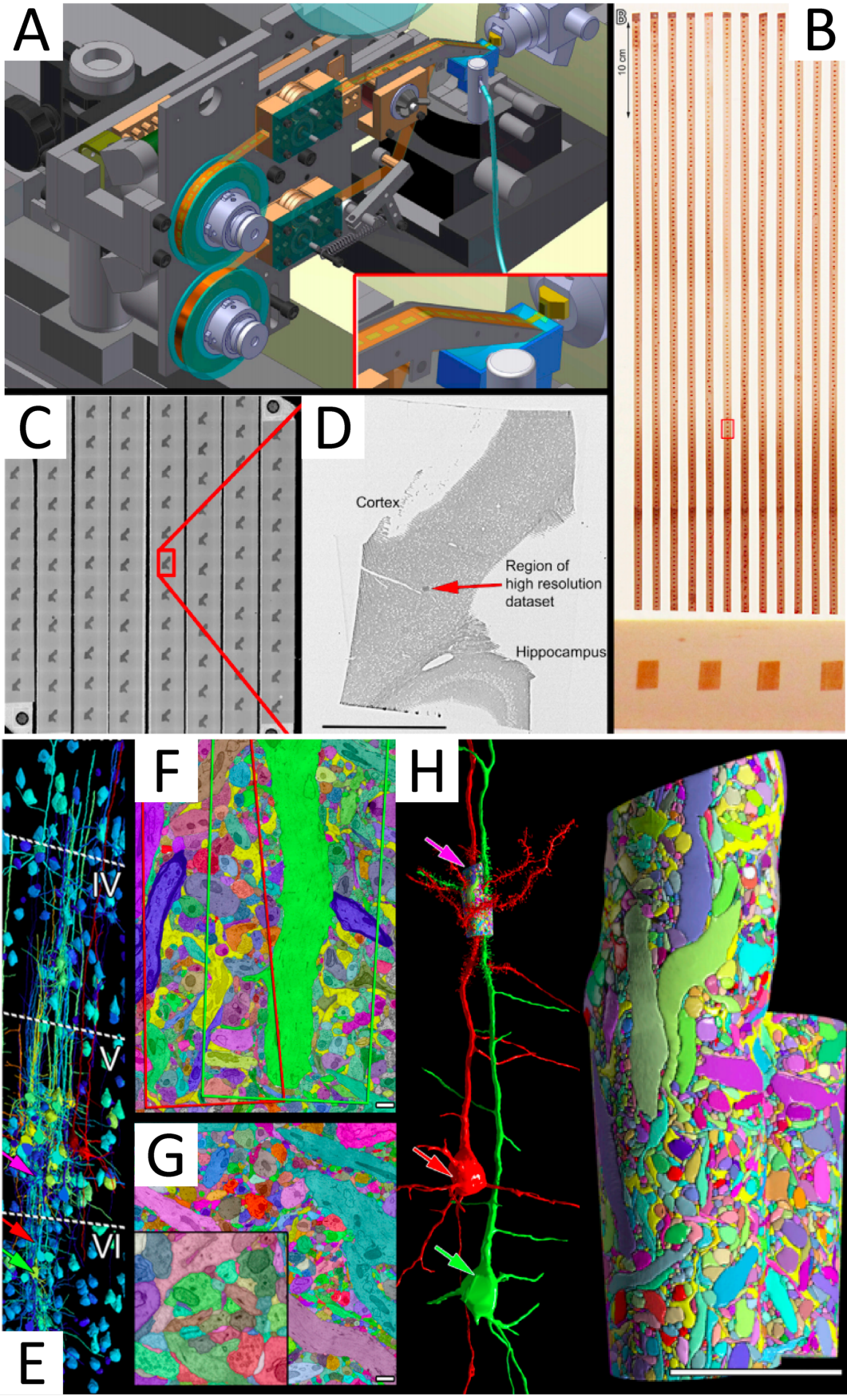


Figure 14. Connectomics by serial-sectioning scanning electron microscopy.

(A) Schematic diagram depicting an automated tape-collecting ultramicrotome (ATUM). Procedure as described by [Kasthuri et al., 2015](#): The bottom reel of the ATUM contains a plastic tape that is fed into the knife boat of a diamond knife mounted on a commercial ultramicrotome. The tape is collected on a take-up reel (top). (Red inset) Close-up view of the tape conveyor positioned in the knife boat. The diamond knife boat (dark blue) is filled with water (light blue). The diamond knife (green rectangle) is at the opposite end of the knife boat from the taping mechanism. It cuts serial ultrathin sections from tissue embedded in a plastic block. The sections then float on the surface of the water in the knife boat until they adhere to the moving tape. (B) 10 m of Kapton tape with 2,000 sections collected. Four of the 29-nm sections (red rectangle) are shown at a higher magnification at the bottom of the panel. (C) The reel of tape is then cut into individual strips and mounted on silicon wafers for post-staining and/or carbon coating. A low-power scanning electron microscopy image of part of a wafer containing 85 brain sections is shown. One of the sections (red rectangle) is shown at a higher magnification in the next panel. (D) One 29-nm section containing neocortex and hippocampus. The region that was studied at high resolution is the dark-looking box (red arrow). Scale bar, 1 mm. (E) Cortical neuronal somata reconstruction to aid in cortical layer boundaries (dotted lines) based on cell number and size. Large neurons are labeled red; intermediate ones are labeled yellow; and small ones are labeled blue. The site of the saturated segmentation is in layer V (pink arrow). These two layer VI pyramidal cell somata (red and green arrows) give rise to the apical dendrites that form the core of the saturated cylinders. (F) A single section of the manually saturated reconstruction of the high-resolution data. The borders of the cylinders encompassing the “red” and “green” apical dendrites are outlined in this section as red and green quadrilaterals. This section runs through the center of the “green” apical dendrite. (G) A single section of a fully automated saturated reconstruction of the high-resolution data. Higher magnification view (lower left inset) shows 2D merge and split errors. (H, left) The two pyramidal cells (red and green arrows) whose apical dendrites lie in the centers of the saturated reconstructions. Dendritic spines reconstructed in the high-resolution image stack only. (H, right) The saturated reconstruction volume. Images obtained from [Kasthuri et al., 2015](#).

4.1.2 From Connectomics to Tunneling Nanotubes: Paving the Road

Due to their small size, and the lack of a TNT-specific marker, nano-Connectomics via ssSEM is the best suited approach. Over the next sub-sections, I will describe the cells and developmental stage in which we hypothesize TNT-like structures can be found *in vivo*.

4.1.2.1 Neuronal Tunneling Nanotubes

TNTs have been identified and described in various neuronal cell lines (e.g. PC12 ([Rustom et al., 2004](#)), CAD ([Gousset et al., 2009](#)), and SH-SY5Y ([Sartori-Rupp et al., 2019](#)) cells) and primary Schwann cells ([Zhu et al., 2016](#)). A previous study from our group also showed that primary cerebellar granule neurons (CGNs) transferred mutant Htt aggregates onto other CGNs in a cell-to-cell contact-dependent manner ([Costanzo et al., 2013](#)). A common factor that characterizes neuronal cells in which TNTs, or functional changes in which TNTs could be used as a mode of communication, is their undifferentiated and precursor state (see also ([Grudina et al., 2019](#)) and ([Vargas et al., 2019](#))). Combined, these features sparked our interest in progenitor cells.

4.1.2.2 *In Vivo* Tunneling Nanotube-like structures

As previously described in *Chapter 1*, *in vivo* TNT-like structures have previously been reported during early stages of development, where cues necessary for migration and coordination could be shared inter-cellularly. These observations argue that TNTs could be used as a mechanism of inter-cellular communication between cells that haven't yet developed other modes of communication (e.g. synapses), and support our work showing undifferentiated or non-polarized neuronal cells and undifferentiated human neuronal precursor cells (hNPCs) ([Grudina et al., 2019](#)) forming TNTs in culture.

4.1.3 Survey of the Developing Cerebellum for Tunneling Nanotubes

4.1.3.1 Cerebellum Anatomy and Ontogenesis

The cerebellum is a major feature of the hindbrain, playing vital functions in the control of gaze, gate, posture, motor learning, and prediction of moments ([Manto et al., 2012](#)).

Anatomically, the cerebellum comprises three layers that make up the cerebellar cortex: the outermost, ‘molecular layer’ (ML), where Golgi, stellate, and basket cells reside; the middle, ‘Purkinje cell layer’ (PCL), where Purkinje cells sit side by side in a 1-cell-thick layer; and the Inner Granular Layer (IGL), where granule cells (GCs) live.

During the first few weeks of postnatal development, the cortical layer of the cerebellum undergoes severe transformations. GCs, the most abundant cell in the cerebellum (Fox and Barnard, 1957), reside in a transitory, mitotically and migratory active region called the external granule layer (EGL). The EGL forms at embryonic day 15 (E15) and GC progenitors (GCPs) continue to divide until the third week of postnatal development (Espinosa and Luo, 2008). After division, GCPs undergo two modes of migration, tangential, which takes place in the EGL, and radial, which takes place across the ML and PCL (Figure 17) (Galas et al., 2017; Komuro and Kumada, 2005; Komuro and Yacubova, 2003).

4.1.3.2 External Granule Layer

The EGL comprises two sub-layers, the outer EGL (oEGL), where GCPs proliferate, and the inner EGL (iEGL), where GCPs migrate. After their final division in the oEGL, GCPs in the neonatal cerebellum orchestrate radial and tangential migrations from the EGL to the IGL without synapse-mediated interactions, as first observed by Cajal in the late 1800s (Cajal, 1888). Improper migration of GCPs can have detrimental effects on the anatomy of the cerebellar cortex and lead to neurological disorders such as dystonia, ataxia, and psychiatric conditions such as autism spectrum disorders (Lackey et al., 2018). We hypothesize that GCPs use TNT-like structures to communicate with each other during migratory movements, prior to synapse formation. To this end, I studied GCPs in the neonate developing cerebellum using ssSEM nanoscale Connectomics. GCPs feature different morphologies depending on their location within the EGL. GCPs in, or close to the oEGL have spherical cell somas with few, if any, protruding neurites. Postmitotic GCPs in the iEGL feature typical morphology of migrating neurons, elongated somas, a leading process, and a thin trailing neurite oriented in the opposite direction (Figure 18).

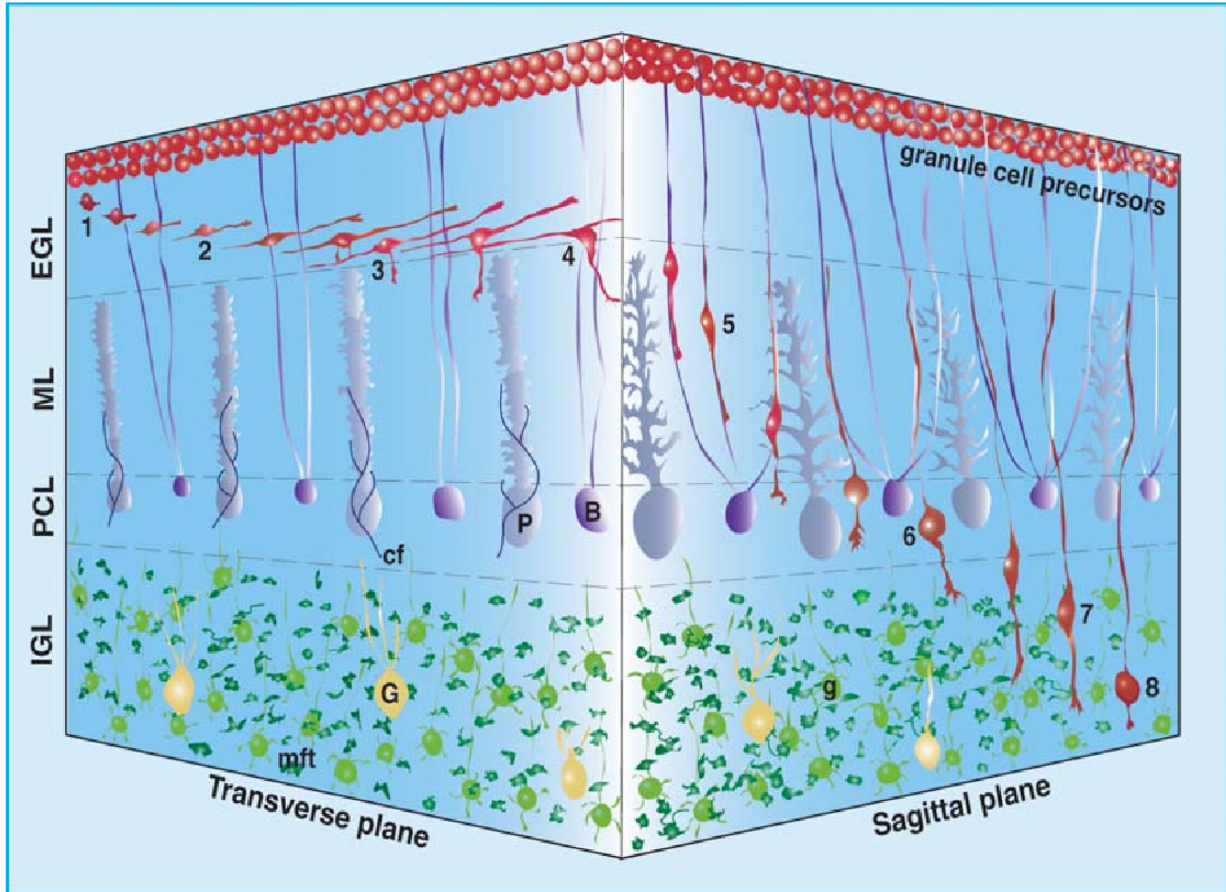


Figure 15. Cerebellar granule cell migration during development.

Schematic diagram depicting a 3D representation of GCP migration from the EGL to the IGL. (1) Extension of two uneven horizontal processes near the top of the EGL. (2), tangential migration in the middle and bottom of the EGL. (3) Bergmann glia- (BG) associated radial migration in the ML (4) stationary state in the PCL. (5) glia-independent radial migration in the IGL. (6), completion of migration in the middle or the bottom of the IGL. Image obtained from (Komuro and Yacubova., 2003).

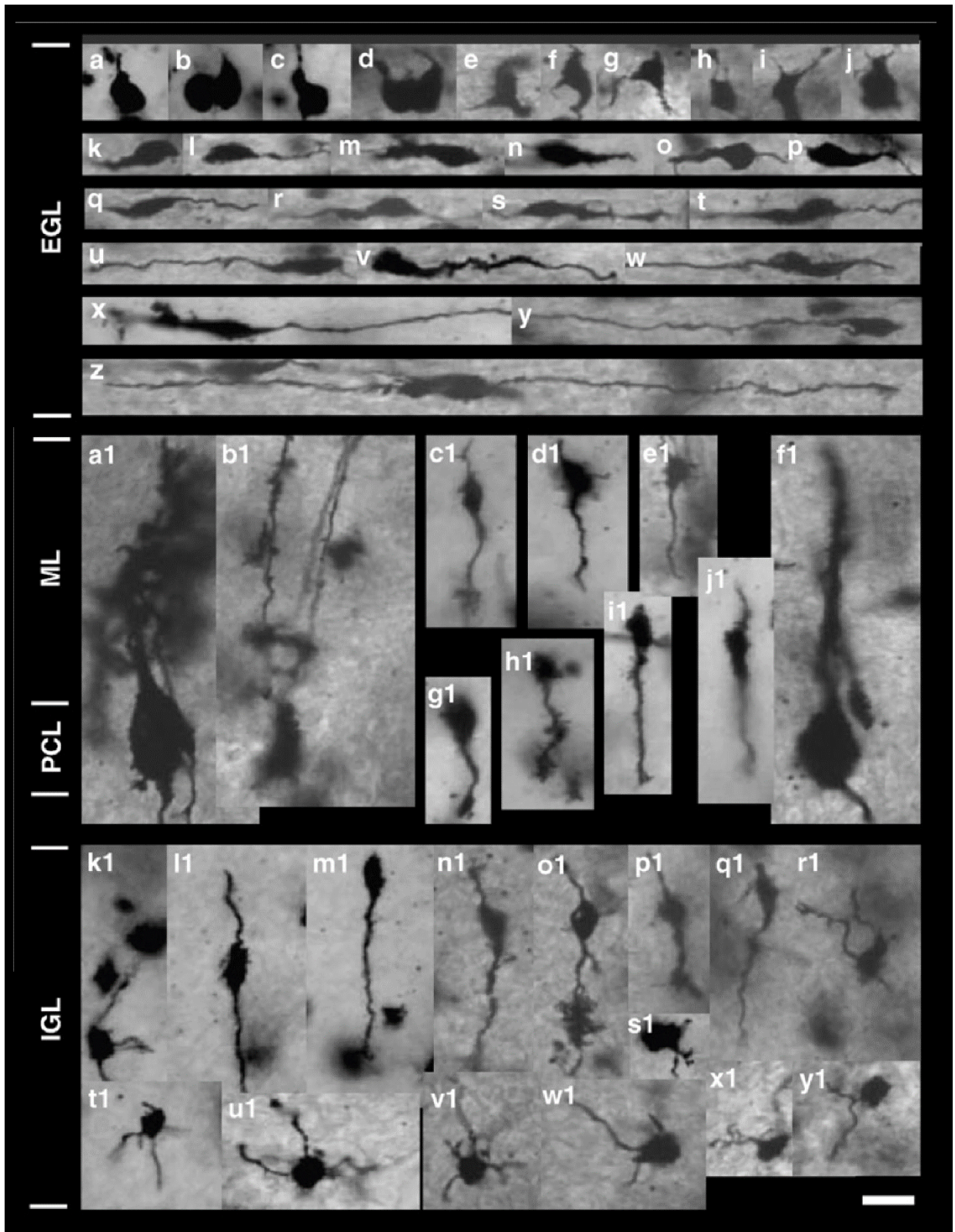


Figure 16. Granule cell progenitor morphology characterization.

Light microscopy micrographs showing the changes in the morphology of granule cells in a P10 mouse cerebellum revealed by Golgi-staining. **(A-J)**, GCPs at the top of the EGL. **(K-Z)**, tangentially migrating GCPs at the middle and bottom of the EGL. a1 and f1, Purkinje cells. b1, Bergmann glial cells. **C1-E1** and **G1-J1**, radially migrating granule cells in the ML. **K1** and **R1-Y1**, postmigratory granule cells in the IGL. **I1-Q1**, radially migrating granule cells in the IGL. Scale bar: **A-Y1**, 10 μm . Image obtained from ([Kumada et al., 2009](#)).

4.2 Results

4.2.1 Datasets

To gain insight into the connectivity and cell-to-cell interactions made by GCPs in the EGL, we studied three large-scale ssSEM datasets of the cerebella of mice at P0, P3, and P7 postnatal stages of development, spanning $5.5 \times 10^5 \mu\text{m}^3$, $1.1 \times 10^6 \mu\text{m}^3$, and $1.7 \times 10^6 \mu\text{m}^3$, respectively (**Figure 11**). All three volumes are columns of cerebellar tissue; in P0 reaching from the pia down to the ML, and in P3 and P7 reaching down to the white matter ([Wilson et al., 2019](#)).

Volumes were cut sagittal using an automatic tape-collecting ultramicrotome (ATUM) ([Kasthuri et al., 2015](#)) at 30 nm thickness. A total of 1450 sections for the P0 block, 2658 sections for the P3 block, and 2514 from the P7 block were used for imaging by SEM. The sections were placed on wafers and images were acquired at 4nm/px in lateral resolution (see methods).

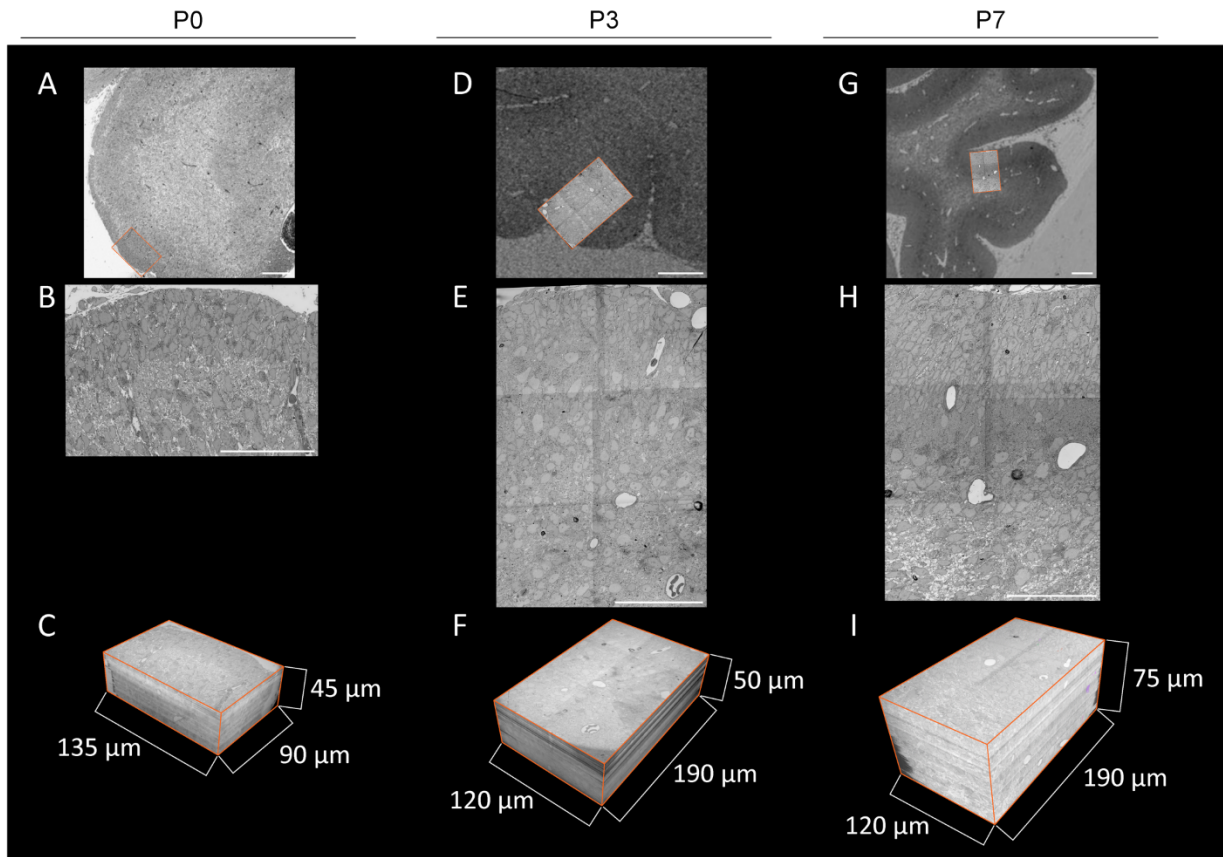


Figure 17. Datasets produced by Serial-Sectioning Scanning Electron Microscopy.

(A, D, & G) Low-resolution electron micrographs of a single section from P0, located in the crown of a folia; P3, located at the edge of the crown; and P7, located at the base of the fissure, respectively. The subregion that was imaged at high-resolution is superimposed onto each section. (B, E, and H) High-resolution electron micrographs of single superimposed images shown in A, D, and G, respectively. (C, F, and I) Electron micrograph volume collected in P0 (x, 135 μm ; y, 90 μm ; z, 45 μm), P3 (x, 120 μm ; y, 190 μm ; z, 50 μm), and P7 (x, 120 μm ; y, 190 μm ; z, 75 μm). Scale bars: A, D, and G, 100 μm ; B, E, and H, 50 μm .

4.2.2 GCPs form Tunneling Nanotube-like connections

For our study, we examined the existence of TNT-like structures between GCPs by identifying and performing a comprehensive screening of GCPs located in the EGL of our high-resolution volumes. Using accepted topological and positioning criteria (Komuro and Yacubova, 2003), we traced the cell soma and every emanating protrusion from 160 cells at P0, 70 cells at P3, and 60 cells at P7, and identified 14, 8, and 48 connected cells in pairs, respectively, which correspond to 7, 4, and 24 connections (Figure 12). These findings account for an 8.7%, 11%, and 80% of the total percentage of cells screened connected (Table 1).

Table 1. Cells connected by TNT-like structures over development.

	P0	P3	P7
# of cells screened	160	70	60
# of connections	7	4	24
% of cells connected	8.7	12	80

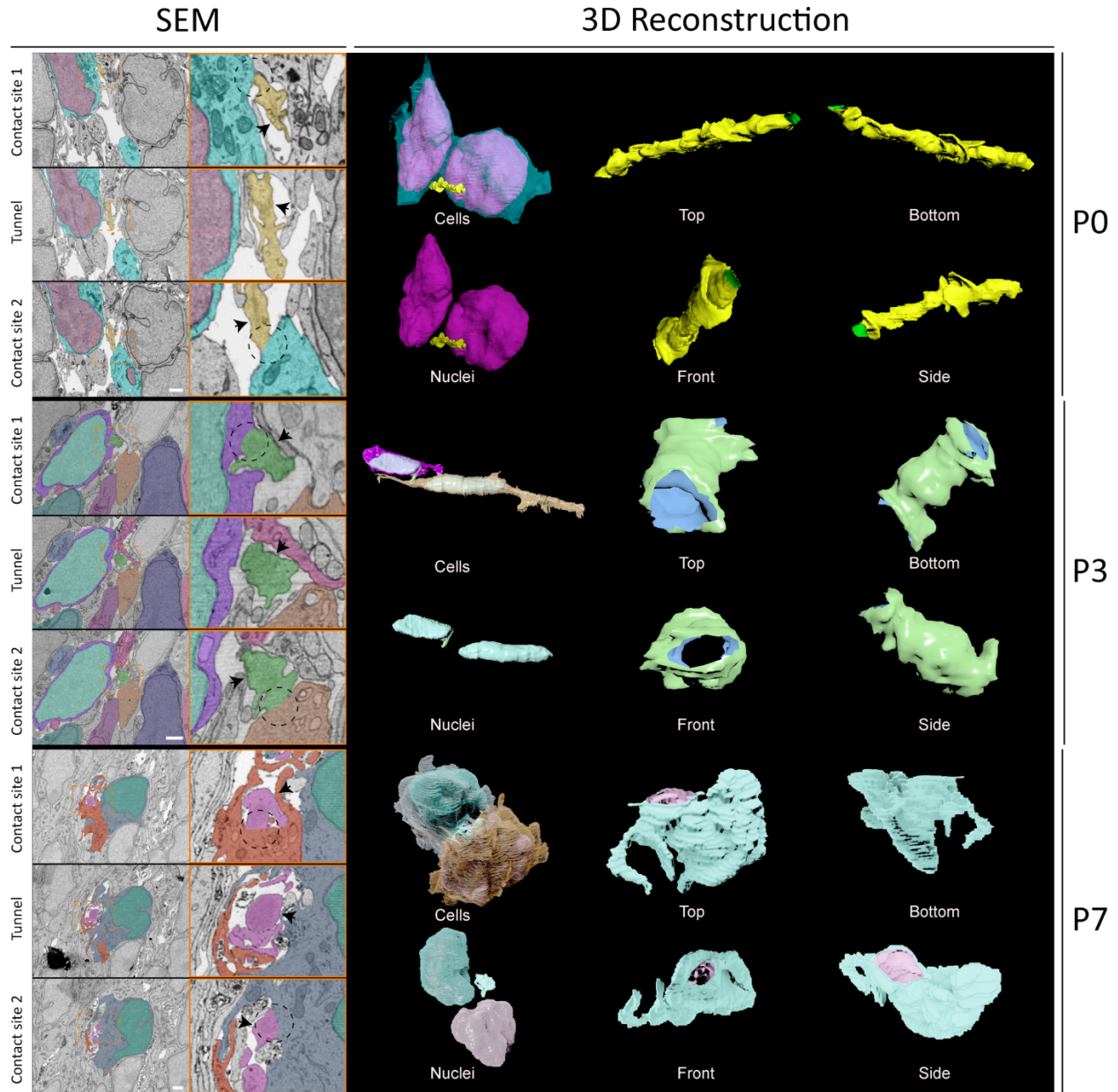


Figure 18. ssSEM Reveals TNT-like connections between GCPs.

Segmented EM images and corresponding 3D reconstructions of TNT-like connections identified at P0, P3, and P7. Raw EM images capture the points of fusion to each of the two connected cells and an intervening slice between both cells. 3D reconstructions illustrate the plasma membranes of the connected cells along with their nuclei and the connection (Cells), the position of the connection relative to the nuclei alone (Nuclei) and the connection alone in top, bottom, front and side orientations. The points of fusion of the tunnel with the connected cells are indicated by a different color inside the connection. Scale bar = 1 μ m.

4.2.3 3D skeletonization of meshes reveals geometrical features.

In order to extract relevant geometrical information (e.g. length and diameter) from the TNT-like structures identified in our ssSEM datasets, we turned to simplifying our connections down to a single-wire curve-skeleton via Kimimaro (see methods), a derivation of the *Tree-structure Extraction Algorithm delivering Skeletons that are Accurate and Robust* (TEASER) (Sato et al., 2000). Kimimaro smoothens the 3D connection mesh and contracts it into a 1-dimensional “wire”, abstracting its shape and topology, all while maintaining connectivity. Through Kimimaro, we obtained the geometries of 3 TNT-like structures identified in our P3 volume with lengths that span 3 – 4 μm and widths of 113 – 265 nm (Example shown in **Figure 21**).

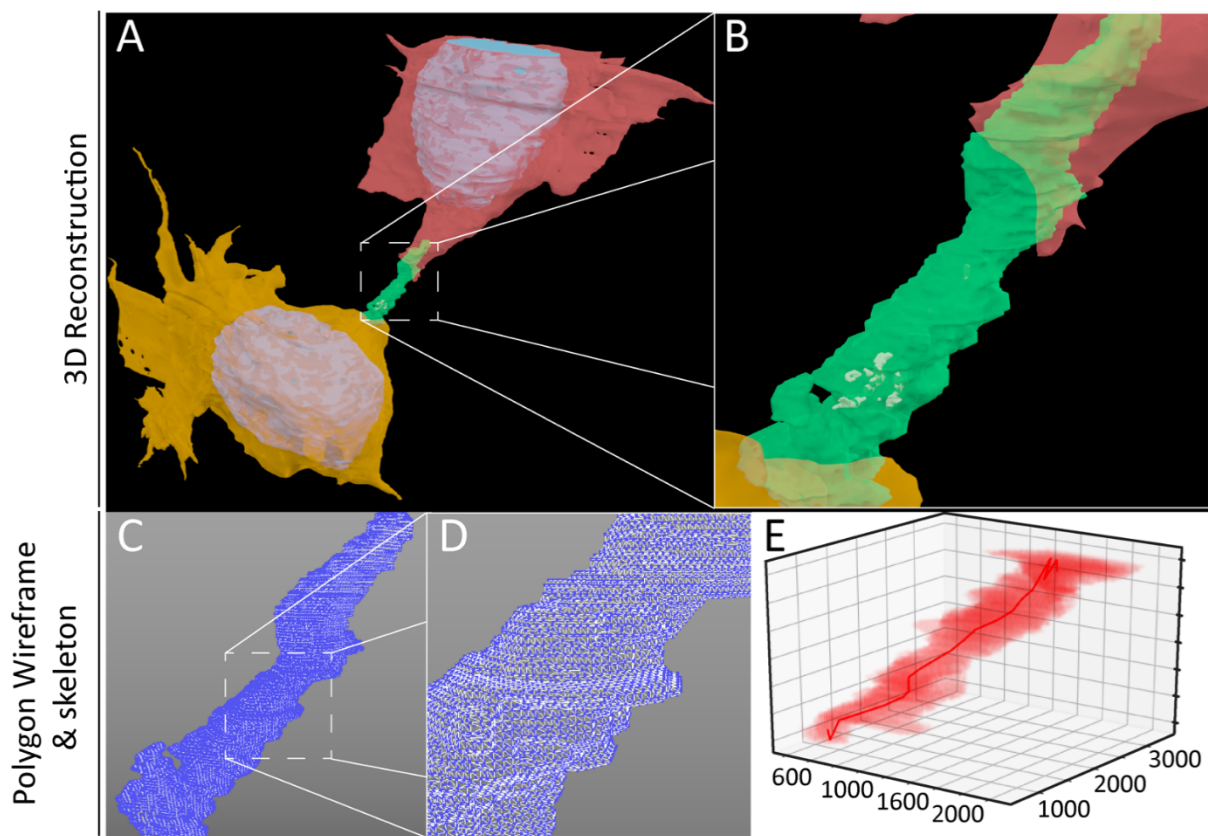


Figure 19. Skeletonization of TNT-like connections.

(A) 3D reconstruction of GCPs connected by a TNT-like protrusion (green) containing small vesicles (gray). (B) Crop of the connection shown in A (white, dashed box). (C and D) 3Ds Max-rendered polygon wireframe of reconstructions shown in A and B, respectively. (E) 3D representation of the reconstruction (red cloud) and single wire obtained by Kimimaro (solid red). Mean length = 4,025 nm; Mean radius = 189.6 nm; Min radius = 113.2 nm; Max radius = 265.9 nm.

4.2.4 Orientation of GCP-GCP vs. dividing GCPs

Due to the higher rate of cell division in the EGL, we needed a method to determine if connected GCPs were indeed evidence for the existence of TNT-like connections or simply remnants of cellular division such as mitotic intercellular bridges or stable intercellular bridges formed by incomplete cytokinesis (Haglund et al., 2011).

Due to existing classifications and studies with information on the spatial orientation of dividing GCPs through many early postnatal developmental stages (Haldipur et al., 2015; Miyashita et al., 2017), we decided to focus on creating a similar classification of our cells connected. Specifically, previous studies have described that finding whether the angle between the pia membrane that envelops the brain and the plane of division between the cells is perpendicular or parallel is a very simple yet effective manner in providing a criterion for defining spatial orientation of cells. By using fluorescence data and this method of analysis, it has been shown that dividing GCPs in P0-P7 developmental stages are either non-discriminant in being either parallel or perpendicular in relation to the pia membrane or that they are predominantly parallel (Haldipur et al., 2015; Miyashita et al., 2017).

Overall these studies outline that an effective way to analyze spatial orientation is through measuring the difference in alignment between the pia membrane that envelops the brain and the plane that divides two cells, in our case bound by a TNT-like structure. Thus, spatial orientation of our connected cells was carried out through comparing their orientation in 3D in relation to the pia membrane. Cell pairs were then classified as either being parallel or perpendicular depending on the angle ϕ between the cell and pia plane (see methods). If the ϕ angle was $<45^\circ$, cells were classified as parallel (**Figure 22, C-G**), while if the ϕ was between $45 - 90^\circ$, cells were classified as perpendicular (**Figure 22, H-L**). Using this system of classification (**Figure 22, A-E**), we found that 100% of cell pairs were perpendicular in P0 (n=5), 75% in P3 cell (n=4), and 75% in P7 (n=12). Similarly, the average of all angles in P0 was 74.6° , 65.7° in P3, and 62.8° in P7, all of which are above the 45° perpendicular threshold. Next, through conducting a two-tailed, unpaired t-test, we found that all stages (P0-P7) had a significant (**, $p=0.0048$) tendency for connected cell pairs to be perpendicular to the pia in orientation (n=21).

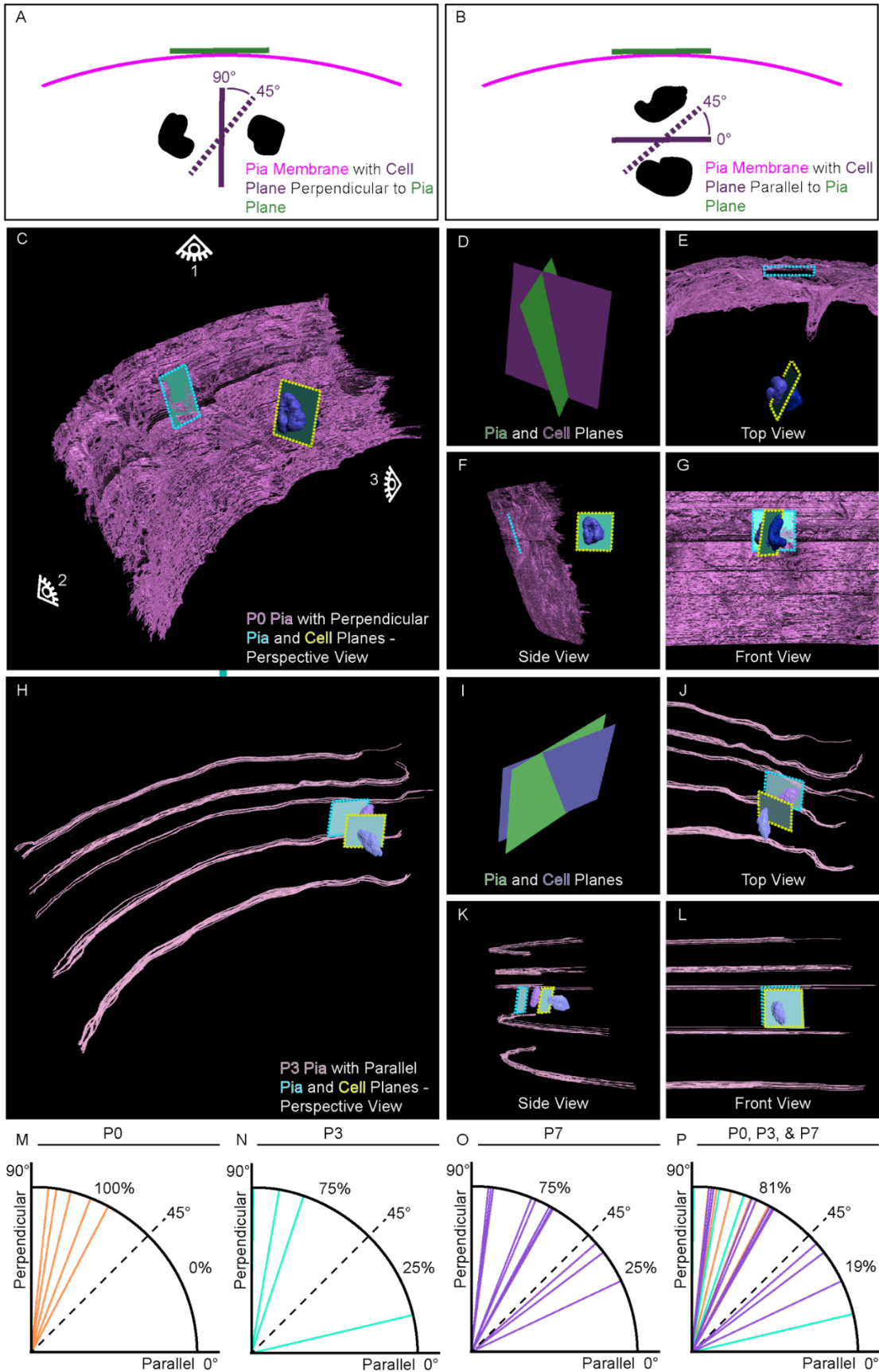


Figure 20. Connected GCPs exhibit perpendicular orientation.

(A) 2D schematic diagram displaying an example of a perpendicularly aligned cell plane (dark purple) and pia plane (green). The cell plane is shown to divide and split the connected cell pair (black) into two parts and the pia plane is shown to be tangential to the pia membrane (pink) at the point closest to the connected cell pair. The dashed purple line shows that perpendicular alignment is characterized by plane ϕ angles in between 45° and 90° . (B) Shows an example of parallel aligned pia and cell planes (color code shown as in A). The dashed purple line shows that parallel alignment is characterized by plane ϕ angles in between 0° and 45° . (C) Gives the perspective view of an example of perpendicularly oriented pia planes (light blue dashed edges) and cell planes (yellow dashed edges), with the pia plane tangential to the P0 pia membrane and the cell plane dividing the two nuclei in the 3D space. The eye symbols represent the different types of viewpoints presented in figures E-G and J-L, with “1” being the Top View, “2” being the Side View, and “3” being the Front View. (D) Shows the pia (green) and cell (purple) planes overlaid in the same spot with perpendicular planes being over 45° from each other. (E-G) Shows assortment of top, side, and front views of the perspective view from C (colors preserved from C). (H) Perspective view of P3 parallel oriented pia and cell planes (colors preserved from C). (I) Shows pia and cell planes overlaid in the same spot with parallel planes being under 45° difference from each other (colors preserved from D). (J-L) Shows assortment of top, side, and front views of the perspective view from H (colors preserved from C). (M-O) Visual distribution and spread of all ϕ angle measurements of every pair of connected cells. Every pair of connected cells is represented by a single line in the 0-90° spread, respective to their unique ϕ angle. 0° represents planes that are perfectly parallel, while 90° represents perfectly perpendicular planes. Lines falling between the dashed 45° line and the 90° axis were classified as perpendicular, while lines falling between the dashed 45° line and the 0° axis were classified as parallel. (M-O) P0, P3, and P7 measurements were indicated by orange, cyan, and magenta lines, respectively, with colors from each developmental stage being preserved in (P) combined P0, P3, & P7 graphic. The percentages represent the proportion of parallel and perpendicular cell pairs there in respect to the total number of cell pairs found in each respective developmental stage.

These results showing that our connected cells are predominantly perpendicular in P0-P7 is in contrast with the previous reports showing either no bias between a perpendicular or parallel axis of cell division or a predominantly parallel axis (Haldipur et al., 2015; Miyashita et al., 2017) (**Figure 14, P**). The discovery that our TNT-like connected cells are significantly more likely to be perpendicular at P0-P7 points in development argues that these connections are unlikely to be generated by dividing cells. Our observations were reinforced by the identification of cells in division, found through identifying midbodies and electron-dense cluster of microtubules (**Figure 15**). While the connected cells followed the pattern of having a tendency towards perpendicular, the dividing cells showed no tendency for either perpendicular or parallel, similar to the dividing cells described by Haldipur et al., (Haldipur et al., 2015).

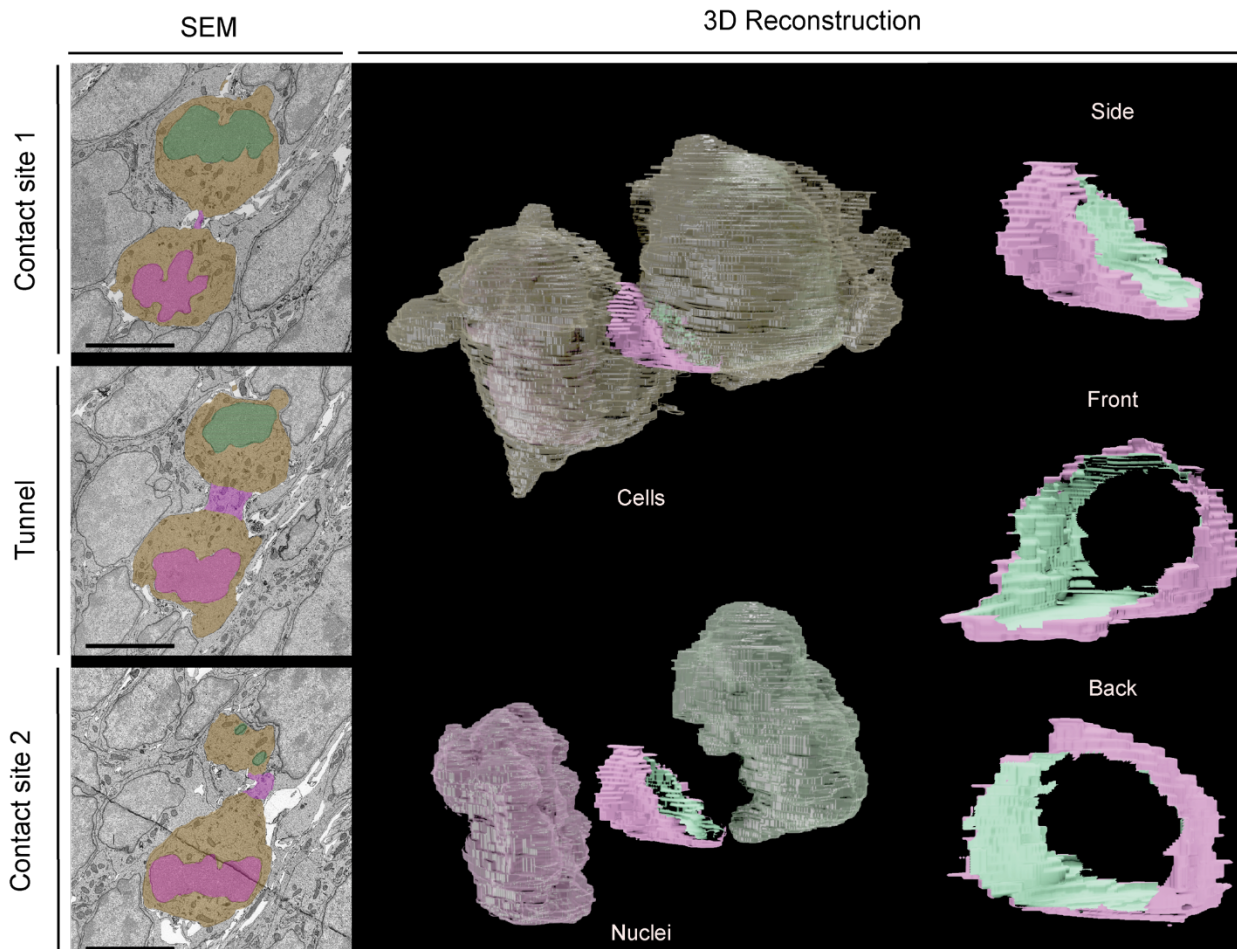


Figure 21. Identification of GCPs undergoing division.

P7 volume segmented SEM micrographs (showing the contact points and middle of the connection) and corresponding 3D reconstructions of cells, nuclei, and intercellular mitotic bridge in a cell about to undergo cytokinesis. The 3D reconstructions show the segmented cells, the segmented nuclei and connection, and different side perspectives of the connection.

4.2.5 Assessment of dividing GCPs in the EGL

Given that by using our morphological criteria we only identified a handful of GCPs undergoing division throughout our connectome screenings, we wondered if GCPs in the EGL tend to divide with a frequency that is lower when compared to the frequency of TNT-like connection between cell pairs described above. To this end, we examined the proliferation of GCPs in tissue slices of mice from the same developmental stages as those used for our connectome analysis via Phosphohistone H3 (PH3) staining, (a marker that labels cell cycle stages S, G2, and M).

We employed two analysis techniques – one focused on the total percentage of dividing cells and another using a method closer to the one applied to identify connections in ssSEM volumes (see methods). Using our first approach, we found that the average percent pixel density of PH3/DAPI+ cells to be 3.9%, 4.5%, and 5.1% in P0, P3, and P7 stages, respectively. Averages per stage range from 2-5% in P0, 4-5% in P3, and 4-6% in P7. Using our second approach, we found that the average percent of PH3+ cells out of 50 randomly selected DAPI cells to be 2.9%, 4.7%, and 7.3% in P0, P3, and P7 stages, respectively. Averages per stage range from 1-4% in P0, 4-6% in P3, and 7-9% in P7.

These findings demonstrate that the number of dividing GCPs in the EGL within the same regions used for our structural analysis to be substantially lower compared to the number of connected cells. The values we obtained by our connectomic approach (see Table 1) demonstrate higher percentage values of connected cells, most noticeably in P7. These findings strengthen our hypothesis that the structures we identified could be TNT-like structures and not simply remnants of cell division or stable intercellular bridges.

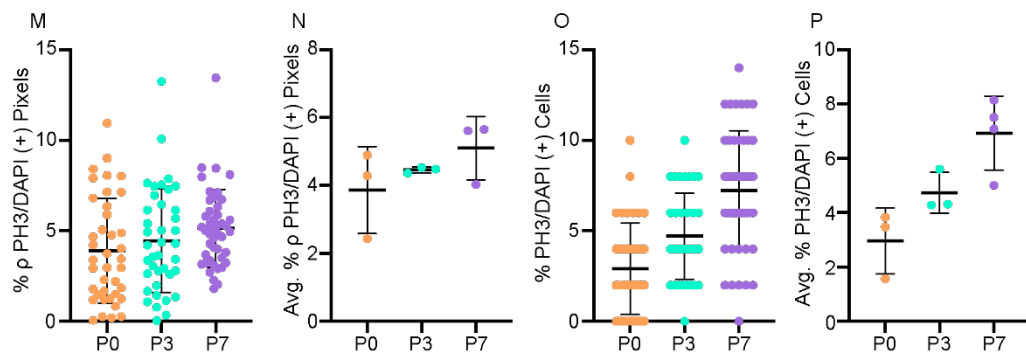
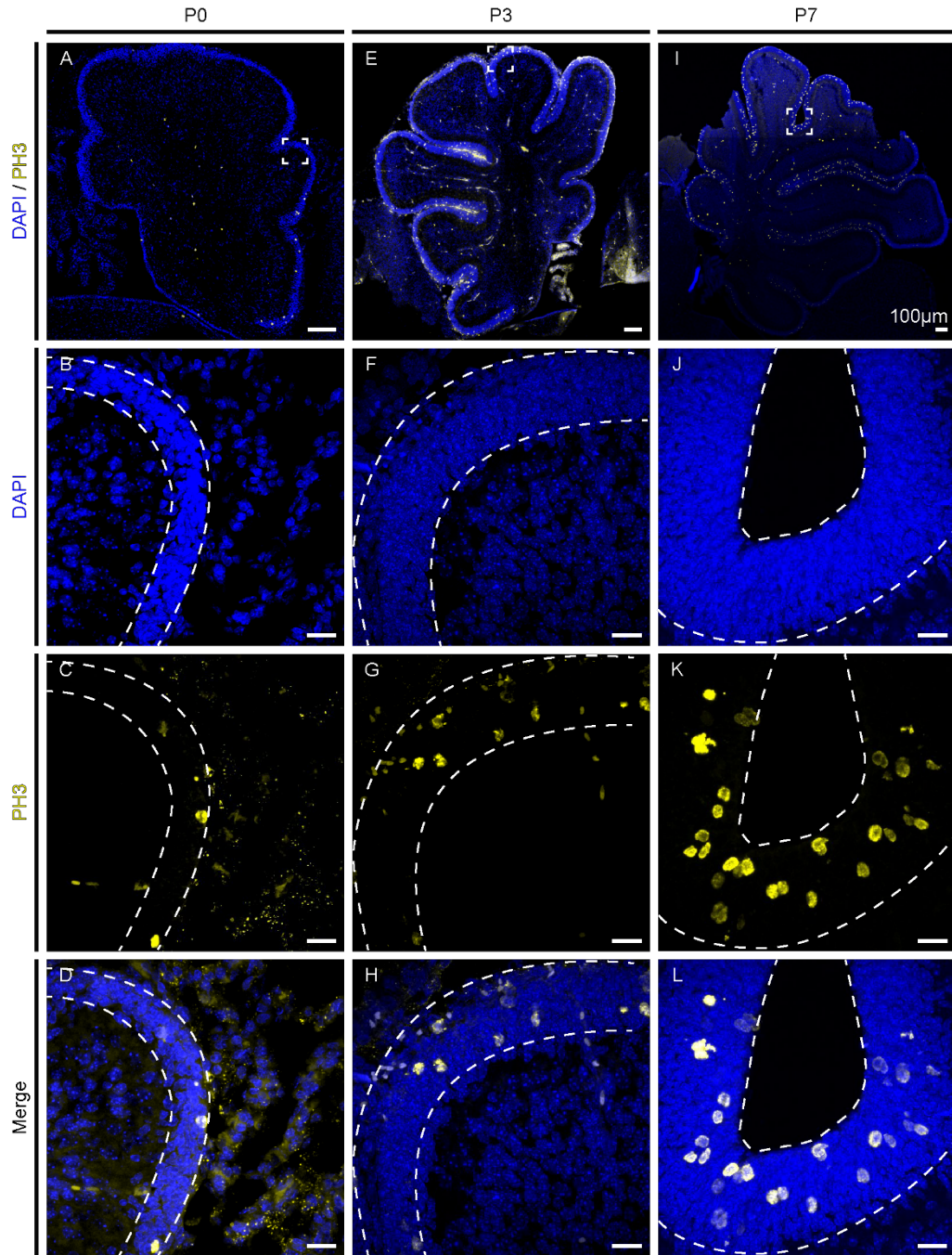


Figure 22. Quantification of PH3+ cells in the Developing Cerebellum.

(A) Representative micrograph of Phosphohistone H3 (PH3) immunohistochemistry (yellow) on P0 mouse cerebellum. Selected EGL region of interest for further imaging and analysis depicted within white box. (B) Magnified view of isolated DAPI channel of ROI depicted in A. (C) Isolated PH3 channel of selected ROI depicted in A and B. (D) Merged DAPI and PH3 channels of P0 cerebellar ROI. (E) Representative micrograph of Phosphohistone H3 (PH3) immunohistochemistry (yellow) on P3 mouse cerebellum. Selected EGL region of interest for further imaging and analysis depicted within white box. (F) Magnified view of isolated DAPI channel of ROI depicted in E. (G) Isolated PH3 channel of selected ROI depicted in E and F. (H) Merged DAPI and PH3 staining of P3 cerebellar ROI. (I) Representative micrograph of PH3 immunohistochemistry (yellow) on P7 mouse cerebellum. Selected EGL region of interest for further imaging and analysis depicted within white box. (J) Magnified view of isolated DAPI channel of ROI depicted in I. (K) Isolated PH3 channel of selected ROI depicted in I and J. (L) Merged DAPI and PH3 staining of P7 cerebellar ROI. (M) Mean and standard deviations of percentage PH3+/DAPI+ pixel density plotted for each age. (N) Average percentage PH3+/DAPI+ pixel density per brain (P0, n=3; P3, n=3; P7, n=4) plotted for each age. (O) Mean and standard deviations of percent PH3+ cells out of 50 randomly selected DAPI+ cells for each age. (P) Average percentage of PH3+ cells chosen out of 50 randomly selected DAPI+ cells per brain (P0 n=3; P3 n=3; P7 n=4) for each stage. Scale bar: A, E, I, 100 μ m; C, D, G, H, K, L, 20 μ m.

4.2.6 Dye-coupling reveals GCP TNT-like structure connectivity

In order to corroborate our findings with an alternative approach that would enable us to assess a larger number of samples, we investigated dye-coupling between GCPs in *ex vivo* cerebellar slices by 2-photon microscopy (see methods). To this end, we sectioned 250 μm acute parasagittal cerebellar slices from 6- to 8-day-old mice. We patch-loaded single GCPs in the EGL of distinct lobules with the fluorescence indicator Alexa 594 and imaged with two-photon laser scanning microscopy (2PLSM) in order to visualize the patched GC and potential connected cells. (**Figure 25A-B**).

In three independent set of experiments we performed to date, we patch-loaded a total of 30 cells. In our first session, we patched 5 GCPs located in the top two-three rows of the EGL (oEGL) and didn't identify any coupling (**Table 2**). Next, we patched 11 GCPs located in the mEGL and identified 7 (63%) GCPs coupled by long, thin, membranous-bound protrusions (**Figure 25C-E**). These structures spanned between 10 – 68.9 μm in length and 400 – 900 nm in diameter (**Table 3**). We observed that 2 out of the 3 GCPs patched coupled with cells in the iEGL using these connections that faced radial migration (**Figure 25B**), while only 1 coupled with a GCP found in the mEGL with a connection that faced tangential migration. Finally, we patched 14 GCPs in the lower 2-3 rows of the EGL (iEGL) and didn't identify any coupling (**Table 2**).

Assessing whether inter-cellular communication mediated by the exchange of cargo was not feasible by dye-coupling; however, in one of our examples (**Figure 25E**), we identified a bulge along one of the connections identified, resembling bumps previously indicative of cargo inside TNTs ([Sartori-Rupp et al., 2019](#)).

Table 2. Summary of patches.

	Outer EGL	Middle EGL	Inner EGL
# of patches	5	11	14
# of connections	0	4	0
# of GCPs connected	-	7	-
% of GCPs connected	-	63%	-

Table 3. Properties of TNT-like structures.

	Connection 1	Connection 2	Connection 3 & 4
# of GCPs connected	2	2	3
Length (μm)	10	68.9	30.6 (*), 32.5(**)
Thickness (nm)	600	900	400

We also found that although some cells visibly connected by TNT-like structures, some GCPs appeared coupled with GCPs immediately adjacent to them (**Figure 25C-H**). During the acquisition of one of our examples (**Figure 25G**), we observed that the pipette displaced the patched GCP and presumably fractured a connection bridging the two cells, leaving behind a gap between the protrusion emanating from the patched GCP and the GCP beside it. Whether internal connections of small size, such as those shown by EM, lie squeezed in-between the pairs of cells coupled was not evident with our imaging setup.

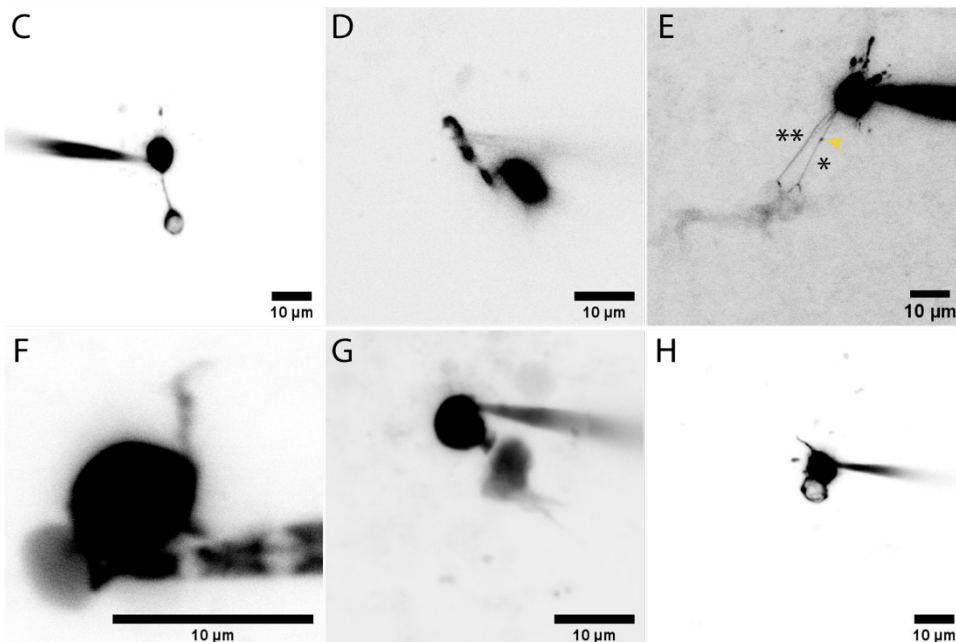
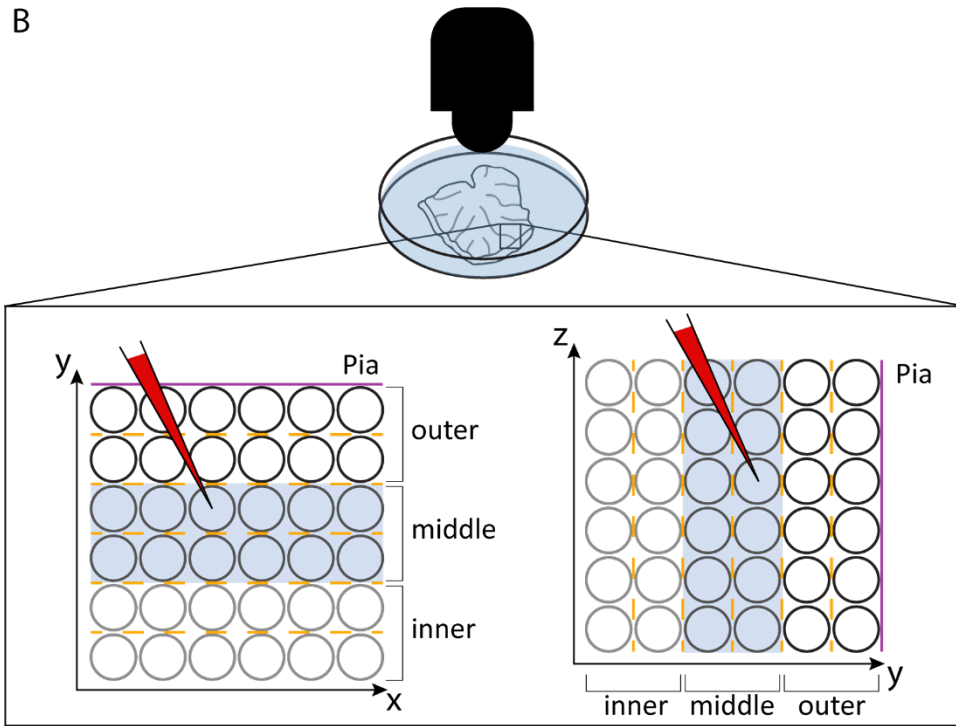
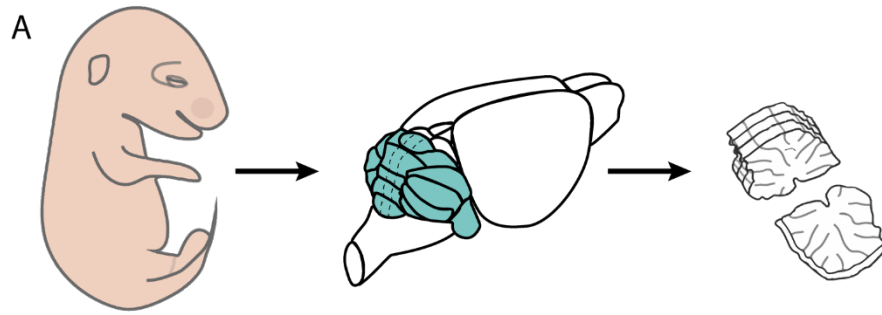


Figure 23. Dye-coupling between GCPs in the EGL reveal TNT-like structures.

(A-B) Schematic diagram displaying the workflow: Harvesting of cerebellar tissue from P6-P8 mice **(A)**, two-photon imaging of the slices in which we patched GCPs located in the EGL of the fissure between lobule VII and VIII. Patches were performed in GCPs located in the Outer, Middle, and Inner EGL, as shown by the diagram in **B** (x, y). In order to obtain complete GCPs and protrusions emanating from their soma, patches were performed in GCPs located deeper in the tissue (z, y), not on those at the surface. **(C-H)** 2-photon micrographs obtained from GCPs patched using the workflow shown in **A** and **B**. **(C)** GCP in the mEGL connected with GCP in the iEGL by a TNT-like structure of 10 μm in length and 600 nm in diameter. **(D)** GCP in the mEGL connected with GCP in the mEGL by a TNT-like structure of 68.9 μm in length and 900 nm in diameter. **(E)** GCP in the mEGL connected with GCP in the mEGL by a TNT-like structure of 30.6 (*), 32.5(**) and 400 nm in diameter. Yellow arrowhead indicates membrane bulge located along the TNT-like protrusion marked by '(*)', presumably cargo being transported along the connection as previously shown for TNTs *in vitro*. **(F-H)** Examples of patched GCPs appearing to be coupled with adjacent GCPs.

4.3 Methods

4.3.1 Connectomics

4.3.1.1 Sample preparation

A P0 CD1 wild-type mouse was anesthetized by hypothermia. The brain was harvested and post-fixed in paraformaldehyde/glutaraldehyde solution overnight at 4°C O/2N. Then, the cerebellum was cut into 300- μm-thick parasagittal sections using a Leica vibrating microtome. The cerebellum was vibratomed in ice-chilled cacodylate buffer solution. a section from the medial part of the vermis and stained it using a reduced osmium-thiocarbohydrazide (TCH)-osmium (ROTO). The ROTO protocol was used to improve membrane contrast further by double-labeling with osmium, using TCH as a link molecule. First, sections were incubated in 2% osmium tetroxide in 0.015 g/mL potassium ferrocyanide in 0.15-M NaCaco, 2-mM CaCl₂ buffer at 4 °C overnight. Then the sample was transferred to the buffer solution for 5 2-hour changes and incubated in 1% TCH in buffer that had been heated to 60 °C for 20 minutes. After washing the tissue again with buffer as described above, the tissue was incubated in 2% osmium tetroxide in buffer at 4 °C overnight. After staining and post-fixing with ROTO, we dehydrated the tissue by washing it in solutions of increasing ethanol content (5 minutes each in ice-cold solutions of 20%, 50%, 70%, 90%, 100%, and 100% ethanol in ddH₂O) and finally by placing the tissue in anhydrous acetone left at room temperature for 10 minutes. We then embedded the tissue in Epon 812 resin mixed according to formula that would result in a medium-to-hard cured product (Electron Microscopy Sciences). We embedded each section in a block of resin by introducing solutions of propylene oxide (PO). Using mixtures of PO and resin thus allows the resin to better penetrate spaces in the tissue. We washed each section 2 times for 5 minutes each in pure PO, then left it in 3:1 PO/resin solution under constant agitation for 1 hour, followed by 1:1 PO/resin under agitation overnight, then 1:3 PO/resin under agitation for 1 hour, then in 100% resin overnight. Finally, we embedded each section in a tube of fresh resin and cured the block at 60 °C for 48 hours.

Next, from each block of embedded tissue we cut a series of ultrathin, serial sections for imaging using an automatic tape-collecting ultra-microtome (ATUM). The ATUM combines an ultra-

microtome with a reel-to-reel tape collecting system so that sections can be continuously cut and collected on the tape with minimal user intervention. The ATUM allows many consecutive sections to be cut, collected onto a reel of tape, and then imaged. Image acquisition, stitching, and alignment of the volume was carried out as previously described (Wilson et al., 2019).

4.3.1.2 Image Visualization

Autodesk 3D Studio Max (3DS Max) is a powerful animation software used by game developers, animators, and other motion graphics purposes. It allows for not only the construction of complex 3D models like a traditional computer-aided design (CAD), but also provides the tools necessary for elaborate motion animation as well as the analysis of in-software structures. Our research relies upon the multiple facets of 3DS Max, not only utilizing it as a visualization method to reconstruct our EM segmentations, but also as a system to collect measurements needed to characterize the spatial arrangement of GCPs within the cerebellum (angle measurements). By using 3DS Max as a tool to collect data on the spatial orientation of TNT-like structures in the cerebellum and specifically the outer EGL, it is possible to cross reference findings with other previous studies about dividing cells.

4.3.2 Skeletonization

Access to Kimimaro skeletonization pipeline code for Python can be accessed, (link: <https://github.com/seung-lab/kimimaro>).

4.3.3 Angle Measurements

The fully-segmented collection of 2D layers, produced by serial sectioning of the EGL in VAST, is fused together in 3DS Max by using custom MatLab script (Berger et al., 2018), in order to produce a full 3D model of a neuronal cell. The MatLab script turns the stack of colored-in (segmented) layers from VAST into .obj files that can then be opened in 3DS Max. These .obj files are already automatically fused into the full 3D model, while preserving features such as the different “children” found in VAST, as well as their global orientation and overall positioning within the EM stack in VAST. This allows manipulation of the different parts of the cells (provided they are colored as different children), such as adjusting translucency, color, and appearance

individually, in order for the optimal animation. The preservation of position within the EM stack also allows for different .obj files to be imported while maintaining the same relative position to each other as in the cerebellum.

This characteristic thus makes it possible for spatial analysis of 3D models produced by .obj files in 3DS Max to accurately reflect that of their corresponding cells and segmentations in the EM stack in-vivo. Our research is novel as it adds in another factor of security into said analysis. Instead of simply measuring the spatial orientation in 2D in-vivo using immunohistochemistry like prior works, we will also do spatial orientation in-vivo, but in 3D instead, since the .obj files represent 3D objects themselves and occupy a 3D space. This gives us the unique opportunity to be the first team to classify and characterize cell orientation in the cerebellum using this more accurate new method. Once the .obj files of each cell are loaded onto 3DS Max, we first need to define how we will represent the orientation of the connected cells and the pia. The orientation of the pia is represented by a single plane (pia plane) that is tangential to the pia membrane at the point of the membrane that is closest in proximity to the connected cells. The orientation of the connected cells is represented by a single plane (cell plane) that divides the two as accurately as possible. Precision of the plane between different cell pairs called for the adoption of a standard, which entails that a line is drawn between the center of the nucleus of one connected cell to the nucleus center of the other connected cell. This serves as the line normal to the cell plane, and the alignment tool in 3DS Max allows for the cell plane to snap into the correct angular orientation when the x, y, and z angles mirror that of said nucleus-to-nucleus line.

Processing of the data created by this series of cell planes and pia planes is done by using the 3DS Max alignment tool to move both planes so that each respective plane's center shares the same point in 3D space, while maintaining their original orientation. Lines of fixed length that are normal to the planes are then added, with each line originating at the center of their respective planes. Each of these normal lines of fixed length are now representative of the angular orientation of their plane, and the angle between them is thus used as a means to find whether the cell plane and pia plane are parallel or perpendicular. If the angle between the normal lines originating at the same point is small ($<45^\circ$), then the planes are parallel, while if the angle of the normal lines is large ($>45^\circ$), then the planes are perpendicular. The use of a single angle

measurement to characterize objects in a 3D space is sufficient, because we only need to understand the position of the cell plane and the pia plane in relation to each other. Therefore, envisioning a spherical coordinate system (r , θ , ϕ) where the pia plane normal line represents $\phi=0$ and the cell plane normal line represents a variable ϕ , we can use the single ϕ angle as a metric for being parallel or perpendicular. If the cell plane normal line ϕ is close to 0° , that means the two normal lines are similar in orientation and thus the planes are parallel, while a ϕ close to 90° would indicate the planes are perpendicular to each other. This method of angle measurement is used as it is efficient in condensing a lot of data from the 3D space and turning it into a single usable metric. This is evident as we only have to use ϕ , with θ not affecting “perpendicularity” and thus allowing us to not have to consider it.

This method of measurement of angles was conducted in P0, P3, and P7 samples. The P0 EM stack yielded 5 connections to analyze, while the P3 yielded 4 connections, and the P7 yielded 22 connections to analyze. The method for referencing the angle in P0 samples was completed by fully coloring and segmenting every layer. The complete segmentation gave clear insight into the curvature of the pia at every point, as well as provided a clear tilt along every slice. The presence and visibility of the pia in the majority of slices of the P0 EM stack allowed us the opportunity to do this one extremely thoroughly, and thus is shown in a supplementary video. The method for referencing the angle in P3 samples was similar to P0, however consisted of segmented and colored layers in only specific areas. Due to issues with the visibility of the pia membrane, segmentation was conducted in chunks every 200-300 slices in the EM stack. As some sections of slices didn't show the pia membrane, segmenting was done in concentrations of 50-100 slices in strategic locations that did show the pia. This still allowed for sufficient awareness of both the pia membrane's curvature and tilt. The method for referencing angle in P7 samples took a combination of methods, as the P7 pia was only visible in the lower third of the slices of the EM stack. Therefore, seeing its general curvature was clear, but there weren't enough slices to fully assess the tilt of the pia. This called for segmenting one of the EM stack's parallel fibers, as they span the entirety of all the slices and are parallel to the pia, allowing us to infer the tilt of the pia from said parallel fibers.

4.3.4 Immunohistochemistry

Brains were removed from P0 (n=3), P3 (n=3), and P7 (n=4) mice pups and postfixed in 4% PFA/PBS overnight at 4°C, then cryopreserved with 20% sucrose. Sections (20 μm) were cut using a Leica cryostat, and mounted onto charged slides. Sections were permeabilized with 0.5% triton in PBS for 10 min and blocked with 2% BSA and 5% donkey serum in PBS for 1 hr at room temperature. Primary antibodies were prepared in blocking solution. Secondary antibodies were prepared in 1% BSA. Sections were incubated with primary antibodies for two nights at 4°C in a humidified chamber. Antibodies used were: Ki67 (Abcam 15580, 1:200), PH3 (Abcam 10543, 1:200), DCX (Abcam 150171, 4:200). All secondary antibodies were diluted 1:500, and incubated for 2 hr at RT. Nuclei were labeled with DAPI diluted 1:2000 for 5 minutes.

4.3.5 Microscopy

Brains were imaged using a Zeiss LSM 700 confocal microscope. P0 images were taken in middle of cerebellum to parallel P0 ROI in EM volume. P3 images were taken in Lobule 8 of cerebellum to parallel P3 ROI in EM volume. P7 images were taken in the fissure between lobules 7/8 to parallel P7 ROI in EM volume.

4.3.6 Image Analysis

Method 1: Images were first analyzed using a MACRO written on FIJI which quantifies an estimate for the amount of PH3+ cells. Because of the extremely high density of granule cells, DAPI cells could not be counted and compared with the number of PH3 positive cells. As most cells could not be properly dissociated from each other, we defined the cell density through the pixel density. The method used is based on utilizing an intensity thresholding and object filter using shape and size characteristic. For quantifying PH3+, we isolate the channel containing the signal PH3+ and we apply a maximum projection in order to get most of the cell signal. A light gaussian blur and background subtraction are applied before automatically thresholding the signal. All threshold objects that are small than a cell or have a too elongated shape are removed. For quantification of DAPI, a similar approach is applied. The user selects the plan to process, otherwise we take the middle of the volume. A light gaussian and background are applied, followed by a threshold. Small threshold objects are then removed. The user can then provide a

Region of Interest (ROI) to process. If no selection is provided, the entire image is used. A density value is computed with detected PH3+ pixels and the detected DAPI pixels on the ROI. We drew an ROI around a specific part of EGL in cerebella in all images and applied this approach to quantify an estimate for percent PH3+ cells.

Method 2: The second analysis approach was employed in order to better compare the data collected within this experiment with past experiments locating tunneling nanotubes in the EGL. It involved randomly choosing 50 DAPI+ cells within the same ROI's of the cerebella and counting how many of these cells are PH3+ throughout the Z-Stack.

4.3.7 Dye Coupling

Acute cerebellar parasagittal slices (250 μm thick) were prepared from immature (postnatal day 6-8) C57B6 mice. Mice were killed by decapitation, the brains rapidly removed and placed in an ice-cold solution containing (in mM): 85 NaCl, 2.5 KCl, 0.5 CaCl₂, 4 MgCl₂, 1.25 NaH₂PO₄, 24 NaHCO₃, 25 glucose, and 75 sucrose, bubbled with 95% O₂ and 5% CO₂. Slices were cut from the dissected cerebellar vermis using a vibratome (Leica VT1200S), incubated at 32°C for 30 minutes before being maintained at room temperature for up to 8 hours in the recording solution containing (in mM): 125 NaCl, 2.5 KCl, 2 CaCl₂, 1 MgCl₂, 1.25 NaH₂PO₄, 25 NaHCO₃, and 25 glucose.

Whole-cell patch-clamp recordings were made from GCs located in the external granule cell layer at temperatures ranging from 33 to 36°C using a Multiclamp 700 amplifier (Axon Instruments, Foster City, Ca, USA) with fire-polished thick-walled glass patch-electrodes (tip resistances of 7-8 M Ω) that were backfilled with a solution containing (in mM): 105 K-MeSO₄, 40 HEPES, 6 NaOH, 5 EGTA, 1.78 CaCl₂, 4.6 MgCl₂, 1 QX-314-Cl, 0.3 NaGTP, 4 NaATP, and 0.03 Alexa 594, adjusted to ~285 mOsm and pH 7.3. Series resistance and capacitance measures were determined directly from the amplifier settings; no series resistance compensation was used.

4.4 Discussion

Connectomics is the study of connectomes: comprehensive maps of connections within the CNS (Lichtman and Sanes, 2008). ssSEM emerged as an unparalleled tool to study connectomes at sufficient resolution to reconstruct entire neuronal diagrams at the synaptic vesicle level within a ‘relatively’ small region of the brain (Kasthuri et al., 2015). On the premise that this method offers the advantage to preserve fine neuronal processes (e.g. dendritic spines) and circumvents the need for TNT-specific markers by labeling everything membranous (Morgan and Lichtman, 2017), we sought out to investigate whether connectomics could also reveal the existence of TNT-like structures *in vivo*, which would otherwise be inaccessible.

Based on our *in vitro* work showing that TNTs form and enable inter-cellular communication in the undifferentiated, neuroblast-like non-polarized CAD (Abounit et al., 2016; Costanzo et al., 2013; Delage et al., 2016; Gousset et al., 2013; Gousset et al., 2009; Zhu et al., 2018; Zhu et al., 2015) and SH-SY5Y cells (Dilsizoglu Senol et al., 2019; Sartori-Rupp et al., 2019), and most recently, undifferentiated hNPCs (Grudina et al., 2019) and primary cortical neurons (Vargas et al., 2019), we hypothesized that neuronal precursors in the brain with similar topological and genetic profiles could also generate and utilize these processes before establishing synaptic communication. Using this criterion, we focused our efforts on the EGL of the developing cerebellum, a transitory sub-region of the cerebellar cortex in which millions of GCs proliferate extensively before relocating to the IGL through elegantly orchestrated migratory events aided by BG (Galas et al., 2017).

The aim of this work was to produce a mineable EM dataset obtained from the EGL of a P0 neonate mouse of sufficient scale to capture hundreds of GCPs in the process of division (oEGL) and migration (iEGL). To scale up our investigations in a manner that would substantially increase our likelihood of detecting these connections, we extended our study onto two other postnatal developmental stages, P3 and P7, using volumes that were previously produced but never used for these type of investigations (Wilson et al., 2019).

To this end, we investigated the presence of TNT-like structures by manually tracing the cell soma of GCPs and processes emanating from them in the EGL (both i- and o-EGL) of all three

volumes. As hypothesized, we observed that TNT-like connections of various lengths and thicknesses formed between GCPs in the EGL across all of the developmental stages studied. Surprisingly, we observed a surge in the formation of these structures over development, notably at P7. Although these connections were never previously described, one possibility that we considered is that they were remnants of cytokinesis. In this case, one possible explanation for the higher number of connections at P7 could be that GCPs tend to divide more at the base of the fissure than at the crown of the lobe. However, previous studies have shown that GCPs located in fissures express a higher mitotic index only until E18.5 (Sudarov and Joyner, 2007), arguing against the likelihood that our connected GCPs are cells in division, tethered by a stable intercellular bridge or remnant of cytokinesis (McLean and Cooley, 2014).

In order to further investigate this matter, we decided to better characterize the proliferative profile of GCPs in cerebellar tissue slices of mice obtained from the same region and developmental stages as those used for our connectomic analyses by quantifying the percentage of GCPs that expressed PH3, a marker that labels cell cycle stages S, G2, and M. Our data indicates that the rate of proliferation between P0 and P7 has a slight tendency to increase, supporting previous published data (Sudarov and Joyner, 2007). These findings are consistent with the knowledge that fissures serve as anchor points for lobules to continue to grow past P7, until the second and third week of development. However, comparing our PH3 data with our connectomic analyses revealed substantial differences between the percentage of cells in division vs. the number of cells connected by ssSEM, whereby 2.9% divide vs. 8.7% connect in P0; 4.7% divide vs. 12% connect in P3; and 7.3% divide vs. 80% connect in P7. Although these results cannot prove that our connected GCPs by ssSEM are not dividing cells, they suggest that (at least the majority of) our connections do not derive from mitosis.

It is also conceivable that the increased number of cells connected in our datasets result from post-mitotic, non-PH3 expressing, GCPs 'holding on to' their intercellular bridges formed by incomplete cytokinesis (McLean and Cooley, 2014). To the best of our knowledge, there isn't any published evidence to support intercellular bridges or ring canals forming between cerebellar GCPs, as these processes have been majorly described in germline and invertebrate somatic cells (e.g. during *Drosophila* oogenesis) (Haglund et al., 2011). Based on the topological criteria

employed to investigate these types of bridges, our connections differ in two significant ways: 1) intercellular bridges are short (0.4-1.8 μm) whereas our connection can exceed 4 μm in length; 2) intercellular bridges display electron-dense outer rims, our connections do not. In order to unequivocally assess the presence and longevity of stable intercellular bridges in the EGL, we plan to perform experiments and examine the expression of Aurora B kinase and Kif20b, markers previously used to effectively label midbodies in the embryonic mouse cerebral cortex ([Janisch and Dwyer, 2016](#)).

Another consideration that we must take into account when interpreting our results is that although all three volumes were obtained from the same region in the cerebellum (vermis of lobule VIII), our analyses were carried out in three slightly distinct regions of one lobule, (crown of folia in P0; edge of the crown in P3; and base of the fissure in P7). Differences in the cytoarchitecture between these different regions might offer the potential to generate useful insights as to whether GCPs could form more/less TNT-like connections depending on where they locate in the lobule.

In an attempt to further characterize our TNT-like connections and test alternative methods to distinguish them from cell division remnants, we decided to classify our ssSEM connected cells according to their spatial orientation in 3D in relation to the pial membrane, using similar approaches used before to classify dividing cells ([Haldipur et al., 2015](#); [Miyashita et al., 2017](#)). Our preliminary data clearly indicate that our cells connected arrange mainly perpendicular to the pia, while the axis of cell division at the stages of development studied were found either non-biased or parallel. These observations were reinforced by the identification of very few cells in division in our ssSEM data, found through identifying midbodies with electron-dense cluster of microtubules. Furthermore, our preliminary data shows that the GCPs we classified as 'dividing', based on the morphological features of intercellular bridges, were oriented randomly in respect to the Pia, in agreement with the dividing cells previously described ([Haldipur et al., 2015](#)).

Although our ssSEM data provided us with hints regarding the role these connections might play in inter-cellular communication and transport of cargo (shown by the presence of mitochondria and vesicles within our connections, we decided to study GCPs in living conditions

and test whether these are functional; that is, capable of transporting or diffusing cargo, we patch-clamped GCPs in the EGL of P6-P8 cerebellar slices and filled them with a fluorescent dye. Our preliminary results revealed dye-coupling between GCPs via TNT-like structures that proved to be open-ended. These connections shared similar thicknesses with TNTs *in vitro* (Gousset et al., 2009), and our connections by ssSEM; however, we observed two differences between our findings using these two different approaches: 1) live-TNTs measure long lengths and 2) form networks of more than two cells, our ssSEM connections do not. This discrepancy can be explained by several factors: (i) our ssSEM datasets span 45 – 75 μm in which long connections would leave the volume and become untraceable; (ii) sample preparation deformation during specimen dehydration and embedding suggest that our (ssSEM) connections could have represented longer connections that shrank substantially; (iii) distortion during sample preparation could have also fractured long connections due to harsh shearing forces that are known to break, bend, and tear TNTs *in vitro* (Rustom et al., 2004; Sartori-Rupp et al., 2019). Interestingly, our patch-clamping data indicates that GCPs that connect via TNT-like connections lie at the middle of the EGL, somewhere along the interface between the o- and iEGL. These observations are in agreement with our ssSEM findings, which also show that 54% of GCPs at P7 locate in the middle of the EGL. Altogether, these observations suggest that TNT-like structures could serve as inter-cellular avenues for GCPs to share information associated with changes in their microenvironment, specifically with respect to the transition between progenitor and migratory state (oEGL and iEGL, respectively). However, further experiments are required to sustain this hypothesis and support these preliminary findings.

In this study, we also attempted to extrapolate geometrical information such as the length and thickness from the 3D meshes obtained by our ssSEM reconstructions via *TEASER*-based *Kimimaro* skeletonization algorithms. We have successfully tested our skeletonization pipeline on a handful of TNT-like structures and obtained accurate length measurements with success; however, our current algorithm only computes the min, mean, and max diameter of our connections. After observing that the diameter of our connections shifts along their length, and when they contain cargo within, (as we also observed *in vitro*, (Sartori-Rupp et al., 2019)), we plan to implement an additional tool that can yield skeleton ‘branches’. These branch-wires

would sprout from the single-wire trunk every n-number of nm along the connection in order to provide us with a radii distribution description of the diameter of our connections.

We also plan to focus on strategies that can increase our throughput. For example, one of the obstacles we face is (i) the time it requires to screen our ssSEM volumes for TNT-like connections between GCPs and (ii) fully tracing/segmenting GCPs after they were found connected. Over the course of this study, we have manually segmented dozens of cells, nuclei, and TNT-like structures that serve as ground-truth for the adaption and implementation of robust automatic segmentation algorithms based on ML (Plaza and Funke, 2018). We are now currently working on applying these approaches on our volumes. Once completed, these algorithms will have the ability to automatically identify and segment TNT-like structures without human input. This approach will be tremendously useful to examining the presence of TNT-like structures in other ssSEM volumes where no connections of this type were ever described, including the fruit fly brain (Zheng et al., 2018), and larval fish (Hildebrand et al., 2017).

From the days of Cajal (Cajal, 1888), neuroscientists have been fascinated with understanding how the brain is wired. The advent of Connectomics has expanded our knowledge of these wires and provided unprecedented context to the remarkable drawings of Cajal. Taking advantage of the benefits offered by the tools used by Connectomics, specifically ultra-high resolution ssSEM and computational processing and reconstructions, we sought out to investigate the presence of TNT-like structures in the GCP subset of the developing cerebellum. Our findings shed light on processes that were never previously described in GCPs, cerebellar development, or brain tissue. Presently, we cannot be certain that there isn't an underlying developmental significance that could explain these findings; therefore, extending this study to other brain area and developmental stages and testing whether these TNT-like connections are functional needs to be addressed. Nonetheless, the identification of these structures has the potential to shift the paradigm and change the way in which we think about brain connectivity.

4.5 References

- Abounit, S., Bousset, L., Loria, F., Zhu, S., de Chaumont, F., Pieri, L., Olivo-Marin, J.C., Melki, R., and Zurzolo, C. (2016). Tunneling nanotubes spread fibrillar alpha-synuclein by intercellular trafficking of lysosomes. *The EMBO journal* 35, 2120-2138.
- Berger, D.R., Seung, H.S., and Lichtman, J.W. (2018). VAST (Volume Annotation and Segmentation Tool): Efficient Manual and Semi-Automatic Labeling of Large 3D Image Stacks. *Front Neural Circuits* 12, 88.
- Bock, D.D., Lee, W.C., Kerlin, A.M., Andermann, M.L., Hood, G., Wetzel, A.W., Yurgenson, S., Soucy, E.R., Kim, H.S., and Reid, R.C. (2011). Network anatomy and in vivo physiology of visual cortical neurons. *Nature* 471, 177-182.
- Cajal, S.R. (1888). Sobre las fibras nerviosas de la capa molecular del cerebelo. In *Rev Trimest Histol Norm Patol* pp. 2:33-49
- Costanzo, M., Abounit, S., Marzo, L., Danckaert, A., Chamoun, Z., Roux, P., and Zurzolo, C. (2013). Transfer of polyglutamine aggregates in neuronal cells occurs in tunneling nanotubes. *J Cell Sci* 126, 3678-3685.
- Delage, E., Cervantes, D.C., Penard, E., Schmitt, C., Syan, S., Disanza, A., Scita, G., and Zurzolo, C. (2016). Differential identity of Filopodia and Tunneling Nanotubes revealed by the opposite functions of actin regulatory complexes. *Scientific reports* 6, 39632.
- Dilsizoglu Senol, A., Pepe, A., Grudina, C., Sassoon, N., Reiko, U., Bousset, L., Melki, R., Piel, J., Gugger, M., and Zurzolo, C. (2019). Effect of tolytoxin on tunneling nanotube formation and function. *Scientific reports* 9, 5741.
- Disanza, A., Bisi, S., Winterhoff, M., Milanesi, F., Ushakov, D.S., Kast, D., Marighetti, P., Romet-Lemonne, G., Muller, H.M., Nickel, W., *et al.* (2013). CDC42 switches IRSp53 from inhibition of actin growth to elongation by clustering of VASP. *The EMBO journal* 32, 2735-2750.
- Espinosa, J.S., and Luo, L. (2008). Timing neurogenesis and differentiation: insights from quantitative clonal analyses of cerebellar granule cells. *The Journal of neuroscience : the official journal of the Society for Neuroscience* 28, 2301-2312.
- Fox, C.A., and Barnard, J.W. (1957). A quantitative study of the Purkinje cell dendritic branchlets and their relationship to afferent fibres. *Journal of anatomy* 91, 299-313.

Galas, L., Benard, M., Lebon, A., Komuro, Y., Schapman, D., Vaudry, H., Vaudry, D., and Komuro, H. (2017). Postnatal Migration of Cerebellar Interneurons. *Brain sciences* 7.

Gousset, K., Marzo, L., Commere, P.H., and Zurzolo, C. (2013). Myo10 is a key regulator of TNT formation in neuronal cells. *J Cell Sci* 126, 4424-4435.

Gousset, K., Schiff, E., Langevin, C., Marijanovic, Z., Caputo, A., Browman, D.T., Chenouard, N., de Chaumont, F., Martino, A., Enninga, J., *et al.* (2009). Prions hijack tunnelling nanotubes for intercellular spread. *Nat Cell Biol* 11, 328-336.

Grudina, C., Kouroupi, G., Nonaka, T., Hasegawa, M., Matsas, R., and Zurzolo, C. (2019). Human NPCs can degrade alpha-syn fibrils and transfer them preferentially in a cell contact-dependent manner possibly through TNT-like structures. *Neurobiol Dis*, 104609.

Haglund, K., Nezis, I.P., and Stenmark, H. (2011). Structure and functions of stable intercellular bridges formed by incomplete cytokinesis during development. *Commun Integr Biol* 4, 1-9.

Haldipur, P., Sivaprakasam, I., Periasamy, V., Govindan, S., and Mani, S. (2015). Asymmetric cell division of granule neuron progenitors in the external granule layer of the mouse cerebellum. *Biol Open* 4, 865-872.

Hase, K., Kimura, S., Takatsu, H., Ohmae, M., Kawano, S., Kitamura, H., Ito, M., Watarai, H., Hazelett, C.C., Yeaman, C., *et al.* (2009). M-Sec promotes membrane nanotube formation by interacting with Ral and the exocyst complex. *Nat Cell Biol* 11, 1427-1432.

Hildebrand, D.G.C., Cicconet, M., Torres, R.M., Choi, W., Quan, T.M., Moon, J., Wetzel, A.W., Scott Champion, A., Graham, B.J., Randlett, O., *et al.* (2017). Whole-brain serial-section electron microscopy in larval zebrafish. *Nature* 545, 345-349.

Janisch, K.M., and Dwyer, N.D. (2016). Imaging and quantitative analysis of cytokinesis in developing brains of Kinesin-6 mutant mice. *Methods in cell biology* 131, 233-252.

Kasthuri, N., Hayworth, K.J., Berger, D.R., Schalek, R.L., Conchello, J.A., Knowles-Barley, S., Lee, D., Vazquez-Reina, A., Kaynig, V., Jones, T.R., *et al.* (2015). Saturated Reconstruction of a Volume of Neocortex. *Cell* 162, 648-661.

Komuro, H., and Kumada, T. (2005). Ca²⁺ transients control CNS neuronal migration. *Cell Calcium* 37, 387-393.

Komuro, H., and Yacubova, E. (2003). Recent advances in cerebellar granule cell migration. *Cell Mol Life Sci* 60, 1084-1098.

Lackey, E.P., Heck, D.H., and Sillitoe, R.V. (2018). Recent advances in understanding the mechanisms of cerebellar granule cell development and function and their contribution to behavior. *F1000Res* 7.

Lichtman, J.W., and Sanes, J.R. (2008). Ome sweet ome: what can the genome tell us about the connectome? *Curr Opin Neurobiol* 18, 346-353.

Manto, M., Bower, J.M., Conforto, A.B., Delgado-Garcia, J.M., da Guarda, S.N., Gerwig, M., Habas, C., Hagura, N., Ivry, R.B., Marien, P., *et al.* (2012). Consensus paper: roles of the cerebellum in motor control--the diversity of ideas on cerebellar involvement in movement. *Cerebellum* 11, 457-487.

McLean, P.F., and Cooley, L. (2014). Bridging the divide: illuminating the path of intercellular exchange through ring canals. *Fly* 8, 13-18.

Miyashita, S., Adachi, T., Yamashita, M., Sota, T., and Hoshino, M. (2017). Dynamics of the cell division orientation of granule cell precursors during cerebellar development. *Mech Dev* 147, 1-7.

Morgan, J.L., and Lichtman, J.W. (2017). Digital tissue and what it may reveal about the brain. *BMC biology* 15, 101.

Plaza, S.M., and Funke, J. (2018). Analyzing Image Segmentation for Connectomics. *Front Neural Circuits* 12, 102.

Rustom, A., Saffrich, R., Markovic, I., Walther, P., and Gerdes, H.H. (2004). Nanotubular highways for intercellular organelle transport. *Science* 303, 1007-1010.

Sartori-Rupp, A., Cordero Cervantes, D., Pepe, A., Gousset, K., Delage, E., Corroyer-Dulmont, S., Schmitt, C., Krijnse-Locker, J., and Zurzolo, C. (2019). Correlative cryo-electron microscopy reveals the structure of TNTs in neuronal cells. *Nat Commun* 10, 342.

Sato, M., Bitter, I., Bender, M.A., A.E., K., and M., N. (2000). TEASAR: Tree-structure Extraction Algorithm for Accurate and Robust Skeletons. *Proc 8th Pacific Conf on Computer Graphics and Applications*.

Schmidt, H., Gour, A., Straehle, J., Boergens, K.M., Brecht, M., and Helmstaedter, M. (2017). Axonal synapse sorting in medial entorhinal cortex. *Nature* 549, 469-475.

Sudarov, A., and Joyner, A.L. (2007). Cerebellum morphogenesis: the foliation pattern is orchestrated by multi-cellular anchoring centers. *Neural development* 2, 26.

Vargas, J., Loria, F., Wu, Y., Córdova, G., Nonaka, T., Bellow, S., Syan, S., Hasegawa, M., van Woerden, G., Trollet, C., *et al.* (2019). The Wnt/Ca²⁺ pathway is involved in interneuronal communication mediated by tunneling nanotubes. *EMBO J.*

Wilson, A.M., Schalek, R., Suissa-Peleg, A., Jones, T.R., Knowles-Barley, S., Pfister, H., and Lichtman, J.W. (2019). The rich get richer: synaptic remodeling between climbing fibers and Purkinje cells in the developing cerebellum begins with positive feedback addition of synapses. *bioRxiv*, 627299.

Zheng, Z., Lauritzen, J.S., Perlman, E., Robinson, C.G., Nichols, M., Milkie, D., Torrens, O., Price, J., Fisher, C.B., Sharifi, N., *et al.* (2018). A Complete Electron Microscopy Volume of the Brain of Adult *Drosophila melanogaster*. *Cell* 174, 730-743 e722.

Zhu, H., Xue, C., Xu, X., Guo, Y., Li, X., Lu, J., Ju, S., Wang, Y., Cao, Z., and Gu, X. (2016). Rab8a/Rab11a regulate intercellular communications between neural cells via tunneling nanotubes. *Cell Death Dis* 7, e2523.

Zhu, S., Bhat, S., Syan, S., Kuchitsu, Y., Fukuda, M., and Zurzolo, C. (2018). Rab11a-Rab8a cascade regulates the formation of tunneling nanotubes through vesicle recycling. *J Cell Sci* 131.

Zhu, S., Victoria, G.S., Marzo, L., Ghosh, R., and Zurzolo, C. (2015). Prion aggregates transfer through tunneling nanotubes in endocytic vesicles. *Prion* 9, 125-135.

Zilles, K. (2018). Brodmann: a pioneer of human brain mapping-his impact on concepts of cortical organization. *Brain* 141, 3262-3278.

Zonouzi, M., Berger, D., Jokhi, V., Kedaigle, A., Lichtman, J., and Arlotta, P. (2019). Individual Oligodendrocytes Show Bias for Inhibitory Axons in the Neocortex. *Cell Rep* 27, 2799-2808 e2793.

5 Dissertation Perspectives

5.1 Conclusion and future work

During my dissertation work, I participated in three projects: (1) the role of actin regulatory networks in neuronal TNT formation, which resulted in an article entitled “Differential identity of Filopodia and Tunneling Nanotubes revealed by the opposite functions of actin regulatory complexes”, of which I am a co-second author; (2) the ultra-structural analyses of neuronal TNTs, which resulted in a second article entitled “Correlative cryo-electron microscopy reveals the structure of TNTs in neuronal cells”, of which I am a co-first author; and (3) the search for TNT-like structures *in vivo* using a *Connectomic* approach, work that is currently in progress.

My first project was conceived and designed to investigate the underlying mechanism of neuronal cells’ TNT formation in contrast to those engaged in filopodia formation. Our work elucidated the opposite role the CDC42/IRSp53/VASP and Eps8 actin regulatory complexes play in the formation of these two structures. In summary, when we overexpressed the CDC42/IRSp53/VASP complex in neuronal CAD cells, we observed a decrease in the number of TNT-connected cells (Delage et al., 2016), opposite from what others previously described for filopodia (Disanza et al., 2013). Similarly, overexpressed Eps8 increased the number of TNT-connected cells, once again, opposite from what the literature reported about the role of Eps8 in the formation of filopodia. These findings led us to hypothesize that TNTs and filopodia of neuronal cells form through distinct molecular pathways and with actin-regulatory proteins behaving in different manners.

My specific role in this project was to examine the role of Rac1 by testing whether its overexpression would affect the generation of TNTs. My results show that Rac1 negatively regulates TNT formation in a similar fashion as CDC42. These findings reinforced our previous data and our hypothesis that filopodia and TNTs harness distinct mechanisms of formation as well as the necessary evidence to recognize TNTs as *bona fide* organelles, and not specialized filopodia. Interestingly, our combined results disagree with those shown by Hanna et al., (Hanna et al., 2017), which indicate that TNT formation in immune cells require CDC42 and Rac1 for their formation, and suggest a cell-specific underlying pathway activated to generate TNTs. This was

supported by other studies, most notably as seen for M-Sec, which was shown to be involved in the formation of TNTs in immune cells (Hase et al., 2009) but not neuronal cells (Gousset et al., 2013). Furthermore, a ground-breaking study by Sowinski et al., (Sowinski et al., 2008) demonstrated that TNTs of immune T cells have a filopodia-like, close-ended tip. Therefore, it is conceivable that TNTs of immune and neuronal cells are equipped with distinct protein arsenals that yield two distinct structures: one close- and one open-ended structure, respectively. These observations led me to study the structure of TNTs in neuronal cells, whose anatomy had never been explored in detail.

To this end, my second project was devised to study the ultra-structure of TNTs in a correlative fashion and with sufficient resolution to compare the actin cytoskeletal topology of TNTs vs. filopodia, assess whether TNTs transport cargo and organelles within its narrow constitution, and investigate whether TNTs connect the cytoplasmic lumen of two (or more) cells via an open-ended connection. To our surprise, our experiments not only revealed that the actin arrangement in TNTs looked notably straight compared to filopodia's, but also shed light on a TNT-specific arrangement we called *iTNTs*, (individual-TNTs), a bundle of several TNTs bundled together. Given that no previous studies had employed the cryo-EM-based approaches that we used, it's currently beyond the bounds of possibility to ascertain that iTNTs are specific to neuronal cells, even though the work by Sowinski et al., (Sowinski et al., 2008) provide structural evidence of single TNTs. To ensure that our observations were not specific to cells of mouse origin, an important goal of this study was to analyze the structure of TNTs in different cell types. Immuno-gold labeling and cryo-EM tomography revealed that N-Cadherin served as links to support and presumably 'stabilize' iTNTs. Based on these observations, we now hypothesize that N-Cadherin interactions could be responsible for establishing (actin-driven mechanism-led) TNTs during their formation by growing filopodia that pull each other towards their cell somas and forming iTNTs upon fusion. Some of my lab peers are now testing this hypothesis. Our analyses also showed that vesicles and organelles squeeze between actin filaments and the membrane that make-up iTNTs, creating bulges along the connection that can also be detected by optical microscopy. Furthermore, in our correlative study, we demonstrate that the actin-based motor protein, MyoX, localizes with vesicles inside iTNTs. Cryo-ET micrographs also showed short electron dense

connections between actin and MyoX-positive vesicles. Whether MyoX carries vesicles inside TNTs needs to be further demonstrated, as it's not currently clear which motors allow the transfer of organelles through the actin-cytoskeleton of TNTs, in particular mitochondria. Finally, by FIB-SEM we demonstrated that iTNTs connect neuronal cells via open-ended tubes, a long standing question in the TNT field. This finding supports a large number of live-imaging and FACS studies from our group showing that cargo gets transported between neuronal cells via TNTs. To scale-up the structural approaches used for this project and investigate the presence of TNTs *in vivo*, I sought out to employ a large-scale, high-resolution ssSEM-based approach devised to study the brain neural wiring, *Connectomics*.

Unlike classical ssTEM previously employed to study TNTs *in vitro* by [Rustom et al., 2004](#) and [Sowinski et al., 2008](#), or even FIB-SEM volumetric imaging utilized for part of my second project described above [Sartori-Rupp et al., 2019](#), ssSEM Connectomics allowed me to investigate TNTs in tissue with a high-throughput, ultra-high-resolution, *in vivo*-optimized approach of significant size to obtain quantitative results. My studies on the cerebellar GCPs reveal TNT-like connections, uninterrupted by GJs or synaptic-like clefts. Many of the connections identified contain vesicles and mitochondria, suggesting that cargo can move along these connections and possibly get transported. The immunohistological and dye-coupling preliminary data presented in this thesis suggests that these connections are unlikely to derive from cytokinesis during cell division; however, future studies will have to examine and better test this possibility. Finally, streamlining the skeletonization methods to obtain accurate geometrical measurements will help us characterize and categorize our observations, and teach us about the heterogeneity of connections in the cerebellum. Although many questions remain open about the possible function these connections play during migratory events in the cerebellum, our findings provide new insights on GCP-to-GCP communication that did not exist prior to this study.

Taken together, my dissertation examined specific questions about TNT formation, structure, and presence *in vivo*. I consider these investigations to have been a worthwhile effort to understand how these organelles function. As a result of these studies, new avenues and projects have spurred in our group, demonstrating the usefulness of the studies described in this thesis.

Mapping Tunneling Nanotubes *In Vitro* & *In Vivo*: A Structural Approach

Keywords: Tunneling Nanotubes, Actin, Neuronal communication, Cerebellum, Connectomics

Abstract: Inter-cellular communication has long been thought to be governed by juxta-, endo-, and paracrine signaling, tight junctions, and more recently, exosomes. However, large efforts from our and other groups revealed that Tunneling Nanotubes (TNTs), actin-rich membranous protrusions that connect the cytoplasm of distant cells and allow the dynamic inter-cellular transport of biological cargo, also provide the infrastructure and machinery for effective cell-to-cell communication. Despite significant progress made to unveil TNT-mediated cell communication, the characterization of these novel organelles has been limited by unanswered questions that hail from the lack of both molecular and structural information. Exploring these gaps in the field using a series of state-of-the-art tools and novel approaches became the main focus of my dissertation. Specifically, I explored the specific role of actin-regulator complexes in the formation of TNTs connecting neuronal cells. My analyses show that molecular pathways known to be involved in the formation of other membranous protrusions behave differently in the generation of TNTs. By employing live imaging microscopy, cryo-correlative electron microscopy and tomography approaches, I also studied the nano-architecture of neuronal TNTs. My findings demonstrated that TNTs of neuronal cells are comprised of multiple individual TNTs capable of transporting vesicles and mitochondria. Owing to the difficulties of identifying TNTs *in vivo*, my work also focused on the implementation of a structural *Connectomic* approach to detect TNTs in tissue without the need for a TNT-specific marker. My findings indicate that TNT-like structures connect migratory cerebellar granule cells of neonate mice, suggesting that inter-cellular communication during migratory events in the brain could be mediated by TNT-like processes. Skeletonization of the structures identified provide my findings with geometrical information that can be compared with observations made by corroborative dye-coupling experiments. Taken together, my dissertation work sheds light on the formation and structure of neuronal TNTs *in vitro*, and novel approaches for the identification of TNTs *in vivo*.